



UNIVERSITY OF
KWAZULU-NATAL
INYUVESI
YAKWAZULU-NATALI

Production of Nanocellulose Composites and Catalytic and Microbial Applications

by

Vashen Moodley

2017

Thesis submitted in fulfilment of the academic requirements for the degree of
Doctor of Philosophy

School of Chemistry & Physics, College of Agriculture, Engineering and Science, University
of KwaZulu-Natal, Durban

As the candidate's supervisor, I have approved this dissertation for submission.



Prof. W. E. van Zyl

22 January 2018

Date

Abstract

This study describes the preparation, isolation, characterization and application of polysaccharide based nanocrystalline cellulose (NCC) from two source materials (filter paper and bleached pulp). The isolated NCCs were utilized as a composite/support material. Hydroxyapatite (HAp), titanium(IV) oxide (anatase phase, TiO₂) and biologically synthesized silver nanoparticles were chosen as the preferred candidates for the incorporation of NCC into their respective matrices, which allowed for the preparation of three new materials. These newly prepared composites were applied in catalytic and anti-microbial studies.

NCC formed the basis of this investigation and was prepared *via* a common acid hydrolysis treatment, using sulfuric acid as the preferred acid hydrolytic medium. The isolated NCCs were obtained in reasonable yields and were characterized using the following techniques: ATR-FTIR, XRD, TEM, HRTEM, FEGSEM equipped with EDX detector, TGA/DTA, NTA (zeta potential) and BET. The rod-shaped particles revealed a high crystallinity, small crystallite sizes and good thermal stabilities. These results led to use the prepared NCC's as a composite material in the pursuit to prepare a new class of materials with a potential array of applications.

The preparation of HAp and subsequently the NCC/HAp (in varied wt%) composite allowed for the use of this newly synthesized material as a versatile catalyst. The catalyst was well characterized and used in the preparation of the two-component one-pot synthesis of triazolidine-3-one derivatives. Preliminary reaction optimization established that the 40 w/w% NCC/HAp composite catalyst returned the best results. The eleven new triazolidine-3-one derivatives (**4a** - **4k**) were synthesized in good yields and maintained good atom economy. The catalyst proved to be an effective tool in this protocol with the supplementary advantage of being recyclable. This approach to organic multicomponent reactions (MCRs) proved to be a cost-effective strategy and allowed for an easy work up with environment-friendly reaction conditions. Compared to non-catalytic protocols this approach required shorter reaction times.

With the prospect of employing the optical properties of the prepared NCC, TiO₂ was then considered for the use in the second newly prepared composite material as a potential photo-catalyst. The NCC/TiO₂ material was synthesized in varying wt% and was characterized *via* a number of optical, spectroscopic and microscopic techniques to establish if it possessed the potential to be used as a photo-catalyst. Proceeding this evaluation, the NCC/TiO₂ material was used in the solar-driven photo-degradation mineralization of *o*-chloranil (2,3,5,6-

tetrachloro-2,5-cyclohexadiene-1,4-dione), a commonly used pesticide. The successful decomposition of *o*-chloranil led to the identifiable products to 2,3-dichloro-4,5-dioxohex-2-enedioic acid (DCA), 2,3-dioxosuccinic acid (DSA) and oxalic acid (OA). This proved that the 20 w/w% NCC/TiO₂ composite could be employed as a successful photo-catalyst, and in particular that NCC could be used as a successful composite material together with TiO₂. The rate of degradation was influenced by various parameters such as substrate concentration and photo-catalyst loading. The intermediate product (DCA) formed during the decomposition process was assumed to slow down the progression of the reaction and provided a useful insight into the degradation pathway of the contaminant.

The final study demonstrated the synthesis of silver nanoparticles (AgNPs) *via* a biological (phyto-mediated) route using *Lippia javanica* plant extract (LPE). The preparation of the colloidal AgNPs involved a variation in the LPE (100 – 400 µL) and AgNO₃ (1 – 10 mM) concentration to determine the ideal morphology of AgNPs formed. This biosynthetic approach proved successful in the formation of AgNPs in colloidal form, with superior advantages over the chemical formation. These AgNPs were used in several applications as demonstrated with the inclusion of NCC as a support. Samples were characterized *via* optical, spectroscopic and microscopic analyses, with the ideal colloidal solution **C9** (400 µL LPE, 10 mM AgNO₃) established as providing the greatest number of AgNPs with the lowest size. This colloid was chosen for the further incorporation of NCC. NCC (filter paper source) was then incorporated into the quasi-spherical shaped nanoparticle matrix and further characterized, analysed and applied as a catalyst to the synthesis of benzylidene-bis-(4-hydroxycoumarin) derivatives and as a potential bactericidal agent. All colloidal samples were biologically tested against 5 bacterial strains and demonstrated good activity, however, samples with the highest concentration of AgNPs were chosen for further Minimal Bactericidal Concentration (MBC) testing. The results showed that all samples were superior in relation to their anti-biotic counterparts used as standards. Sample **C9e** (1000 mg NCC, 4 mL of LPE in 10 mL of 10 mM AgNO₃ and made up to 50 mL), proved to be an efficient catalyst for a three-component reaction. This led to the catalytic preparation of nine benzylidene-bis-(4-hydroxycoumarin) derivatives (**6a – 6i**).

Declarations

Declaration 1: Plagiarism

I, Vashen Moodley, declare that:

1. The research reported in this thesis, except where otherwise indicated, is my original research.
2. This thesis has not been submitted for any degree or examination at any other university.
3. This thesis does not contain other persons' data, pictures, graphs or other information unless specifically acknowledged as being sourced from other persons.
4. This thesis does not contain other persons' writing unless specifically acknowledged as being sourced from other researchers. Where other written sources have been quoted, then:
 - a. Their words have been re-written but the general information attributed to them has been referenced
 - b. Where their exact words have been used, then their writing has been placed in italics and inside quotation marks and referenced.
5. This thesis does not contain text, graphics or tables copied and pasted from the Internet, unless specifically acknowledged, and the source being detailed in the thesis and in the References sections.

Signed

Vashen Moodley

Declaration 2: Publications

DETAILS OF CONTRIBUTION TO PUBLICATIONS that form part and/or include research presented in this thesis.

Publication 1 (published)

Vashen Moodley, Suresh Maddila, Sreekantha B. Jonnalagadda, Werner E. van Zyl. **Synthesis of triazolidine-3-one derivatives through the nanocellulose/hydroxyapatite-catalyzed reaction of aldehydes and semicarbazide.** *New Journal of Chemistry* **2017**, *41 (14)*, 6455-6463.

Contributions: I carried out the synthesis and characterisation of the materials and compounds. I also prepared and modified the draft through to publication.

Publication 2 (manuscript in preparation)

Vashen Moodley, Suresh Maddila, Sreekantha B. Jonnalagadda, Werner E. van Zyl. **Solar Photocatalytic Degradation of o-Chloranil on nanocrystalline Cellulose Doped Titania.**

Contributions: I carried out the synthesis and characterisation of the materials and isolated degradation compounds. I also prepared and modified the draft toward the publication paper.

Publication 3 (manuscript in preparation)

Vashen Moodley, Werner E. van Zyl. **Bioactivity and catalyzed synthesis of biscoumarin derivatives using biologically synthesized silver nanoparticles supported by nanocrystalline cellulose.**

Contributions: I carried out the synthesis and characterisation of the materials and compounds. I also prepared and modified the draft toward the publication paper.

DETAILS OF CONTRIBUTION TO PUBLICATIONS that does not form part and/or include research presented in this thesis.

Publication 1 (published)

Ramakanth Pagadala, Suresh Maddila, Vashen Moodley, Werner E. van Zyl, Sreekantha B. Jonnalagadda. **An efficient method for the multicomponent synthesis of multisubstituted pyridines, a rapid procedure using Au/MgO as the catalyst.** *Tetrahedron Letters.* **2014**, *55 (29)*, 4006-4010.

Contributions: I carried out the synthesis and characterisation of the catalyst. Dr Pagadala prepared the compounds involved in this publication as well as prepared and modified the draft through to publication.

Publication 2 (published)

Vashen Moodley, Londiwe Mthethwa, Michael N. Pillay, Bernard Omondi, Werner E. van Zyl. **The silver(I) coordination polymer [AgO₂PPh₂]_n and unsupported Ag...Ag interactions derived from aminophosphinate and phosphinic acid.** *Polyhedron* **2015**, *99*, 87-95.

Contributions: I carried out the synthesis and characterisation of the two compounds. I also prepared and modified the draft through to publication. Ms Mthetwa carried out the synthesis and characterisation of one compound. Drs. Pillay and Omondi provided X-ray crystallographic analysis.

Publication 3 (published)

Mohan Varkolu, Vashen Moodley, Fezile S. W. Potwana, Sreekantha B. Jonnalagadda, Werner E. van Zyl. **Esterification of levulinic acid with ethanol over bio-glycerol derived carbon-sulfonic-acid.** *Reaction Kinetics, Mechanisms and Catalysis* **2017**, *120 (1)*, 69-80.

Contributions: I carried out certain characterisation of the catalyst as well as certain reaction optimizations. Dr Potwana carried out certain reaction optimizations. Dr Varkolu carried out the synthesis and certain characterisations of the catalyst and prepared and modified the draft through to publication.

Publication 4 (published)

Segun A. Ogundare, Vashen Moodley, Werner E. van Zyl. **Nanocrystalline cellulose isolated from discarded cigarette filters.** *Carbohydrate Polymers.* **2017**, *175*, 273-281.

Contributions: I carried out certain characterisation of the isolated nanocrystalline cellulose. Mr Ogundare carried the synthesis and certain characterisation of prepared NCC and prepared and modified the draft through to publication.

Signed: _____

Declaration 3: Conference proceedings

1. Vashen Moodley, Werner E. van Zyl. Novel Silver(I) Amidophosphine- And Gold(I) Dithiophosfonate Complexes. (Poster presented at 41st International Conference on Coordination Chemistry (ICCC41), Singapore, 2014.)

To my family

“Nature uses only the longest threads to weave her patterns, so each small piece of her fabric reveals the organization of the entire tapestry.”

Richard P. Feynman

“Education is the most powerful weapon which you can use to change the world.”

Nelson R. Mandela

Acknowledgements

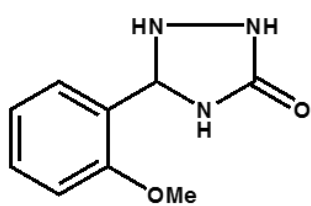
I would like to take this opportunity to acknowledge following people and extend my sincere gratitude for helping me make this **PhD** thesis a possibility.

- To my parents and family, thank you for your patience, support and the opportunities that you afforded me through my endeavours. Words on a piece of paper cannot express my gratitude.
- Prof. Werner E. van Zyl, for his guidance and mentorship. I thank you for your encouragement during my research and allowing me to grow as a scientist. Your invaluable advice and constructive criticisms is a testament to this thesis.
- To my best friend and better half, Hegandrie. Thank you for your love, support and understanding during this undertaking.
- Dr Suresh Maddila, Dr Mohan Varkolu, Dr Kranthi Gangu, Dr Surya Maddila and Prof. Sreekantha B. Jonnalagadda. I thank you for the knowledge and wisdom imparted to me during my research.
- Dr Magdi Gibril, Dr Viren Chunilall, Dr Prabashni Lekha and Prof. Bruce Sithole. Thank you for insight into the field of nanocellulose and for assisting me in obtaining the bleached pulp.
- Dr Moses A. Ollengo, Prof. Bice S. Martincigh, Prof. Vincent O. Nyamori and the UKZN nanotechnology platform for assistance during this endeavour.
- Prof. Neil A. Koorbanally and Dr Chunderka Mocktar for assistance during anti-bacterial studies.
- Ms Nelisha Murugan, Mr Vishal Bharuth, Mr Phillip Christopher and Mr Subashen Naidu from the EM Unit (UKZN, Westville Campus). Thank you for your assistance with electron microscopy and imparting your expertise on to me.
- Mr Dilip Jagjivan, Mr Raj Somaru, Mrs Malini Padyachee, Mrs Anita Naidoo, Ms Unathi Bongoza, Mr Kishore Singh, Mrs Vashti Reddy, Mr Gregory Moodley, Mr

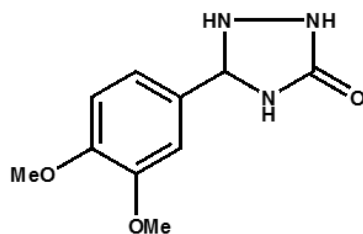
Miler Nundkumar, Mr Shannon Soodeyal and Mr Mpho Sehoto for their support, and willingness to assist me with minuscule tasks during the course of this work.

- My friends and lab-mates Ashiq, Chrisanne, Denisha, Drushan, Emmanuel, Eric, Fezile, Harinarayana, Kaalin, Kadwa, Kavashan, Kershen, Kyle, Lewis, Lynette, Michael, Nadia, Sachen, Samashen, Sandeep, Saravanan, Segun, Sicelo, Shirveen, Thaveshan, Tomilola, Tonderai, Veresha, Vincent, Vishalin and Yashmika who in some small part made an invaluable contribution.
- The technical and academic staff at UKZN, School of Chemistry and Physics, Westville Campus.
- The University of KwaZulu-Natal.
- CSIR: Forest and Fisheries.
- The National Research Foundation/Department of Science and Technology (NRF/DST) for financial support through an Innovation and Scarce Skills Scholarship.

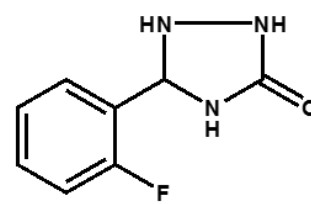
List of Molecular Compounds



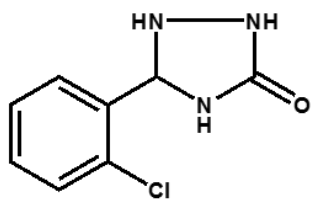
4a



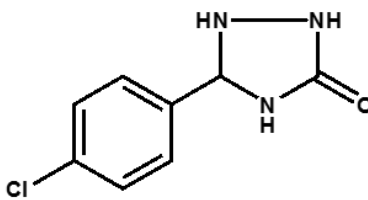
4b



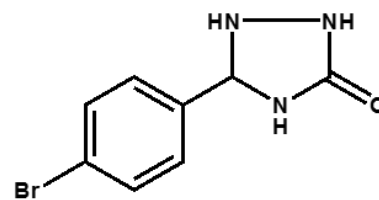
4c



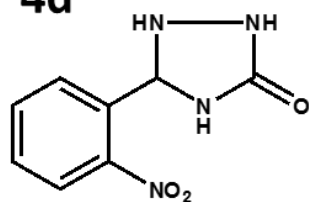
4d



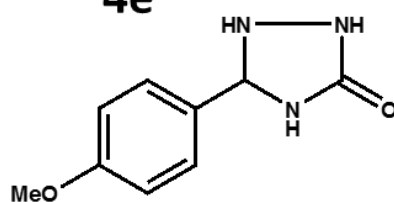
4e



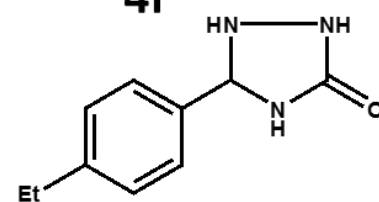
4f



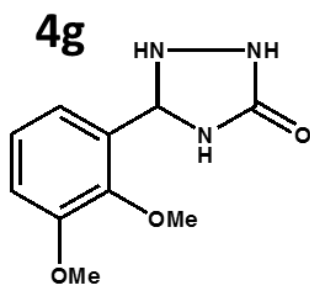
4g



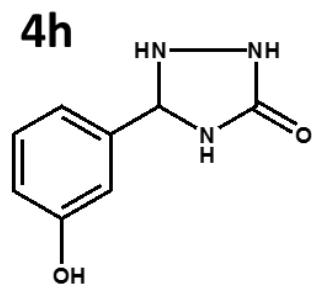
4h



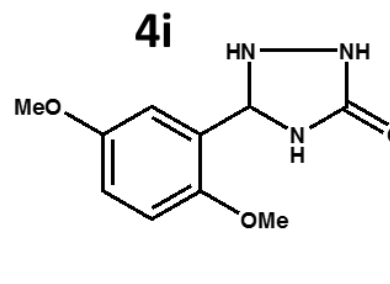
4i



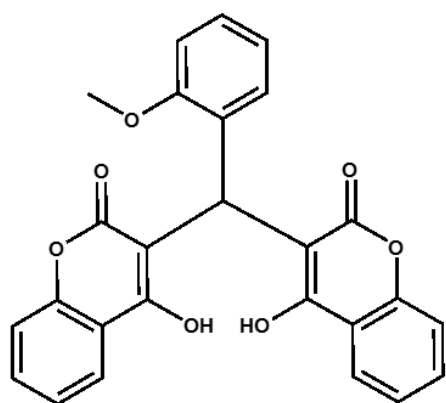
4j



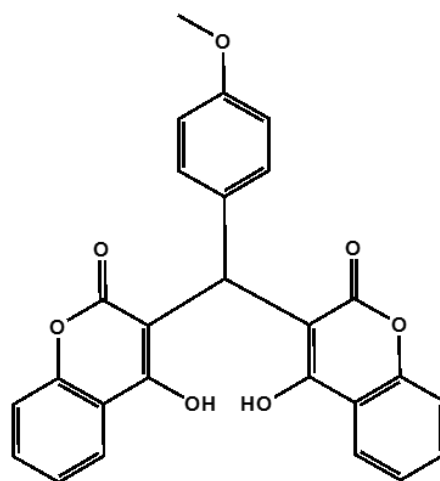
4k



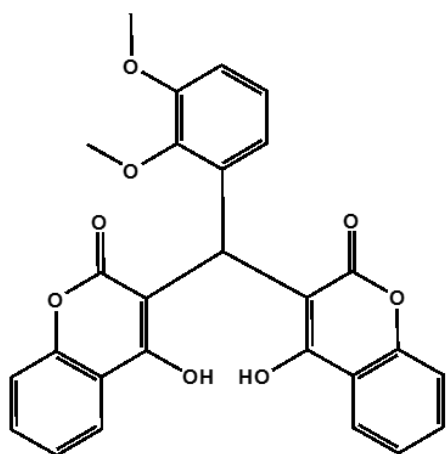
4l



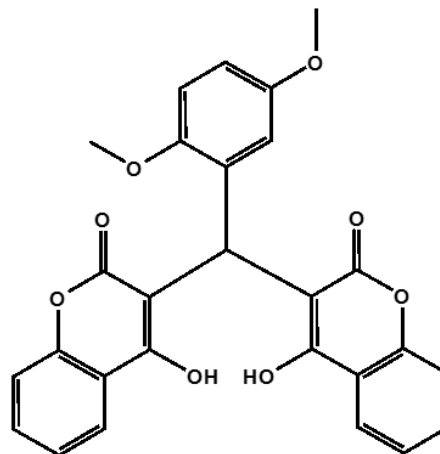
6a



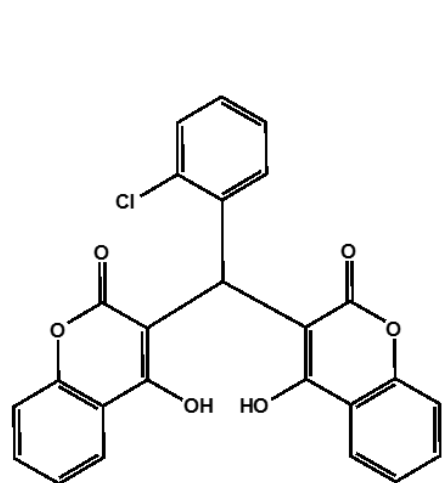
6b



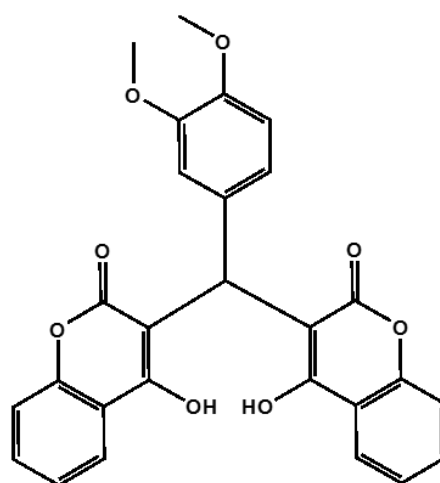
6c



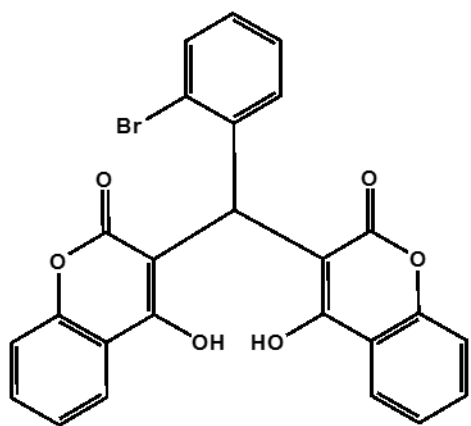
6d



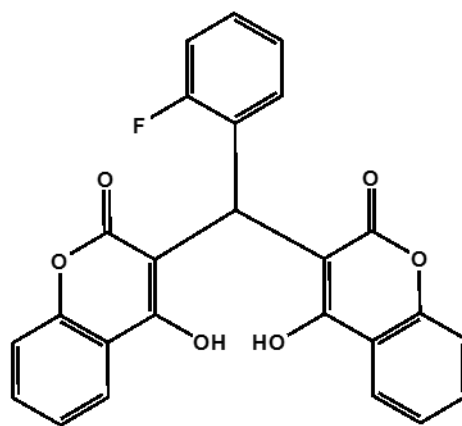
6e



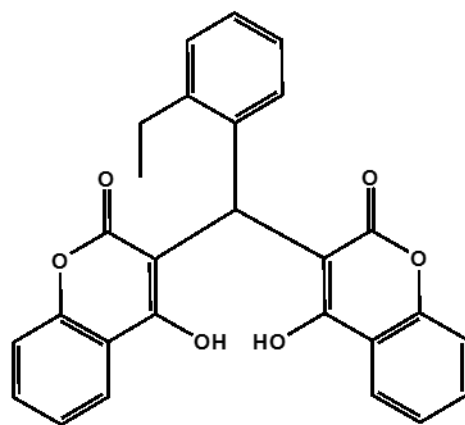
6f



6g



6h



6i

List of Figures

Figure 1.1. Set-up for the solar driven photodegradation of <i>o</i> -chloranil.....	5
Figure 1.2. TEM micrograph of particles with different shapes from highest concentration	6
Figure 2.1. Glucose, cellobiose and linear cellulose molecular chain	10
Figure 2.2. Schematic of (a) idealized cellulose microfibril showing one of the suggested configurations of the crystalline and amorphous regions, and (b) cellulose nanocrystals after acid hydrolysis dissolved the disordered regions)	11
Figure 2.3. Packing arrangement of cellulose I α and I β (viewed along the fibre direction). redrawn from crystallographic open database using the crystallographic information file (CIF) for each system (Cellulose I α CIF: 411438225b and Cellulose I β CIF: 411499425a)	14
Figure 2.4. Unit cell structure of cellulose I α and I β	15
Figure 2.5. Hydrogen bonding system in native cellulose crystalline structure: the OH \cdots O bonds dominate the intra-sheet interaction (interaction of cellulose chains within the same sheet), CH \cdots O and van der waals collectively are responsible for the inter-sheet interaction (interaction of cellulose chains between two different sheets).	17
Figure 2.6. Three possible conformations at C6 primary hydroxyl group.....	18
Figure 2.7. Schematic representation of the classification of the composition (consisting of the polysaccharides and lignin) found within the secondary cell wall of spruce (softwood) tracheids	19
Figure 2.8. Images of different types of nanocelluloses	20
Figure 2.9. Classification of nanocellulose fabrication approaches (top-down and bottom-up).....	23
Figure 2.10. Scheme depicting the general approach toward the preparation of cellulose-based nanocomposites by solvent casting	30
Figure 3.1. Tem micrographs derived from (a) whatman® filter paper, (b) soft wood kraft pulp and (c) discarded cigarette filters	52
Figure 3.2. ATR-FTIR Spectra Of NCC-FP And NCC-BP.....	59
Figure 3.3. TEM And HR-TEM* micrographs of NCC-BP (A), NCC-BP (B), NCC-FP (C) And NCC-FP (D).	60
Figure 3.4. Lengths, Widths And Aspect Ratios Distributions Of The Isolated NCCs From Fp (A And B) And Bp (C And D).	61
Figure 3.5. SEM Micrographs Of NCC-FP (A) And NCC-BP (B). Inset: Corresponding EDX Spectrum.	62
Figure 3.6. X-Ray diffractograms of the isolated NCCs. inset: corresponding gaussian fit.....	63
Figure 3.7. Thermograms (A) and DTA Curves (B) of the isolated NCCs	65
Figure 3.8. Bet isotherms of the isolated NCCs [FP (a) and BP (b)]. inset: corresponding pore size distribution.	66

Figure 3.9. Zeta potential plots of the isolated NCCs [BP (a) and FP (b)]. particle size distribution of the isolated NCCs [BP (c) and FP (d)].	67
Figure 4.1. Powder X-ray diffractograms of pure HAp, 40% NCC/HAp and spent catalyst.	92
Figure 4.2. TEM micrograph of 40% NCC/HAp catalyst, (a) unstained and (b) stained	93
Figure 4.3. (a) SEM micrograph and (b) EDS spectra of 40% NCC/HAp catalyst.	94
Figure 4.4. N ₂ adsorption-desorption isotherms and (inset) pore size distribution of 40% NCC/HAp catalyst.	95
Figure 4.5. Recyclability of NCC/HAp catalyst.	96
Figure 4.6 N ₂ sorption of 40% NCC/HAp spent catalyst.	96
Figure 5.1. ATR-FTIR spectra of prepared NCC/TiO ₂ photo-catalysts	108
Figure 5.2. N ₂ adsorption-desorption isotherm plots of synthesized catalysts with pore volume density (insets)	110
Figure 5.3. TEM micrographs of unstained and stained 10% (2a-2b), 20% (2c-2d), 40% (2e-2f) and 80% (2g-2h) NCC/TiO ₂ catalysts. bare TiO ₂ (2i) and NCC (2j) are shown.	111
Figure 5.4. Particle size distribution graphs of 10% (a), 20% (b), 40% (c) and 80% (d) NCC/TiO ₂ catalysts.	112
Figure 5.5. SEM micrographs of 10%, 20%, 40% and 80% (a-d) NCC/TiO ₂ catalysts. bare TiO ₂ (e) and NCC (f). magnification (g-h).	113
Figure 5.6. SEM-EDX mapping of 10% NCC/TiO ₂ .	114
Figure 5.7. The P-XRD pattern of (inset) pure NCC bare TiO ₂ (anatase), 10%, 20%, 40% and 80% NCC-TiO ₂ .	115
Figure 5.8. UV-DRS of bare TiO ₂ and synthesized (% w/w) NCC doped TiO ₂ catalysts	116
Figure 5.9. Photoluminescence spectra of bare TiO ₂ and synthesized (% w/w) NCC doped TiO ₂ catalysts	116
Figure 5.10. Influence of the amount of catalyst loading on the <i>o</i> -chloranil photo-degradation.	117
Figure 5.11. The photo-degradation <i>o</i> -chloranil as a function of time	118
Figure 5.12. Degradation products confirmed by gas chromatography (5.12a) and lc mass spectra of degradation products (5.12b, 5.12c and 5.12d)	119
Figure 6.1. (a) Flowers and leaves of <i>lippia javanica</i> (burm.f.) spreng. (photographer: BT Wursten) ³⁵ and (b) <i>l. javanica</i> herbal tea known as Zumbani. ³⁶	130
Figure 6.2. Coumarin (2 <i>H</i> -1-benzopyran-2-ones) moiety	133
Figure 6.3. ATR-FTIR spectra of (a) <i>l. javanica</i> plant extract (lpe), (b) agnp synthesized from plant extract (c9)	143
Figure 6.4. ATR-FTIR spectra of prepared ncc supported agnp (C9e) and bare ncc prepared from filter paper	144
Figure 6.5. TEM micrographs and corresponding particle size distribution of colloids C1 (a-b), C2 (c-d), and C3 (e-f).	146

Figure 6.6. UV-Vis spectra of colloids C1 – C3, after (a) 24 hours and (b) 7 days.....	147
Figure 6.7. TEM micrographs and corresponding particle size distribution of colloids C4 (a-b), C5 (c-d), and C6 (e-f).....	148
Figure 6.8. UV-Vis spectra of colloids C4 – C6, after (a) 24 hours and (b) 7 days.....	148
Figure 6.9. TEM micrographs and corresponding particle size distribution of colloids C7 (a-b), C8 (c-d), and C9 (e-f).....	149
Figure 6.10. UV-Vis spectra of colloids C7 – C9, after (a) 24 hours and (b) 7 days.....	149
Figure 6.11. TEM micrographs of stained and unstained colloids C9a (a-b), C9b (c-d), C9c (e-f), C9d (g-h), and C9e (i-j).	152
figure 6.12. particle size distribution of colloids C9a (a), C9b (b), C9c (c), C9d (d), and C9e (e)....	153
figure 6.13. UV-Vis spectra of colloids C9a – C9e, after (a) 24 hours and (b) 7 days.	154
Figure 6.14. SEM micrographs of colloids C9a (a), C9b (b), C9c (c), C9d (d) and C9e (e)	155
Figure 6.15. SEM micrographs of (a) colloid C9e (crushed and seived) and (b) C9e (film).....	156
Figure 6.16. (a) SEM micrograph of cross-section of C9e sample, (b) SEM-EDX elemental analysis of cross-section of C9e sample and (c) SEM-EDX mapping of cross-section of C9e sample with each present mapped element (d) oxygen, (e) carbon and (f) silver.....	156
Figure 6.17. The P-XRD pattern of bulk sample C9e and dried colloidal sample C9 (in bulk)	157
Figure 6.18. TEM micrograph of dried sample colloids C9e (a) and corresponding particle size distribution (b).....	158
Figure 6.19. Recyclability of NCC supported agnp catalyst.....	163

List of Schemes

Scheme 1.1. Isolation of NCC from bleached pulp	3
Scheme 1.2. Simplistic representation of the NCC/HAp catalysed formation 1,2,4-triazolidin-3-one derivatives.	4
Scheme 1.3. Preparation of the <i>Lippia javanica</i> plant extract: (a) <i>Lippia javanica</i> (Burm.f.) Spreng, (b) drying of the stems and leaves, (c) crushed sample of stems and leaves, (d) aqueous extract of <i>Lippia javanica</i> , (e). Synthesis of silver colloids using <i>Lippia javanica</i> plant extract, (f) synthesis of silver colloids using <i>Lippia javanica</i> plant extract.....	6
Scheme 4.1. Synthesis of 1,2,4-triazolidin-3-one derivatives.....	86
Scheme 4.2. Proposed mechanism for the formation of triazolidine-3-one derivatives using a NCC/HAp catalyst.....	91
Scheme 5.1. The proposed mechanism for the photo-degradation <i>o</i> -chloranil.....	120
Scheme 6.1. Formation of AgNP with the introduction of NCC into samples with (a) an external reduction source, (b) a modified nanocellulose surface as the reducing agent and (c) unaltered nanocellulose as the reducing agent.....	151
Scheme 6.2. Synthesis of benzylidene-bis-(4-hydroxycoumarin) derivatives.....	159
Scheme 6.3. The proposed mechanism for the formation of benzylidene-bis-(4-hydroxycoumarin derivatives.	162

List of Tables

Table 3.1. Lengths (nm) and Widths (nm) of NCCs from different sources.	54
Table 3.2. Mean lengths (nm), widths (nm) and aspect ratios (L/W) of the isolated NCCs.	59
Table 3.3. Elemental compositions of NCC-FP and NCC-BP from EDX.	62
Table 3.4. Crystalline indices and crystallite sizes of the isolated NCCs.	62
Table 3.5. The results of TGA, DTA and kinetic parameters of the isolated NCCs.	64
Table 4.1. Optimal condition for the synthesis of 3a by 40% NCC/HAp catalyst ^a	87
Table 4.2. Optimization of various solvent conditions for 40% NCC/HAp catalyst ^a	88
Table 4.3. Optimization of various weight % for 40% NCC/HAp catalyst ^a	89
Table 4.4. Synthesis of triazolidine-3-one derivatives with NCC/HAp catalyst ^a	90
Table 5.1. Surface area and pore volumes of synthesized catalysts.	109
Table 6.1. List of plant species used in the biosynthesis of AgNPs with corresponding sizes.	129
Table 6.2. Selected Phenolic compounds isolated from the plant species <i>L. javanica</i>	131
Table 6.3. Sample codes denoting each colloidal solution	145
Table 6.4. Sample codes denoting each NCC supported colloidal solution	150
Table 6.5. Optimization of various solvent conditions for C9e catalyst ^a	159
Table 6.6. Optimization of various weight % for C9e catalyst ^a	160
Table 6.7. Synthesis of benzylidene-bis-(4-hydroxycoumarin) derivatives with C9e catalyst ^a	161
Table 6.8. Diameter of Zones of Inhibition (mm) of the samples against the bacterial strains.	164
Table 6.9. Diameter of Inhibition (mm) of the Colloids against the bacterial strains. Lowest MBC values are indicated in blue.	166

List of Abbreviations

AgNP	Silver Nano-Particles
BNC	Bacterial Nanocellulose
<i>Ca.</i>	Circa
DMSO	Dimethy Sulfoxide
DP	Degree of Polymerization
EtOH	Ethanol
HAp	Hydroxyapatite
LODP	Level Of Degree of Polymerization
LPE	<i>Lippia Javanica</i> Plant Extract
MCC	Microcrystalline Cellulose
MFC	Microfibrillated Cellulose
MS	Mass spectrometry
NCC	Nanocrystalline Cellulose
NFC	Nanofibrillated Cellulose
NMR	Nuclear Magnetic resonance
ppm	parts per million
s	singlet
d	doublet
t	triplet
q	quartet
m	quintet
dd	doublet of doublets

Table of Contents

Abstract	II
Declarations	IV
Declaration 1: Plagiarism	IV
Declaration 2: Publications.....	V
Declaration 3: Conference proceedings.....	VII
Acknowledgements	X
List of Molecular Compounds	XII
List of Figures	XV
List of Schemes	XVIII
List of Tables	XIX
List of Abbreviations	XX
Table of Contents	XXI
Chapter1: Introduction	1
1.1 Background and Motivation	1
1.2. Scope and coverage	2
1.2.1. Preparation and characterization of NCC from the two sources (Chapter 3).....	2
1.2.2. Preparation, characterization and application of HAp/NCC (Chapter 4).....	3
1.2.3. Photocatalytic Degradation of o-Chloranil on NanoCrystalline Cellulose Doped Titania (Chapter 5)	4
1.2.4. Biosynthesis of Nanocrystalline cellulose supported silver nanoparticles from Lippia javanica (Burm.f.) Spreng extract and the catalytic and bactericidal application (Chapter 6).....	5
1.3. Significance	7
1.4 References	8
Chapter 2: Literature Review	10
2.1. Cellulose	10
2.1.1. Structure and Morphology of Cellulose	10
2.1.2. Sources and Market.....	11
2.1.3. Basic properties and applications of cellulose	12
2.2. The fundamental characteristics of cellulose.....	13
2.2.1. Crystallinity in cellulose.....	13

2.2.1.1 Packing arrangement of cellulose	13
2.2.1.2. Crystallinity determination	16
2.2.2. Cellulose hydrogen bonding.....	16
2.2.3. The presence of cellulose in the cell wall of wood	18
2.3. Nanocellulose leading to nanocrystalline cellulose (NCC) and its preparation	20
2.3.1. Nanocellulose	20
2.3.1.1. Definition and classification	20
2.3.2 Properties and applications.....	21
2.3.3 Preparation Methods	22
2.3.3.1. Common top-down approaches	24
2.3.3.2 Common bottom-up approaches	26
2.4. Nanocomposites and cellulose-based derivatives.....	27
2.4.1. Nanocomposite Definition	27
2.4.1.1. Bionanocompoite definition	28
2.4.2. Cellulose-based nanocomposites.....	28
2.4.2.1. Hydrosoluble Systems	30
2.4.2.2. Emulsion Systems.....	31
2.4.2.3. Non-Hydrosoluble Systems	31
2.4.3 Properties of Cellulose-Based Nanocomposites.....	32
2.4.3.1. Mechanical Properties.....	32
2.4.3.2. Thermal Properties.....	32
2.4.3.3. Barrier Properties	33
2.5 References	34
Chapter 3: Preparation of NCC	51
3.1. Introduction	51
3.1.1. Nanocrystalline cellulose	51
3.1.2. Preparation of Nanocrystalline Cellulose.....	52
3.1.3. Morphology and Dimension of Nanocrystalline Cellulose	54
3.2. Materials and Methods	55
3.2.1. Materials.....	55
3.2.2. Isolation of NCC-BP and NCC-FP	55
3.2.3. Characterization Techniques	55
3.3. Results	58
3.4. Conclusion.....	68
3.5 References	69

Chapter 4: Synthesis of triazolidine-3-one derivatives through the nanocellulose/hydroxyapatite-catalyzed reaction of aldehydes and semicarbazide 77

4.1. Introduction	77
4.1.1. Hydroxyapatite (HAp) as a heterogeneous catalyst	77
4.1.2. Triazoles moiety	78
4.2. Materials and Methods	79
4.2.1. Materials.....	79
4.2.2. Preparation of HAp	79
4.2.3. Preparation of NCC.....	79
4.2.4. Preparation of NCC loaded HAp catalyst	80
4.2.5. General procedure for the synthesis of triazolidine-3-one derivatives (4a-1).....	80
4.2.6. Characterization Techniques	84
4.3. Results	86
4.4 Conclusion.....	97
4.5 References	98

Chapter 5: Solar Photocatalytic Degradation of o-Chloranil on Nanocrystalline Cellulose Doped Titania..... 102

5.1. Introduction	102
5.1.1. Photo-catalysis process	102
5.1.2. Titania (TiO ₂) as a photocatalyst.....	103
5.2. Materials and Methods	104
5.2.1. Materials.....	104
5.2.2. Photocatalytic study	104
5.2.3. Catalyst preparation.....	105
5.2.4. Characterization Techniques	105
5.3. Results and Discussion	108
5.4. Conclusion.....	121
5.5. References	122

Chapter 6: Bioactivity and catalyzed synthesis of biscoumarin derivatives using biologically synthesized silver nanoparticles supported by nanocrystalline cellulose..... 127

6.1. Introduction	127
6.1.1. Silver nanoparticles	128
6.1.2. Plant-mediated synthesis of silver nanoparticles.....	128
6.1.3. The plant species <i>Lippia javanica</i> (Burm.f.) Spreng.	130
6.1.4. NCC supported Silver Nanoparticles	131

6.1.5. Background to Biological activity.....	132
6.1.6. Biscoumarin and its derivatives	133
6.2. Materials and Methods	134
6.2.1. Materials.....	134
6.2.2. Preparation of aqueous extract of <i>Lippia javanica</i>	134
6.2.3. Synthesis of silver colloids using <i>Lippia javanica</i> plant extract (LPE).....	134
6.2.4. Preparation of NCC.....	135
6.2.5. Preparation of NCC supported AgNPs.....	135
6.2.6. General procedure for the synthesis of benzylidene-bis-(4-hydroxycoumarin) deraivatives (6a-i).....	135
6.2.7. Antibacterial Assay	140
6.2.7.1. Microbial Strains.....	140
6.2.7.2. Disc diffusion method.....	140
6.2.7.3. Determination of minimum bactericidal concentration (MBC).....	140
6.2.8. Characterization Techniques	141
6.3. Results and Discussion	143
6.4. Conclusion.....	167
6.5. References	169
Chapter 7: Conclusions and Future Work	180
7.1. Conclusion.....	180
7.2 Future work.....	182

Chapter1: Introduction

1.1 Background and Motivation

Cellulose is an extraordinary biomaterial used in modern industrialized society and it has, amongst others, facilitated mass communication (newspapers), enabled information archiving and storage (books), introduced new means to eliminate the spread of diseases (personal hygienic materials), initiated the textile industry, and transformed the arms industry (nitrocellulose). The chemical structure of cellulose was first determined by French chemist A. Payen in 1838 from plant matter.¹ Less than a decade later (1846), Schönbein developed the process for one of the first commercial derivatives of cellulose (nitrocellulose) *via* a serendipitous mistake. Many other industrialized chemicals like cellulose acetate and carboxymethylcellulose were also created from cellulose afterwards.² With its chemical composition known, research centered on its native structure and in 1913 the first X-ray scattering pattern demonstrated cellulose had a certain degree of molecular symmetry (crystallinity).³ Additional studies to determine the structure of cellulose included work by Rånby who was the first to report cellulose “micelles” that were obtained after acid hydrolysis of cotton fibers which was the initial characterization study of isolated cellulose in its nanoscale form.⁴ Thereafter, in 1951 Patel reported the oxidation of fibers using sodium hypobromite and isolating cellulose fibrils after blending, providing one of the first methods to produce a material that would later become microfibrillated cellulose in the 1980’s.⁵

Today, nanocellulose is defined as isolated cellulose particles with at least one dimension in the nanometer range (typically with widths below 100 nm and lengths between 100 – 500 nm) whilst exhibiting novel properties associated with its nanostructure.⁶ Nanocellulose is an emerging material that has received increased attention over the past decade, presenting unique chemical, physical, optical and mechanical properties which has led to numerous applications and patents in different fields, *i.e.*: food ingredients, cosmetic additives, packaging materials, hygienic products, pharmaceuticals, film and absorbance media, and nano-composite reinforcement agent.⁷ Nanocellulose can be prepared through either top-down approaches with the natural fibre resized to smaller particles (e.g.: homogenization, hydrolysis, combined chemical-mechanical processes) or bottom-up approaches (e.g.: electrospinning, bacterial biosynthesis) from multiple raw material sources (e.g. wood pulp, cotton, bacterial, algae).^{7a,8}

In this thesis, a combined chemical-mechanical process (top-down) was employed, using two sources *i.e.* locally sourced dissolving hardwood pulp (typically from eucalyptus trees) and Whatman® filter paper. From this process, nanocrystalline cellulose (NCC) was isolated after mechanical modification, chemical degradation and ultrasonication. Incorporating the properties of NCC, three new composites were prepared and applied to a combination of applications, including organic multicomponent reaction catalysis, organic pollutant photodegradation catalysis and bactericidal analysis. The first of the selection of composites included the wet impregnation of hydroxyapatite (HAp) into an NCC matrix. This was then followed by the co-precipitation of NCC and titania (TiO₂) in basic media. The final study incorporated the synthesis of silver nanoparticles *via* biological route using NCC as a support.

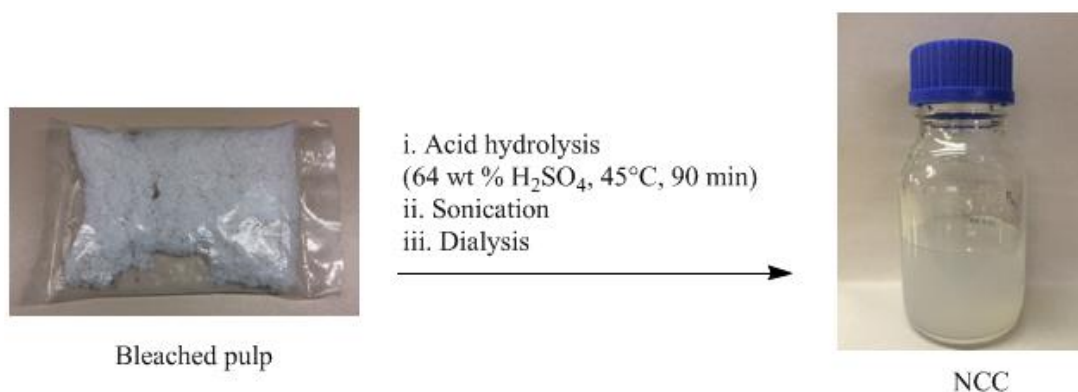
These new materials and their applications largely shaped the framework of the thesis, which revolved around the following points: synthesizing the NCC from source materials and fabricating the composites, characterizing NCC and composites, and applying these unique in the aforementioned applications.

1.2. Scope and coverage

The thesis research involved four major areas of investigation: preparation and characterization of NCC from two sources *i.e.* bleached pulp (BP) and Whatman® filter paper (FP), and preparation, characterization and application of composite and supported materials *i.e.* HAp/NCC composite, NCC/TiO₂ composite and NCC supported silver nanoparticles.

1.2.1. Preparation and characterization of NCC from the two sources (Chapter 3)

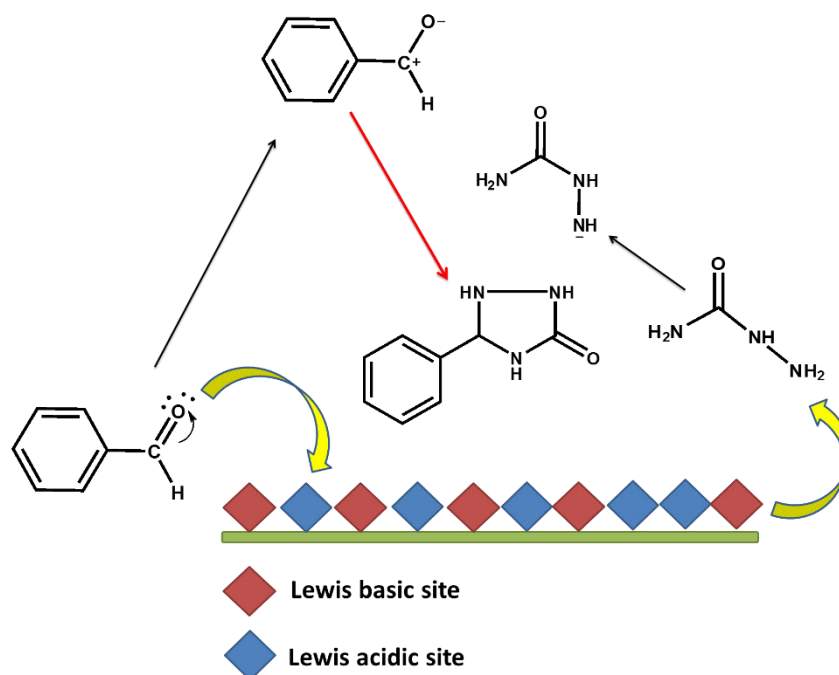
Nanocrystalline cellulose was prepared through a combined mechanochemical approach, where cellulose raw material (BP sourced from Sappi and received from the CSIR, Forest and Fisheries department and FP) was first mechanically modified *via* blending and agitation--sonication (Scheme 1.1). The mechanically treated cellulose was then chemically modified *via* acid hydrolysis and in turn, the surface chains' C6 primary hydroxyl group selectively converted into sulphate groups,⁹ which introduced anionic charges onto the surface of NCC, allowing separation *via* dialysis. The prepared NCC was systematically characterized through a series of techniques including ATR-FTIR, XRD, TEM, HRTEM, FEGSEM equipped with EDX detector, TGA/DTA, BET and Zeta potential measurements.



Scheme 1.1. Isolation of NCC from bleached pulp

1.2.2. Preparation, characterization and application of HAp/NCC (Chapter 4)

The first of the composites was a nanocellulose/hydroxyapatite heterogeneous catalyst, which was synthesized *via* a wet-impregnation method. Both the HAp and NCC were initially synthesized prior to the formation of the NCC/HAp composite. The composite was made from a predetermination of various materials that were suitable for the chosen catalytic reaction as well as ease of inclusion of NCC. It was then used in the one-pot, two-component synthesis of triazolidine-3-one derivatives, produced from the cyclocondensation reaction between semicarbazide and an aromatic aldehyde. With the use of ethanol as the ideal solvent, the products of the condensation reaction formed after short reaction times (<30 min). The catalyst was characterized by ATR-FTIR, XRD, BET, TEM and FEGSEM equipped with EDX detector. The advantages of this protocol were excellent yields of the products obtained as well as the mild and environmentally friendly reaction conditions. Good atom-economy was achieved *via* a simple and fast work-up with the added benefit of a recyclable catalyst negating the need of chromatographic separations of intermediates. The triazolidine-3-one derivatives were then characterized by ¹H, ¹³C and ¹⁵N NMR, FT-IR, and HR-MS and represented a new family of compounds containing the 1,2,4-triazolidin-3-one moiety.¹⁰



Scheme 1.2. A simplistic representation of the NCC/HAp catalysed formation 1,2,4-triazolidin-3-one derivatives.

1.2.3. Photocatalytic Degradation of *o*-Chloranil on NanoCrystalline Cellulose Doped Titania (Chapter 5)

A second composite material was prepared for the photocatalytic degradation of *o*-chloranil via aqueous mixtures of nanocrystalline cellulose (NCC) doped titanium dioxide (TiO₂). Different loadings of catalysts NCC/TiO₂ (10, 20, 40 and 80%) was synthesized and characterized by analytical material characterization techniques (PXRD, FEGSEM equipped with EDX detector, TEM, BET, ICP, PL, FTIR and GC-MS). This photo-catalyst enabled the NCC to enhance the properties of TiO₂ *i.e.* using the chiral nematic nature of NCC and potentially acting as a potential charge carrier, and in turn, potentially increasing the efficiency of TiO₂ as a photo-catalyst by lowering the rate of electron recombination.¹¹

The degradation was examined by observing the variation in substrate concentration employing UV spectroscopic analysis as a function of irradiation time in the presence of UV light at neutral pH condition. The 20% NCC/TiO₂ catalyst showed excellent degradation and mineralization of *o*-chloranil in 2 h. The degradation products were analysed and identified using GC-MS. The photo-catalyst offers many benefits such as easy preparation, non-hazardous, inexpensive, high stability and recyclability with no loss of activity.¹²



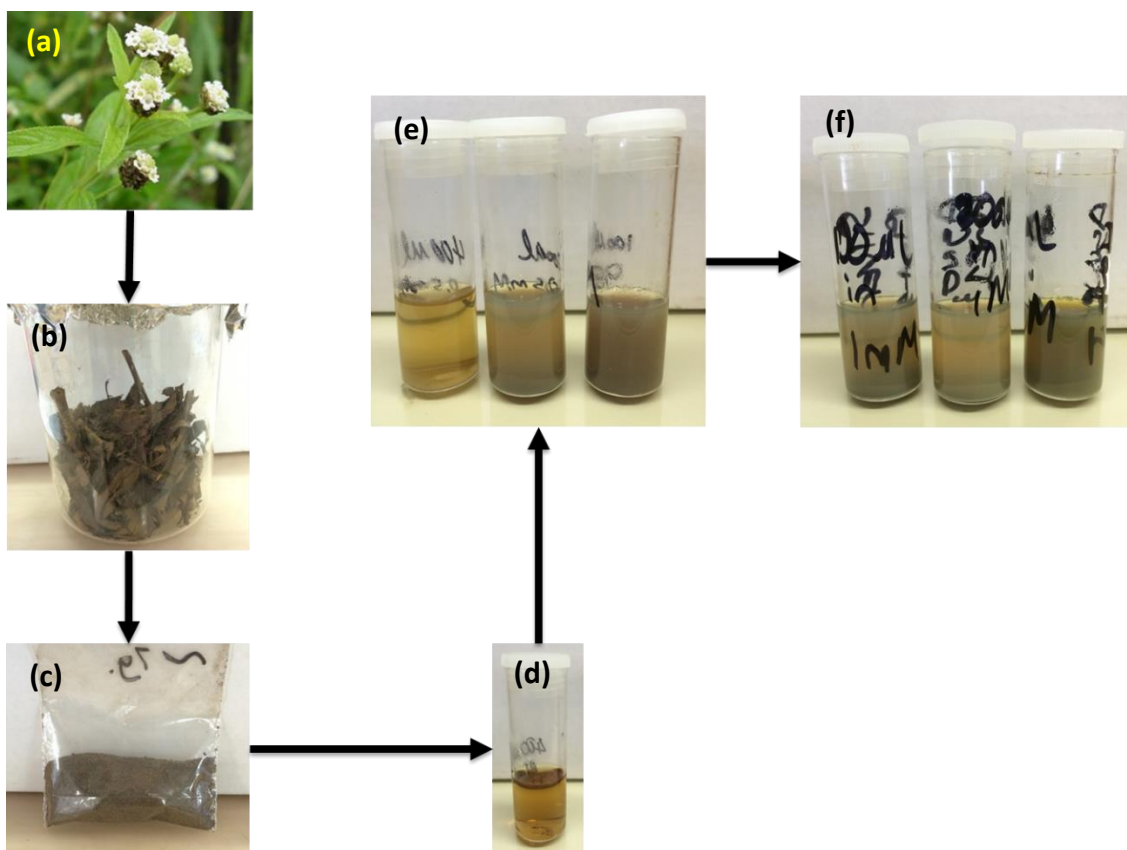
Figure 1.1. Set-up for the solar driven photodegradation of *o*-chloranil

1.2.4. Biosynthesis of nanocrystalline cellulose supported silver nanoparticles from *Lippia javanica* (Burm.f.) Spreng extract and the catalytic and bactericidal application (Chapter 6)

Formation of silver nanoparticles (AgNPs) using *Lippia javanica* (Burm.f.) Spreng aqueous extract as a reducing and stabilizing agent was explored. Variation in silver nitrate concentration and volume of plant extract was assessed to determine the ideal size and number of nanoparticles (Scheme 1.3). Nanocrystalline cellulose was then introduced as a support for the freshly prepared nanoparticles in varied wt%. Using this green approach, applied catalytic testing and bactericidal effects were investigated.

The AgNPs (supported and unsupported) were characterized by XRD, TEM, SEM-EDS and UV-VIS analysis. The AgNPs were formed with an average particle size between 10 – 40 nm and were stable over a long period. This protocol demonstrated that plant extract is a suitable reducing and stabilizing agent for the preparation of AgNPs. The addition of NCC hindered the initial reduction of Ag⁺ ions, however, the reduction was complete after 7 days. Particles with different shapes were found (Figure 1.2) after a short period (7 days).

In addition, an attempt to utilize the synthesized AgNPs as a tool to combat ‘drug resistant’ microorganisms led to a study of the antibacterial activity against several bacterial strains. A further application investigating the catalytic activity of the NCC supported AgNPs were tested in the synthesis of benzylidene-bis-(4-hydroxycoumarin) derivatives.



Scheme 1.3. Preparation of the *Lippia javanica* plant extract: (a) *Lippia javanica* (Burm.f.) Spreng, (b) drying of the stems and leaves, (c) crushed sample of stems and leaves, (d) aqueous extract of *Lippia javanica*, (e). Synthesis of silver colloids using *Lippia javanica* plant extract, (f) synthesis of silver colloids using *Lippia javanica* plant extract

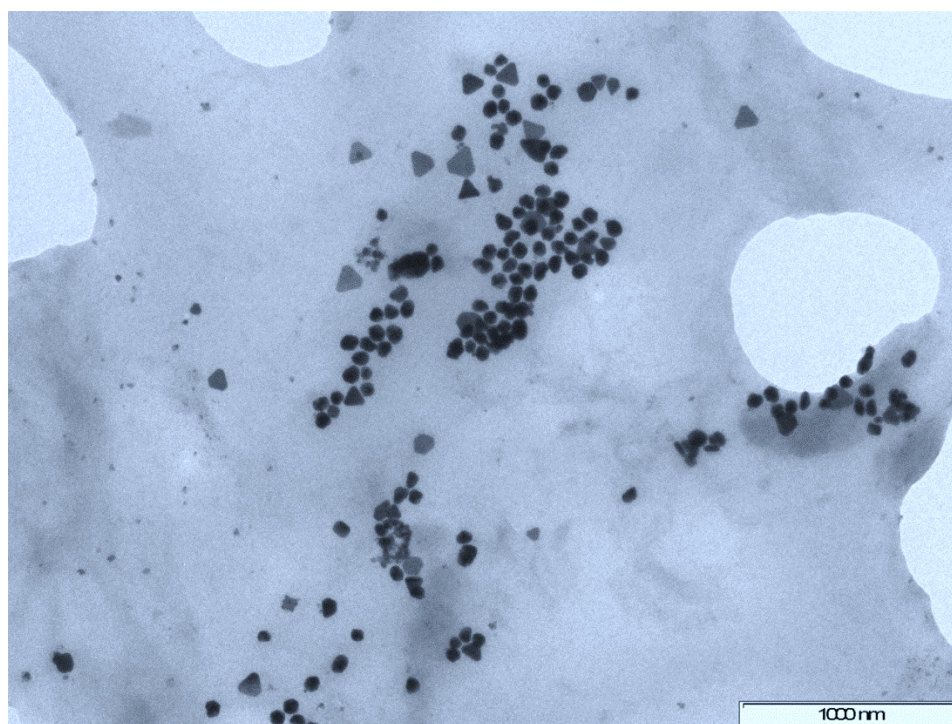


Figure 1.2. TEM micrograph of particles with different shapes from highest concentration

1.3. Significance

The significance of this work is reflected in the following aspects:

- 1) The work developed a facile approach to produce NCCs from the obtained cellulose sources of filter paper and bleached pulp *via* acid hydrolysis. The results showed that NCC-FP and NCC-BP could be considered as a potential composite material with excellent physicochemical and mechanical properties.
- 2) The NCC/HAp composite proved to be a versatile catalyst in the preparation of triazolidine-3-one derivatives. This allowed for a cost-effective and easy work up, with environment-friendly reaction conditions.
- 3) The preparation of an NCC/TiO₂ composite illustrated its use as an ideal catalyst in the photodegradation of *o*-chloranil. The catalyst proved successful and could prove useful in the degradation of other contaminants.
- 4) The successfully prepared AgNP colloidal solution, from the aqueous extract of *Lippia javanica*, showed excellent results in the bactericidal effects in a low concentration of silver. With the implementation of NCC into the system, the colloids could be further used as a catalyst in the preparation of benzylidene-bis-(4-hydroxycoumarin) derivatives.
- 5) NCC is a flexible and robust biopolymer that enhances many inorganic materials *via* enhancement of strength, expansion of surface area or thixotropic effects. NCC may also enhance the electron double layer of certain electronic/optical based materials which in turn augments the intrinsic properties of certain materials as evidenced in chapter 5. For this reason NCC was chosen as a supportive material throughout all studies.

1.4 References

1. (a) Brogniart, A.; Pelonze, A.; Dumas, R., Report on a Memoir of M. Payen, on the Composition of the Woody Nature. *Comptes Rendus* **1839**, 8, 51-53; (b) Payen, A., Memoir on the composition of the tissue of plants and of woody material. *Comptes Rendus Biologies* **1838**, 7, 1052-1056.
2. Cross, C. F.; Beven, E. J.; Beadle, C., *Cellulose: An Outline of the Chemistry of the Structural Elements of Plants with Reference to Their Natural History and Industrial Uses*. Longmans, Green, and Company: **1895**.
3. Nishikawa, S.; Ono, S., Transmission of X-Rays through Fibrous, Lamellar and Granular Substances. *Proceedings of the Tokyo Mathematico-Physical Society. 2nd Series* **1913**, 7 (8), 131-138.
4. Ranby, B. G., Aqueous colloidal solutions of cellulose micelles. *Munksgaard Int Publ Ltd* **1949**, 3, 649-650.
5. Patel, G. M., Optical investigations on oxycelluloses. *Die Makromolekulare Chemie* **1951**, 7 (1), 12-45.
6. (a) Klemm, D.; Kramer, F.; Moritz, S.; Lindström, T.; Ankerfors, M.; Gray, D.; Dorris, A., Nanocelluloses: A New Family of Nature-Based Materials. *Angewandte Chemie International Edition* **2011**, 50 (24), 5438-5466; (b) Klemm, D.; Schumann, D.; Kramer, F.; Heßler, N.; Hornung, M.; Schmauder, H.-P.; Marsch, S., Nanocelluloses as innovative polymers in research and application. *Polysaccharides II* **2006**, 49-96.
7. (a) Moon, R. J.; Martini, A.; Nairn, J.; Simonsen, J.; Youngblood, J., Cellulose nanomaterials review: structure, properties and nanocomposites. *Chemical Society Reviews* **2011**, 40 (7), 3941-3994; (b) Isogai, A.; Saito, T.; Fukuzumi, H., TEMPO-oxidized cellulose nanofibers. *Nanoscale* **2011**, 3 (1), 71-85; (c) Eichhorn, S. J., Cellulose nanowhiskers: promising materials for advanced applications. *Soft Matter* **2011**, 7 (2), 303-315; (d) Habibi, Y.; Lucia, L. A.; Rojas, O. J., Cellulose Nanocrystals: Chemistry, Self-Assembly, and Applications. *Chemical Reviews* **2010**, 110 (6), 3479-

- 3500; (e) Eichhorn, S. J.; Dufresne, A.; Aranguren, M.; Marcovich, N. E.; Capadona, J. R.; Rowan, S. J.; Weder, C.; Thielemans, W.; Roman, M.; Renneckar, S.; Gindl, W.; Veigel, S.; Keckes, J.; Yano, H.; Abe, K.; Nogi, M.; Nakagaito, A. N.; Mangalam, A.; Simonsen, J.; Benight, A. S.; Bismarck, A.; Berglund, L. A.; Peijs, T., Review: current international research into cellulose nanofibres and nanocomposites. *Journal of Materials Science* **2009**, *45* (1), 1-33; (f) Johnson, R. K.; Zink-Sharp, A.; Renneckar, S. H.; Glasser, W. G., A new bio-based nanocomposite: fibrillated TEMPO-oxidized celluloses in hydroxypropylcellulose matrix. *Cellulose* **2009**, *16* (2), 227-238; (g) Siqueira, G.; Bras, J.; Dufresne, A., Cellulosic Bionanocomposites: A Review of Preparation, Properties and Applications. *Polymers* **2010**, *2* (4), 728.
8. Hentze, H.-P., From nanocellulose science towards applications. *Developments in advanced biocomposites* **2010**, *71*.
 9. Niu, F.; Li, M.; Huang, Q.; Zhang, X.; Pan, W.; Yang, J.; Li, J., The characteristic and dispersion stability of nanocellulose produced by mixed acid hydrolysis and ultrasonic assistance. *Carbohydrate Polymers* **2017**, *165*, 197-204.
 10. Moodley, V.; Maddila, S.; Jonnalagadda, S. B.; van Zyl, W. E., Synthesis of triazolidine-3-one derivatives through the nanocellulose/hydroxyapatite-catalyzed reaction of aldehydes and semicarbazide. *New Journal of Chemistry* **2017**, *41* (14), 6455-6463.
 11. Ola, O.; Maroto-Valer, M. M., Review of material design and reactor engineering on TiO₂ photocatalysis for CO₂ reduction. *Journal of Photochemistry and Photobiology C: Photochemistry Reviews* **2015**, *24*, 16-42.
 12. Mills, G.; Hoffmann, M. R., Photocatalytic degradation of pentachlorophenol on titanium dioxide particles: identification of intermediates and mechanism of reaction. *Environmental Science & Technology* **1993**, *27* (8), 1681-1689.

Chapter 2: Literature Review

2.1. Cellulose

Cellulose is an abundant naturally-occurring biopolymer, and is regarded as an almost inexhaustible resource for the ever increasing demand of environmentally friendly and biocompatible products.¹ French chemist Anselme Payen was the first to identify the chemical composition of cellulose in 1838² with the French Academy later devising the term in 1939.^{2d,2f} Payen first attained “cellulose” through the purification of plant tissue samples with an acid-base treatment followed by aqueous, alcohol, and ether extractions, which led to the isolation of a uniform carbohydrate C(H₂O), Carbon 44.4%, Oxygen 49.4%, Hydrogen 6.2%).^{2a,2d,2f}

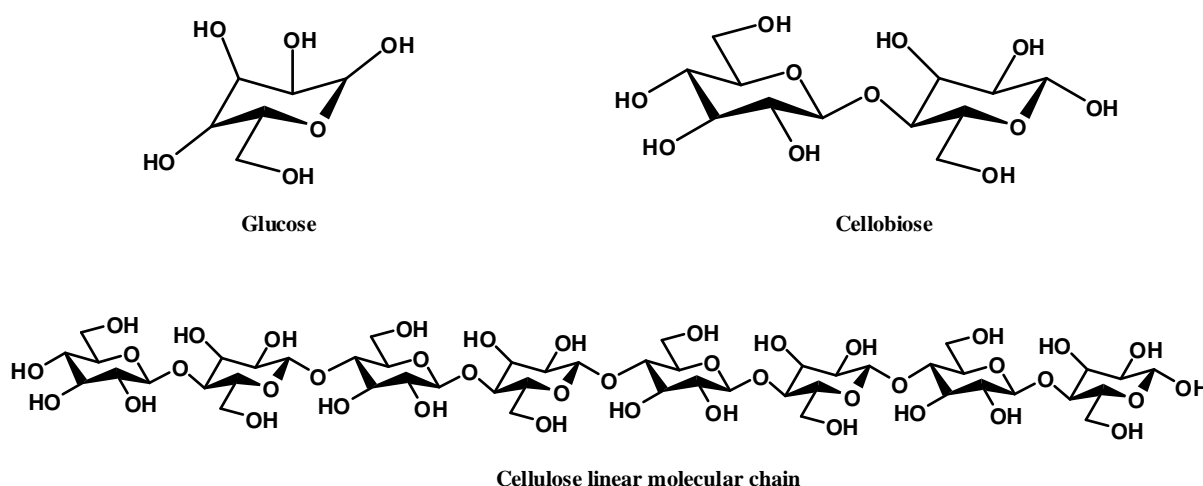


Figure 2.1. Glucose, cellobiose and linear cellulose molecular chain

The chemical structure of cellulose is a linear homopolysaccharide composed of β -1,4-linked anhydro-D-glucose units with the repeating unit (cellobiose) consisting of two glucose moieties with every alternating glucose unit inverted because of the β -linkage (Figure 2.1). Cellulose molecules in general have a strong affinity to align and form intra- and intermolecular hydrogen bonds due to its linear based structure (Figure 2.1). This disposition influences the properties of cellulose, mainly the physical and chemical properties.³

2.1.1. Structure and Morphology of Cellulose

The linear chain of ringed glucose molecules tends to form a flat ribbon-like conformation. Cellobiose (Figure 2.1) is comprised of two anhydroglucose rings ((C₆H₁₀O₅)_n, where n = 10000 to 15000 and is dependent on the cellulose source material) linked together by an oxygen atom covalently bonded to C1 of one glucose ring and C4 of the adjacent ring (1 - 4 linkage)

and so-called the β -1 \rightarrow 4 glucosidic bond.⁴ The linkage is stabilized by intrachain hydrogen bonds between hydroxyl moieties and oxygen atoms *via* adjacent rings, resulting in the linear configuration of the cellulose chain.^{3b} Intermolecular hydrogen bonds between hydroxyl moieties and oxygen atoms between neighbouring molecules lead to the stacking of multiple cellulose chains forming elementary parallel fibrils and later microfibrils *via* aggregation.^{2b,3b,5} These fibrils possess a diameter of 5 to 50 nm and several micrometers in length. Through this network of hydrogen bonding, these fibrils possess high axial stiffness and are extraordinarily stable.^{1f,6} This stability leads to the cellulose fibrils as the focal point for nature's reinforcement, found in trees, plants, tunicates, algae and some bacteria.^{5a,7} There are two sub-structural regions, namely the crystalline (highly ordered) and amorphous (disordered), found in cellulose fibres (Figure 2.2 a). The distribution and structure of these regions remain unresolved owing to the complex inter- and intra-hydrogen bonds found in the highly complex biological systems.^{1d} However, partially destroying the amorphous region and extracting the crystalline region within the cellulose fibrils, results in the extraction of crystalline cellulose fibres and crystals (Figure 2.2 b).^{2c,2d,8}

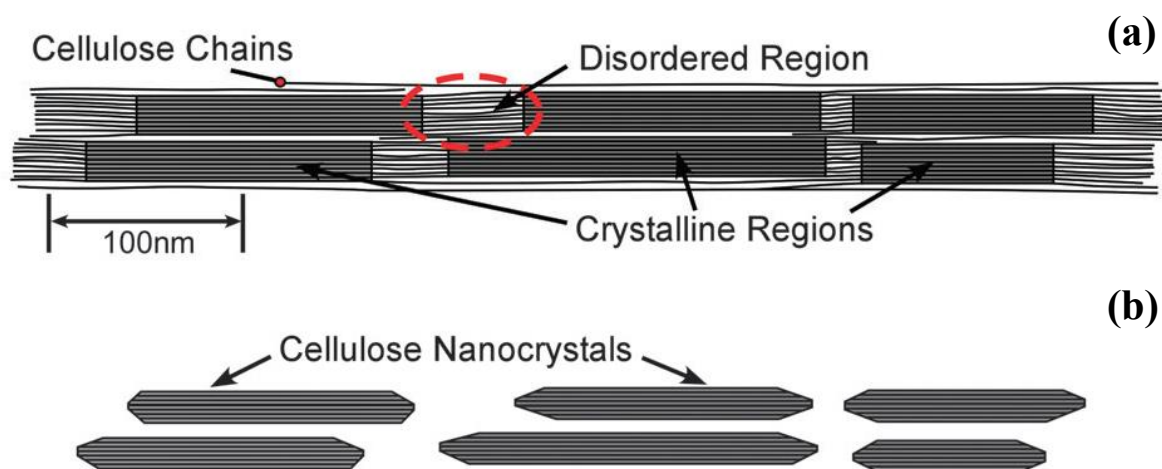


Figure 2.2. Schematic of (a) idealized cellulose microfibril showing one of the suggested configurations of the crystalline and amorphous regions, and (b) cellulose nanocrystals after acid hydrolysis dissolved the disordered regions.^{1b}

2.1.2. Sources and Market

Biologically, most cellulose production occurs in vascular plants.⁹ However, other natural sources include the cellular slime mold *Dictyostelium*, certain bacterial species, most groups of algae, and tunicates (the only species that produces cellulose in the animal kingdom).^{5a,7} It is estimated that about 1.5 trillion tons of cellulose is produced each year from various biological

sources.^{2b} The global market for nanocellulose based products is projected to rapidly expand from 2015 to 2023.¹⁰ The market's valuation is expected to grow from 55 million US\$ in 2014 to 700 million US\$ in 2023.¹⁰⁻¹¹ Apart from these, renewable sources from waste streams are becoming important material for the cellulosic materials.¹²

2.1.3. Basic properties and applications of cellulose

Vascular plants use this polysaccharide as a structural polymer for support of the physical structure. This function is different to that of starch (an energy reserve polymer), which contains the same monomer (glucose). These two polymers have distinct physical and mechanical properties, which is illustrated in the strength and solubility of each. Cellulose is strong and insoluble in water, whereas starch is amorphous and soluble.^{1c,3a,12c,13} The poor solubility of cellulose is primarily attributed to the strong intra- and inter-molecular hydrogen bonding interactions observed between single chains within its predominant crystalline lattice.¹³⁻¹⁴

Cellulose fibrils are in general tough, biodegradable, and recyclable.¹⁵ These fibrils have an extremely high aspect ratio, exhibiting great rigidity (100-160 GPa), low thermal expansion (0.1 ppm/K), and low density (1.6g/cm³).^{1c,6} Additionally, these attributes of cellulose lends itself toward the renewability, sustainability and abundance which facilitates the broad field of applications.^{1a, 2b}

Among the different natural sources, wood pulp has garnered the greatest importance as a raw material for the processing of cellulose. Although the majority of this raw material (5×10^{11} metric tons) is used in the production of paper, cardboard and packaging, a fraction of this quantity (2%) is industrially recoverable.¹⁶ Examining smaller industries, it is estimated that only 3.2×10^6 tons is used for the isolation of cellulose fibres, films, and a large number of cellulosic based esters and ethers.^{1a} These minor derivatives are then used as important active constituents in coatings, optical films, sorption media and additives in building materials, drilling fluids, pharmaceuticals, dietary production, and cosmetics.^{3a,4,13,17}

With the emergence of the “nano-era”, a major body of cellulose based research has shifted into the nanoscale paradigm.^{1a,1d,1e,2a,2b,4,5b,18} Nanocellulose (in fibrillated or crystalline forms) reveal unique properties in the solid or colloidal phase such as the following: solution thickening agents at low concentrations, thixotropic during processing, the ability to form transparent or coloured films dependent upon nanoparticle ordering, expansive surface area,

capability of forming highly porous foams and hydrogels, high specific strength and modulus, high sound attenuation, and a reasonably reactive surface structure.¹⁹ These unique properties allow for potential uses in the fields of food product enhancers (non/low calorie food (low-fat yoghurts), food thickening agent (soups and sources), oxygen-barrier layers (food packaging), emulsion stabilizer (in mayonnaise), cosmetics constituents (thickener (liquid foundations), dispenser (make-up applicators), bodying agent (creams and lotions), paint and coating additives/fillers, oil field facilities (drilling), medical applications (binders, wound dressing), pharmaceuticals (excipient, filler, drug delivery agents), reinforcement in nanocomposites (flexible display panels), tissue engineering scaffolds, filtration media, value-added papermaking (filler retention aid, coating and dye carrier in paper tinting, gas-barrier and moisture-resistant paper laminate for packaging), and major component in sanitary products (disposal diapers, wipes, napkins, incontinence pads).^{1a,2b,4,10,17,19-20}

2.2. The fundamental characteristics of cellulose

2.2.1. Crystallinity in cellulose

During experiments performed by Nishikawa and Ono in 1913, the X-ray diffraction patterns of various plant fibre bundles were obtained which revealed the crystalline nature of cellulose.²¹ The molecular arrangements of these fibrous bundles consisted of aggregated cellulose molecular chains. These chains were stabilized by strong inter-chain hydrogen bonding and exhibited a planar symmetry. This symmetry was confirmed by the X-ray diffraction patterns, which further illustrated the crystalline characteristics of cellulose.^{2d,22} However, many physical and chemical studies on cellulose microfibrils (fibrous bundles) lean toward the indication that there are two distinct regions. One region consists of highly ordered cellulose chains (crystalline region) while the other is composed of less ordered cellulose chains (paracrystalline region).^{2c,2d}

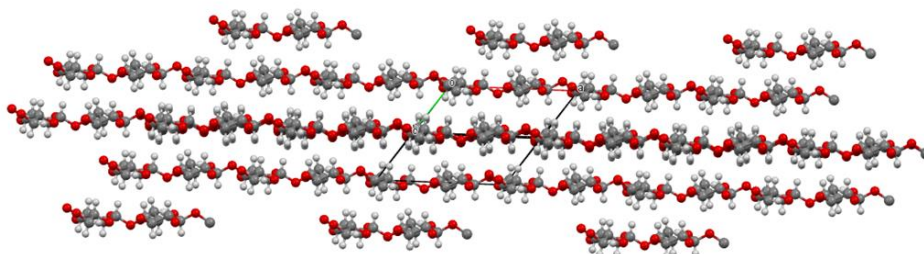
2.2.1.1 Packing arrangement of cellulose

Depending on the specific packing arrangements in the crystal lattice, cellulose can be categorized accordingly. Cellulose possesses four known polymorphs (I, II, III and IV) of which cellulose I is the predominant crystal packing arrangement found in nature.^{2c,14} Cellulose I can be further divided into two subgroups *i.e.* I α and I β .²³ The I α subgroup has a

triclinic arrangement and has a lower symmetry than the I β subgroup which occupies a monoclinic unit cell. Although in less abundance, cellulose II is the most stable structure commanding greater relevance of the four. It is found in a monoclinic crystal system and is rarely produced in nature.^{1d,2c,4} A bacterium (*Acetobacter xylinum*) that usually produces cellulose I, can synthesize cellulose II through a mutation.^{5a} Commonly, Cellulose II is produced *via* two procedures: mercerization (a series of aqueous sodium hydroxide treatments) and regeneration (a process dissolution and recrystallization).^{2b} Cellulose III can be formed from Cellulose I or II through liquid ammonia treatments, and subsequent thermal treatments can then be used to form Cellulose IV.²⁴

The different crystalline sub-allomorphs I α and I β were first identified by Atalla and Van der Hart in 1984 *via* cross polarization magic angle spinning (CP-MAS) ¹³C NMR spectroscopy²³ and was later more accurately determined by Nishiyama and co-workers using a synchrotron X-ray and neutron fibre diffraction.²⁵ Cellulose sources such as algae and bacteria are found to be rich in I α , while cellulose from cotton, wood, ramie and tunicates usually contain I β .²⁶ The chain packing arrangements can be converted between one another under certain conditions, for example, by annealing metastable cellulose I α , it can be converted to I β .^{5a}

Cellulose I α



Cellulose I β

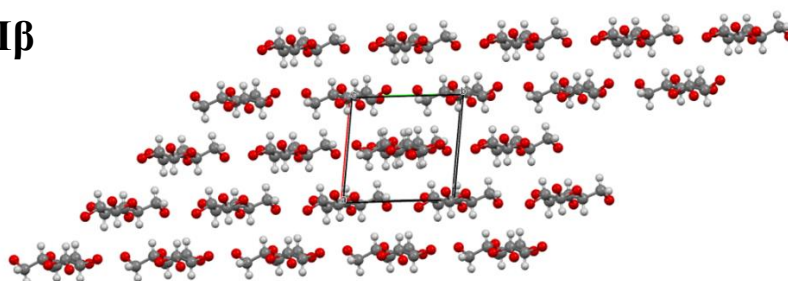


Figure 2.3. Packing arrangement of cellulose I α and I β (viewed along the fibre direction). Redrawn from crystallographic open database using the Crystallographic Information File (CIF) for each system (Cellulose I α CIF: 411438225b and Cellulose I β CIF: 411499425a)

In 2002 and 2003, Nishiyama and co-workers determined the crystal structures of Cellulose I β and I α , respectively (Figure 2.3).²⁵ The triclinic unit cell of Cellulose I α is assigned a space group of P_1 and has $Z = 1$ (a single chain in one unit cell),^{25b} whereas monoclinic Cellulose I β has a space group of $P2_1$ and a $Z = 2$ (2 cellulose chains in one unit cell) (Figure 2.4).^{14,25a} The two chains found in the unit cell of Cellulose I β are parallel with the reducing ends following the same direction (Figure 2.3).^{1d,27} The major difference between these two allomorphs is how the repeated hydrogen-bonded planes align on top of each other: there is a unidirectional axial shift of each subsequent sheet of cellulose molecules in the I α structure which results in the chains in the I α structure being shifted by half a repeating unit (along the fibre axis) relative to the other chains.^{1d,28}

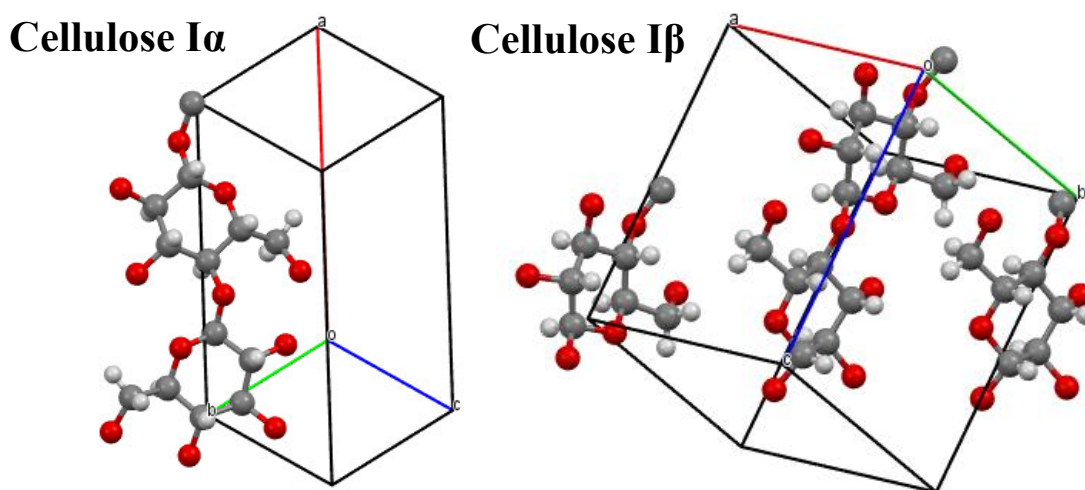


Figure 2.4. Unit cell structure of cellulose I α and I β .²⁵

This difference in packing arrangement that results in the formation I β is thermodynamically favourable compared to that of the I α form.²⁹ The Cellulose I β crystal structure differs from cellulose I α and the primitive cellulose I model by exhibiting two distinctive chains that displays unique hydrogen-bonding patterns.^{25a} This distinction brings about three possible packing arrangements for the two chains (defined as corner chain and centre chain). These two arrangements are generally referred to as “parallel up”, “parallel down” (collectively known as “parallel”), and “antiparallel”. The “Parallel” and “antiparallel” modes refer to the two chains having the reducing ends pointing in the same and opposite orientations, respectively.^{28,30}

A Cellulose I β molecule is defined as being “parallel up”, if in the unit cell, the z-coordinate of O5 is greater than that of C5, if not it is oriented “parallel down”.²⁸ The Meyer-Misch model (1937) presented an antiparallel orientation for cellulose I which was later disproved; Sarko *et*

al., (1976) later proposed a parallel orientation for cellulose I and an antiparallel orientation for cellulose II based on the packing energy calculation; Maurer and Fengel (1992) using end group labelling method experimentally suggested that both cellulose I and II were parallel oriented.³¹

2.2.1.2. Crystallinity determination

The determination of crystallinity in cellulose has generated a significant body of research. There have been numerous methods used to determine crystallinity, which include: X-ray diffraction, Fourier Transform infrared, Raman, nuclear magnetic resonance (NMR) spectroscopies as well as density measurements, and chemical methods (e.g. deuterium exchange kinetics, hygroscopicity measurements, hydrolysis, periodate oxidation, substitution).^{2c,2d,32} Cellulosic materials have varying response to different quantitative techniques. However, each method has variation in the way that it is defined and interpreted, which leads to an estimation of crystallinity.^{2d} These estimates lead to the portion of the crystalline region within cellulose of between 50-90% (generally around 70%) for natural cellulose. Wood based cellulose has slightly lower values to that of cotton and ramie based derivatives.^{2d,32a}

2.2.2. Cellulose hydrogen bonding

Natural cellulose possess three distinct orientations of the hydroxyl groups (OH) which contribute to the formation of the inter- and intramolecular hydrogen bonds. These include the secondary OH at the C-2 position, the primary OH at the C-6 position, and the secondary OH group at C-3 position (in order of polarity or reactivity in water).^{3b} All OH groups are bound to the glucopyranose ring in the equatorial position while the CH moieties are bound axially with respect to the glucopyranose ring, which results in the position of a localised hydrophilic site parallel to the ring plane and hydrophobic sites perpendicular to the ring.^{3b, 18b}

Taking into account the factors above with regard to the cellulose crystalline structure, the OH · · · O hydrogen bond (note: “· · · ” designates the hydrogen bond occurring between the hydrogen atom on the hydroxyl group and an adjacent oxygen atom) governs the cellulose intra-sheet interactions (including both intra- and inter-chain hydrogen bonding). The CH · · · O hydrogen bonding and van der Waals interactions lead to the inter-sheet bonding (stacked cellulose chains, Figure 2.5).^{25a} The CH · · · O hydrogen bonding located between each sheet (inter-sheet) and Van der Waals interactions are assumed to be of equal

magnitude.^{18b,29} Computational studies indicate that the inter-sheet interaction energies are approximately eight times in magnitude weaker than that of intra-sheet interaction.²⁹

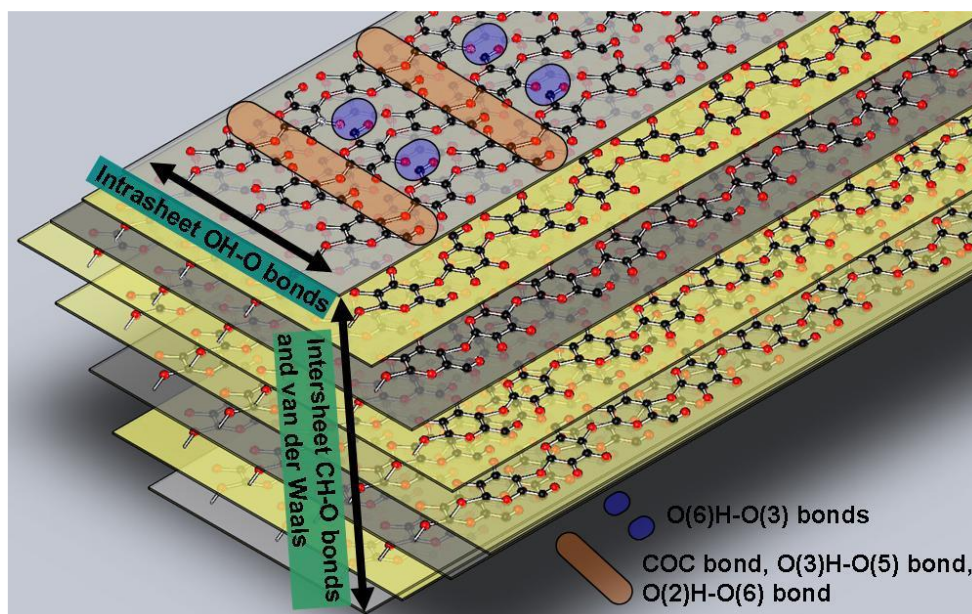


Figure 2.5. Hydrogen bonding system in native cellulose crystalline structure: The OH · · · O bonds dominate the intra-sheet interaction (interaction of cellulose chains within the same sheet), CH · · · O and Van der Waals collectively are responsible for the inter-sheet interaction (interaction of cellulose chains between two different sheets).³³

The hydroxyl group at the C6 position can occupy three potential conformations. This includes *gt*, *tg* and *gg* conformations (Figure 2.6). The *gt* conformation is the thermodynamically preferred orientation which represents two thirds of the total conformations,^{3b} while the *gg* conformation allows for the formation of O(6)H · · · O(2) inter-sheet hydrogen bonding. This is due to the conformation of the primary alcohol groups that are mainly perpendicular to the average planes of the anhydroglucose rings, such that these hydroxyl groups point upward in the direction of the original chains within the layers above.³⁴

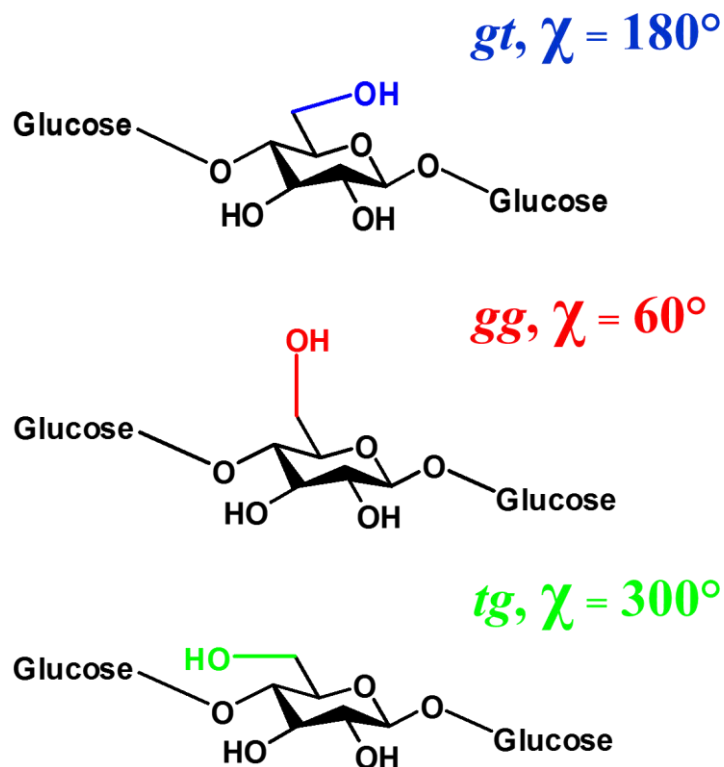


Figure 2.6. Three possible conformations at C6 primary hydroxyl group.

2.2.3. The presence of cellulose in the cell wall of wood

The cell wall of wood is a complex amalgamation, which is fundamentally made up of highly ordered lamellae of polysaccharides and lignin (Figure 2.7).^{3a,35} The available polysaccharides include cellulose, glucomannan, xylan, xyloglucan, glucuronoxylan, and arabinoxylan (with the latter five collectively known as hemicellulose). Polysaccharides are comprehensively characterized and are well understood. However, the chemical composition of lignin is still not specifically defined due to the absence of a discriminatory protocol for the quantitative isolation of this polymer in its virgin form.^{35b,35c}

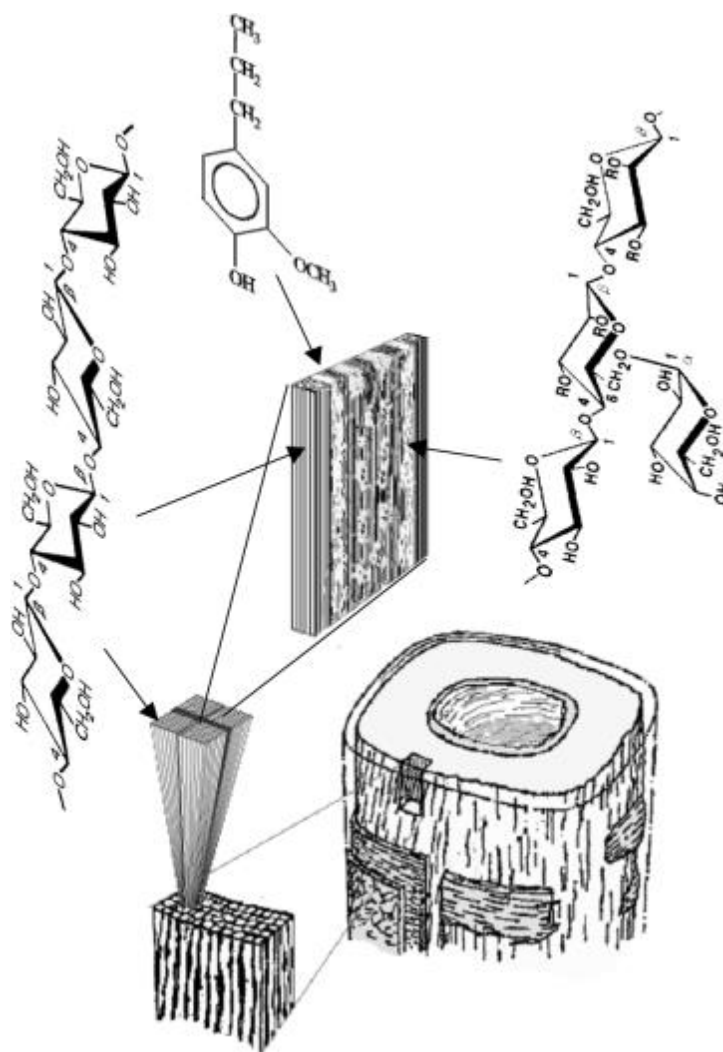


Figure 2.7. Schematic representation of the classification of the composition (consisting of the polysaccharides and lignin) found within the secondary cell wall of spruce (softwood) tracheids.³⁶

Evidence shows that the cellulose microfibrils are linked to glucuronan and xylan in different orientations, with the interaction between each fibril related to hydrogen bonding.³⁶⁻³⁷ The structures of xylan and glucuronan are mechanically and chemically altered during the pulping process. Thus the interactions between hemicellulose and cellulose are different to those found in the cell wall of natural wood.^{35b} There are other associative bonds that contribute to the interactions between polysaccharides. These include glycosidic bonds and ester bonds (which occur between hydroxyls on neighbouring polysaccharides and carboxyl groups of uronic acid residues).^{35b} Lignins assemble in a hetero-polysaccharides matrix and is thought to act as a templating agent for the formation of lignin. This is due to the fact that the hetero-polysaccharides and lignin are linked by both covalent and non-covalent bonds which

forms a lignin-polysaccharide complex (Figure 2.7).^{35b,37} The removal of hemicellulose and lignin leads to the isolation of pure cellulose and in turn the preparation of nanocellulose.³⁸

2.3. Nanocellulose leading to nanocrystalline cellulose (NCC) and its preparation

2.3.1. Nanocellulose

2.3.1.1. Definition and classification

Nanocellulose refers to isolated cellulose particles with at least one dimension in the nanometer range (below 100 nm), whilst exhibiting novel properties associated with its nanostructure.^{1a,39} Based on the different (mechanical and chemical) preparation methods and origin of raw materials, nanocelluloses are classified into three sub-categories (Figure 2.8)

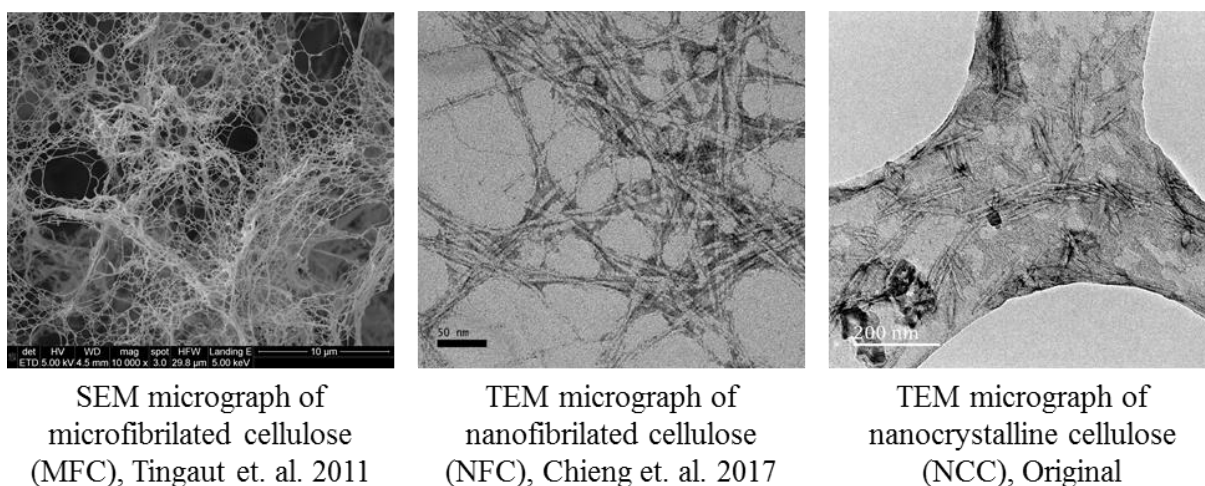


Figure 2.8. Images of different types of nanocelluloses.^{38c,40}

Microfibrillated cellulose (MFC): MFC is also known as microfibril, nanofibril or nanofibrillated cellulose (NFC). It is an extruded fibrous form of nanocellulose, which is prepared from natural sources such as wood and other plant fibres. It is obtained *via* mechanical, chemical or combination of both treatments. NFC is usually associated with shorter fibril lengths.^{38c}

Nanocrystalline cellulose (NCC): NCC may also be referred to as cellulose nanocrystals, crystallites, whiskers or rod-like cellulose microcrystals. The crystal form of nanocellulose is usually synthesized from a wider range of raw materials. These include plant-derived cellulose,

tunicin, algae and bacterial-derived celluloses, as well as commercially prepared microcrystalline cellulose (Avicel®), *via* an acid or enzymatic hydrolytic treatment.

Bacterial nanocellulose (BNC): BNC may also be denoted as bacterial cellulose, microbial cellulose or biocellulose and is commonly found as a built network of nanocellulose fibres. It is a natural constituent of the biofilm produced by certain bacterial strains *via* their biological processes. These bacteria only consume low-molecular-weight sugars and alcohols.^{39,41}

2.3.2 Properties and applications

Nanocelluloses in their three categories retain fundamental cellulose properties. These include hydrophilicity, a broad potential for chemical-modification, and the formation of versatile semi-crystalline fibre-like morphologies. Additionally, the expanded surface area may enhance specific properties related to filtration and sensor material development and applications.³⁹ Nanocelluloses also possess exceptional mechanical properties, particularly the elastic modulus (ranging from 20 extending to 200 GPa and greater). The magnitude of the elastic modulus is comparable to that of the bulk properties of carbon fibres, steel, and titanium alloys.^{1b,39,42} The thermal properties of nanocelluloses are respectable with relative stability. The degradation temperatures range between 200-300 °C, dependent upon the rate of heating, particle classification and morphology, and surface modifications.^{1b} Analysis of rheological properties displays nanocellulose based suspensions with a shear thinning property (which is dependant on the Zeta-potential and concentration of the solution). The shear thinning may be time-dependent, i.e. thixotropic effects (for HCl derived crystals in high concentrations and MFC). At certain w/w concentration, MFC and NCC form stable gels in water (subjective to certain threshold levels e.g.: 0.5% w/w% for MFC).^{1b} Lastly, nanocelluloses display remarkable optical properties, which lends itself to the formation of transparent films, exhibiting liquid crystallinity properties as well as birefringence due to the anisotropic structural orientation of singular particles.^{1b}

Besides these properties, nanocelluloses may also display distinctive properties based on the specific raw materials used, protocols, and industrial engineering. This allows for the use of nanocelluloses in different applications which exploit these unique properties. One such instance is that bacterial cellulose can be moulded during the metabolic process, which has led it to be applied to the growth of artificial blood vessels using the pre-designed templates.^{1a,2b,43}

MFC applications are primarily based on the paper making sector as reinforcement agents⁴⁴ or functional coatings (e.g. grease proofing or moisture absorbing).⁴⁵ MFC found in food, cosmetics, pharmaceutical, and hygiene products are used as emulsion and/or dispersion agents.⁴⁶ Nanocomposites and films which contain MFC are used as structural components.⁴⁷ These applications hinge upon MFC's distinctive combination of properties including water retention, bond enhancing, aspect ratio, specific strength, optical and rheological characteristics. The universal bio-friendliness of formed products aids the use of MFC in the megaton range.^{1a, 1b, 39}

NCC may be used in the above-mentioned applications, however, it possesses an interesting property of self-ordering (seen in sulphated and carboxylated NCC's).⁴⁸ This self-ordered property is known as the chiral nematic phase. Common applications centre around its mechanical properties. NCC is used as a strengthening agent in composite based films to increase shear strength and dimension stability.^{1e, 49} NCC also finds novel applications in drug delivery systems, due to its biocompatibility and chemical modification capacity.⁵⁰ Common methods for the formation of NCC nanocomposites include compression moulding, extrusion, solution casting (followed by cross-linking or polymerization), and self-assembly (by spin coating or dip coatings).⁴⁸ In the industrial magnitude, conventional methods such as injection moulding, extrusion and pressing are the preferred routes, whereas solvent casting on a large scale would incur great difficulties due to the use of volatile organic solvents on a large scale (although this process leads to the production of superior films).^{1b, 1c, 39}

BNC, due to its biosynthetic origin, possesses distinctive properties, not seen in MFC and NCC. These unique properties include a stable nanofiber network, shape altering ability during the biosynthetic process, non-cytotoxic and non-genotoxic characteristics. With most nanocelluloses it exhibits exceptional mechanical strength while proving exceedingly flexible in solution. This allows BNC to be thrust into novel applications such as artificial blood vessels,⁵¹ wound dressing material,⁵² fuel cell membranes,⁵³ as well as production of films for use in electronic appliances.⁵⁴

2.3.3 Preparation Methods

Nanocellulose can be prepared *via* a number of synthetic strategies which can be classified based on the raw material and the design approach. These approaches can be separated into

two broad categories: the top-down and bottom-up approach.^{1b,46c,55} The top-down approach utilizes extraction methods to gain cellulose particles from various sources at a nanoscale level.³⁴ This category is further subdivided into three subsections: mechanical, chemical, and mechano-chemical. The latter approach (bottom-up) entails the assembly of cellulose based nanostructures from either a solution state hierarchy of cellulose molecules or a biosynthetic approach.^{39,55a} Through either approach (“extraction” or “assembly”), the obtained nanostructured cellulose based materials are fairly uniform particles (in size and morphology) and possess a greater surface area than that of the materials that they are based on. This brings about many of the favourable properties (discussed above) that essentially lays the foundation for many diverse applications.^{1a} Figure 2.9 illustrates the described classification of nanocellulose fabrication approaches.

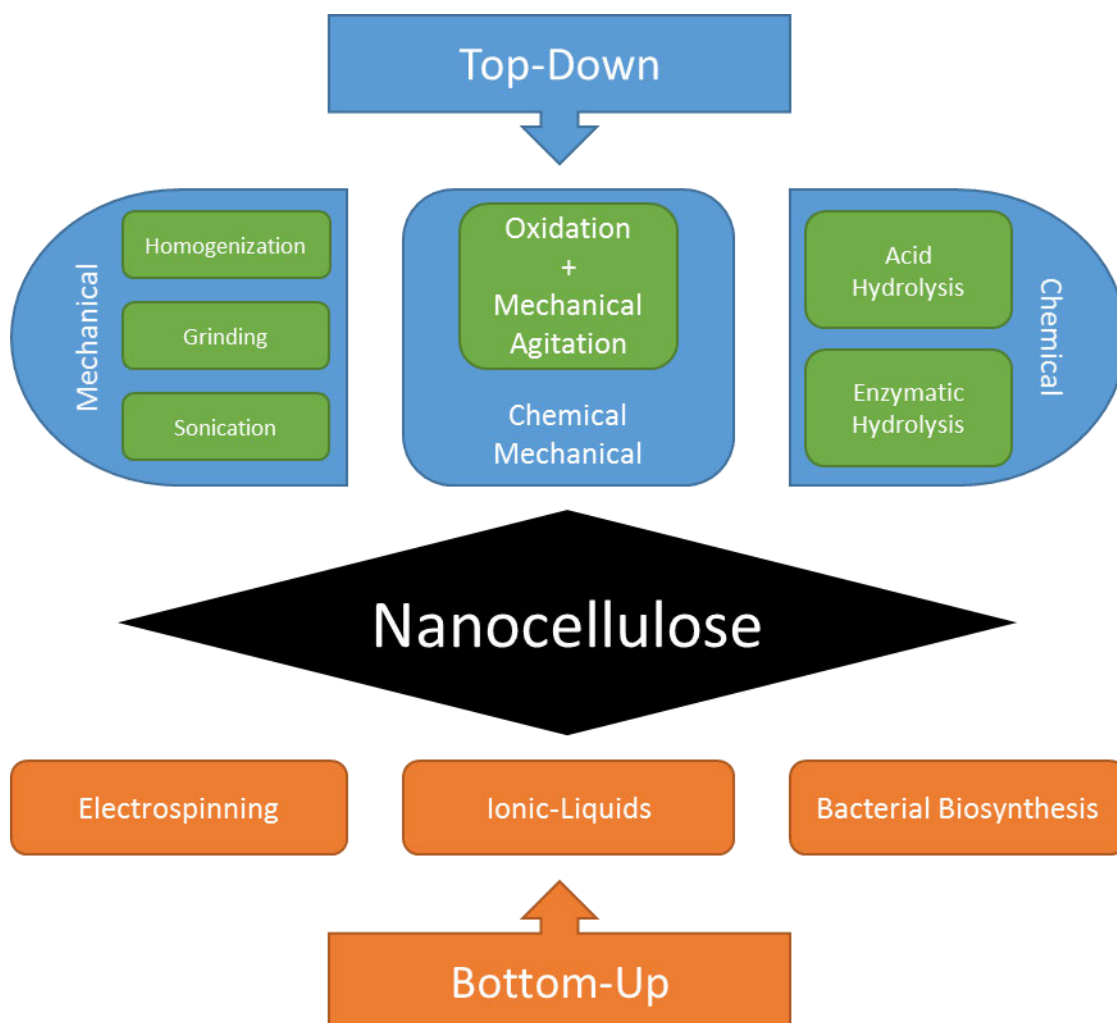


Figure 2.9. Classification of nanocellulose fabrication approaches (Top-Down and Bottom-up).

2.3.3.1. Common top-down approaches

The top-down approaches, as the name implies, typically starts from natural raw materials sources like wood chips, pulps and cotton linters. These sources require a chemical, a mechanical or a combination of both (mechano-chemical) method to liberate the nanocelluloses from their native complex structures (large fibrous bundles of the cell wall). High purity raw materials like cotton linters readily release individual microfibrils from the larger fibre bundles. Whereas more complex raw materials such as wood chips that exist in a natural composite form, require a more intensive top-down approach to first separate the cellulose from its lignin-hemicellulose matrix before the adapted nanocellulose particles are isolated from large cellulose fibrous bundles.

(a) The mechanical approaches

Homogenization: Turbak *et al.* first described the homogenization process using different types of pulps. This process used an intensive homogenization treatment with a controlled number of passes, followed by extrusion through a small orifice under high pressures (55 MPa or 8000 psi).¹⁷ The final end product possesses a “net-like” structure, with diameters ranging from 25-100 nm in the dried state. This process leads to an increase in the relative surface area, which allows the produced MFC to have an increased water retention rate of more than 400% (compared to 50-90% for pure wood pulps).^{17,19h} The major impedance to this process is a large energy consumption (25,000 kWh/t), which hinders its commercial realisation.^{39,56}

Sonication: The first reported MFC production using mechanical agitation was reported by Wuhrmann *et al.* in 1946. It was described that plant fibres from ramie, hemp, and cotton were exposed to a rigorous sonication treatment. As the intensity of mechanical agitation increased, the finer the fibrils that formed (ranging from 6-7 nm in width).⁵⁷

Wet grinding: In 2007, Abe and co-workers employed the wet grinding approach to process lignin-containing plant fibres. This process generated nanocellulose fibrils with a width of 12-16 nm and a uniform distribution.^{19b} Lignin and hemicellulose content was removed *via* a pre-treatment prior to the grinding process. The pre-treated delignified samples were then passed through a grinder at 1500 rpm in slurry state (1 wt%) to isolate the nanocellulose fibrils.^{19b}

Aqueous counter collision (also known as ultrahigh-pressure water jet treatment): Kose *et al.* established an innovative protocol to prepare nanocellulose fibrils *via* a jet counter collision apparatus. This method subjected suspensions of cellulose in aqueous medium (≤ 0.4 wt%) to

ultrahigh pressure (200 MPa), which yielded “single-cellulose nanofibers” in water.⁵⁸ This resulted in nanocellulose with a width profile of less than a 100 nm and a length profile of a few microns.^{58b}

Thus far only fibrous cellulose has been gathered from mechanical processes. To attain nanocrystalline cellulose one needs to employ a chemical approach (with more complex natural sources requiring a combination of both).⁵⁹

(b) The chemical approaches

Acid hydrolysis: Acid hydrolysis is a well-recognized process for removing inaccessible areas within natural cellulose and producing nanocrystalline cellulose (NCC).^{34,56,59a} This approach involves the treatment of different initial cellulosic sources (pulps, plant-based cellulose, bacterial cellulose, tunicate cellulose, etc.) with concentrated mineral acid (most commonly sulfuric acid or hydrochloric acid). This process is known as hydrolysis or mineralization of cellulose and occurs under elevated temperatures (ranging from 45 to 65 °C) with varied time periods.⁶⁰ The final product yields rod-like particles with widths ranging from 2-50 nm and lengths reaching a few hundreds of nanometers in length. These dimensions are dependent upon the source of starting materials as well as prior processing conditions. The particles obtained *via* sulfuric acid hydrolysis treatment can lead to the formation of birefringent gels and liquid crystalline structures. These particles exhibit a helicoidally self-ordering phenomena (also known as the chiral nematic phase) in certain concentration range.^{1b,1c,60c}

TEMPO-mediated oxidation: Although this falls under the category of surface modification rather than a production method, pure TEMPO-mediated oxidation yielded nanofibrillated cellulose (NFC).⁶¹ In conjunction with acid hydrolysis nanocelluloses (NCC in particular) with unique properties were synthesized.⁶² De Nooy and co-workers, first demonstrated this process involving the application of a stable nitroxyl radical, the 2,2,6,6-tetramethylpiperidine-1-oxyl (TEMPO), in the presence of NaBr and NaOCl. This process showed that only the hydroxymethyl groups of polysaccharides were oxidized, while the secondary hydroxyls remained unaffected.⁶³ Isogai *et al.* later demonstrated the TEMPO-mediated synthesis of nanocellulose (specifically NFC) from a slurry of cellulose.⁶⁴

(c) Chemical-mechanical approaches

Different employed chemical pre-treatments (e.g.: oxidation,⁶⁵ acid hydrolysis,^{60a} and enzymatic hydrolysis⁶⁶), mechanical agitations (e.g.: sonication, homogenization, blending,

etc.), as well as the combination of both approaches have been broadly examined. The most common chemical-mechanical approach is to first oxidize or hydrolyze the cellulose (e.g.: TEMPO oxidation,⁶⁷ chloroacetic acid etherification,⁶⁸ enzymatic hydrolysis,⁶⁶ and carboxymethylation⁶⁹) followed by mild to intensive mechanical treatments to liberate carboxylated MFC from the cellulosic sources.^{1f} The nanocellulose end product adopts a long nanofibril form.^{33, 70} This fabrication approach has been pioneered by Isogai *et al.* with many research groups adopting the procedure.⁶⁴

2.3.3.2 Common bottom-up approaches

Contrary to the top-down approaches, the bottom-up approaches produce nanocellulose through assembly on a molecular level using glucose as construction medium. Two approaches are dominant in literature, *i.e.* Electrospinning and Bacterial biosynthesis. Electrospinning builds on the regeneration of solid fibres from the solution state. Bacterial cellulose synthesis employs the polymerization of UDP-glucose *via* the bacterial metabolic activity to produce the nanocellulose.

(a) Electrospinning: A typical setup involves the use of a polymer solution (or polymer melt) to spin continuous fibres *via* the application of a potential difference. Under the applied high voltage, the solution or melt deforms due to the repulsive forces at the surface of the drop. Once this repulsive force overcomes the force of surface tension a fine jet of the polymer is ejected towards the collector to form the nanocellulose. Electrospinning typically yields nanocellulose in non-woven fibre mat (using a flat or plate collector) or oriented fibre strand (using a rotating cylindrical or drum collector). Fibre diameters range from the nanometer to micron level.^{1b,1c,71}

(b) Bacterial biosynthesis: Bacterial nanocellulose (BNC) is produced *via* the biosynthetic approach of certain bacteria's processes which converts low-molecular-weight sugars to cellulose molecular chains. These chains are then excreted in fibrous form into the medium in which the culture is incubated. The fibres further combine to form ribbon like network which further collects to form a 3D nanofiber framework. Impurities are removed *via* a simple purification process and leave behind pure cellulose fibres with diameters in the nanometer range.³⁹

2.4. Nanocomposites and cellulose-based derivatives

2.4.1. Nanocomposite Definition

The term -nano is used to classify objects with dimensions in the nanometer scale (10^{-9} m). A nanometer is equivalent to a billionth of a meter, or roughly 30,000 times thinner than a human skin cell.⁷² The nanometer range covers sizes larger than several atoms but smaller than the wavelength range of visible light.⁶⁵ The increased interest in nanoscale materials and devices from the scientific community stems from the introduction of the nanotechnology concept by Richard Feynman in 1959.⁷³ However, nanocomposite materials research has only seen a paradigm shift toward concentrated applications and devices in the last 2 decades.⁷⁴ Nanocomposites constitute a new class of hybrid materials which aims to bring about singular advantages of each material into one broad spectrum “super” material. Currently, nanocomposites are defined as materials with at least one dimension smaller than 100 nm.⁷⁵ One class of nanocomposites, polymer nanocomposites, are defined as polymers containing a small quantity of well-dispersed nanofillers. The motive behind the low filler to polymer ratio is to achieve high mechanical properties. This allows for the nanostructures to gain features not present in material singularly but also allows for the advancement of the production superior composites.⁷⁶ The components of nanocomposite materials can be constituted of inorganic-inorganic, inorganic-organic or organic-organic sources.⁷⁷

The recent resurgence of interest in nanocomposites can be related to several reasons. (1) These hybrid nanomaterials possess unrivalled chemical and physical properties which make it an attractive venture for major industries that are pushing the boundaries for faster, smaller and brighter products; (2) nanoscale fillers contain little or no defects and their application in the composite arena allows for move from the micro to nano scale; (3) due to the high specific surface area, nanocomposites present a large volume of interfacial matrix material (interphase) with properties different from those of the bulk polymer. A uniform dispersion of nanoparticles leads to a very large matrix-filler interfacial area. This brings about change in the molecular mobility, relaxation behaviour and ensuing thermal and mechanical properties.⁷⁷⁻⁷⁸

Recently, attention has been shifted towards determining and developing superior composites by exploiting the unique physical properties that the underlying nanomaterials possess.⁷⁹ This increased interest is attributed to a growing recognition that moves beyond formulating polymers with nanoparticulate fillers, and towards highly engineered, designed, and functional nanocomposites.^{78c, 79-80}

The drawback associated with extensive research of nanocomposites, intended for advanced applications, is a hindered hindsight into the properties that these nanocomposites possess. Although there are various techniques available to manipulate the surface chemistry and structure of the nanoparticles, classical models impede the prediction of the impact of the nanoscale filler surface with regard to morphology, dynamics, and certain properties of the surrounding polymer chains.^{78b} Another key point focuses on the health problems associated with nanoparticles. This subject has necessitated research into understanding and alleviating the problems associated with this phenomena.⁸¹ This focus on health is important due to previous health pandemics related to materials (e.g. asbestosis).⁸² The term nanoparticles are not clearly defined, with only one dimension below 100 nm used to classify nanoparticles. Focus revolves around their shape and chemical surface structure which is important, however, the behaviour of bulk nanocomposites in different environments remain unclear.⁸³ Recent works into determining the toxicity of nanocrystalline cellulose which has been published in Canada, points towards a positive (low toxicity) initial result.⁸⁴

2.4.1.1. Bionanocomposite definition

Bionanocomposites are bio-based nanocomposites, a subgroup of nanocomposites which represents an emerging group of nanostructured hybrid materials in polymer and bio-based reinforcement. By expanding the concept of biocomposites⁸⁵ toward nanostructured hybrid materials, bionanocomposites can be defined in the following two ways: It could differentiate nanocomposites as materials made from (1) renewable nanoparticles (e.g., NCC and MFC) or (2) petroleum-derived polymers like polypyrrole, polyethylene, and epoxies. It should be noted that nanocomposites derived from biopolymers (e.g., polylactic acid and polyhydroxyalkanoates) and synthetic or inorganic nanofillers (e.g., carbon nanotubes and nanoclay) also fall under this subgroup of bionanocomposites.^{80,86}

2.4.2. Cellulose-based nanocomposites

The use of nanocelluloses (e.g. NCC and MFC) as reinforcement in nanocomposites is a relatively new area of interest.^{86a} The raw materials of cellulosic-based particles in nanocomposites involve low costs and several advantages e.g., low density, renewability, biodegradability, low energy consumption and a relatively reactive surface. These features allow for the grafting of specific groups and an almost unlimited availability.^{4,86a,87} With all

the positive features associated with nanocellulose, some disadvantages arise, for instance, nanocellulose based materials are notorious for moisture absorption, poor wettability, incompatibility with most of polymeric matrices and constraints with respect to processing temperatures. The fillers that can be sequestered within a lignocellulosic materials matrix can be hindered by the degradation temperature of 220 °C.^{4,88}

Another drawback associated with the use of NCC-based polymer nanocomposites is the inherent difficulty of these particles to diffuse in non-polar medium, due to their polar surface.^{14,86c} This has minimized the incorporation of nanocelluloses only into aqueous or polar environments. Two different protocols are used to prepare cellulose based nanocomposite films,⁸⁰ namely: (1) Aqueous or organic solvent evaporation by solvent casting and (2) Extrusion with freeze-dried cellulose nanoparticles.

Solvent casting is the more common technique of the two and can be further sub-categorized into three systems dependant on the polymer used as the matrix, i.e., (i) water-soluble polymers, (ii) polymer emulsions, and (iii) non-hydrosoluble polymers. With regard to the third instance, two further subdivisions occur. This allows for the attainment of non-flocculated dispersions of nanocellulose in an appropriated organic medium^{75c}:

(1) Coating of the surface of the cellulose nanocrystals with surfactants containing polar heads and long hydrophobic tails;

(2) Grafting of hydrophobic chains at the surface of nanocellulose. These protocols allow for the preparation of nanocomposites by mixing the nanoparticle suspensions in organic medium with a solution of polymer.⁸⁰

The second way to obtain nanocellulose reinforced nanocomposites is a melt technique (extrusion method). This is a recent method of preparing such kinds of nanocomposites, and not extensively researched.^{86c,89} The nanocellulose are worked in the dry state. As the nanocellulose dry, strong Van der Waals interactions are formed and aggregates are generated, limiting the nanosized reinforcement. This is evidenced by the preparation of an NCC/latex composite *via* the casting and evaporating technique, which displayed better mechanical properties when compared freeze-drying and hot-pressing.⁹⁰ The process of casting and evaporation of materials was attributed to the formation of a rigid NCC rod/rod network, probably linked by hydrogen bonds (The evaporation technique would allow for interactions

between the NCC network as compared to the rapid forced removal of solvent *via* a hot-press). It was proposed that the formation of this network is more predominant in the evaporated films due to lower processing times.^{89a} Figure 2.10 illustrates the different strategies in the preparation of cellulose based-nanocomposites by solvent casting technique.

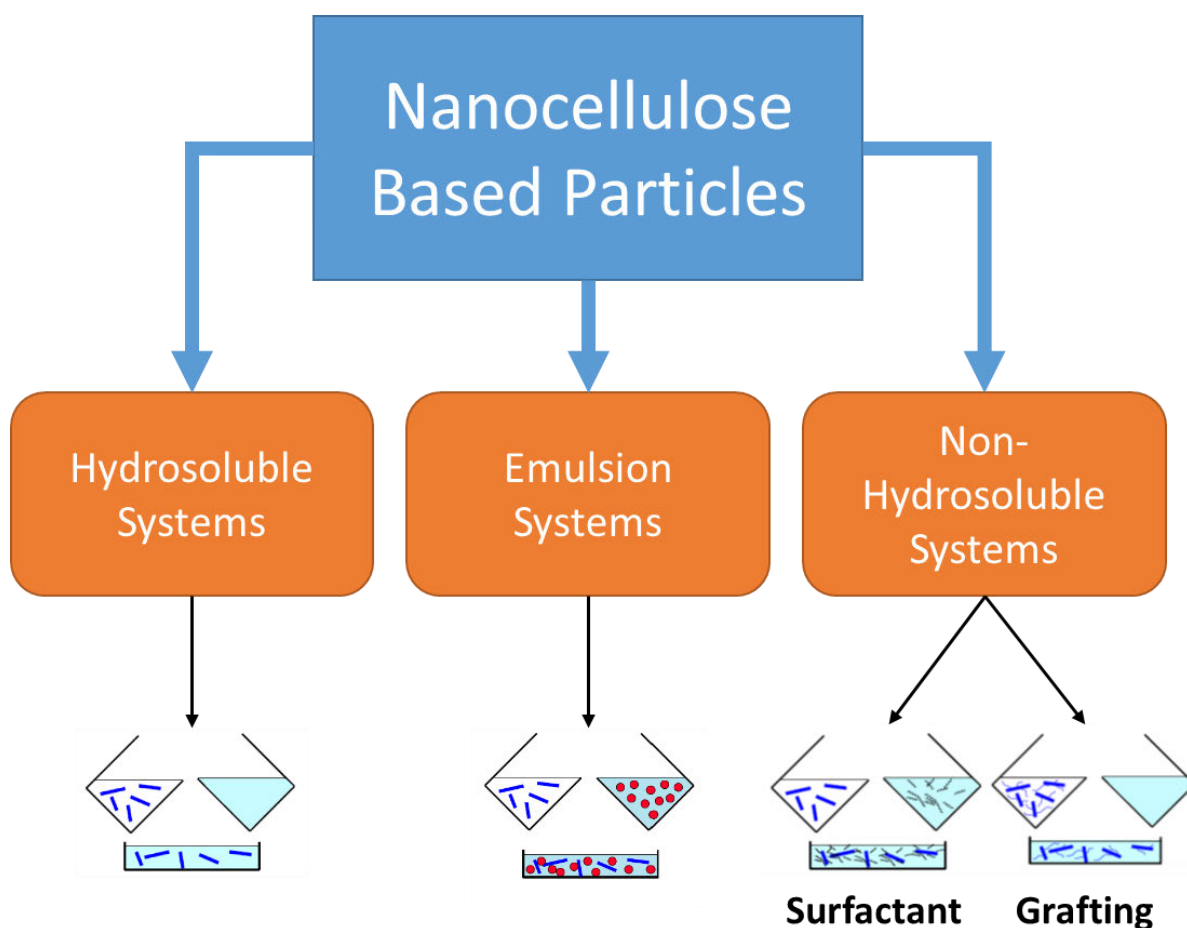


Figure 2.10. Scheme depicting the general approach toward the preparation of cellulose-based nanocomposites by solvent casting.⁹¹

2.4.2.1. Hydrosoluble Systems

NCC particles are recovered in water suspensions after acid hydrolysis. Due to the great stability possessed by cellulose nanoparticles in aqueous mediums, water is the preferred medium for the preparation of nanocomposite films.^{89a} Films are formed by mixing the cellulose-based suspension with a particular polymer that is dissolved in aqueous media prior to the mixing, which is followed by the evaporation of the liquid. However, this particular system is restricted to water-soluble polymers.^{89a} The polymeric systems are highly sensitive

to humidity. This makes it difficult to predict the amount of water retention in these films after evaporation which requires important attention. Researchers tend to store films in an oven and under vacuum. These definitive environments are essential, as demonstrated by research on polyvinyl acetate (PVA),⁹² and hydroxypropyl cellulose (HPC).^{47a} Water present in films induces a strong plasticizing effect and greatly affects the properties of these film.^{89a}

2.4.2.2. Emulsion Systems

An alternative to further the range of polymer matrices consists of using the polymer in the form of a latex. The main interest is attributed to the use of non-polar and partially hydrophobic polymers while maintaining an aqueous medium for the processing of the films to preserve the dispersion of the nanoparticles.^{89a} Favier *et al.* embraced this methodology of solvent casting using a synthetic latex obtained by the copolymerization between styrene (35 wt%) and butyl-acrylate (65 wt%) (poly(S-co-BuA)).⁹³ The research involved the mixing of the prepared NCC crystal in an aqueous suspension with the polymer latex. Nanocomposite films were later obtained by evaporation of water and particle combination at a temperature higher than transition temperature (T_g) of poly (S-co-BuA), around 0 °C.⁹⁴

Later, research was driven toward the processing of nanocomposites by using alternative matrices such as poly(β -hydroxyoctanoate) (PHO),^{90b} polyvinylchloride (PVC),⁹⁵ waterborne epoxy,⁹⁶ natural rubber,⁹⁷ and polyvinyl acetate (PVAc).⁹⁸ These reports illustrated that the cellulose nanoparticles suspensions were dispersed within the polymer emulsion system in water.

2.4.2.3. Non-Hydrosoluble Systems

Surfactants have great potential in obtaining stable suspensions of NCC crystals in organic media. Bonini *et al.* described a protocol⁹⁹ that was based on a previous patent¹⁰⁰ by obtaining cellulose whiskers coated with a surfactant. The suspension of tunicin whiskers were prepared by an acid hydrolysis treatment based on the method of Marchessault *et al.*¹⁰¹ Thereafter the suspension was mixed with the surfactant (a phosphoric ester of poly(ethylene oxide) (9) nonylphenyl (PEPNP)) in a ratio of 4:1 (by weight PEPNP/cellulose whiskers). The obtained composite was freeze-dried (from the aqueous media) to obtain pellets which were later dispersed in toluene with excess surfactant removed by centrifugation.¹⁰² This protocol allows for the preparation of nanocomposites by dispersing the suspension of coated crystals in a polymer solution dispersed in organic media.

Grafting could allow long chains (contained in the nanofiller) to be transformed into a co-continuous material by increasing its polarity. This is achieved *via* the use of grafting agents that contain a reactive end group and a long “compatibilizing” tail. This approach of surface modification allows for the processing of nanocomposites by classical methods such as hot-pressing, injection moulding or thermoforming. The modification of NCC and MFC with organic compounds *via* the reactive surface hydroxyl groups has been carried out with different grafting agents such as isocyanates,¹⁰³ anhydrides,¹⁰³ chlorosilanes¹⁰⁴ or silanes.¹⁰⁴

2.4.3 Properties of Cellulose-Based Nanocomposites

2.4.3.1. Mechanical Properties

Cellulose nanoparticles such as NCC and MFC possess a high specific area and remarkable mechanical properties, making both potential candidates to improve mechanical properties of a neat matrix.¹⁰⁵ The size and morphology of nanocellulose are dependent on the source material. This, in turn, commands the mechanical properties of the nanocelluloses and to a greater degree the nanocomposites.¹⁰⁶ The aspect ratios (L/D , where L = length and D = diameter) of nanocelluloses usually gives an indication of the strength possessed. Higher aspect ratios tend to lead to greater mechanical strength.¹⁰⁵ However other factors such as dispersion and orientation also tend to dictate the mechanical properties of nanocelluloses.¹⁰⁷

Dynamical mechanical analysis (DMA) is a powerful tool for the analysis of linear mechanical behaviour within nanocomposites under different temperature/frequency ranges. Non-linear properties are usually determined *via* classical tensile or compressive tests.^{5b} Recently, research has been focused toward the elucidation of the origin of the mechanical reinforcing effect in nanocomposites.¹⁰⁵

2.4.3.2. Thermal Properties

The use of nanocelluloses as reinforcement in nanocomposites⁹³⁻⁹⁴ (on account of its exceptional properties) has gathered interest as of late. However, the low thermal stability of nanocellulose is a limitation to nanocomposites’ production at high temperatures, which is a challenge to researchers and commercialisation as a whole.^{5b} The analysis of thermal properties allow for the determination of processing and operating temperature of materials.^{88b} Thus it is important to determine the main characteristics of polymeric systems such as glass-

rubber transition temperature (T_g), melting point (T_m) and thermal stability through differential scanning calorimetry (DSC), thermogravimetric analysis (TGA), thermomechanical analysis (TMA), and dynamic mechanical thermal analysis (DMTA).^{88b}

2.4.3.3. Barrier Properties

Interest in nanoparticles for composite applications often originate from the extraordinary mechanical properties that they possess. With the use of low nanocellulose volume fractions, improved properties can be attained, without major disturbance of other properties such as impact resistance or plastic deformation capability.¹⁰⁸ However, there is an increasing interest in the barrier properties due to increased tortuosity provided by nanoparticles. Recently, the majority of food packaging materials are based on petrochemical polymers which are near non-degradable. This phenomenon represents a serious environmental risk. The ease of processability, their low cost and excellent barrier properties sustain their use within this commercial sector.¹⁰⁹ Development of a new class of biodegradable materials with good barrier properties is thus an ongoing endeavour. Gas barrier and selected diffusion properties, as well as permeability and water absorption attributes, make up the barrier properties of nanocelluloses and the composites based on them.^{88a}

2.4.4 Application of nanocellulose based materials in catalysis

Metal NP-nanocellulose hybrid composites have been applied towards catalysis at a progressive rate, especially in the last 5 years. Nanocelluloses provides interesting properties compared to conventional supports and thus afford novel catalytic systems, with unique features, notably in terms of NP stability, NP reactivity and selectivity, but also with the goal of afford sustainable alternatives to known methods.¹¹⁰ Nanocelluloses have been used in catalytic reductions,¹¹¹ oxidations,¹¹² and coupling reactions.¹¹³ Apart from these nanocellulose based materials have also been used in electro-catalysis¹¹⁴ and photocatalysis.¹¹⁵

2.5 References

1. (a) Klemm, D.; Schumann, D.; Kramer, F.; Heßler, N.; Hornung, M.; Schmauder, H.-P.; Marsch, S., Nanocelluloses as innovative polymers in research and application. *Polysaccharides II* **2006**, 49-96; (b) Moon, R. J.; Martini, A.; Nairn, J.; Simonsen, J.; Youngblood, J., Cellulose nanomaterials review: structure, properties and nanocomposites. *Chemical Society Reviews*. **2011**, *40* (7), 3941-3994; (c) Eichhorn, S. J., Cellulose nanowhiskers: promising materials for advanced applications. *Soft Matter* **2011**, *7* (2), 303-315; (d) Nishiyama, Y., Structure and properties of the cellulose microfibril. *Journal of Wood Science* **2009**, *55* (4), 241-249; (e) Habibi, Y.; Lucia, L. A.; Rojas, O. J., Cellulose nanocrystals: chemistry, self-assembly, and applications. *Chemical Reviews* **2010**, *110* (6), 3479-3500; (f) Eichhorn, S. J.; Dufresne, A.; Aranguren, M.; Marcovich, N. E.; Capadona, J. R.; Rowan, S. J.; Weder, C.; Thielemans, W.; Roman, M.; Renneckar, S.; Gindl, W.; Veigel, S.; Keckes, J.; Yano, H.; Abe, K.; Nogi, M.; Nakagaito, A. N.; Mangalam, A.; Simonsen, J.; Benight, A. S.; Bismarck, A.; Berglund, L. A.; Peijs, T., Review: current international research into cellulose nanofibres and nanocomposites. *Journal of Materials Science* **2009**, *45* (1), 1-33.
2. (a) Zugenmaier, P., *Cellulose*. Springer: 2008; (b) Klemm, D.; Heublein, B.; Fink, H.-P.; Bohn, A., Cellulose: Fascinating biopolymer and sustainable raw material. *Angewandte Chemie International Edition* **2005**, *44* (22), 3358-3393; (c) O'Sullivan, A. C., Cellulose: the structure slowly unravels. *Cellulose* **1997**, *4* (3), 173-207; (d) Hon, D. N. S., Cellulose: a random walk along its historical path. *Cellulose* **1994**, *1* (1), 1-25; (e) Payen, A., Memoir on the composition of the tissue of plants and of woody material. *Comptes Rendus Biologies* **1838**, *7*, 1052-1056; (f) Brogniart, A.; Pelonze, A.; Dumas, R., Report on a Memoir of M. Payen, on the Composition of the Woody Nature. *Comptes Rendus* **1839**, *8*, 51-53.
3. (a) Sjostrom, E., *Wood chemistry: fundamentals and applications*. Elsevier: **2013**; (b) Kondo, T., Hydrogen bonds in cellulose and cellulose derivatives. In *Polysaccharides: Structural diversity and functional versatility*, Marcel Dekker, New York: **1998**; pp 131-172.

4. Azizi Samir, M. A. S.; Alloin, F.; Dufresne, A., Review of recent research into cellulosic whiskers, their properties and their application in nanocomposite field. *Biomacromolecules* **2005**, *6* (2), 612-626.
5. (a) Saxena, I. M.; Brown, J. R. M., Cellulose Biosynthesis: Current Views and Evolving Concepts. *Annals of Botany* **2005**, *96* (1), 9-21; (b) Siqueira, G.; Bras, J.; Dufresne, A., Cellulosic bionanocomposites: a review of preparation, properties and applications. *Polymers* **2010**, *2* (4), 728-765.
6. Saito, T.; Hirota, M.; Tamura, N.; Kimura, S.; Fukuzumi, H.; Heux, L.; Isogai, A., Individualization of nano-sized plant cellulose fibrils by direct surface carboxylation using tempo catalyst under neutral conditions. *Biomacromolecules* **2009**, *10* (7), 1992-1996.
7. (a) Ranby, B., Physico-chemical investigations on animal cellulose (Tunicin). *Arkiv for Kemi* **1952**, *4* (3), 241-&; (b) Ranby, B., Physico-chemical investigations on bacterial cellulose. *Arkiv for Kemi* **1952**, *4* (3), 249-257.
8. Bower, D. I., *An introduction to polymer physics*. Cambridge University Press: **2002**.
9. Chen, H., Chemical composition and structure of natural lignocellulose. in *biotechnology of lignocellulose: theory and practice*, Springer Netherlands: Dordrecht, **2014**; pp 25-71.
10. Nanocellulose market by by product type (nanocrystalline cellulose, nanofibrillated cellulose, bacterial nanocellulose); by end-users (composites, oil & gas, paper processing, food & beverages, paints & coatings, personal care, and other - Global Industry Analysis and Forecast 2015 – 2023. <https://www.marketresearchengine.com/reportdetails/nanocellulose-market-report> (accessed 17/03/2017).
11. The global market for nanocellulose 2017-2027. <https://futuremarketsinc.com/nanocellulosemarket/> (accessed 26/08/2017).
12. (a) Mohamed, M. A.; Salleh, W. N. W.; Jaafar, J.; Asri, S. E. A. M.; Ismail, A. F., Physicochemical properties of "green" nanocrystalline cellulose isolated from recycled newspaper. *RSC Advances* **2015**, *5* (38), 29842-29849; (b) Khawas, P.; Deka, S. C., Isolation and characterization of cellulose nanofibers from culinary banana peel using

- high-intensity ultrasonication combined with chemical treatment. *Carbohydrate Polymer* **2016**, *137*, 608-616; (c) Ogundare, S. A.; Moodley, V.; van Zyl, W. E., Nanocrystalline cellulose isolated from discarded cigarette filters. *Carbohydrate Polymer*. **2017**, *175*, 273-281.
13. Dechant, J., Polymer handbook. 3rd edition. New York: John Wiley & Sons 1989. Cloth bound, ca. 1850 pages, £ 115.00, \$175.00. *Acta Polymerica* **1990**, *41* (6), 361-362.
 14. Ioelovich, M., Characterization of various kinds of nanocellulose. In *Handbook of Nanocellulose and Cellulose Nanocomposites*, Wiley-VCH Verlag GmbH & Co. KGaA: **2017**; pp 51-100.
 15. Kamel, S.; Ali, N.; Jahangir, K.; Shah, S.; El-Gendy, A., Pharmaceutical significance of cellulose: a review. *Express Polymer Letters* **2008**, *2* (11), 758-778.
 16. Tosh, B., Synthesis and sustainable applications of cellulose esters and ethers: a review. *International Journal of Energy and Sustainable Environmental Engineering* **2014**, *1*, 56-78.
 17. Turbak, A. F.; Snyder, F. W.; Sandberg, K. R. Microfibrillated cellulose, a new cellulose product: properties, uses, and commercial potential, *Journal of Applied Polymeric Science: Applied Polymer Symposium*;(United States), ITT Rayonier Inc., Shelton, WA: **1983**.
 18. (a) Filson, P. B.; Dawson-Andoh, B. E., Sono-chemical preparation of cellulose nanocrystals from lignocellulose derived materials. *Bioresource Technology* **2009**, *100* (7), 2259-2264; (b) Jarvis, M., Cellulose stacks up. *Nature* **2003**, *426*, 611.
 19. (a) Lasseuguette, E.; Roux, D.; Nishiyama, Y., Rheological properties of microfibrillar suspension of TEMPO-oxidized pulp. *Cellulose* **2008**, *15* (3), 425-433; (b) Abe, K.; Iwamoto, S.; Yano, H., Obtaining cellulose nanofibers with a uniform width of 15 nm from wood. *Biomacromolecules* **2007**, *8* (10), 3276-3278; (c) Nogi, M.; Handa, K.; Nakagaito, A. N.; Yano, H., Optically transparent bionanofiber composites with low sensitivity to refractive index of the polymer matrix. *Applied Physics Letters* **2005**, *87* (24), 243110; (d) Iwamoto, S.; Nakagaito, A. N.; Yano, H.; Nogi, M., Optically transparent composites reinforced with plant fiber-based nanofibers. *Applied Physics A* **2005**, *81* (6), 1109-1112; (e) Nakagaito, A. N.; Yano, H., The effect of morphological

- changes from pulp fiber towards nano-scale fibrillated cellulose on the mechanical properties of high-strength plant fiber based composites. *Applied Physics A* **2004**, *78* (4), 547-552; (f) Nakagaito, A. N.; Yano, H., Novel high-strength biocomposites based on microfibrillated cellulose having nano-order-unit web-like network structure. *Applied Physics A* **2005**, *80* (1), 155-159; (g) Herrick, F. W.; Casebier, R. L.; Hamilton, J. K.; Sandberg, K. R., Microfibrillated cellulose: morphology and accessibility, *Journal of Applied Polymer Science: Applied Polymers Symposium*; (United States), ITT Rayonier Inc., Shelton, WA: **1983**; (h) Herrick, F., Review of the treatment of cellulose with liquid ammonia, *Journal of Applied Polymer Science: Applied Polymers Symposium*, **1983**; 993-1023.
20. (a) Hasan, N.; Biak, D. R. A.; Kamarudin, S., Application of bacterial cellulose (BC) in natural facial scrub. *International Journal on Advanced Science, Engineering and Information Technology* **2012**, *2* (4), 272-275; (b) Czaja, W.; Krystynowicz, A.; Bielecki, S.; Brown, R. M., Microbial cellulose—the natural power to heal wounds. *Biomaterials* **2006**, *27* (2), 145-151; (c) Amnuakit, T.; Chusuit, T.; Raknam, P.; Boonme, P., Effects of a cellulose mask synthesized by a bacterium on facial skin characteristics and user satisfaction. *Medical Devices (Auckland, N.Z.)* **2011**, *4*, 77-81; (d) Xue, J.; Song, F.; Yin, X.-w.; Wang, X.-l.; Wang, Y.-z., Let It Shine: A Transparent and Photoluminescent Foldable Nanocellulose/Quantum Dot Paper. *ACS Applied Materials & Interfaces* **2015**, *7* (19), 10076-10079; (e) Syverud, K., Tissue engineering using plant-derived cellulose nanofibrils (cnf) as scaffold material. In *Nanocelluloses: Their Preparation, Properties, and Applications*, American Chemical Society: **2017**; 1251, 171-189; (f) Maladen, R. D.; Manifold, J. A.; Ostendorf, W. W.; Sheehan, J. G.; Barkey, D. J., Sanitary tissue products and methods for making same. The Procter & Gamble Company, *US Patent no.: 9,617,684*; **2017**.
21. Nishikawa, S.; Ono, S., Transmission of X-Rays through Fibrous, Lamellar and Granular Substances. *Proceedings of the Tokyo Mathematico-Physical Society. 2nd Series* **1913**, *7* (8), 131-138.
22. (a) Langan, P.; Nishiyama, Y.; Chanzy, H., A revised structure and hydrogen-bonding system in cellulose II from a neutron fiber diffraction analysis. *Journal of the American Chemical Society* **1999**, *121* (43), 9940-9946; (b) Balashov, V.; Preston, R. D., Fine structure of cellulose and other microfibrillar substances. *Nature* **1955**, *176*, 64.

23. Atalla, R. H.; VanderHart, D. L., Native cellulose: a composite of two distinct crystalline forms. *Science* **1984**, *223*, 283-286.
24. Ishikawa, A.; Okano, T.; Sugiyama, J., Fine structure and tensile properties of ramie fibres in the crystalline form of cellulose I, II, III and IV. *Polymer* **1997**, *38* (2), 463-468.
25. (a) Nishiyama, Y.; Langan, P.; Chanzy, H., Crystal structure and hydrogen-bonding system in cellulose I β from synchrotron x-ray and neutron fiber diffraction. *Journal of the American Chemical Society* **2002**, *124* (31), 9074-9082; (b) Nishiyama, Y.; Sugiyama, J.; Chanzy, H.; Langan, P., Crystal structure and hydrogen bonding system in cellulose I α from synchrotron x-ray and neutron fiber diffraction. *Journal of the American Chemical Society* **2003**, *125* (47), 14300-14306.
26. Sugiyama, J.; Vuong, R.; Chanzy, H., Electron diffraction study on the two crystalline phases occurring in native cellulose from an algal cell wall. *Macromolecules* **1991**, *24* (14), 4168-4175.
27. Viëtor, R. J.; Mazeau, K.; Lakin, M.; Pérez, S., A priori crystal structure prediction of native celluloses. *Biopolymers* **2000**, *54* (5), 342-354.
28. Finkenstadt, V. L.; Millane, R. P., Crystal structure of *Valonia* cellulose I β . *Macromolecules* **1998**, *31* (22), 7776-7783.
29. Qian, X.; Ding, S.-Y.; Nimlos, M. R.; Johnson, D. K.; Himmel, M. E., Atomic and electronic structures of molecular crystalline cellulose I β : a first-principles investigation. *Macromolecules* **2005**, *38* (25), 10580-10589.
30. Gardner, K. H.; Blackwell, J., The structure of native cellulose. *Biopolymers* **1974**, *13* (10), 1975-2001.
31. (a) Maurer, A.; Fengel, D., Parallel orientation of the molecular chains in cellulose I and cellulose II deriving from higher plants. *European Journal of Wood and Wood Products: Holz als Roh- und Werkstoff* **1992**, *50* (12), 493; (b) Stipanovic, A. J.; Sarko, A., Packing Analysis of Carbohydrates and Polysaccharides. 6. Molecular and Crystal Structure of Regenerated Cellulose II. *Macromolecules* **1976**, *9* (5), 851-857.

32. (a) Park, S.; Baker, J. O.; Himmel, M. E.; Parilla, P. A.; Johnson, D. K., Cellulose crystallinity index: measurement techniques and their impact on interpreting cellulase performance. *Biotechnology for Biofuels* **2010**, *3* (1), 10; (b) Kim, U.-J.; Kuga, S.; Wada, M.; Okano, T.; Kondo, T., Periodate Oxidation of crystalline cellulose. *Biomacromolecules* **2000**, *1* (3), 488-492.
33. Li, Q.; Renneckar, S., Supramolecular structure characterization of molecularly thin cellulose I nanoparticles. *Biomacromolecules* **2011**, *12* (3), 650-659.
34. Atalla, R. H.; Brady, J. W.; Matthews, J. F.; Ding, S.-Y.; Himmel, M. E., Structures of plant cell wall celluloses. In *Biomass Recalcitrance*, Blackwell Publishing Ltd.: **2009**; 188-212.
35. (a) Fengel, D., Ultrastructural behaviour of cell wall polysaccharides. *Tappi* **1970**, *53* (3), 497-503; (b) Scheible, W.-R.; Bashir, S.; Rose, J. K., 10 Plant cell walls in the post-genomic era. *The Plant Cell Wall* **2003**, *8*, 325; (c) Fengel, D., Characterization of cellulose by deconvoluting the OH valency range in FTIR spectra. *Holzforchung-International Journal of the Biology, Chemistry, Physics and Technology of Wood* **1992**, *46* (4), 283-288.
36. Åkerholm, M.; Salmén, L., The oriented structure of lignin and its viscoelastic properties studied by static and dynamic FT-IR spectroscopy. *Holzforchung-International Journal of the Biology, Chemistry, Physics and Technology of Wood* **2003**, *57* (5), 459-465.
37. (a) Salmén, L.; Olsson, A.-M., Interaction between hemicelluloses, lignin and cellulose: structure-property relationships. *Journal of Pulp and Paper Science* **1998**, *24* (3), 99-103; (b) Terashima, N.; Kitano, K.; Kojima, M.; Yoshida, M.; Yamamoto, H.; Westermark, U., Nanostructural assembly of cellulose, hemicellulose, and lignin in the middle layer of secondary wall of ginkgo tracheid. *Journal of Wood Science* **2009**, *55* (6), 409.
38. (a) Jonoobi, M.; Harun, J.; Mishra, M.; Oksman, K., Chemical composition, crystallinity and thermal degradation of bleached and unbleached kenaf bast (*Hibiscus cannabinus*) pulp and nanofiber. *BioResources* **2009**, *4* (2), 626-639; (b) Owolabi, A. F.; Haafiz, M. K. M.; Hossain, M. S.; Hussin, M. H.; Fazita, M. R. N., Influence of alkaline hydrogen peroxide pre-hydrolysis on the isolation of microcrystalline cellulose

- from oil palm fronds. *International Journal of Biological Macromolecules* **2017**, *95*, 1228-1234; (c) Chieng, B.; Lee, S.; Ibrahim, N.; Then, Y.; Loo, Y., Isolation and Characterization of Cellulose Nanocrystals from Oil Palm Mesocarp Fiber. *Polymers* **2017**, *9* (8), 355; (d) Sun, J. X.; Sun, X. F.; Zhao, H.; Sun, R. C., Isolation and characterization of cellulose from sugarcane bagasse. *Polymer Degradation and Stability* **2004**, *84* (2), 331-339; (e) Bhatnagar, A.; Sain, M., Processing of Cellulose Nanofiber-reinforced Composites. *Journal Reinforced Plastics and Composites* **2005**, *24* (12), 1259-1268.
39. Klemm, D.; Kramer, F.; Moritz, S.; Lindström, T.; Ankerfors, M.; Gray, D.; Dorris, A., Nanocelluloses: a new family of nature-based materials. *Angewandte Chemie International Edition* **2011**, *50* (24), 5438-5466.
 40. Tingaut, P.; Eyholzer, C.; Zimmermann, T., Functional polymer nanocomposite materials from microfibrillated cellulose. In *Advances in Nanocomposite Technology*, InTech: Rijeka, **2011**; Ch. 14.
 41. Ross, P.; Mayer, R.; Benziman, M., Cellulose biosynthesis and function in bacteria. *Microbiological reviews* **1991**, *55* (1), 35-58.
 42. Nishino, T.; Takano, K.; Nakamae, K., Elastic modulus of the crystalline regions of cellulose polymorphs. *Journal of Polymer Science Part B: Polymer Physics* **1995**, *33* (11), 1647-1651.
 43. (a) Malm, C. J.; Risberg, B.; Bodin, A.; Bäckdahl, H.; Johansson, B. R.; Gatenholm, P.; Jeppsson, A., Small calibre biosynthetic bacterial cellulose blood vessels: 13-months patency in a sheep model. *Scandinavian Cardiovascular Journal* **2012**, *46* (1), 57-62; (b) Petersen, N.; Gatenholm, P., Bacterial cellulose-based materials and medical devices: current state and perspectives. *Applied Microbiology and Biotechnology* **2011**, *91* (5), 1277.
 44. Bulota, M.; Kreitsmann, K.; Hughes, M.; Paltakari, J., Acetylated microfibrillated cellulose as a toughening agent in poly(lactic acid). *Journal of Applied Polymer Science* **2012**, *126* (S1), 449-458.
 45. Aulin, C.; Gällstedt, M.; Lindström, T., Oxygen and oil barrier properties of microfibrillated cellulose films and coatings. *Cellulose* **2010**, *17* (3), 559-574.

46. (a) Bonner, P.; Kaminski, C.; Lorenzetti, D. L.; Maitra, P.; Moscardi, J. S.; Wu, J. M., Rinse-off skin care compositions containing cellulosic materials. U.S. Patent 9,549,889, **2017**; (b) Lee, H.; Sundaram, J.; Mani, S., Production of cellulose nanofibrils and their application to food: a review. In *Nanotechnology: Food and Environmental Paradigm*, Springer Singapore: Singapore, **2017**; 1-33; (c) Carreño, N. L. V.; Barbosa, A. M.; Noremborg, B. S.; Salas, M. M. S.; Fernandes, S. C. M.; Labidi, J., Advances in nanostructured cellulose-based biomaterials. In *Advances in Nanostructured Cellulose-based Biomaterials*, Springer International Publishing: Cham, **2017**; 1-32; (d) Evenou, F.; Couderc, S.; Kim, B.; Fujii, T.; Sakai, Y., Microfibrillated cellulose sheets coating oxygen-permeable PDMS membranes induce rat hepatocytes 3D aggregation into stably-attached 3D hemispheroids. *Journal of Biomaterials Science, Polymer Edition* **2011**, 22 (11), 1509-1522.
47. (a) Johnson, R. K.; Zink-Sharp, A.; Renneckar, S. H.; Glasser, W. G., A new bio-based nanocomposite: fibrillated TEMPO-oxidized celluloses in hydroxypropylcellulose matrix. *Cellulose* **2009**, 16 (2), 227-238; (b) Svagan, A. J.; Azizi Samir, M. A. S.; Berglund, L. A., Biomimetic polysaccharide nanocomposites of high cellulose content and high toughness. *Biomacromolecules* **2007**, 8 (8), 2556-2563; (c) Siqueira, G.; Bras, J.; Dufresne, A., Cellulose whiskers versus microfibrils: influence of the nature of the nanoparticle and its surface functionalization on the thermal and mechanical properties of nanocomposites. *Biomacromolecules* **2009**, 10 (2), 425-432.
48. Arcot, L. R.; Gröschel, A. H.; Linder, M. B.; Rojas, O. J.; Ikkala, O., Self-assembly of native cellulose nanostructures. In *Handbook of Nanocellulose and Cellulose Nanocomposites*, Wiley-VCH Verlag GmbH & Co: **2017**; 123-174.
49. (a) Boujemaoui, A.; Cobo Sanchez, C.; Engström, J.; Bruce, C.; Fogelström, L.; Carlmark, A.; Malmström, E., Polycaprolactone Nanocomposites reinforced with cellulose nanocrystals surface-modified *via* covalent grafting or physisorption: a comparative study. *ACS Applied Materials & Interfaces* **2017**, 9 (40), 35305-35318; (b) Lam, N. T.; Saewong, W.; Sukyai, P., Effect of varying hydrolysis time on extraction of spherical bacterial cellulose nanocrystals as a reinforcing agent for poly(vinyl alcohol) composites. *Journal of Polymer Research* **2017**, 24 (5), 71; (c) Yu, H.-Y.; Wang, C.; Abdalkarim, S. Y. H., Cellulose nanocrystals/polyethylene glycol as

- bifunctional reinforcing/compatibilizing agents in poly(lactic acid) nanofibers for controlling long-term in vitro drug release. *Cellulose* **2017**, *24* (10), 4461-4477.
50. (a) Wijaya, C. J.; Saputra, S. N.; Soetaredjo, F. E.; Putro, J. N.; Lin, C. X.; Kurniawan, A.; Ju, Y.-H.; Ismadji, S., Cellulose nanocrystals from passion fruit peels waste as antibiotic drug carrier. *Carbohydrate Polymers* **2017**, *175*, 370-376; (b) Jackson, J. K.; Letchford, K.; Wasserman, B. Z.; Ye, L.; Hamad, W. Y.; Burt, H. M., The use of nanocrystalline cellulose for the binding and controlled release of drugs. *International journal of nanomedicine* **2011**, *6*, 321; (c) Dong, S.; Roman, M., Fluorescently labeled cellulose nanocrystals for bioimaging applications. *Journal of the American Chemical Society* **2007**, *129* (45), 13810-13811.
 51. Lee, S. E.; Park, Y. S., The role of bacterial cellulose in artificial blood vessels. *Molecular & Cellular Toxicology* **2017**, *13* (3), 257-261.
 52. Khalid, A.; Khan, R.; Ul-Islam, M.; Khan, T.; Wahid, F., Bacterial cellulose-zinc oxide nanocomposites as a novel dressing system for burn wounds. *Carbohydrate Polymers*. **2017**, *164*, 214-221.
 53. Gadim, T. D. O.; Loureiro, F. J. A.; Vilela, C.; Rosero-Navarro, N.; Silvestre, A. J. D.; Freire, C. S. R.; Figueiredo, F. M. L., Protonic conductivity and fuel cell tests of nanocomposite membranes based on bacterial cellulose. *Electrochimica Acta* **2017**, *233*, 52-61.
 54. Lay, M.; González, I.; Tarrés, J. A.; Pellicer, N.; Bun, K. N.; Vilaseca, F., High electrical and electrochemical properties in bacterial cellulose/polypyrrole membranes. *European Polymer Journal* **2017**, *91*, 1-9.
 55. (a) Hentze, H.-P., From nanocellulose science towards applications. *Developments in advanced biocomposites* **2010**, *71*; (b) Kargarzadeh, H.; Ioelovich, M.; Ahmad, I.; Thomas, S.; Dufresne, A., Methods for extraction of nanocellulose from various sources. In *Handbook of Nanocellulose and Cellulose Nanocomposites*, Wiley-VCH Verlag GmbH & Co. KGaA: **2017**; 1-49.
 56. Spence, K. L.; Venditti, R. A.; Rojas, O. J.; Habibi, Y.; Pawlak, J. J., A comparative study of energy consumption and physical properties of microfibrillated cellulose produced by different processing methods. *Cellulose* **2011**, *18* (4), 1097-1111.

57. Wuhrmann, K.; Heuberger, A.; Muhlethaler, K., Electron-microscopic investigations of cellulose fibers after supersonic treatment. *Experientia* **1946**, *2* (2012), 105-107.
58. (a) Yoshioka, M.; Sakaguchi, K.; Ohno, T.; Nishio, Y.; Shiraishi, N., Fabrication of pulverized cellulose by ultra high-pressure water jet treatment and usage in polymer nanocomposites and graft copolymerization. *Journal of Wood Science* **2009**, *55* (5), 335; (b) Kose, R.; Mitani, I.; Kasai, W.; Kondo, T., "Nanocellulose" As a Single Nanofiber Prepared from Pellicle Secreted by *Gluconacetobacter xylinus* Using Aqueous Counter Collision. *Biomacromolecules* **2011**, *12* (3), 716-720.
59. (a) Tang, Y.; Yang, S.; Zhang, N.; Zhang, J., Preparation and characterization of nanocrystalline cellulose *via* low-intensity ultrasonic-assisted sulfuric acid hydrolysis. *Cellulose* **2014**, *21* (1), 335-346; (b) Liu, Y.; Wang, H.; Yu, G.; Yu, Q.; Li, B.; Mu, X., A novel approach for the preparation of nanocrystalline cellulose by using phosphotungstic acid. *Carbohydrate Polymers* **2014**, *110*, 415-422; (c) Cui, S.; Zhang, S.; Ge, S.; Xiong, L.; Sun, Q., Green preparation and characterization of size-controlled nanocrystalline cellulose *via* ultrasonic-assisted enzymatic hydrolysis. *Industrial Crops and Products* **2016**, *83*, 346-352.
60. (a) Bondeson, D.; Mathew, A.; Oksman, K., Optimization of the isolation of nanocrystals from microcrystalline cellulose by acid hydrolysis. *Cellulose* **2006**, *13* (2), 171; (b) Luo, Y.; Liu, X.; Huang, J., Heterogeneous nanotubular anatase/rutile titania composite derived from natural cellulose substance and its photocatalytic property. *Crystal Engineering Communication* **2013**, *15* (28), 5586-5590; (c) Revol, J. F.; Bradford, H.; Giasson, J.; Marchessault, R. H.; Gray, D. G., Helicoidal self-ordering of cellulose microfibrils in aqueous suspension. *International Journal of Biological Macromolecules*. **1992**, *14* (3), 170-172.
61. (a) Chen, Y.; Chen, S.; Wang, B.; Yao, J.; Wang, H., TEMPO-oxidized bacterial cellulose nanofibers-supported gold nanoparticles with superior catalytic properties. *Carbohydrate Polymers* **2017**, *160*, 34-42; (b) Saito, T.; Kimura, S.; Nishiyama, Y.; Isogai, A., Cellulose Nanofibers Prepared by TEMPO-Mediated Oxidation of Native Cellulose. *Biomacromolecules* **2007**, *8* (8), 2485-2491; (c) Mishra, S. P.; Thirree, J.; Manent, A.-S.; Chabot, B.; Daneault, C., Ultrasound-catalyzed TEMPO-mediated oxidation of native cellulose for the production of nanocellulose: Effect of process variables. *BioResources* **2010**, *6* (1), 121-143.

62. Li, B.; Xu, W.; Kronlund, D.; Määttä, A.; Liu, J.; Smått, J.-H.; Peltonen, J.; Willför, S.; Mu, X.; Xu, C., Cellulose nanocrystals prepared *via* formic acid hydrolysis followed by TEMPO-mediated oxidation. *Carbohydrate Polymers* **2015**, *133*, 605-612.
63. De Nooy, A. E. J.; Besemer, A. C.; van Bekkum, H., Highly selective tempo mediated oxidation of primary alcohol groups in polysaccharides. *Recueil des Travaux Chimiques des Pays-Bas* **1994**, *113* (3), 165-166.
64. Isogai, A.; Saito, T.; Fukuzumi, H., TEMPO-oxidized cellulose nanofibers. *Nanoscale* **2011**, *3* (1), 71-85.
65. Saito, T.; Nishiyama, Y.; Putaux, J.-L.; Vignon, M.; Isogai, A., Homogeneous suspensions of individualized microfibrils from TEMPO-catalyzed oxidation of native cellulose. *Biomacromolecules* **2006**, *7* (6), 1687-1691.
66. Pääkkö, M.; Ankerfors, M.; Kosonen, H.; Nykänen, A.; Ahola, S.; Österberg, M.; Ruokolainen, J.; Laine, J.; Larsson, P. T.; Ikkala, O.; Lindström, T., Enzymatic hydrolysis combined with mechanical shearing and high-pressure homogenization for nanoscale cellulose fibrils and strong gels. *Biomacromolecules* **2007**, *8* (6), 1934-1941.
67. de Nooy, A. E. J.; Besemer, A. C.; van Bekkum, H., Selective oxidation of primary alcohols mediated by nitroxyl radical in aqueous solution. Kinetics and mechanism. *Tetrahedron* **1995**, *51* (29), 8023-8032.
68. Eyholzer, C.; Bordeanu, N.; Lopez-Suevos, F.; Rentsch, D.; Zimmermann, T.; Oksman, K., Preparation and characterization of water-redispersible nanofibrillated cellulose in powder form. *Cellulose* **2010**, *17* (1), 19-30.
69. Wågberg, L.; Winter, L.; Ödberg, L.; Lindström, T., On the charge stoichiometry upon adsorption of a cationic polyelectrolyte on cellulosic materials. *Colloids and Surfaces* **1987**, *27* (1), 163-173.
70. Li, Q.; Renneckar, S., Molecularly thin nanoparticles from cellulose: isolation of sub-microfibrillar structures. *Cellulose* **2009**, *16* (6), 1025.
71. Frey, M. W., Electrospinning cellulose and cellulose derivatives. *Polymer Reviews* **2008**, *48* (2), 378-391.

72. Pickwell, E.; Cole, B. E.; Fitzgerald, A. J.; Pepper, M.; Wallace, V. P., In vivo study of human skin using pulsed terahertz radiation. *Physics in Medicine & Biology* **2004**, *49* (9), 1595.
73. (a) Drexler, K. E., Nanotechnology: from Feynman to funding. *Bulletin of Science, Technology & Society* **2004**, *24* (1), 21-27; (b) Khademhosseini, A.; Langer, R., Drug delivery and tissue engineering. *Chemical Engineering Progress* **2006**, *102* (2), 38-42.
74. Dalmas, F.; Cavail  , J.-Y.; Gauthier, C.; Chazeau, L.; Dendievel, R., Viscoelastic behavior and electrical properties of flexible nanofiber filled polymer nanocomposites. Influence of processing conditions. *Composites Science and Technology* **2007**, *67* (5), 829-839.
75. (a) Dufresne, A., Cellulose-based composites and nanocomposites. *Monomers, polymers and composites from renewable resources* **2008**, 401-418; (b) Pandey, J. K.; Kim, C.-S.; Chu, W.-S.; Lee, C. S.; Jang, D.-Y.; Ahn, S.-H., Evaluation of morphological architecture of cellulose chains in grass during conversion from macro to nano dimensions. *e-Polymers* **2009**, *9* (1), 1221-1235; (c) Kamel, S., Nanotechnology and its applications in lignocellulosic composites, a mini review. *Express Polymer Letters* **2007**, *1* (9), 546-575.
76. Lopes, A. C.; Martins, P.; Lanceros-Mendez, S., Aluminosilicate and aluminosilicate based polymer composites: Present status, applications and future trends. *Progress in Surface Science* **2014**, *89* (3), 239-277.
77. Esteves, A. C. C.; Barros-Timmons, A.; Trindade, T., Nanocomp  sitos de matriz polim  rica: estrat  gias de s  ntese de materiais h  bridos. *Qu  mica Nova* **2004**, *27*, 798-806.
78. (a) Azeredo, H. M. C. d., Nanocomposites for food packaging applications. *Food Research International* **2009**, *42* (9), 1240-1253; (b) Schadler, L. S.; Brinson, L. C.; Sawyer, W. G., Polymer nanocomposites: A small part of the story. *Journal of Minerals* **2007**, *59* (3), 53-60; (c) Kargarzadeh, H.; Ahmad, I.; Thomas, S.; Dufresne, A., *Handbook of Nanocellulose and Cellulose Nanocomposites*. Wiley Online Library: **2017**.

79. Mariano, M.; Dufresne, A., Nanocellulose: common strategies for processing of nanocomposites. In *Nanocelluloses: Their Preparation, Properties, and Applications*, American Chemical Society: **2017**; Vol. 1251, 203-225.
80. Hubbe, M. A., Hybrid filler (cellulose/noncellulose) reinforced nanocomposites. In *Handbook of Nanocellulose and Cellulose Nanocomposites*, Wiley-VCH Verlag GmbH & Co.: **2017**; 273-299.
81. (a) Laurent, A.; Harkema, J. R.; Andersen, E. W.; Owsianiak, M.; Vea, E. B.; Jolliet, O., Human health no-effect levels of TiO₂ nanoparticles as a function of their primary size. *Journal of Nanoparticle Research* **2017**, *19* (4), 130; (b) Panyala, N. R.; Peña-Méndez, E. M.; Havel, J., Silver or silver nanoparticles: a hazardous threat to the environment and human health? *Journal of Applied Biomedicine (De Gruyter Open)* **2008**, *6* (3); (c) Sahoo, S. K.; Parveen, S.; Panda, J. J., The present and future of nanotechnology in human health care. *Nanomedicine: Nanotechnology, Biology and Medicine* **2007**, *3* (1), 20-31.
82. Selikoff, I. J.; Lee, D. H. K., *Asbestos and disease*. Academic Press, Inc. 111 Fifth Avenue, New York: **1978**.
83. Haraguchi, K.; Takada, T., Characteristic sliding frictional behavior on the surface of nanocomposite hydrogels consisting of organic-inorganic network structure. *Macromolecular Chemistry and Physics* **2005**, *206* (15), 1530-1540.
84. (a) Kovacs, T.; Naish, V.; O'Connor, B.; Blaise, C.; Gagné, F.; Hall, L.; Trudeau, V.; Martel, P., An ecotoxicological characterization of nanocrystalline cellulose (NCC). *Nanotoxicology* **2010**, *4* (3), 255-270; (b) Shatkin, J. A.; Kim, B., Environmental health and safety of cellulose nanomaterials and composites. In *Handbook of Nanocellulose and Cellulose Nanocomposites*, Wiley-VCH Verlag GmbH & Co.: **2017**; 683-729.
85. Mohanty, A. K.; Misra, M.; Drzal, L. T., *Natural fibers, biopolymers, and biocomposites* **2005**.
86. (a) Ferrer Carrera, A., Coupling agent usage in the preparation of cellulose nanofibril (CNF)- and cellulose nanocrystal (CNC)-based nanocomposites. In *Handbook of Nanocellulose and Cellulose Nanocomposites*, Wiley-VCH Verlag GmbH & Co.: **2017**; 335-364; (b) Darder, M.; Aranda, P.; Ruiz-Hitzky, E., Bionanocomposites: a new

- concept of ecological, bioinspired, and functional hybrid materials. *Advanced Materials* **2007**, *19* (10), 1309-1319; (c) Oksman, K.; Mathew, A. P.; Bondeson, D.; Kvien, I., Manufacturing process of cellulose whiskers/polylactic acid nanocomposites. *Composites Science and Technology* **2006**, *66* (15), 2776-2784.
87. Hamad, W. Y., Cellulose nanocrystals and nanofibrils in advanced applications. In *Handbook of Nanocellulose and Cellulose Nanocomposites*, Wiley-VCH Verlag GmbH & Co.: **2017**; 799-832.
 88. (a) Fu, S.; Tian, C.; Lucia, L. A., Water sorption and barrier properties of cellulose nanocomposites. In *Handbook of Nanocellulose and Cellulose Nanocomposites*, Wiley-VCH Verlag GmbH & Co.: **2017**; 649-681; (b) Sheltami, R. M.; Kargarzadeh, H.; Abdullah, I.; Ahmad, I., Thermal properties of cellulose nanocomposites. In *Handbook of Nanocellulose and Cellulose Nanocomposites*, Wiley-VCH Verlag GmbH & Co.: **2017**; 523-552.
 89. (a) Karimi, S., Thermoplastic cellulose nanocomposites. In *Handbook of Nanocellulose and Cellulose Nanocomposites*, Wiley-VCH Verlag GmbH & Co.: **2017**; 175-216; (b) Mathew, A. P., Elastomeric Nanocomposites Reinforced with Nanocellulose and Nanochitin. In *Handbook of Nanocellulose and Cellulose Nanocomposites*, Wiley-VCH Verlag GmbH & Co. KGaA: 2017; pp 217-234; (c) Mngomezulu, M. E.; John, M. J., Thermoset cellulose nanocomposites: flammability characteristics. In *Handbook of Nanocellulose and Cellulose Nanocomposites*, Wiley-VCH Verlag GmbH & Co.: **2017**; 235-272.
 90. (a) Dufresne, A.; Cavail , J.-Y.; Helbert, W., Thermoplastic nanocomposites filled with wheat straw cellulose whiskers. part II: effect of processing and modeling. *Polymer Composites* **1997**, *18* (2), 198-210; (b) Dufresne, A.; Kellerhals, M. B.; Witholt, B., Transcrystallization in MCL-PHAS/cellulose whiskers composites. *Macromolecules* **1999**, *32* (22), 7396-7401.
 91. Siqueira, G.; Bras, J.; Dufresne, A., Cellulosic Bionanocomposites: A Review of Preparation, Properties and Applications. *Polymers* **2010**, *2* (4), 728.
 92. (a) Kvien, I.; Oksman, K., Orientation of cellulose nanowhiskers in polyvinyl alcohol. *Applied Physics A* **2007**, *87* (4), 641-643; (b) Roohani, M.; Habibi, Y.; Belgacem, N. M.; Ebrahim, G.; Karimi, A. N.; Dufresne, A., Cellulose whiskers reinforced polyvinyl

- alcohol copolymers nanocomposites. *European Polymer Journal* **2008**, *44* (8), 2489-2498.
93. Favier, V.; Chanzy, H.; Cavaille, J. Y., Polymer nanocomposites reinforced by cellulose whiskers. *Macromolecules* **1995**, *28* (18), 6365-6367.
94. Favier, V.; Canova, G. R.; Cavaillé, J. Y.; Chanzy, H.; Dufresne, A.; Gauthier, C., Nanocomposite materials from latex and cellulose whiskers. *Polymers for Advanced Technologies* **1995**, *6* (5), 351-355.
95. Chazeau, L.; Cavaillé, J. Y.; Canova, G.; Dendievel, R.; Bouterin, B., Viscoelastic properties of plasticized PVC reinforced with cellulose whiskers. *Journal of Applied Polymer Science* **1999**, *71* (11), 1797-1808.
96. Ruiz, M. M.; Cavaillé, J. Y.; Dufresne, A.; Graillat, C.; Gérard, J.-F., New waterborne epoxy coatings based on cellulose nanofillers. *Macromolecular Symposia* **2001**, *169* (1), 211-222.
97. Bendahou, A.; Habibi, Y.; Kaddami, H.; Dufresne, A., Physico-chemical characterization of palm from phoenix *Dactylifera-l*, preparation of cellulose whiskers and natural rubber based nanocomposites. *Journal of Biobased Materials and Bioenergy* **2009**, *3* (1), 81-90.
98. Garcia de Rodriguez, N. L.; Thielemans, W.; Dufresne, A., Sisal cellulose whiskers reinforced polyvinyl acetate nanocomposites. *Cellulose* **2006**, *13* (3), 261-270.
99. Bonini, C.; Heux, L.; Cavaillé, J.-Y.; Lindner, P.; Dewhurst, C.; Terech, P., Rodlike cellulose whiskers coated with surfactant: a small-angle neutron scattering characterization. *Langmuir* **2002**, *18* (8), 3311-3314.
100. Heux, L.; Bonini, C., Dispersion de microfibrilles et/ou de microcristaux, notamment de cellulose, dans un solvant organique. WO 00/77088, filed June 14, **1999**.
101. Marchessault, R.; Morehead, F.; Walter, N., Liquid crystal systems from fibrillar polysaccharides. *Nature* **1959**, *184* (4686), 632-633.
102. Heux, L.; Chauve, G.; Bonini, C., Nonflocculating and Chiral-Nematic Self-ordering of cellulose microcrystals suspensions in nonpolar solvents. *Langmuir* **2000**, *16* (21), 8210-8212.

103. Gopalan Nair, K.; Dufresne, A.; Gandini, A.; Belgacem, M. N., Crab shell chitin whiskers reinforced natural rubber nanocomposites. 3. Effect of Chemical Modification of Chitin Whiskers. *Biomacromolecules* **2003**, *4* (6), 1835-1842.
104. Goussé, C.; Chanzy, H.; Excoffier, G.; Soubeyrand, L.; Fleury, E., Stable suspensions of partially silylated cellulose whiskers dispersed in organic solvents. *Polymer* **2002**, *43* (9), 2645-2651.
105. Yu, H.-Y.; Yan, C.-F., Mechanical properties of cellulose nanofibril (CNF)- and cellulose nanocrystal (CNC)-based nanocomposites. In *Handbook of Nanocellulose and Cellulose Nanocomposites*, Wiley-VCH Verlag GmbH & Co.: **2017**; 393-443.
106. (a) Ioelovich, M., Cellulose as a nanostructured polymer: a short review. *BioResources* **2008**, *3* (4), 1403-1418; (b) Bledzki, A. K.; Gassan, J., Composites reinforced with cellulose based fibres. *Progress in Polymer Science* **1999**, *24* (2), 221-274.
107. Surve, M.; Pryamitsyn, V.; Ganesan, V., Polymer-bridged gels of nanoparticles in solutions of adsorbing polymers. *The Journal of chemical physics* **2006**, *125* (6), 064903-1 064903-12.
108. Dufresne, A., Polymer nanocomposites from biological sources. *Encyclopedia of nanoscience and nanotechnology* **2010**, *21*, 219-250.
109. Syverud, K.; Stenius, P., Strength and barrier properties of MFC films. *Cellulose* **2008**, *16* (1), 75.
110. Kaushik, M.; Moores, A., Review: nanocelluloses as versatile supports for metal nanoparticles and their applications in catalysis. *Green Chemistry* **2016**, *18* (3), 622-637.
111. (a) Tang, J.; Shi, Z.; Berry, R. M.; Tam, K. C., Mussel-Inspired Green Metallization of Silver Nanoparticles on Cellulose Nanocrystals and Their Enhanced Catalytic Reduction of 4-Nitrophenol in the Presence of β -Cyclodextrin. *Industrial & Engineering Chemistry Research* **2015**, *54* (13), 3299-3308; (b) Ramaraju, B.; Imae, T.; Destaye, A. G., Ag nanoparticle-immobilized cellulose nanofibril films for environmental conservation. *Applied Catalysis A: General* **2015**, *492*, 184-189.

112. Gopiraman, M.; Bang, H.; Yuan, G.; Yin, C.; Song, K.-H.; Lee, J. S.; Chung, I. M.; Karvembu, R.; Kim, I. S., Noble metal/functionalized cellulose nanofiber composites for catalytic applications. *Carbohydrate Polymers* **2015**, *132*, 554-564.
113. (a) Huang, J.-L.; Gray, D. G.; Li, C.-J., A3-Coupling catalyzed by robust Au nanoparticles covalently bonded to HS-functionalized cellulose nanocrystalline films. *Beilstein Journal of Organic Chemistry* **2013**, *9*, 1388-1396; (b) Rezayat, M.; Blundell, R. K.; Camp, J. E.; Walsh, D. A.; Thielemans, W., Green One-Step Synthesis of Catalytically Active Palladium Nanoparticles Supported on Cellulose Nanocrystals. *ACS Sustainable Chemistry & Engineering* **2014**, *2* (5), 1241-1250.
114. (a) Evans, B. R.; O'Neill, H. M.; Malyvanh, V. P.; Lee, I.; Woodward, J., Palladium-bacterial cellulose membranes for fuel cells. *Biosensors and Bioelectronics* **2003**, *18* (7), 917-923; (b) Johnson, L.; Thielemans, W.; Walsh, D. A., Synthesis of carbon-supported Pt nanoparticle electrocatalysts using nanocrystalline cellulose as reducing agent. *Green Chemistry* **2011**, *13* (7), 1686-1693.
115. (a) Yang, J.; Yu, J.; Fan, J.; Sun, D.; Tang, W.; Yang, X., Biotemplated preparation of CdS nanoparticles/bacterial cellulose hybrid nanofibers for photocatalysis application. *Journal of Hazardous Materials* **2011**, *189* (1), 377-383; (b) Sun, D.; Yang, J.; Wang, X., Bacterial cellulose/TiO₂ hybrid nanofibers prepared by the surface hydrolysis method with molecular precision. *Nanoscale* **2010**, *2* (2), 287-292.

Chapter 3: Preparation of NCC

3.1. Introduction

3.1.1. Nanocrystalline cellulose

Nickerson and Habrle first observed that the degradation brought about by boiling cellulose fibres in an acidic solution (both hydrochloric-acid and sulfuric acid media) reached a limit of digestion after a certain period of treatment.¹ This work inspired Bengt G. Rånby, who later reported colloidal suspensions of cellulose. These suspensions were obtained *via* the controlled sulfuric acid-catalyzed degradation of cellulose fibres.² The presence of needle-shaped aggregated particles was first observed *via* micrographs obtained by transmission electron microscopy (TEM). The rods obtained *via* dried suspensions of acid treated cellulose were further analysed with electron diffraction to reveal that the crystalline structure was the same as the original fibres.³ Concurrent experiments developed by Battista⁴ included the production of microcrystalline cellulose (MCC). This process involved the hydrochloric acid-assisted degradation of cellulose fibres, followed by sonication treatments, which led to the development of the commercial process for the isolation of microcrystalline cellulose (MCC).⁵ Following the development of MCC and its intrinsic properties (stability, chemical inactivity, physiological inertness and binding properties), a significant opportunity for multiple uses arose. MCC is used as a tablet binder in the pharmaceutical industry, as a texturizing agent and fat replacement in food, an additive in paper and as a co-material in composites in a multiple arrays of applications. The optimization of acid hydrolysis conditions led to the observation of nematic liquid crystalline alignment of nanocrystalline cellulose (NCC) colloidal suspensions were observed.⁶ Further developments into NCC has seen the enhancement of mechanical properties of nanocomposites containing NCC.⁷ This has led to a great shift into substantial research of NCC composites because of the growing interest in fabricating materials from renewable resources. These rod-shaped particles are often referred to as microcrystals, whiskers, nanocrystals, nanoparticles, microcrystallites, or nanofibers, however, herein it shall be referred to as NCC.⁸

3.1.2. Preparation of Nanocrystalline Cellulose

Acid hydrolysis is the main process in the formation of NCC from cellulosic fibres. This treatment aims to preferentially hydrolyse the disordered or paracrystalline regions of cellulose. With the removal of the amorphous regions of the cellulose the crystalline regions, which have a higher resistance to acid attack, remain intact and lead to the production of cellulose rod-like nanocrystals.⁹ Although visually different these NCCs have a morphology and crystallinity similar to that of the original cellulose fibres (Figure 3.1).

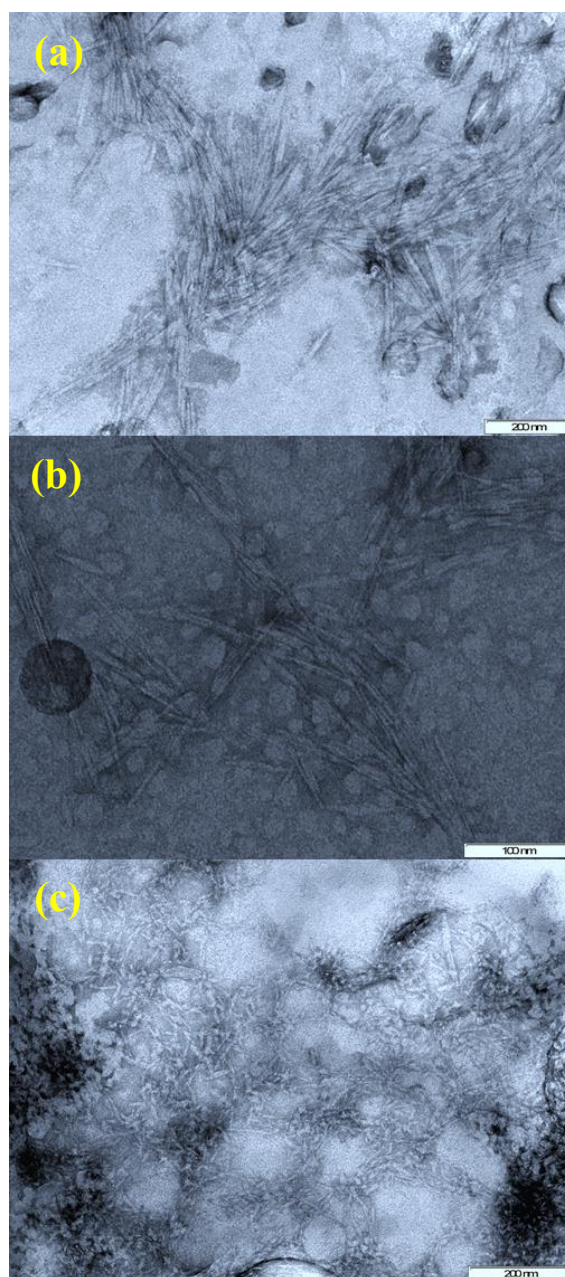


Figure 3.1. TEM micrographs derived from (a) Whatman® filter paper, (b) softwood kraft pulp and (c) discarded cigarette filters.¹⁰

The kinetics of hydrolysis between the amorphous and crystalline region is the arbitrary factor of the acid cleavage process in cellulose. Thus acid hydrolysis of cellulose leads to the prompt decrease in the degree of polymerization (DP) to a relative level-off DP (LODP). The DP decreases progressively slower, even during prolonged hydrolysis times.^{5,11} The LODP is linked to the crystal sizes along the cellulose chain prior to the hydrolysis step.^{11d}

This premise is subjected to the assumption that the disordered or amorphous regions are dispersed along the cellulose fibril chains and are therefore vulnerable to cleavage during the hydrolysis step (This assumption relies on the fact that the crystalline regions are less impervious to attack). After the hydrolysis step, it is understood that a homogeneous suspension of crystallites is harnessed.^{11e} Confirmations of these assumptions were obtained by X-ray crystal diffraction,¹² electron microscopy with iodine-staining,¹² small-angle X-ray diffraction,^{11b} and neutron diffraction analyses.¹³ The LODP values obtained correlate to corresponding crystallite size and depend on the raw source material used.^{4-5,13-14}

The conventional procedures presently employed for the production of NCCs consist of subjecting pure cellulosic material (natural or synthetic) to strong acid hydrolysis under controlled conditions of temperature, agitation, and time. The acid employed and the acid-to-cellulose fibre ratio are also important parameters that affect the preparation of NCCs.¹⁵ The resulting suspension is subsequently diluted and washed with water through successive centrifugations. Dialysis against distilled water is then performed to remove any free acid from the dispersion. Additional processing steps such as filtration,¹⁶ differential centrifugation,¹⁷ or ultracentrifugation (using a saccharose gradient)¹⁸ have been also reported.

Sulfuric and hydrochloric acids are the commonly used hydrolysis mediums in the preparation of NCC.¹⁵ However, phosphoric¹⁹ and hydrobromic²⁰ acids have also been reported for these intended purposes.

When sulfuric acid is employed as the hydrolytic medium, the surface hydroxyl groups react with the acid and in turn, are displaced by the sulfate esters (only ~10% of hydroxyl groups are converted to surface esters). This process leads to a charged surface which allows for easy dispersion with in an aqueous medium, resulting in important properties that will be discussed shortly.^{15,21} The concentration of sulfuric acid in hydrolysis reactions to obtain NCCs does not differ from a typically used value of *ca.* 65% (wt). The corresponding temperature at which this process occurs varies from room temperature up to 70 °C and the hydrolysis times are inversely proportional to the relative temperature and vary from 30 min to 24 hours.^{10,15,22}

3.1.3. Morphology and Dimension of Nanocrystalline Cellulose

The source of cellulosic material used and the parameters under which hydrolysis occurs yields a wide variety of geometries (lengths, L, and widths, W). These variations are partially due to the diffusion controlled nature of the acid hydrolysis. The morphological characteristics are commonly obtained *via* the usual microscopy techniques (TEM, AFM, E-SEM,²³ etc.) or light scattering techniques, including small angle neutron scattering (SANS)²⁴ and polarized and depolarized dynamic light scattering (DLS, DDLS).²⁵ TEM micrographs of NCCs typically depict aggregation of the particles. This occurs during sample preparation specifically at the drying phase, post negative staining. Elazzouzi-Hafraoui *et al.* reported the use of cryo-TEM (cryogenic mode) to prevent this aggregation.¹⁶ The typical geometrical characteristics for NCCs derived from an array cellulose sources are summarized in Table 3.1.

Table 3.1. Lengths (nm) and Widths (nm) of NCCs from different sources.

<i>Source</i>	<i>L (nm)</i>	<i>w (nm)</i>	<i>reference</i>
Bacterial	100 – 1000	10 – 50	26
	100 – 1000	5 – 10 x 30 – 50	27
Cotton	100 – 150	5 – 10	28
	70 – 170	~7	29
	200 – 300	8	30
	255	15	25
	150 – 210	5 – 11	23
Cotton Linter	100 – 200	10 – 20	31
	25 – 320	6 – 70	16
	300 – 500	15 – 30	32
MCC	35 – 265	3 – 48	16
	250 – 270	23	33
	~500	10	34
Ramie	150 – 250	6 – 8	35
	50 – 150	5 – 10	36
Sisal	100 – 500	3 – 5	37
	150 – 280	3.5 – 6.5	38
Tunicate		8.8 x 18.2	24
	1160		25
	500 – 1000	10	39
	1000 – 3000	15 – 30	40
	100 – 1000	15	30
Valonia	1073	28	16
	>1000	10 – 20	41
Soft Wood	100 – 200	3 – 4	21, 42
	100 – 150	4 – 5	43
Hard Wood	140 – 150	4 – 5	43

In particular, the isolation of NCCs from standard filter paper (FP) and bleached pulp (BP) will be discussed in this chapter. NCCs were isolated from FP and BP *via* acid-hydrolysis treatment using sulfuric acid and were characterized *via* a variety of spectroscopies and microscopies in addition to elemental composition determination, X-ray diffraction (XRD), thermogravimetric analysis (TGA) and differential thermal analysis (DTA) studies.

3.2. Materials and Methods

3.2.1. Materials

BP was provided by the CSIR, Durban, South Africa and Whatman® FP, Ethanol, Sodium hydroxide pellets and sulfuric acid were purchased from Sigma-Aldrich. All chemicals were used as received. Double distilled water was used for all reactions and dialysis.

3.2.2. Isolation of NCC-BP and NCC-FP

After blending cellulose obtained from BP and FP with a domestic blender, NCCs were isolated using 20 mL/g 64 wt% (BP and FP) sulfuric acid at 45 °C in an oil bath for 45 minutes to remove the amorphous regions. After the completion of the hydrolysis, the suspensions were repeatedly diluted and centrifuged at 6000 rpm for 10 min to reduce the sulfuric acid concentration. The suspensions were sonicated using a UP400S Ultrasonic processor, Hielscher, Germany at 50% amplitude and 0.5 cycle for 15 minutes to ensure complete dispersion of NCCs before dialysis to *ca.* pH 7 of the eluent. The obtained NCCs were denoted as NCC-BP and NCC-FP. The percentage yields of the isolated NCCs were determined gravimetrically as shown in Equation 3.1.

$$\% \text{ Yield of NCC} = \frac{\text{weight of NCC isolated (g)}}{\text{Weight of Cellulose used (g)}} \times 100\% \quad (3.1)$$

3.2.3. Characterization Techniques

Fourier transform infrared spectroscopy

The identification of the isolated NCCs was confirmed by FTIR study in the range 380-4000 cm^{-1} at a resolution of 4 cm^{-1} using Spectrum 100 infrared spectrometer equipped with universal attenuated total reflection (UATR) accessory Perkin Elmer, USA.

Morphological structure analysis

The morphological characterisation, dimensions and elemental composition of the isolated NCCs from the two cellulosic materials were established with the aid of electron microscopic study using JEOL 1010 transmission electron microscope (TEM), Japan, JEOL 2100 high resolution transmission electron microscope (HRTEM), Japan and ZEISS Ultra Plus field emission gun scanning electron microscope (FEGSEM) equipped with energy dispersive X-ray (EDX) detector, Germany. TEM and HRTEM images of all samples were acquired using NCC suspension of each sample deposited on TEM-grid. The TEM-grid was negatively stained with 2 w/v% Uranyl acetate to aid visualization. Similarly, samples for SEM images were coated with gold with the aid of sputter coater to minimize charging.

X-ray diffraction analysis

Powder X-ray diffraction (XRD) analysis of NCCs isolated from BP and FP was conducted using an X-ray diffractometer (Bruker AXS D8 Advance, Germany), equipped with Cu K α radiation source (wavelength = 0.154 nm) operating at 40 kV and 40 mA. NCC suspension of each sample was dried at room temperature and the obtained film was crushed to a powder. The XRD pattern of the NCC powder was recorded over the angular range $2\theta = 10\text{--}90^\circ$ at room temperature. The crystallinity index (*CI*) was calculated using Segal's method⁴⁴ based on reflected intensity of the peak at around $2\theta = 22^\circ$ which corresponded to the maximum intensity, associated with both crystalline and amorphous regions of the sample, of the lattice diffraction peak 200, labeled as I_{200} and the intensity minimum usually at around $2\theta = 18^\circ$ which corresponded to the intensity of x-ray scattered by the amorphous region of the sample, labeled as I_{am} as shown in Equation 3.2.

$$CI (\%) = \frac{I_{200} - I_{am}}{I_{200}} \times 100\% \quad (3.2)$$

Crystallite size (D_{hkl}) of the isolated NCCs were calculated using Scherrer's formula⁴⁵ as shown in Equation 3.3 where λ is the X-ray wavelength (0.154 nm), β is the angular width at half maximum intensity determined with the aid of Gaussian fit of the peaks on the diffractograms of the isolated NCC and θ is the Bragg angle. The crystallographic plane adopted for the estimation was 200.

$$D_{hkl} \text{ (nm)} = 0.89\lambda/\beta \cos \theta \quad (3.3)$$

Thermogravimetric analysis (TGA)

Thermal stability and kinetics of thermal degradation of the isolated NCCs were carried out using Simultaneous Thermal Analyzer STA 6000, Perkin-Elmer. The thermal analyses were conducted using sample mass in the range 5-6 mg under a nitrogen atmosphere (flow rate of 20 mL/min) with a constant heating rate of 10 °C/min and at a temperature of 20–700 °C, the samples were held at 700 °C for 5 min. The weight loss (%) at the cellulose decomposition temperature and the kinetics of thermal decomposition were determined, as well as the residual char (%) at 700 °C.

Specific surface area and porosity measurements

The nitrogen adsorption–desorption isotherms of the degassed samples (at 90 °C under vacuum for 24 h using Micromeritics VacPrep 061 sample degas system, USA) were measured at a bath temperature of -195.8 °C (77.2 K) by surface area and porosity analyzer, Micromeritics Tristar II 3020 2.00, USA. Specific surface areas were calculated from the linear region of the isotherms using the Brunauer–Emmett–Teller (BET) equation in a relative P/P_o pressure range of 0.063 - 0.3. Pore size distributions were derived from the adsorption branch of the isotherms by Barrett–Joyner–Halenda (*BJH*) method. The total pore volumes were estimated from the amount adsorbed at a relative pressure of $P/P_o = 0.996$. Samples were dried, crushed and sieved (300 µm mesh size).

Zeta potential and solution based bulk particle size measurements

The Zeta potential and particle size determination were measured at using a Malvern Nanosight NS500 Zetasizer (Malvern Instruments, United Kingdom). Measurements were done at ambient conditions with a laser wavelength of 405 nm (Violet, depolarized). The nanocellulose suspension at 5% (w/v) was diluted in water at the ratio of 1:1000 (v/v). The instrument uses dynamic light scattering to measure the diffusion of particles moving under Brownian motion and converts this to size and size distribution. The particle size was calculated by the Stokes-Einstein equation. Using Nanoparticle Tracking Analysis (NTA), the zeta potential is calculated from the measurements of the velocity of a particle in suspension when an electric

field is applied (electrophoretic velocity and electro-osmosis). The NanoSight NS500 recorded the total drift velocity for each tracked particle, which is composed of elements of both types of movement. This data was collected at a constant voltage of 24.0 V and a current range of 0.43 – 0.47 μA .

3.3. Results

The FTIR spectra of the isolated NCC-BP and NCC-FP showed identical absorption bands in comparison with the FTIR spectrum of the obtained cellulose but with greater intensities due to loss of the amorphous regions. The FTIR absorption spectra of NCC-FP (blue) and NCC-BP (red) are shown in Figure 3.2. The bands at 3380-3350, 2920-2910, 1705-1675, 1458-1435, 1382-1341, 1035-1030 and 870-833 cm^{-1} are attributed to O-H stretching, C-H asymmetric stretching, bending vibration due to absorbed moisture, CH_2 symmetric bending deformation, C-H asymmetric bending deformation, C-O-C stretching and C-H deformation mode of the β -glycosidic linkage ($^4\text{C}_1$) between the anhydroglucose rings respectively.⁴⁶ The calculated yields of NCCs from the cellulose sources determined gravimetrically were NCC-FP (71%) and NCC-BP (56%).

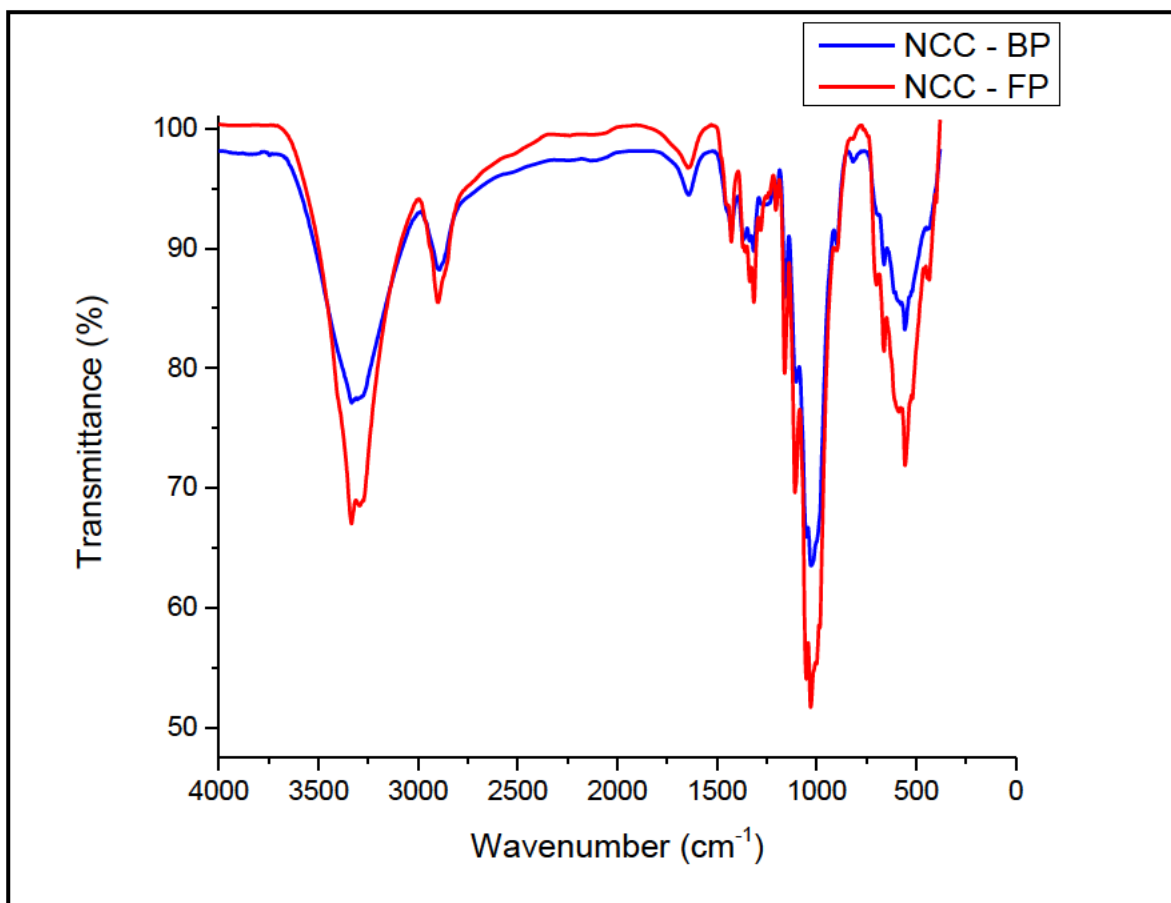


Figure 3.2. ATR-FTIR spectra of NCC-FP and NCC-BP.

The morphological structures of the isolated NCCs established *via* TEM and HRTEM (Figure 3.3) showed that the nanoparticles were needlelike. The calculated mean lengths were 161.76 ± 59.65 nm (NCC-FP) and 135.09 ± 38.44 nm (NCC-BP). The calculated mean widths were 11.04 ± 4.98 nm (NCC-FP) and 6.41 ± 2.88 nm (NCC-BP). This resulted in aspect ratios of 17.66 ± 11.18 (NCC-FP) and 25.10 ± 13.51 (NCC-BP) respectively (Table 3.2).

Table 3.2. Mean lengths (nm), widths (nm) and aspect ratios (L/W) of the isolated NCCs.

Dimension	NCC-FP	NCC-BP
Length (nm)	176.36 ± 62.72	148.37 ± 40.86
Width (nm)	16.48 ± 5.54	10.89 ± 3.48
Aspect ratio (L/W)	11.32 ± 4.39	14.68 ± 5.21

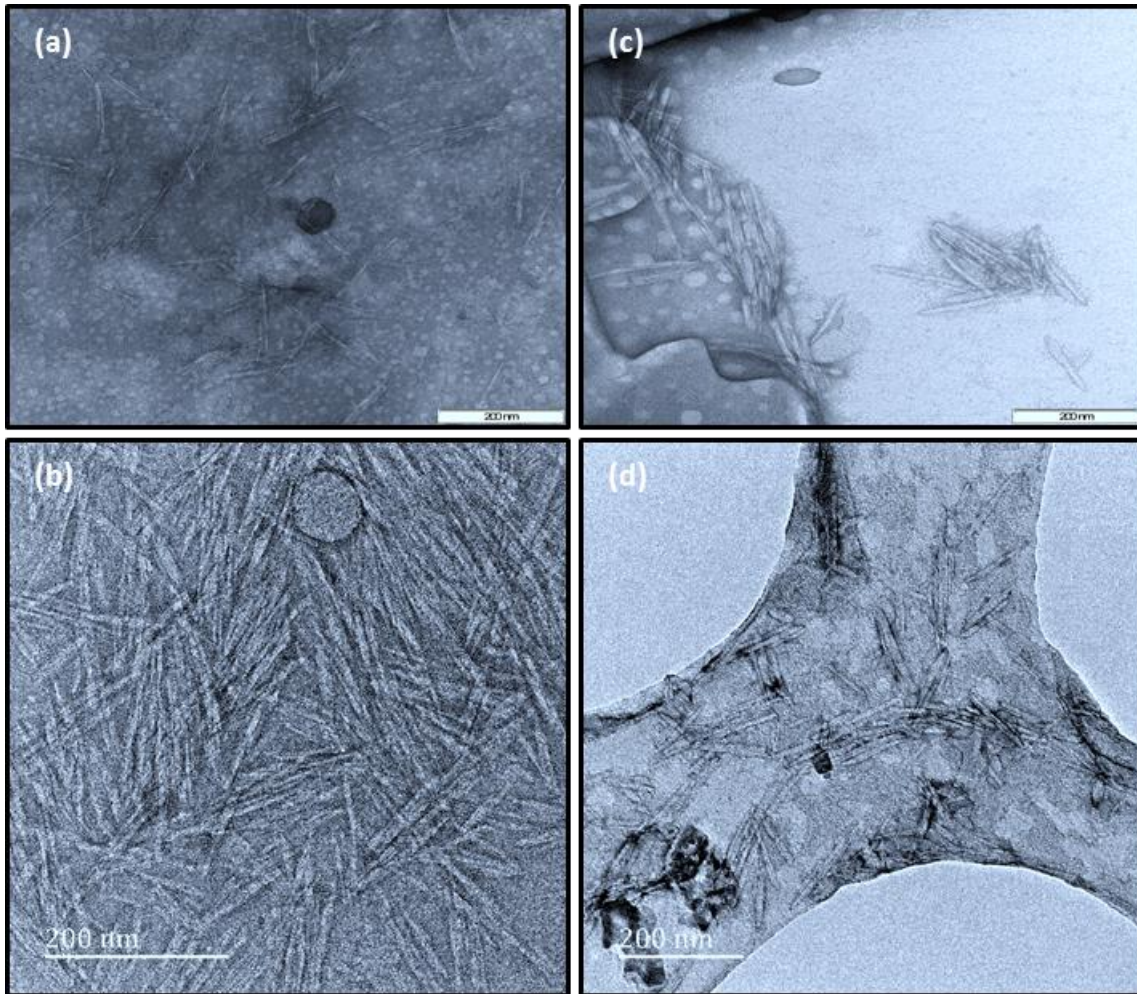


Figure 3.3. TEM and HRTEM* micrographs of NCC-BP (a), NCC-BP (b), NCC-FP (c) and NCC-FP (d).

The high standard deviations of the dimensions showed that the nanoparticles were polydispersed⁴⁷ as revealed by the distributions of the dimensions shown in Figure 3.4 (due to a limited particle count) with aspect ratios above 10 (the minimum aspect ratio for an ideal stress transfer within the interaction between fibres and matrix).⁴⁸ The isolated NCCs have capacities to provide strong reinforcement, high thermal and mechanical stabilities when included in polymer composites irrespective of the percentage in such composites.⁴⁸⁻⁴⁹ The observed morphology, size, dimensions and distributions of the isolated NCCs were similar to those reported in the related literature on the isolation of NCCs from waste cotton fabrics,⁵⁰ bamboo fibre,⁴⁷ sugarcane bagasse,⁵¹ newspaper,^{46b} and pseudo-stems of banana.^{49b} The observed aggregation of the nanoparticles in the TEM and HRTEM micrographs resulted from the drying effect of the dispersion medium when samples were prepared.^{46b,48b,52}

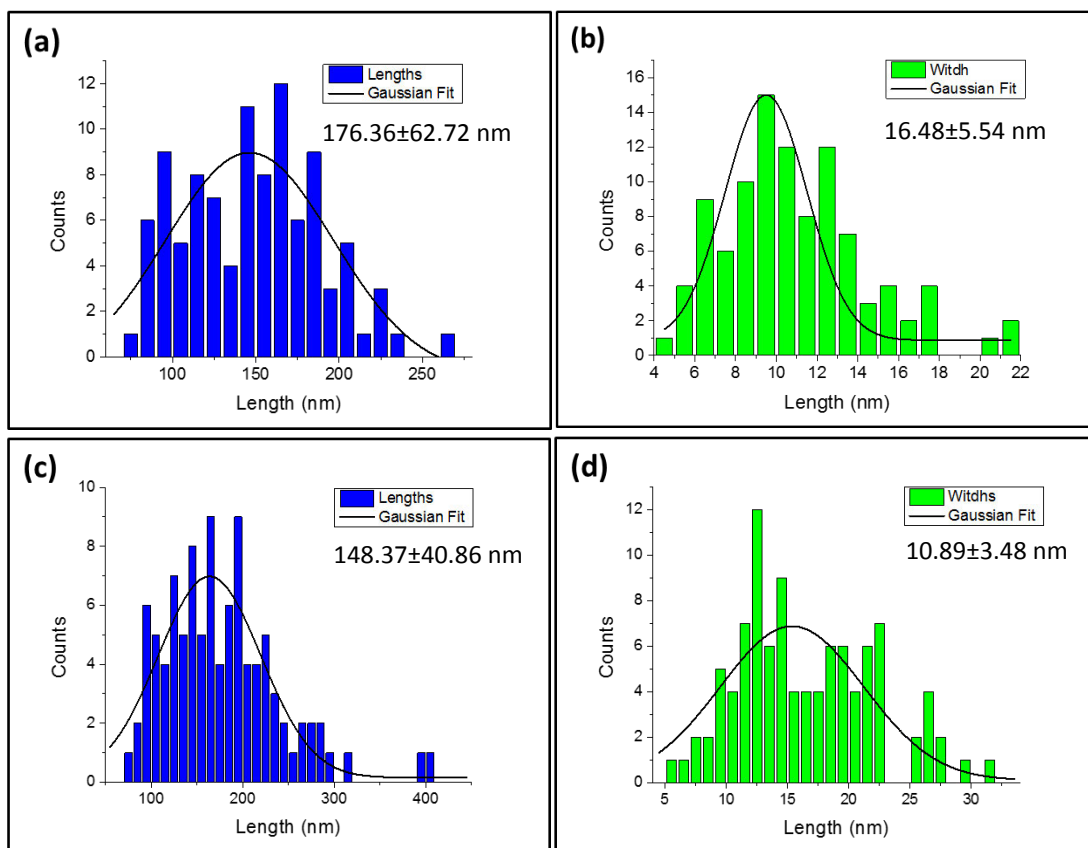


Figure 3.4. Lengths, widths and aspect ratios distributions of the isolated NCCs from FP (a and b) and BP (c and d).

The FEGSEM micrographs (Figure 3.5a and 3.5b) showed the topological morphology of the isolated NCCs, revealing the compact nature and the surface texture of the isolated NCC films. The presence of sulfur (S) (inset, Figure 3.5) is evident from the small but noticeable binding energy peak present. This is due to the residual sulfate after acid hydrolysis. Peaks corresponding to the binding energies of carbon (C), oxygen (O) were noticeable in the spectra. The percentage sulfur content (0.74% and 0.78%) of NCC-FP and NCC-BP was in proximity of the 0.85% reported for NCC isolated from cotton but greater than that of the 0.60% reported for NCC isolated from rice straw *via* sulfuric acid hydrolysis.⁵³

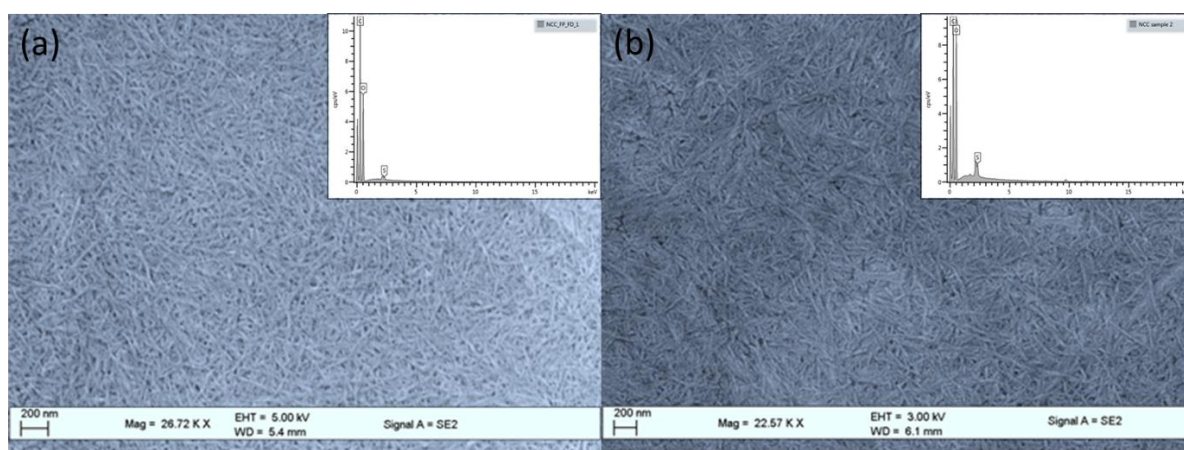


Figure 3.5. FEGSEM micrographs of NCC-FP (a) and NCC-BP (b). Inset: Corresponding EDX spectrum.

Table 3.3. Elemental compositions of NCC-FP and NCC-BP from EDX.

Element	NCC-FP	NCC-BP
C (wt%)	50.80	50.22
O (wt%)	48.42	49.03
S (wt%)	0.78	0.74

The XRD patterns of the isolated NCC-FP and NCC-BP (Figure 3.6) showed peaks in the regions $2\theta = 16^\circ$ (2 peaks), 22° and 34° associated with the crystallographic planes 110 1-10, 200 and 004⁵⁴ of monoclinic cellulose I lattice. All the isolated NCCs showed a high degree of crystallinity with calculated indices (% *CI*) and D_{hkl} (nm) corresponding to 99.98% and 6.29 nm (NCC-FP), 92.63% and 3.88 nm (NCC-BP) respectively. The high % *CI* showed the efficiency of the acid hydrolysis step in removing the amorphous region of the cellulose leaving behind the highly crystalline region.

Table 3.4. Crystalline indices and crystallite sizes of the isolated NCCs.

Calculation	NCC-FP	NCC-BP
Crystalline index (%)	99.98	92.69
Crystallite size (nm)	6.29	3.88

This results in a material with high stiffness and rigidity with the added potential of mechanical strength and reinforcing capacity.⁵⁴⁻⁵⁵

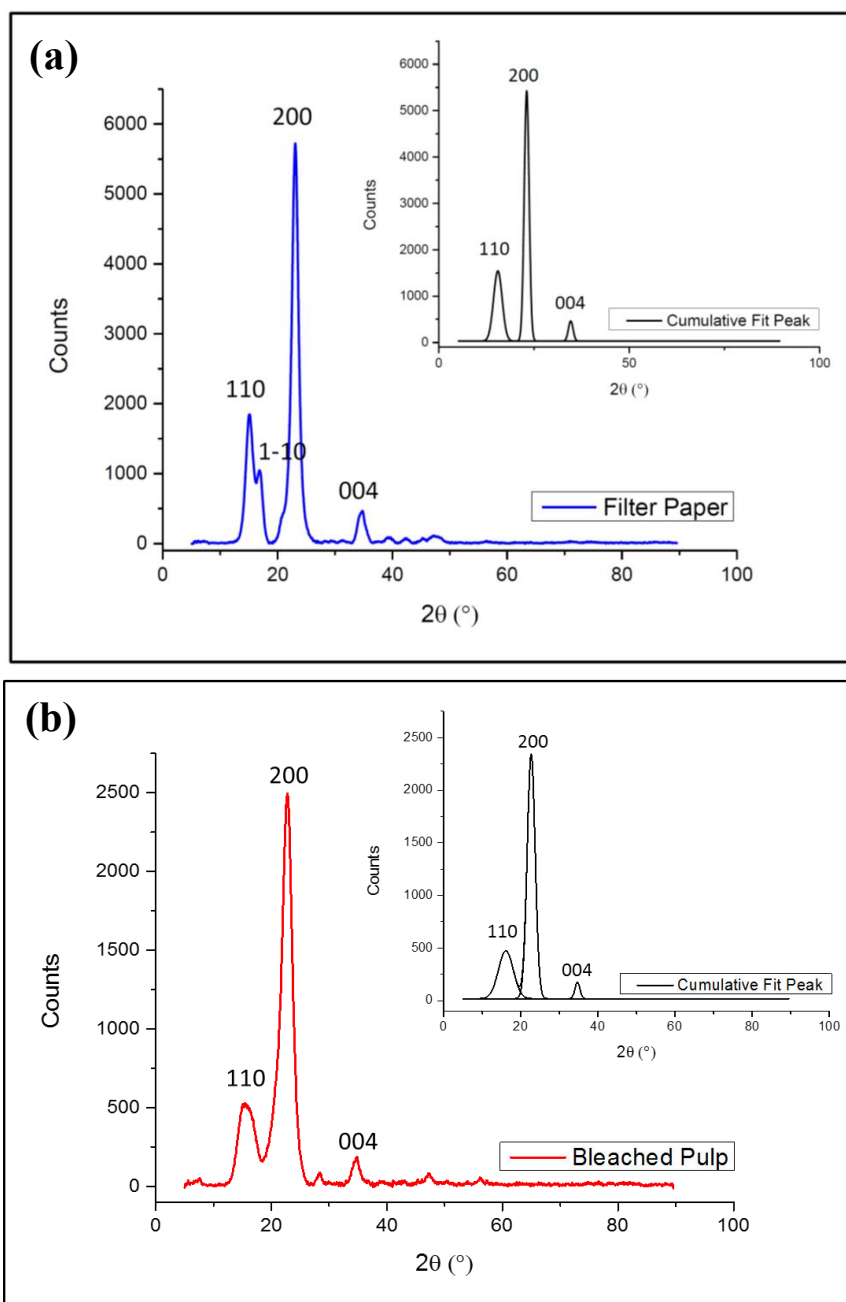


Figure 3.6. X-ray diffractograms of the isolated NCCs. Inset: Corresponding Gaussian fit

The isolated NCCs were characterized by thermogravimetric analysis to obtain information on their thermal behaviour. The thermograms and the DTA curves of the isolated NCCs (Figure 3.7) revealed similar thermal degradation profiles suggesting the same thermal degradation mechanism. The decomposition stages, corresponding characteristic temperatures, associated mass losses and char remains at 700 °C are presented in Table 3.5. The mass loss observed in the temperature range 20-110 °C could be attributed to the loss of absorbed moisture on

evaporation as the temperature increased. The observed percentage loss due to the moisture of the isolated NCCs was 1.67% for NCC-BP and 2.26% for NCC-FP. This observed increase in the moisture content of NCC-FP over NCC-BP correlates to an increased presence of hydroxyl groups and larger fibre diameter. This is shown in FTIR with a sharper peak present for NCC-FP. Two prominent thermal degradation stages were observed in the DTA curves of the isolated NCCs.

Table 3.5. The results of TGA, DTA and kinetic parameters of the isolated NCCs.

Sample	T_i (°C)	T_p (°C)	T_f (°C)	Mass loss at T_m (%)	Char at 700 °C (%)	
NCC-FP	Stage 1	113.44	175.66	280.00	11.05	18.61
	Stage 2	301.33	386.00	510.89	56.70	
NCC-BP	Stage 1	133.46	174.21	280.09	6.34	25.67
	Stage 2	280.09	364.84	448.67	47.35	

Initial temperature (T_i), peak temperature (T_p), final temperature (T_f), activation energy (E_a) and frequency factor (Z)

The first stage, involving the dehydration of anhydroglucopyranose chain segments⁵⁶ and hydrolysis of outer sulfated cellulose,⁵⁷ occurred in the temperature ranges 113-280 °C (NCC-FP) and 133-280 °C (NCC-BP). At the peak temperature (T_p) for the stage 1 degradation interval, the correlating loss in percentage mass was 11.05% (NCC-FP) and 6.34% (NCC-BP). Similarly, for stage 2 degradation, the percentage mass loss was 47.35% and 56.70% for NCC-BP and NCC-FP respectively. At this stage, chain decomposition and oxidative degradation of the non-sulfated crystal interior of the isolated NCCs were dominant^{56,58} leading to the formation of charred products.

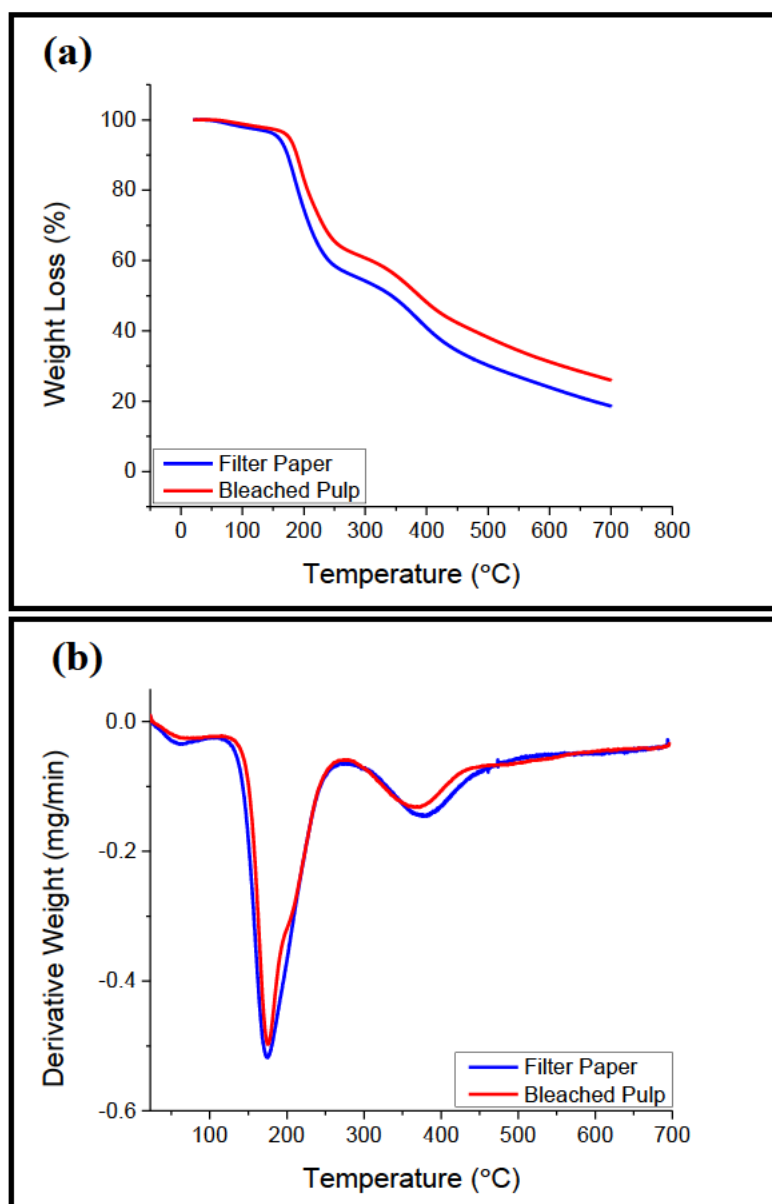


Figure 3.7. Thermograms (a) and DTA curves (b) of the isolated NCCs

The percentage of the ash contents (Charred products) at 700 °C, revealed that NCC-BP had an ash content of 25.67% compared to NCC-FP (18.61%).

The powdered films of the isolated NCCs showed similar sorption isotherms typical of type II for nonporous or macroporous materials with almost reversible adsorption and desorption isotherms (Figure3.8). The observed BET specific surface areas and pore volumes of NCC-FP (0.4225 m²/g and 0.0019cm³/g) and NCC-BP (0.2480 m²/g and 0.0044 cm³/g) powdered films were reduced in comparison to freeze-dried NCCs.^{53,59} This illustrates the impact of close packing due to strong hydrogen bonding interaction on the specific surface area of NCC when allowed to self-assemble at room temperature. Unlike drying at room temperature, drying of rapidly frozen nanocellulose in liquid nitrogen at -196 C (freeze-drying) prevented extensive

self-assembly of the nanocrystals because of inhibition induced by narrow confinement in small ice crystals.⁵⁹

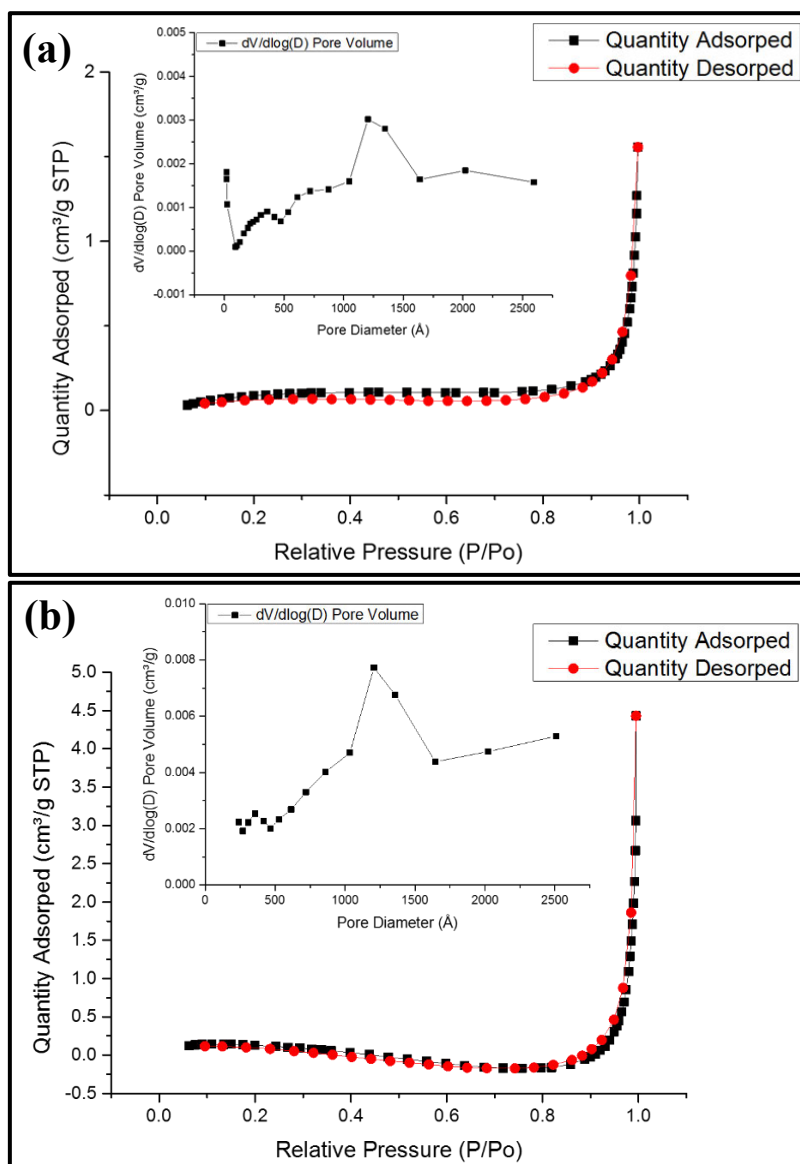


Figure 3.8. BET isotherms of the isolated NCCs [FP (a) and BP (b)]. Inset: Corresponding Pore size distribution.

Zeta potential is derived from measuring the mobility distribution of a dispersion of charged particles as they are subjected to an electric field. Mobility is defined as the velocity of a particle per electric field unit and is measured by applying an electric field to the dispersion of particles and measuring their average velocity. The Smoluchowski equation was used to obtain the zeta potential from the measured mobility. The cellulosic surfaces generally show bipolar character with prevalent acidic contribution due to the proton of the hydroxyl functional group as well as of present carboxyl groups.⁶⁰ The zeta potential for NCC-FP and NCC-BP has a mean value

of -38.8 ± 1.6 and -36.4 ± 0.5 mV respectively. These suspensions of NCC are considered stable because the absolute value is higher than 25 mV.⁶¹

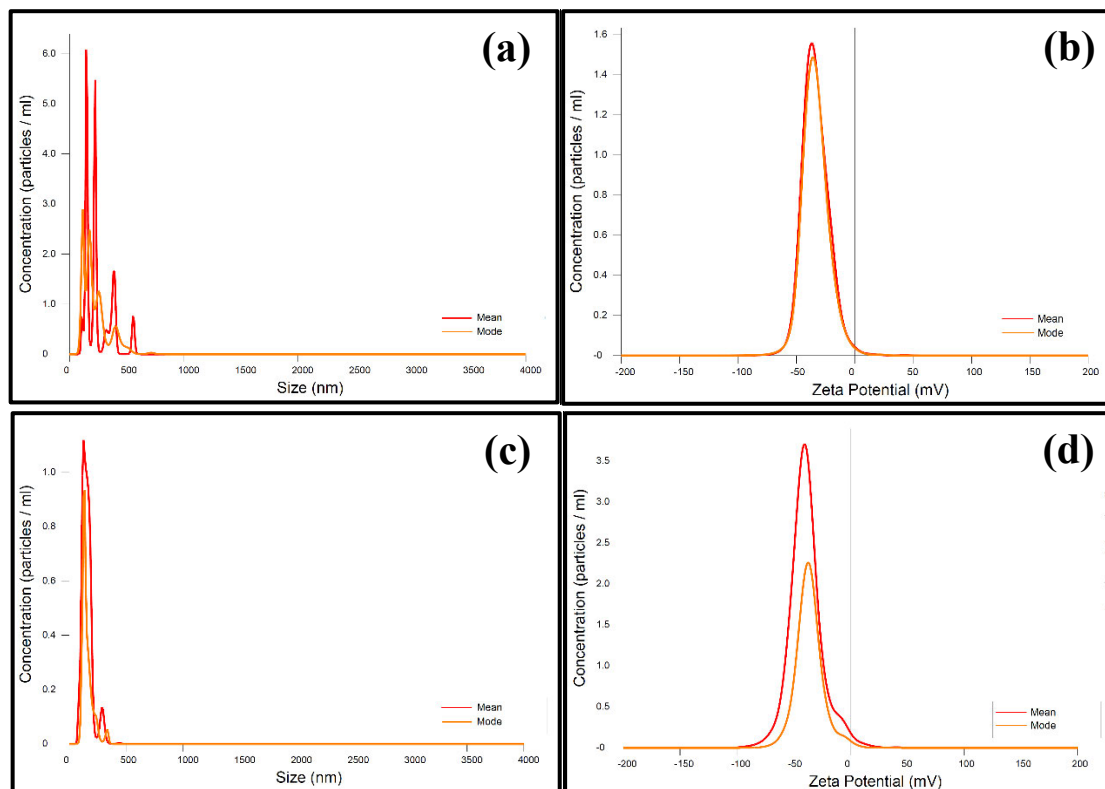


Figure 3.9. Zeta potential plots of the isolated NCCs [BP (a) and FP (b)]. Particle size distribution of the isolated NCCs [BP (c) and FP (d)].

To determine the particle size distribution, the suspended nanoparticles were diluted appropriately and analysed in DLS particle size analyser. The intensity of light scattered in a particular direction by dispersed particles tends to periodically change with time. These fluctuations in the intensity vs. time profile are caused by the constant changing of particle positions brought on by Brownian motion. DLS instruments obtain, from the intensity vs. time profile, a correlation function. This exponentially decaying correlation function is analysed for characteristic decay times, which are related to diffusion coefficients and then by the Stokes-Einstein equation, to a particle radius.⁶⁰ The particle size distribution resulted in a mean value of 128.8 ± 1.8 and 131.6 ± 16.5 nm for NCC-FP and NCC-BP respectively (Figure 3.6). The particle size measured by light scattering cannot be precisely distinguished with regard to the crystals' length and width dimensions.⁶²

3.4. Conclusion

NCCs were isolated from the obtained cellulose sources of filter paper and bleached pulp *via* acid hydrolysis. The obtained NCCs were produced with satisfactory yields and were well characterized using the following techniques: ATR-FTIR, XRD, TEM, HRTEM, FEGSEM equipped with EDX detector, TGA/DTA and BET. The whisker-like nature of the NCCs was shown by TEM and HRTEM while FEGSEM showed the surface morphology with the EDX revealing residual amounts of sulfur present due to sulfonic groups on the NCC. The XRD analysis of the film obtained at room temperature showed that the isolated NCCs were highly crystalline with slight variations in crystallinity [NCC-FP (99.98%) > NCC-BP (92.69%)] and crystallite size [NCC-FP (6.29 nm) > NCC-CF (6.26 nm)]. The thermographic study of the TGA/DTA results and percentage char left at 700 °C showed the relatively good thermal stabilities and flame-retardant capacities of the isolated NCCs. BET specific surface area studies showed the influence of close packing of nanocrystals within the films obtained at room temperature. The results of this study showed that NCC-FP and NCC-BP could be considered as a potential co-composite material with excellent physicochemical and mechanical properties.

3.5 References

1. Nickerson, R. F.; Habrle, J. A., Cellulose intercrystalline structure. *Industrial & Engineering Chemistry* **1947**, *39* (11), 1507-1512.
2. (a) Rånby, B. G., Aqueous colloidal solutions of cellulose micelles. *Acta Chemica Scandinavica* **1949**, *3*(5), 649-650.; (b) Rånby, B. G.; Ribí, E., Über den Feinbau der Zellulose. *Experientia* **1950**, *6* (1), 12-14; (c) Rånby, B. G., Fibrous macromolecular systems. Cellulose and muscle. The colloidal properties of cellulose micelles. *Discussions of the Faraday Society* **1951**, *11* (0), 158-164.
3. (a) Mukherjee, S. M.; Woods, H. J., X-ray and electron microscope studies of the degradation of cellulose by sulfuric acid. *Biochimica et Biophysica Acta* **1953**, *10*, 499-511; (b) Mukherjee, S. M.; Sikorski, J.; Woods, H. J., Electron-Microscopy of Degraded Cellulose Fibres. *Journal of the Textile Institute Transactions* **1952**, *43* (4), T196-T201.
4. Battista, O. A., Hydrolysis and crystallization of cellulose. *Industrial & Engineering Chemistry* **1950**, *42* (3), 502-507.
5. Battista, O. A.; Coppick, S.; Howsmon, J. A.; Morehead, F. F.; Sisson, W. A., Level-off degree of polymerization. *Industrial & Engineering Chemistry* **1956**, *48* (2), 333-335.
6. Marchessault, R.; Morehead, F.; Walter, N., Liquid crystal systems from fibrillar polysaccharides. *Nature* **1959**, *184* (4686), 632-633.
7. (a) Favier, V.; Canova, G. R.; Cavaillé, J. Y.; Chanzy, H.; Dufresne, A.; Gauthier, C., Nanocomposite materials from latex and cellulose whiskers. *Polymers for Advanced Technologies* **1995**, *6* (5), 351-355; (b) Favier, V.; Chanzy, H.; Cavaille, J. Y., Polymer Nanocomposites Reinforced by Cellulose Whiskers. *Macromolecules* **1995**, *28* (18), 6365-6367.
8. (a) Klemm, D.; Kramer, F.; Moritz, S.; Lindström, T.; Ankerfors, M.; Gray, D.; Dorris, A., Nanocelluloses: a new family of nature-based materials. *Angewandte Chemie International Edition* **2011**, *50* (24), 5438-5466; (b) Klemm, D.; Schumann, D.; Kramer, F.; Heßler, N.; Hornung, M.; Schmauder, H.-P.; Marsch, S., Nanocelluloses as innovative polymers in research and application. *Polysaccharides II* **2006**, 49-96; (c) Klemm, D.; Heublein, B.; Fink, H.-P.; Bohn, A., Cellulose: fascinating biopolymer and sustainable raw material. *Angewandte Chemie International Edition* **2005**, *44* (22), 3358-3393; (d) Eichhorn, S. J., Cellulose nanowhiskers: promising materials for

- advanced applications. *Soft Matter* **2011**, 7 (2), 303-315; (e) Eichhorn, S. J.; Dufresne, A.; Aranguren, M.; Marcovich, N. E.; Capadona, J. R.; Rowan, S. J.; Weder, C.; Thielemans, W.; Roman, M.; Renneckar, S.; Gindl, W.; Veigel, S.; Keckes, J.; Yano, H.; Abe, K.; Nogi, M.; Nakagaito, A. N.; Mangalam, A.; Simonsen, J.; Benight, A. S.; Bismarck, A.; Berglund, L. A.; Peijs, T., Review: current international research into cellulose nanofibres and nanocomposites. *Journal of Materials Science* **2009**, 45 (1), 1-33; (f) Moon, R. J.; Martini, A.; Nairn, J.; Simonsen, J.; Youngblood, J., Cellulose nanomaterials review: structure, properties and nanocomposites. *Chemical Society Reviews* **2011**, 40 (7), 3941-3994; (g) Habibi, Y.; Lucia, L. A.; Rojas, O. J., Cellulose nanocrystals: chemistry, self-assembly, and applications. *Chemical Reviews* **2010**, 110 (6), 3479-3500; (h) Kargarzadeh, H.; Ahmad, I.; Thomas, S.; Dufresne, A., *Handbook of Nanocellulose and Cellulose Nanocomposites*. Wiley Online Library: **2017**.
9. (a) Anglès, M. N.; Dufresne, A., Plasticized starch/tunicin whiskers nanocomposite materials. 2. mechanical behavior. *Macromolecules* **2001**, 34 (9), 2921-2931; (b) Ruiz, M. M.; Cavaillé, J. Y.; Dufresne, A.; Graillat, C.; Gérard, J.-F., New waterborne epoxy coatings based on cellulose nanofillers. *Macromolecular Symposia* **2001**, 169 (1), 211-222.
 10. Ogundare, S. A.; Moodley, V.; van Zyl, W. E., Nanocrystalline cellulose isolated from discarded cigarette filters. *Carbohydrate Polymers* **2017**, 175, 273-281.
 11. (a) Sharples, A., The hydrolysis of cellulose and its relation to structure. Part 2. *Transactions of the Faraday Society* **1958**, 54 (0), 913-917; (b) Yachi, T.; Hayashi, J.; Takai, M.; Shimizu, Y. Supermolecular structure of cellulose: stepwise decrease in LODP and particle size of cellulose hydrolyzed after chemical treatment.[Leveling-off degree of polymerization], *Journal of Applied Polymer Science*. Applied Polymer Symposium;(United States), Tokai Univ., Hiratsuka, Japan: **1983**; (c) Chang, M., Folding chain model and annealing of cellulose. *Journal of Polymer Science Part C: Polymer Symposia* **1971**, 36 (1), 343-362; (d) Chang, M. M. Y., Crystallite structure of cellulose. *Journal of Polymer Science: Polymer Chemistry Edition* **1974**, 12 (7), 1349-1374; (e) Håkansson, H.; Ahlgren, P., Acid hydrolysis of some industrial pulps: effect of hydrolysis conditions and raw material. *Cellulose* **2005**, 12 (2), 177-183.
 12. Schurz, J.; John, K., Long periods in native and regenerated celluloses. *Cellulose Chemistry and Technology* **1975**.
 13. (a) Nishiyama, Y.; Langan, P.; Chanzy, H., Crystal structure and hydrogen-bonding system in cellulose I β from synchrotron X-ray and neutron fiber diffraction. *Journal of*

- the American Chemical Society* **2002**, *124* (31), 9074-9082; (b) Nishiyama, Y.; Sugiyama, J.; Chanzy, H.; Langan, P., Crystal structure and hydrogen bonding system in cellulose I α from synchrotron X-ray and neutron fiber diffraction. *Journal of the American Chemical Society* **2003**, *125* (47), 14300-14306.
14. Kai, A., The fine structure of valonia microfibril gel permeation chromatographic studies of Valonia cellulose. *Sen'i Gakkaishi* **1976**, *32* (8), T326-T334.
 15. Kargarzadeh, H.; Ioelovich, M.; Ahmad, I.; Thomas, S.; Dufresne, A., Methods for extraction of nanocellulose from various sources. In *Handbook of Nanocellulose and Cellulose Nanocomposites*, Wiley-VCH Verlag GmbH & Co.: **2017**; 1-49.
 16. Elazzouzi-Hafraoui, S.; Nishiyama, Y.; Putaux, J.-L.; Heux, L.; Dubreuil, F.; Rochas, C., The shape and size distribution of crystalline nanoparticles prepared by acid hydrolysis of native cellulose. *Biomacromolecules* **2008**, *9* (1), 57-65.
 17. Bai, W.; Holbery, J.; Li, K., A technique for production of nanocrystalline cellulose with a narrow size distribution. *Cellulose* **2009**, *16* (3), 455-465.
 18. de Souza Lima, M. M.; Borsali, R., Static and Dynamic Light Scattering from Polyelectrolyte Microcrystal Cellulose. *Langmuir* **2002**, *18* (4), 992-996.
 19. (a) Koshizawa, T., Degradation of wood cellulose and cotton linters in phosphoric acid. *Japan Tappi Journal* **1960**, *14* (7), 455-458,475; (b) Okano, T.; Kuga, S.; Wada, M.; Araki, J.; Ikuina, J., Nisshin Oil Mills Ltd. *Patent JP* **1999**, *98*, 151052; (c) Usuda, M.; Suzuki, O.; Nakano, J.; Migita, N., Acid hydrolysis of cellulose in concentrated phosphoric acid: effects of modified groups of cellulose on the rate of hydrolysis. *Kogyo Kagaku Zasshi* **1967**, *70*, 349-352.
 20. Sadeghifar, H.; Filpponen, I.; Clarke, S. P.; Brougham, D. F.; Argyropoulos, D. S., Production of cellulose nanocrystals using hydrobromic acid and click reactions on their surface. *Journal of Materials Science* **2011**, *46* (22), 7344-7355.
 21. Araki, J.; Wada, M.; Kuga, S.; Okano, T., Flow properties of microcrystalline cellulose suspension prepared by acid treatment of native cellulose. *Colloids and Surfaces A: Physicochemical and Engineering Aspects* **1998**, *142* (1), 75-82.
 22. Moodley, V.; Maddila, S.; Jonnalagadda, S. B.; van Zyl, W. E., Synthesis of triazolidine-3-one derivatives through the nanocellulose/hydroxyapatite-catalyzed reaction of aldehydes and semicarbazide. *New Journal of Chemistry* **2017**, *41* (14), 6455-6463.

23. Miller, A. F.; Donald, A. M., Imaging of anisotropic cellulose suspensions using environmental scanning electron microscopy. *Biomacromolecules* **2003**, *4* (3), 510-517.
24. Terech, P.; Chazeau, L.; Cavaille, J. Y., A small-angle scattering study of cellulose whiskers in aqueous suspensions. *Macromolecules* **1999**, *32* (6), 1872-1875.
25. De Souza Lima, M. M.; Wong, J. T.; Paillet, M.; Borsali, R.; Pecora, R., Translational and rotational dynamics of rodlike cellulose whiskers. *Langmuir* **2003**, *19* (1), 24-29.
26. Araki, J.; Kuga, S., Effect of trace electrolyte on liquid crystal type of cellulose microcrystals. *Langmuir* **2001**, *17* (15), 4493-4496.
27. (a) Roman, M.; Winter, W. T., Effect of sulfate groups from sulfuric acid hydrolysis on the thermal degradation behavior of bacterial cellulose. *Biomacromolecules* **2004**, *5* (5), 1671-1677; (b) Grunert, M.; Winter, W. T., Nanocomposites of cellulose acetate butyrate reinforced with cellulose nanocrystals. *Journal of Polymers and the Environment* **2002**, *10* (1), 27-30.
28. Araki, J.; Wada, M.; Kuga, S., Steric Stabilization of a cellulose microcrystal suspension by poly(ethylene glycol) grafting. *Langmuir* **2001**, *17* (1), 21-27.
29. Dong, X. M.; Kimura, T.; Revol, J.-F.; Gray, D. G., Effects of ionic strength on the isotropic–chiral nematic phase transition of suspensions of cellulose crystallites. *Langmuir* **1996**, *12* (8), 2076-2082.
30. Heux, L.; Chauve, G.; Bonini, C., Nonflocculating and chiral-nematic self-ordering of cellulose microcrystals suspensions in nonpolar solvents. *Langmuir* **2000**, *16* (21), 8210-8212.
31. Roohani, M.; Habibi, Y.; Belgacem, N. M.; Ebrahim, G.; Karimi, A. N.; Dufresne, A., Cellulose whiskers reinforced polyvinyl alcohol copolymers nanocomposites. *European Polymer Journal* **2008**, *44* (8), 2489-2498.
32. Li, Q.; Zhou, J.; Zhang, L., Structure and properties of the nanocomposite films of chitosan reinforced with cellulose whiskers. *Journal of Polymer Science Part B: Polymer Physics* **2009**, *47* (11), 1069-1077.
33. Capadona, J. R.; Shanmuganathan, K.; Trittschuh, S.; Seidel, S.; Rowan, S. J.; Weder, C., Polymer Nanocomposites with nanowhiskers isolated from microcrystalline cellulose. *Biomacromolecules* **2009**, *10* (4), 712-716.
34. Pranger, L.; Tannenbaum, R., Biobased nanocomposites prepared by in situ polymerization of furfuryl alcohol with cellulose whiskers or montmorillonite clay. *Macromolecules* **2008**, *41* (22), 8682-8687.

35. Habibi, Y.; Goffin, A.-L.; Schiltz, N.; Duquesne, E.; Dubois, P.; Dufresne, A., Bionanocomposites based on poly(ϵ -caprolactone)-grafted cellulose nanocrystals by ring-opening polymerization. *Journal of Material Chemistry* **2008**, *18* (41), 5002-5010.
36. Junior de Menezes, A.; Siqueira, G.; Curvelo, A. A. S.; Dufresne, A., Extrusion and characterization of functionalized cellulose whiskers reinforced polyethylene nanocomposites. *Polymer* **2009**, *50* (19), 4552-4563.
37. Garcia de Rodriguez, N. L.; Thielemans, W.; Dufresne, A., Sisal cellulose whiskers reinforced polyvinyl acetate nanocomposites. *Cellulose* **2006**, *13* (3), 261-270.
38. Siqueira, G.; Bras, J.; Dufresne, A., Cellulose whiskers versus microfibrils: influence of the nature of the nanoparticle and its surface functionalization on the thermal and mechanical properties of nanocomposites. *Biomacromolecules* **2009**, *10* (2), 425-432.
39. Anglès, M. N.; Dufresne, A., Plasticized starch/tunicin whiskers nanocomposites. 1. structural analysis. *Macromolecules* **2000**, *33* (22), 8344-8353.
40. Kimura, F.; Kimura, T.; Tamura, M.; Hirai, A.; Ikuno, M.; Horii, F., Magnetic alignment of the chiral nematic phase of a cellulose microfibril suspension. *Langmuir* **2005**, *21* (5), 2034-2037.
41. Revol, J. F., On the cross-sectional shape of cellulose crystallites in *Valonia ventricosa*. *Carbohydrate Polymer* **1982**, *2* (2), 123-134.
42. Araki, J.; Wada, M.; Kuga, S.; Okano, T., Influence of surface charge on viscosity behavior of cellulose microcrystal suspension. *Journal of Wood Science* **1999**, *45* (3), 258-261.
43. Beck-Candanedo, S.; Roman, M.; Gray, D. G., Effect of reaction conditions on the properties and behavior of wood cellulose nanocrystal suspensions. *Biomacromolecules* **2005**, *6* (2), 1048-1054.
44. Segal, L.; Creely, J. J.; A.E. Martin, J.; Conrad, C. M., An empirical method for estimating the degree of crystallinity of native cellulose using the X-ray diffractometer. *Textile Research Journal* **1959**, *29* (10), 786-794.
45. Patterson, A. L., The Scherrer formula for X-ray particle size determination. *Physical Review* **1939**, *56* (10), 978-982.
46. (a) Khawas, P.; Deka, S. C., Isolation and characterization of cellulose nanofibers from culinary banana peel using high-intensity ultrasonication combined with chemical treatment. *Carbohydr. Polym.* **2016**, *137*, 608-616; (b) Mohamed, M.; Salleh, W.; Jaafar, J.; Asri, S.; Ismail, A., Physicochemical properties of “green” nanocrystalline cellulose isolated from recycled newspaper. *RSC Advances* **2015**, *5* (38), 29842-29849;

- (c) Xiang, Z.; Gao, W.; Chen, L.; Lan, W.; Zhu, J.; Runge, T., A comparison of cellulose nanofibrils produced from *Cladophora glomerata* algae and bleached eucalyptus pulp. *Cellulose* **2016**, *23* (1), 493-503; (d) Hu, Y.; Tang, L.; Lu, Q.; Wang, S.; Chen, X.; Huang, B., Preparation of cellulose nanocrystals and carboxylated cellulose nanocrystals from borer powder of bamboo. *Cellulose* **2014**, *21* (3), 1611-1618.
47. Brito, B. S.; Pereira, F. V.; Putaux, J.-L.; Jean, B., Preparation, morphology and structure of cellulose nanocrystals from bamboo fibers. *Cellulose* **2012**, *19* (5), 1527-1536.
48. (a) Chen, Y. W.; Lee, H. V.; Juan, J. C.; Phang, S.-M., Production of new cellulose nanomaterial from red algae marine biomass *Gelidium elegans*. *Carbohydrate Polymers* **2016**, *151*, 1210-1219; (b) Silvério, H. A.; Neto, W. P. F.; Dantas, N. O.; Pasquini, D., Extraction and characterization of cellulose nanocrystals from corncob for application as reinforcing agent in nanocomposites. *Industrial Crops and Products* **2013**, *44*, 427-436.
49. (a) Deepa, B.; Abraham, E.; Cordeiro, N.; Mozetic, M.; Mathew, A. P.; Oksman, K.; Faria, M.; Thomas, S.; Pothan, L. A., Utilization of various lignocellulosic biomass for the production of nanocellulose: a comparative study. *Cellulose* **2015**, *22* (2), 1075-1090; (b) Mueller, S.; Weder, C.; Foster, E. J., Isolation of cellulose nanocrystals from pseudostems of banana plants. *RSC Advances* **2014**, *4* (2), 907-915; (c) Rosa, M.; Medeiros, E.; Malmonge, J.; Gregorski, K.; Wood, D.; Mattoso, L.; Glenn, G.; Orts, W.; Imam, S., Cellulose nanowhiskers from coconut husk fibers: Effect of preparation conditions on their thermal and morphological behavior. *Carbohydrate Polymers* **2010**, *81* (1), 83-92; (d) do Nascimento, D. M.; Dias, A. F.; de Araújo Junior, C. P.; de Freitas Rosa, M.; Morais, J. P. S.; de Figueirêdo, M. C. B., A comprehensive approach for obtaining cellulose nanocrystal from coconut fiber. Part II: Environmental assessment of technological pathways. *Industrial Crops and Products* **2016**; (e) Costa, L. A. D. S.; Fonseca, A. F.; Pereira, F. V.; Druzian, J. I., Extraction and characterization of cellulose nanocrystals from corn stover. *Cellulose Chemistry And Technology* **2015**, *49* (2), 127-133.
50. Cao, J.; Sun, X.; Lu, C.; Zhou, Z.; Zhang, X.; Yuan, G., Water-soluble cellulose acetate from waste cotton fabrics and the aqueous processing of all-cellulose composites. *Carbohydrate polymers* **2016**, *149*, 60-67.

51. (a) Mandal, A.; Chakrabarty, D., Isolation of nanocellulose from waste sugarcane bagasse (SCB) and its characterization. *Carbohydrate Polymers* **2011**, *86* (3), 1291-1299; (b) Camargo, L.; Pereira, S.; Correa, A.; Farinas, C.; Marconcini, J.; Mattoso, L., Feasibility of manufacturing cellulose nanocrystals from the solid residues of second-generation ethanol production from sugarcane bagasse. *BioEnergy Research* **2016**, *1*-13; (c) de Morais Teixeira, E.; Bondancia, T. J.; Teodoro, K. B. R.; Corrêa, A. C.; Marconcini, J. M.; Mattoso, L. H. C., Sugarcane bagasse whiskers: extraction and characterizations. *Industrial Crops and Products* **2011**, *33* (1), 63-66.
52. Kampeerappun, P., Extraction and characterization of cellulose nanocrystals produced by acid hydrolysis from corn husk. *Journal of Metals, Materials and Minerals* **2015**, *25* (1).
53. Lu, P.; Hsieh, Y.-L., Preparation and characterization of cellulose nanocrystals from rice straw. *Carbohydrate Polymers* **2012**, *87* (1), 564-573.
54. Jiang, F.; Hsieh, Y.-L., Chemically and mechanically isolated nanocellulose and their self-assembled structures. *Carbohydrate Polymers* **2013**, *95* (1), 32-40.
55. Yu, H.-Y.; Yan, C.-F., Mechanical properties of cellulose nanofibril (CNF)- and cellulose nanocrystal (CNC)-based nanocomposites. In *Handbook of Nanocellulose and Cellulose Nanocomposites*, Wiley-VCH Verlag GmbH & Co. KGaA: 2017; pp 393-443.
56. Dahiya, J.; Rana, S., Thermal behaviour and spectral studies on cotton cellulose modified with phosphorus, sulphur and metals. *INDIAN JOURNAL OF CHEMISTRY SECTION A* **2005**, *44* (10), 2024.
57. Camarero Espinosa, S.; Kuhnt, T.; Foster, E. J.; Weder, C., Isolation of thermally stable cellulose nanocrystals by phosphoric acid hydrolysis. *Biomacromolecules* **2013**, *14* (4), 1223-1230.
58. Bano, S.; Negi, Y. S., Studies on cellulose nanocrystals isolated from groundnut shells. *Carbohydrate Polymers* **2017**, *157*, 1041-1049.
59. Jiang, F.; Hsieh, Y.-L., Assembling and redispersibility of rice straw nanocellulose: effect of tert-butanol. *ACS applied materials & interfaces* **2014**, *6* (22), 20075-20084.
60. Satyamurthy, P.; Jain, P.; Balasubramanya, R. H.; Vigneshwaran, N., Preparation and characterization of cellulose nanowhiskers from cotton fibres by controlled microbial hydrolysis. *Carbohydr. Polym.* **2011**, *83* (1), 122-129.
61. Mirhosseini, H.; Tan, C. P.; Hamid, N. S. A.; Yusof, S., Effect of Arabic gum, xanthan gum and orange oil contents on ζ -potential, conductivity, stability, size index and pH

- of orange beverage emulsion. *Colloids and Surfaces A: Physicochemical and Engineering Aspects* **2008**, 315 (1), 47-56.
62. Braun, B.; Dorgan, J. R.; Chandler, J. P., Cellulosic Nanowhiskers. Theory and Application of Light Scattering from Polydisperse Spheroids in the Rayleigh–Gans–Debye Regime. *Biomacromolecules* **2008**, 9 (4), 1255-1263.

Chapter 4: Synthesis of triazolidine-3-one derivatives through the nanocellulose/hydroxyapatite-catalyzed reaction of aldehydes and semicarbazide

4.1. Introduction

Catalysis plays a major role in large-scale industrialized chemical processes with the vast majority of these processes using catalysts in at least one of the steps.¹ Heterogeneous catalysts have distinct physical and chemical properties that include thermal stability, controlled miscibility and low volatility which lead to their facile recovery and recyclability.² Furthermore, heterogeneous systems have gathered significant interest due to improved selectivity, high conversion, simpler synthetic approaches and low cost.³ Recently, heterogeneous catalysts have started to play a leading role in multicomponent reactions (MCRs). The one-pot synthesis of multiple reactants has become a huge research focus with the emergence of technological advancements in both the biological and medicinal fields.⁴ MCRs also allow for a comparatively simple synthesis of heterocycles⁵ and the application of green chemistry principles, which are all relevant in the context of the present study.⁶

4.1.1. Hydroxyapatite (HAp) as a heterogeneous catalyst

Hydroxyapatite (HAp) is a bifunctional material with both acidic and basic properties that are dependent on its composition.⁷ The general chemical formula for HAp is $\text{Ca}_{10-x}(\text{HPO}_4)_x(\text{PO}_4)_{6-x}(\text{OH})_{2-x}$. Stoichiometric HAp has $x = 0$ giving $\text{Ca}_{10}(\text{PO}_4)_6(\text{OH})_2$, whereas calcium deficient, non-stoichiometric HAp has $0 \leq x \leq 1$. Used as a basic catalyst for the Michael addition of metacarpenes to chalcone derivatives, HAp demonstrated higher yields, better conversion and selectivity compared to other phosphate catalysts.⁸ HAp has also been used as a catalyst in a number of reactions, including the conversion of ethanol to ethylene, 1-butanol and 1,3-butadiene⁹ and the oxidation of benzene to phenol in the presence of air and ammonia.¹⁰ Bio-composite materials composed of NCC and HAp have been previously applied to the preparation of water-resistant transparent coatings,¹¹ however, currently there are no cited occurrences in literature of NCC/HAp composites used in any catalytic application.

4.1.2. Triazoles moiety

Heterocyclic compounds have become significant in the field of industrial-, agro- and pharmaceuticals chemicals. Research endeavours to find simple and facile approaches for the formation of complex heterocycles remain a crucial aspect and ongoing challenge in heterocyclic chemistry. Triazoles and their derivatives are important building blocks in modern heterocyclic chemistry due to their biological¹² and pharmaceutical properties.¹³ Triazole derivatives are well known for their anticancer,¹⁴ antimicrobial,¹⁵ antihypertensive,¹⁶ anti-inflammatory,¹⁷ antiviral,¹⁸ and antihistaminic¹⁹ activities. Several triazoles are also used as herbicidal and insecticidal agents.²⁰ Triazole moiety protocols have been developed using catalysts such as PEG-400,²¹ [C₁₆MPy]AlCl₃Br,²² and sulfamic acid.²³ Ranu and co-workers reported a solvent-free, one-pot synthesis of 1,2,3 triazoles by a 'click' reaction using boronic acids and sodium azide over a Cu/Al₂O₃ surface.²⁴ Al-Zaydi reported a green chemistry approach by using microwave and ultrasound as an eco-friendly energy source.²⁵ Many of these reports have drawbacks, such as the use of toxic reagents, strict reaction conditions, costly reagents and catalysts, long reaction times, low product yields and /or non-recyclability, which limits their scope in practical applications.

In the continued effort in the development of efficient, environmentally benign and green methodologies for the synthesis of diverse heterocyclic compounds, typically through multicomponent reaction approaches,²⁶ newly reported methodologies for the synthesis of various biologically interesting products was undertaken.²⁷ The present study focuses on the synthesis of novel NCC/HAp material to be used as a catalyst for the first time, and its use in the synthesis of triazolidine-3-ones by the reaction of aromatic aldehydes and semicarbazide at room temperature with ethanol as green solvent. The twelve triazolidine-3-one derivatives synthesized are a new family of compounds with the 1,2,4-triazolidin-3-one moiety.

4.2. Materials and Methods

4.2.1. Materials

The following chemicals were purchased from Aldrich Chemical Co.: 2-methoxybenzaldehyde (96%); 3,4-dimethoxybenzaldehyde (99%); 2-fluorobenzaldehyde (97%); 2-Chlorobenzaldehyde (99%); 4-Chlorobenzaldehyde (97%); 4-bromobenzaldehyde (99%); 2-nitrobenzaldehyde (98%); p-anisaldehyde (98%); 4-ethylbenzaldehyde ($\geq 97\%$); 2,3-dimethoxybenzaldehyde (98%); 3-hydroxybenzaldehyde (99%); 2,5-dimethoxybenzaldehyde (99%). Diammonium hydrogen orthophosphate (98.5%); calcium nitrate (99%) was obtained from Merck. Dissolving pulp provided by the CSIR, Durban, South Africa.

4.2.2. Preparation of HAp

The synthesis of hydroxyapatite (HAp) followed a co-precipitation approach.^{26b} A solution of diammonium hydrogen orthophosphate, $(\text{NH}_4)_2\text{HPO}_4$ (5.6 g, 0.0426 mol) was adjusted to pH 11.0 using a dilute ammonia solution (which was further diluted in 250 mL double distilled water). Similarly, a solution of $\text{Ca}(\text{NO}_3)_2 \cdot 4\text{H}_2\text{O}$ (23.7 g, 0.167 mol) was prepared and the pH was adjusted to 11.0. The ensuing solution was diluted to 250 mL using double distilled water. The $(\text{NH}_4)_2\text{HPO}_4$ solution was added dropwise to the prepared $\text{Ca}(\text{NO}_3)_2 \cdot 4\text{H}_2\text{O}$ solution, with vigorous stirring for 1 h at room temperature. The pH was maintained at 11 throughout, using diluted ammonia. The resultant precipitate was heated to and maintained at 85 °C for 1.5 h and then allowed to cool to room temperature. The precipitate was filtered under vacuum and washed repeatedly until a neutral pH was obtained, ensuring the removal of excess ammonia. The HAp was dried in an oven at 120 °C for 12 h, and then calcined at 500 °C for 6 h.

4.2.3. Preparation of NCC

The NCC was prepared from dissolving (hardwood) pulp using a sulfuric acid (65% w/w) hydrolysis treatment. Dissolving pulp (5.0 g) was mixed with 100 mL of sulfuric acid solution, and the mixture was stirred vigorously (700 rpm) at 64 °C for 1 hour. The mixture was diluted 10-fold with deionized water to stop the hydrolysis reaction and the diluted mixture was then centrifuged at 9000 rpm for 15 min to concentrate the cellulose and remove excess acid. The precipitated material was rinsed with distilled water and centrifuged again, this process was repeated 3 times and then dialyzed in dialysis sacks, with an average flat width 25 mm, MWCO 12,000 Da, against deionized water for one week until a pH of 7 was reached. The dialyzed

nanocellulose was sonicated for 5 min with cooling in an ice bath at 75% output and 0.7 cycles to obtain the NCC colloidal solution.

After blending cellulose obtained from Bleached Pulp (BP) with a domestic blender, NCCs were isolated using 20 mL/g 64 wt% sulfuric acid at 45 °C in an oil bath for 45 minutes to remove the amorphous regions. After the completion of the hydrolysis, the suspensions were repeatedly diluted and centrifuged at 6000 rpm for 10 min to reduce the sulfuric acid concentration. The suspensions were later sonicated using UP400S Ultrasonic processor, Hielscher, Germany at 50% amplitude and 0.5 cycle for 15 minutes to ensure complete dispersion of NCCs before dialysis to near neutral pH.

4.2.4. Preparation of NCC loaded HAp catalyst

NCC doped HAp was prepared *via* a pseudo wet impregnation technique. NCC (400 mg) was suspended in 50 mL of double distilled water and mixed with previously prepared HAp (605 mg). The mixture was stirred for 5 h using a magnetic stirrer at RT. Thereafter, it was heated to 80 °C for 7 h. After heating, the precipitate was sonicated in 30 min. intervals for 2 h. The precipitate was dried in an oven exposed to air at 90-100 °C for 12 h, to afford the 10%, 20% and 40% w/w NCC/HAp catalysts.

4.2.5. General procedure for the synthesis of triazolidine-3-one derivatives (4a-l)

In a 100 mL round bottom flask at room temperature, aromatic aldehyde (1.0 mmol), semicarbazide (1.0 mmol) and NCC/HAp (40 mg) were added under stirring using ethanol solvent. The progress of reaction was monitored by TLC. After completion of the reaction, sufficient ethanol was added to dissolve the organic compound formed and the solid catalyst was recovered by filtration. The final product was recovered after evaporation of ethanol under vacuum. The products were characterized and validated by various techniques (¹H NMR, ¹⁵N NMR, ¹³C NMR and HR-MS). All the spectral instrumentation details are reported in the Supplementary Information.

5-(2-Methoxyphenyl)-1,2,4-triazolidin-3-one (4a): White solid; mp 214 – 216 °C; FT-IR (selected values) $\nu_{\text{max}}/\text{cm}^{-1}$: 3459 (NH), 1604 (CO); ¹H NMR (400 MHz, DMSO-*d*₆) δ = 3.82 (s, 3H, OCH₃), 6.42 (s, 2H, NH), 6.94 (t, *J* = 8.00 Hz, 1H, ArH), 6.95 (t, *J* = 7.50 Hz, 1H, ArH), 7.04 (d, *J* = 8.13 Hz, 1H, ArH), 7.32 (t, *J* = 3.48 Hz, 1H, ArH), 7.97 (d, *J* = 3.09 Hz, 1H, ArH),

8.17 (s, 1H, CH); ^{13}C NMR (100 MHz, DMSO- d_6): δ 55.53, 111.50, 120.48, 122.73, 125.48, 134.67, 156.71, 157.01; HRMS of $[\text{C}_9\text{H}_{11}\text{N}_3\text{O}_2 + \text{Na}]$ (m/z): 193.0848; Calcd.: 193.0851.

5-(3,4-Dimethoxyphenyl)-1,2,4-triazolidin-3-one (4b): White solid; mp 205 – 206 °C; FT-IR (selected values) $\nu_{\text{max}}/\text{cm}^{-1}$: 3465 (NH), 1604 (CO); ^1H NMR (400 MHz, DMSO- d_6) δ = 3.77 (s, 3H, OCH₃), 3.80 (s, 3H, OCH₃), 6.48 (s, 2H, NH), 6.71 (d, J = 8.29 Hz, 1H, ArH), 7.07 (d, J = 3.34 Hz, 1H, ArH), 7.42 (s, 1H, ArH), 7.75 (s, 1H, CH), 10.09 (s, 1H, NH); ^{13}C NMR (100 MHz, DMSO- d_6): δ 55.45, 55.55, 108.17, 111.24, 120.82, 127.62, 139.39, 149.03, 149.84, 156.83; HRMS of $[\text{C}_{10}\text{H}_{13}\text{N}_3\text{O}_3 + \text{Na}]$ (m/z): 223.0956; Calcd.: 223.0957.

5-(2-Fluorophenyl)-1,2,4-triazolidin-3-one (4c): White solid; mp 229 – 231 °C; FT-IR (selected values) $\nu_{\text{max}}/\text{cm}^{-1}$: 3464 (NH), 1607 (CO); ^1H NMR (400 MHz, DMSO- d_6) δ = 6.55 (s, 2H, NH), 7.22 (m, 2H, ArH), 7.38 (m, 1H, ArH), 8.05 (s, 1H, CH), 8.11 (s, 1H, NH); ^{13}C NMR (100 MHz, DMSO- d_6): δ 115.56, 122.25, 124.56, 126.35, 130.72, 131.60, 156.52, 158.98, 161.45; HRMS of $[\text{C}_8\text{H}_8\text{FN}_3\text{O} + \text{Na}]$ (m/z): 181.0650; Calcd.: 181.0651.

5-(2-Chlorophenyl)-1,2,4-triazolidin-3-one (4d): White solid; mp 218 – 221 °C; FT-IR (selected values) $\nu_{\text{max}}/\text{cm}^{-1}$: 3464 (NH), 1656 (CO); ^1H NMR (400 MHz, DMSO- d_6) δ = 6.57 (s, 2H, NH), 7.34-7.36 (m, 2H, ArH), 7.44-7.46 (m, 1H, CH), 8.17-8.20 (m, 1H, ArH), 8.23 (s, 1H, CH), 10.48 (s, H, NH); ^{13}C NMR (100 MHz, DMSO- d_6): δ 126.92, 127.24, 129.60, 130.33, 131.89, 132.19, 135.05, 156.50; HRMS of $[\text{C}_8\text{H}_8\text{ClN}_3\text{O} + \text{Na}]$ (m/z): 197.0354; Calcd.: 197.0356.

5-(4-Chlorophenyl)-1,2,4-triazolidin-3-one (4e): White solid; mp 240 – 242 °C; FT-IR (selected values) $\nu_{\text{max}}/\text{cm}^{-1}$: 3460 (NH), 1664 (CO); ^1H NMR (400 MHz, DMSO- d_6) δ = 6.51 (s, 2H, NH), 7.43 (d, J = 8.53 Hz, 2H, ArH), 7.75 (d, J = 8.53 Hz, 2H, ArH), 7.81 (s, H, CH), 10.30 (s, 1H, NH); ^{13}C NMR (100 MHz, DMSO- d_6): δ 128.16, 128.55, 133.29, 133.77, 156.62; HRMS of $[\text{C}_8\text{H}_8\text{ClN}_3\text{O} + \text{Na}]$ (m/z): 197.0352; Calcd.: 197.0356.

5-(4-Bromophenyl)-1,2,4-triazolidin-3-one (4f): White solid; mp 197 – 198 °C; FT-IR (selected values) $\nu_{\text{max}}/\text{cm}^{-1}$: 3460 (NH), 1664 (CO); ^1H NMR (400 MHz, DMSO- d_6) δ = 6.52 (s, 2H, NH), 7.56 (d, J = 8.49 Hz, 2H, ArH), 7.68 (d, J = 8.52 Hz, 2H, ArH), 7.80 (s, 1H, CH), 10.31 (s, 1H, NH); ^{13}C NMR (100 MHz, DMSO- d_6): δ 122.01, 128.42, 131.45, 134.11, 137.89, 156.61; HRMS of $[\text{C}_8\text{H}_8\text{BrN}_3\text{O} + \text{Na}]$ (m/z): 240.9851/242.9830; Calcd.: 240.9851/242.9830.

5-(2-Nitrophenyl)-1,2,4-triazolidin-3-one (4g): Yellow solid; mp 239 – 241 °C; FT-IR (selected values) $\nu_{\text{max}}/\text{cm}^{-1}$: 3459 (NH), 1598 (CO); ^1H NMR (400 MHz, DMSO- d_6) δ = 6.52 (s, 2H, NH), 7.57 (td, J = 7.77 Hz, 1.14, 1H, ArH), 7.71 (t, J = 7.36 Hz, 1H, ArH), 7.98 (d, J = 8.13 Hz, 1H, ArH), 8.23 (s, 1H, CH), 8.33 (dd, J = 8.03 Hz, 1.51, 1H, ArH), 10.60 (s, 1H, NH);

^{13}C NMR (100 MHz, DMSO- d_6): δ 124.31, 127.85, 128.74, 129.53, 133.14, 133.91, 147.73, 156.33; HRMS of $[\text{C}_8\text{H}_8\text{N}_4\text{O}_3 + \text{Na}]$ (m/z): 208.0592; Calcd.: 208.0596.

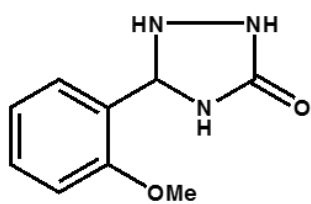
5-(4-Methoxyphenyl)-1,2,4-triazolidin-3-one (4h): White solid; mp 221 – 223 °C; FT-IR (selected values) $\nu_{\text{max}}/\text{cm}^{-1}$: 3451 (NH), 1680 (CO); ^1H NMR (400 MHz, DMSO- d_6) δ = 3.78 (s, 3H, OCH₃), 6.41 (s, 2H, NH), 6.94 (d, J = 8.73 Hz, 2H, ArH), 7.64 (d, J = 9.18, 2H, ArH), 7.78 (s, 1H, CH), 10.09 (s, 1H, NH); ^{13}C NMR (100 MHz, DMSO- d_6): δ 55.17, 114.02, 127.40, 127.99, 139.16, 156.81, 159.99; HRMS of $[\text{C}_9\text{H}_{11}\text{N}_3\text{O}_2 + \text{Na}]$ (m/z): 193.0847; Calcd.: 193.0581.

5-(4-Ethylphenyl)-1,2,4-triazolidin-3-one (4i): White solid; mp 246 – 248 °C; FT-IR (selected values) $\nu_{\text{max}}/\text{cm}^{-1}$: 3455 (NH), 1643 (CO); ^1H NMR (400 MHz, DMSO- d_6) δ = 1.17 (t, J = 7.56 Hz, 3H, CH₃), 2.61 (q, J = 7.62 Hz, 2H, CH₂), 6.44 (s, 2H, NH), 7.22 (d, J = 8.08 Hz, 2H, ArH), 7.61 (d, J = 8.17 Hz, 2H, ArH), 7.81 (s, 1H, CH), 10.12 (s, 1H, NH); ^{13}C NMR (100 MHz, DMSO- d_6): δ 15.37, 27.98, 126.54, 127.95, 132.29, 139.34, 144.88, 156.73; HRMS of $[\text{C}_{10}\text{H}_{13}\text{N}_3\text{O} + \text{Na}]$ (m/z): 191.1051; Calcd.: 191.1059.

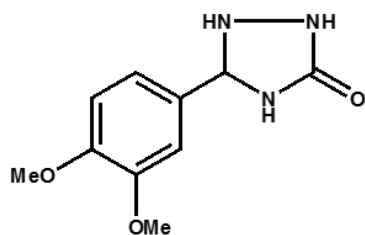
5-(2,3-Dimethoxyphenyl)-1,2,4-triazolidin-3-one (4j): White solid; mp 186 – 189 °C; FT-IR (selected values) $\nu_{\text{max}}/\text{cm}^{-1}$: 3453 (NH), 1687 (CO); ^1H NMR (400 MHz, DMSO- d_6) δ = 3.73 (s, 3H, OCH₃), 3.81 (s, 3H, OCH₃), 6.45 (s, 2H, NH), 6.99 – 7.07 (m, 2H, ArH), 7.59 (dd, J = 7.53, 2.28 Hz, 2H, ArH), 8.13 (s, 1H, CH), 10.24 (s, 1H, NH); ^{13}C NMR (100 MHz, DMSO- d_6): δ 55.65, 61.00, 113.12, 117.14, 124.03, 128.16, 134.84, 147.24, 152.50, 156.64; HRMS of $[\text{C}_{10}\text{H}_{13}\text{N}_3\text{O}_3 + \text{Na}]$ (m/z): 223.0949; Calcd.: 223.0957.

5-(3-Hydroxyphenyl)-1,2,4-triazolidin-3-one (4k): Cream solid; mp 202 – 204 °C; FT-IR (selected values) $\nu_{\text{max}}/\text{cm}^{-1}$: 3473 (NH), 1660 (CO); ^1H NMR (400 MHz, DMSO- d_6) δ = 6.41 (s, 2H, NH), 6.75 (d, J = 8.04 Hz, 1H, ArH), 7.06 – 7.19 (m, 3H, ArH), 7.75 (s, 1H, CH), 9.48 (s, 1H, OH), 10.18 (s, 1H, NH); ^{13}C NMR (100 MHz, DMSO- d_6): δ 112.86, 116.22, 117.66, 129.98, 135.98, 139.60, 156.68, 157.48; HRMS of $[\text{C}_8\text{H}_9\text{N}_3\text{O}_2 + \text{Na}]$ (m/z): 179.0690; Calcd.: 179.0695.

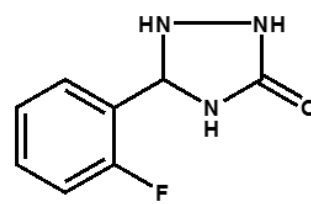
5-(2,5-Dimethoxyphenyl)-1,2,4-triazolidin-3-one (4l): White solid; mp 230 – 232 °C; FT-IR (selected values) $\nu_{\text{max}}/\text{cm}^{-1}$: 3480 (NH), 1692 (CO); ^1H NMR (400 MHz, DMSO- d_6) δ = 3.74 (s, 3H, OCH₃), 3.76 (s, 3H, OCH₃), 6.52 (s, 2H, NH), 6.89 (dd, J = 8.99, 3.10 Hz, 1H, ArH), 6.97 (d, J = 9.05 Hz, 1H, ArH), 7.54 (d, J = 3.08 Hz, 2H, ArH), 8.15 (s, 1H, CH), 10.24 (s, 1H, NH); ^{13}C NMR (100 MHz, DMSO- d_6): δ 55.53, 55.08, 109.65, 112.96, 116.27, 123.41, 134.61, 151.53, 153.32, 156.76; HRMS of $[\text{C}_{10}\text{H}_{13}\text{N}_3\text{O}_3 + \text{Na}]$ (m/z): 223.0955; Calcd.: 223.0957.



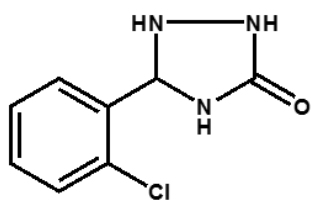
4a



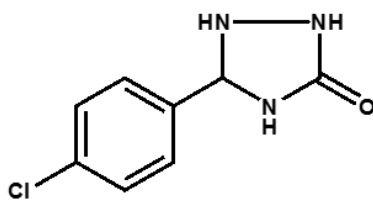
4b



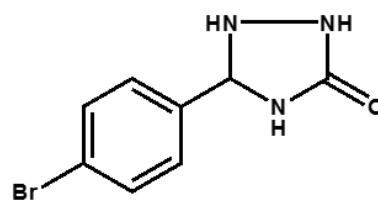
4c



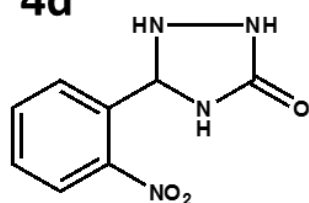
4d



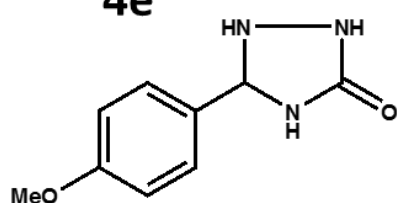
4e



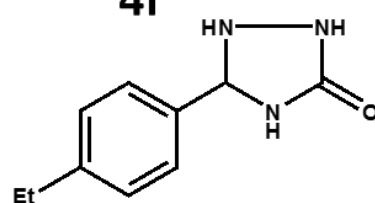
4f



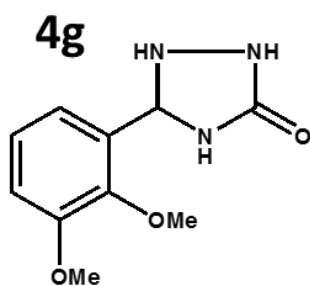
4g



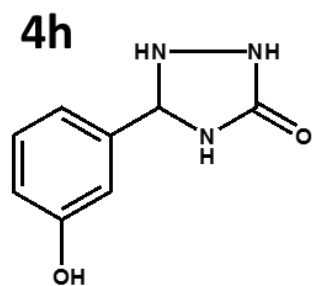
4h



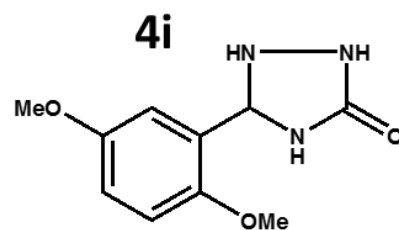
4i



4j



4k



4l

4.2.6. Characterization Techniques

^1H , ^{13}C and ^{15}N NMR spectroscopy

^1H , ^{13}C and ^{15}N NMR spectra of isolated triazole moieties were recorded on a Solution NMR experiments were carried out on a Bruker Avance 400 MHz spectrometer in deuterated dimethyl sulfoxide solvent.

Mass Spectral Analysis

Mass spectral analyses were performed on a Waters API Quattro Micro spectrometer. 500 ppm solutions of each sample were made up in dimethyl sulfoxide solvent. This followed with a direct injection into the instrument.

Fourier transform infrared spectroscopy

The identification of the HAp/NCC catalyst and resultant triazole compounds were confirmed by FTIR study in the range 380-4000 cm^{-1} at a resolution of 4 cm^{-1} using Spectrum 100 infrared spectrometer equipped with universal attenuated total reflection (UATR) accessory Perkin Elmer, USA.

Morphological structure analysis

The morphological characterisation, dimensions and elemental composition of the HAp/NCC catalyst were established with the aid of electron microscopic study using; JEOL 1010 transmission electron microscope (TEM), Japan and ZEISS Ultra Plus field emission gun scanning electron microscope (FEGSEM) equipped with energy dispersive x-ray (EDX) detector, Germany. TEM images of all samples were acquired using the HAp/NCC catalyst, which was deposited on the TEM-grid. The TEM-grids were also negatively stained with Uranyl acetate to aid visualization of NCC with the HAp/NCC catalyst matrix. Similarly, samples for SEM images were coated with gold with the aid of sputter coater to minimize charging.

X-ray diffraction analysis

Powder X-ray diffraction (XRD) analysis of the HAp/NCC catalyst was conducted using an X-ray diffractometer (Bruker AXS D8 Advance, Germany), equipped with Cu $K\alpha$ radiation source (wavelength = 0.154 nm) operating at 40 kV and 40 mA. The XRD pattern of the catalyst was recorded over the angular range $2\theta = 10-90^\circ$ at room temperature.

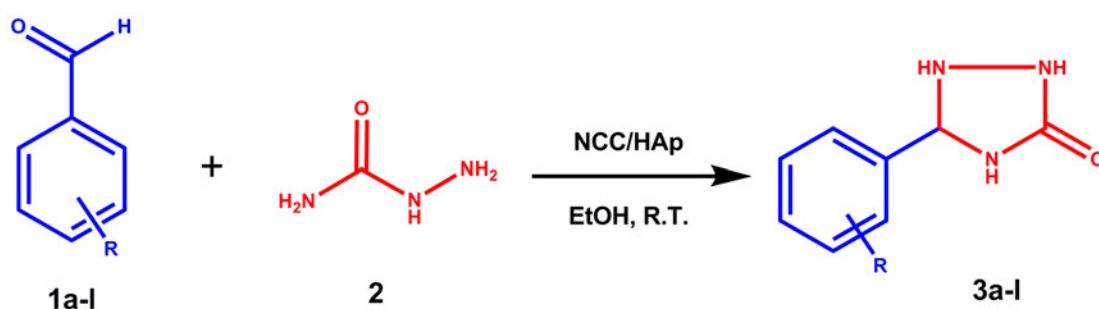
Specific surface area and porosity measurements

The nitrogen adsorption–desorption isotherms of the degassed samples (at 100 °C under vacuum for 24 h using Micromeritics VacPrep 061 sample degas system, USA) were measured at bath temperature of -195.8 °C (77.2 K) by surface area and porosity analyzer, Micromeritics Tristar II 3020 2.00, USA. Specific surface areas were calculated from the linear region of the isotherms using the Brunauer–Emmett–Teller (BET) equation in a relative P/P_o pressure range of 0.05 – 0.56. Pore size distributions were derived from the adsorption branch of the isotherms by Barrett–Joyner–Halenda (*BJH*) method. The total pore volumes were estimated from the amount adsorbed at a relative pressure of $P/P_o = 0.996$.

4.3. Results

Reaction optimization

The fully optimized (model conditions) two-component reaction of substituted aldehydes and semicarbazide using an NCC/HAp catalyst is shown in Scheme 4.1. The model reaction of 2-methoxybenzaldehyde and semicarbazide (molar ratio 1:1) was performed. Optimization of the reaction started with varying the catalyst-type. Under catalyst-free and solvent-free conditions, no reaction was observed, at neither RT nor reflux conditions, even after 12 h of stirring (Table 4.1, entries 1 & 2).



Scheme 4.1. Synthesis of 1,2,4-triazolidin-3-one derivatives

Introduction of various catalysts to the synthetic model was investigated at RT in either EtOH or solvent-free conditions. Acid catalysts such as *p*-toluenesulphonic acid (PTSA) and AcOH were tested but failed to afford a product after 12 h of stirring (Table 4.1, entries 3 & 4). The use of ionic liquids L-proline and (Bmim)BF₄ under solvent-free synthesis showed trace amounts of the desired product (Table 4.1, entries 5 & 6). Basic organic and inorganic catalysts such as triethylamine (TEA), pyridine, and NaOH at RT in EtOH exhibited low yields (Table 4.1, entries 7-9). The bio-organic polymers (NCC and chitosan) were then tested and was chosen due to their abundance. Moderate yields were obtained using the model conditions (Table 4.1, entries 10 & 11). Due to the widely used application of fluoroapatite (FAP) and HAp in catalysis, these calcium phosphate-based compounds were chosen and proved suitable catalysts. FAP, under the model conditions, showed adequate results similar to those of the bio-organic polymers (Table 4.1, entry 12). HAp showed a positive result with the highest yield of the selected catalysts (Table 4.1, entry 13). It is known that nano-HAp by itself can act as an efficient heterogeneous catalyst for three-component one-pot synthesis of 2,3-dihydroquinazolin-4(1*H*)-one derivatives in aqueous media.²⁸

Based on these promising results, a composite material was prepared to improve the efficiency of the reaction, materials were prepared with varied wt% (20%, 40% & 80%) loading of NCC on HAp supports. When using 20% NCC on HAp, the product yield was 90% within 45 min of stirring under standard model conditions (Table 4.1, entry 14).

Table 4.1. Optimal condition for the synthesis of 3a by 40% NCC/HAp catalyst^a

Entry	Catalyst	Solvent	Condition	Time (h)	Yield (%) ^b
1	--	--	RT	12	--
2	--	--	Reflux	12	--
3	PTSA	EtOH	RT	12	--
4	AcOH	EtOH	RT	12	--
5	L-proline	--	RT	8.0	19
6	(Bmim)BF ₄	--	RT	7.5	13
7	TEA	EtOH	RT	5.5	28
8	Pyridine	EtOH	RT	5.0	33
9	NaOH	EtOH	RT	4.5	37
10	NCC	EtOH	RT	2.5	68
11	Chitosan	EtOH	RT	3.5	54
12	FAp	EtOH	RT	3.0	51
13	HAp	EtOH	RT	1.5	80
14	20% NCC/HAp	EtOH	RT	0.75	89
15	40% NCC/HAp	EtOH	RT	0.25	96
16	80% NCC/HAp	EtOH	RT	0.30	92

^a All products were characterised by IR, ¹H NMR, ¹³C NMR, ¹⁵N NMR & HR-MS spectral analysis. ^b Isolated yields. -- No reaction

At 40% NCC loading, an optimum result was observed with 96% yield within 15 min (Table 4.1, entry 15). A further increase of NCC loading (80%) led to a slight decrease in yield of 92%

(Table 4.1, entry 16). Based on this evaluation of progressive results, it is evident that the 40% NCC/HAp catalyst revealed the most remarkable catalytic results, presumably due to the most active sites available for conversion when compared to the other entries. Hence, 40% NCC/HAp catalyst was chosen for all further reactions.

Solvent effects were subsequently evaluated. The 40% NCC/HAp catalysed reaction was carried out using various polar and non-polar solvents such as THF, DMF, MeOH, EtOH, *n*-hexane, toluene and isopropyl-alcohol, as well as solvent-free conditions (Table 4.2).

Table 4.2. Optimization of various solvent conditions for 40% NCC/HAp catalyst^a

Entry	Solvent	Time (minutes)	Yield* (%)
1	No solvent	90	NR
2	<i>n</i> -hexane	90	NR
3	toluene	90	NR
4	THF	60	37
5	DMF	60	48
6	MeOH	45	87
7	EtOH	25	97
8	isopropanol	60	70

^aReaction conditions: 2-methoxybenzaldehyde (1 mmol) and semicarbazide (1 mmol), catalyst (40 mg) and solvent (10 mL) were stirred at room temperature. * = Isolated yields. NR = No Reaction observed.

No yield was obtained under solvent-free conditions (Table 4.2, entry 1). The model reaction was carried out in the presence of non-polar solvents, i.e. *n*-hexane and toluene, with no reaction observed (Table 4.2, entries 2 & 3), whereas polar aprotic solvents of THF and DMF showed a moderate yield (Table 4.2, entries 4 & 5). Much better results were obtained when polar protic solvents, MeOH, EtOH and isopropyl-alcohol were used (Table 4.2, entries 5-8). Based on the criteria such as reaction times, greener approach, cost-effectiveness and excellent yields, EtOH proved to be the best solvent candidate for the present procedure and was used for all further reactions of substituted 1,2,4-triazolidin-3-ones.

The 40% NCC/HAp catalyst proved to be a versatile catalyst for this system. Variation in catalyst loading per model substrate (2-methoxybenzaldehyde) was observed. The summarised

results (Table 4.3, entries 1-3) indicate that an increase in mass of catalyst of 40% NCC/HAp from 20 mg to 40 mg, resulted in an increased yield of 96% from 76% and also a decrease in reaction time. A further increase in wt% of catalyst had no further positive effect on product yield, even with an increase in reaction time (Table 4.3, entries 4-5). Hence 40 mg of catalyst was used for the additional reactions.

Table 4.3. Optimization of various weight % for 40% NCC/HAp catalyst^a

Entry	Catalyst (mg)	Time (min)	Yield (%)
1	20	120	72
2	30	60	80
3	40	15	96
4	50	30	96
5	60	30	96

^aReaction conditions: 2-methoxybenzaldehyde (1 mmol) and semicarbazide (1 mmol), catalyst and solvent (10 mL) were stirred at room temperature. * = Isolated yields

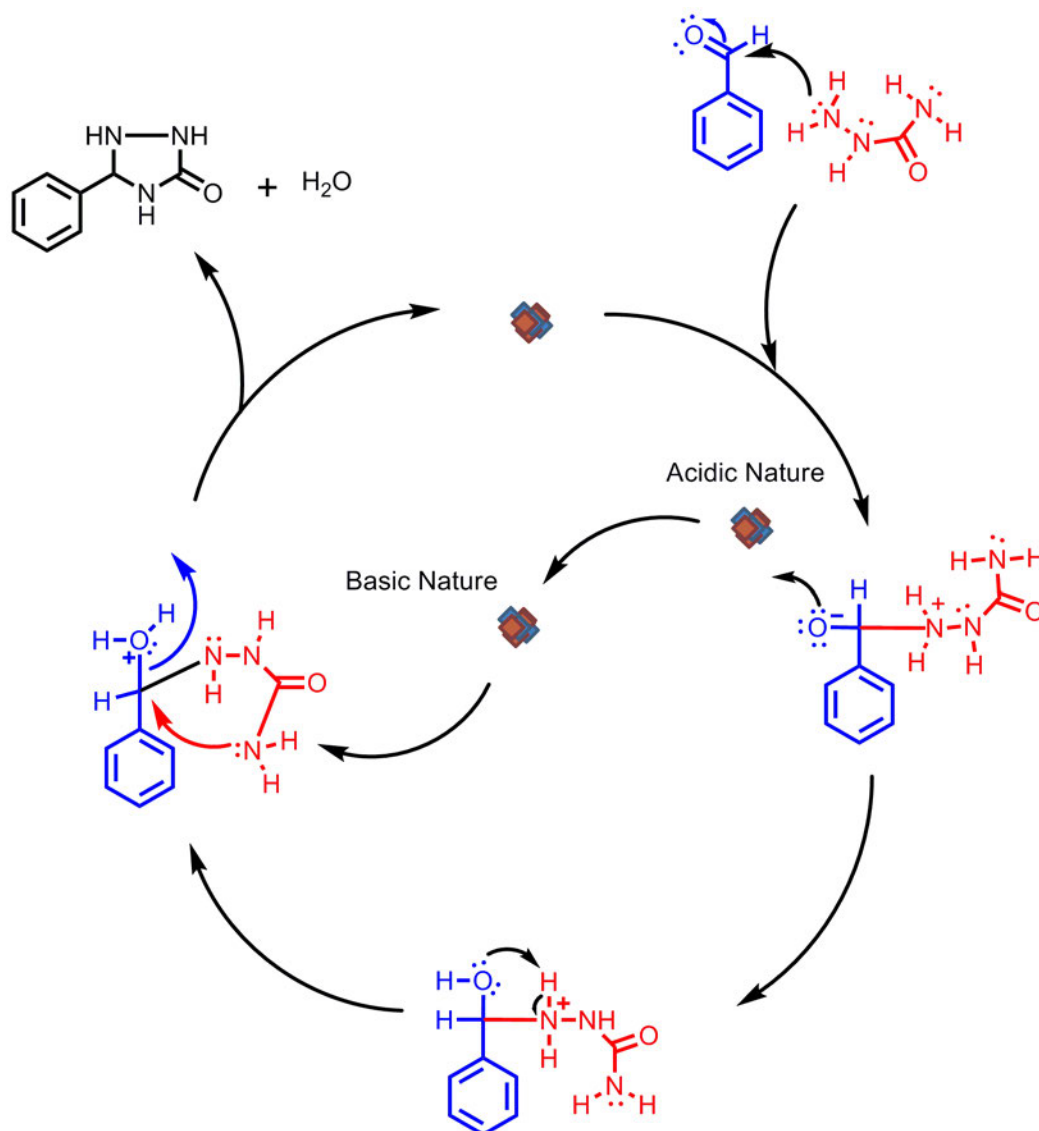
Employing the optimised reaction conditions, the procedure was applied toward the synthesis of 1,2,4-triazolidin-3-one derivatives from various substituted aromatic aldehydes. The 40% NCC/HAp heterogeneous catalyst proved to catalyse the facile one-pot synthesis of 1,2,4-triazolidin-3-one derivatives with excellent yields. All the 1,2,4-triazolidin-3-one derivatives with supplementary details are shown in Table 4.4. Notably, the aldehydes with both electron-donating and electron-withdrawing (*ortho*, *meta* and *para*) substituents performed efficiently under the reaction conditions in forming the corresponding target products (**4a-1**).

Table 4.4. Synthesis of triazolidine-3-one derivatives with NCC/HAp catalyst^a

Entry	R	Product	Yield* (%)	Mp °C
1	2-OMe	3a	96	214-216
2	3,4-(MeO) ₂	3b	91	205-206
3	2-F	3c	90	229-231
4	2-Cl	3d	94	218-221
5	4-Cl	3e	91	240-242
6	4-Br	3f	90	197-198
7	2-NO ₂	3g	92	239-241
8	4-OMe	3h	96	221-223
9	4-Et	3i	95	246-248
10	2,3-(OMe) ₂	3j	94	186-189
11	3-OH	3k	93	202-204
12	2,5-(OMe) ₂	3l	94	230-232

^aReaction conditions: semicarbazide (1mmol), substituted benzaldehyde (1 mmol), catalyst (40 mg) and ethanol solvent (10 mL) were stirred at room temperature. R = substituted benzaldehydes. * = Isolated yields

On the basis of these results, but without conclusive experimental evidence for the formation of possible intermediates, we propose a mechanism for the cyclocondensation reaction of aldehydes and semicarbazide catalyzed by NCC/HAp, shown in Scheme 4.2.



Scheme 4.2. Proposed mechanism for the formation of triazolidine-3-one derivatives using an NCC/HAp catalyst.

In a first step, the more reactive of the two NH₂ groups on the semicarbazide (i.e. the one furthest away from the carbonyl group) provides nucleophilic attack on the aldehyde carbonyl group presumably forming a short-lived zwitterionic intermediate that becomes protonated by the acidic NCC/HAp/(protic solvent) combination. The cyclization is complete upon elimination of water, presumably aided by the basic nature of HAp, and finally, the catalyst is released back into the catalytic cycle.

XRD analysis

The PXRD pattern of the 40% NCC/HAp catalyst (Figure 4.1) showed characteristic peaks for HAp. The correlation of the experimental pattern to the reference pattern of HAp (JCPDS file

no. 9-930) showed that HAp had been successfully synthesized and the structure was maintained after NCC was incorporated to form the composite. The diffraction peaks located at $2\theta = 26^\circ, 32.4^\circ, 33.6^\circ, 34.5^\circ$ and 36° are indexed to the (002), (211), (300), (202), (301), (222), (213) and (004) planes of HAp.²⁸ The NCC peaks were shown in the XRD diffractogram at $2\theta = 16^\circ$ and 22° . This implies that the HAp lattice remained unaffected during the wet impregnation process and subsequent low-thermal treatment.

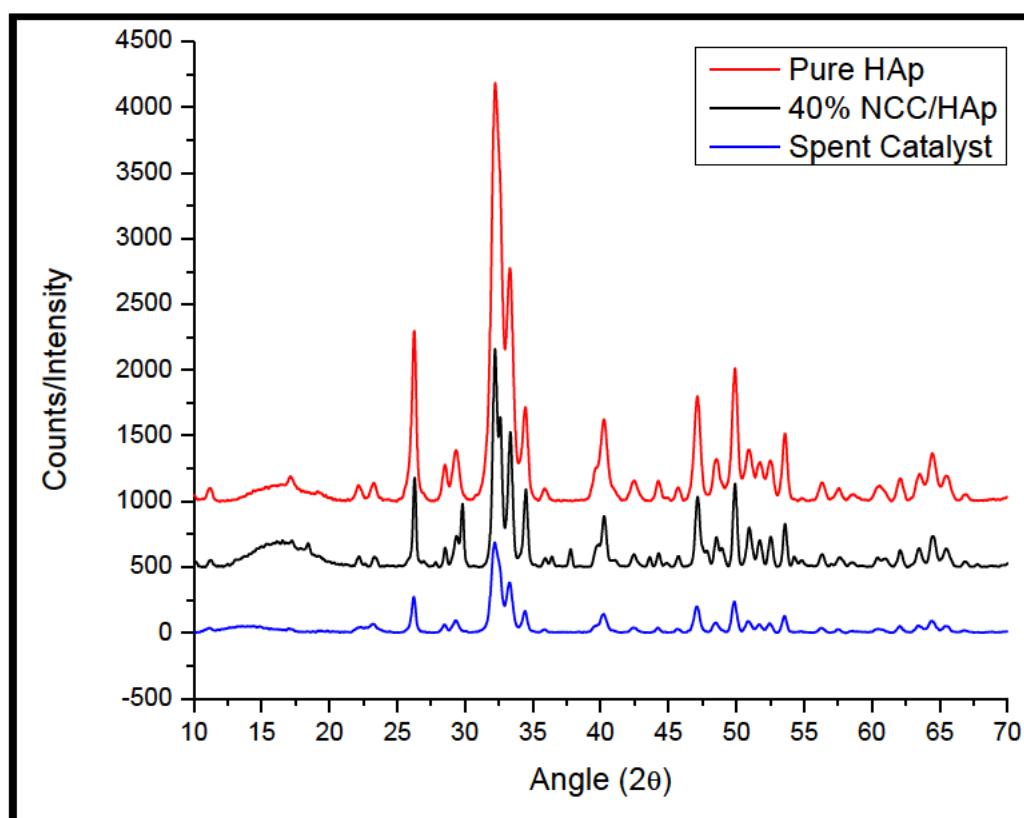


Figure 4.1. Powder X-ray diffractograms of pure HAp, 40% NCC/HAp and spent catalyst.

TEM and SEM-EDX analysis

The transmission electron microscope (TEM) micrograph of HAp (Figure 4.2a) showed rod-shaped particles with sizes ranging between 70 – 100 nm in length. The TEM micrographs of the HAp deposited on the NCC catalysts are shown in Figure 4.2b. The size of HAp particles deposited on the NCC catalysts showed no significant changes when compared to the original HAp particles, however, bone-like NCC particles are evident upon staining of samples (Figure 4.2b). Sizes of NCC particles range between 100 – 500 nm in length which is in agreement with NCC benchmarks.⁸ With the introduction of NCC into the HAp matrix, the rod-like particles showed signs of aggregation, forming small clusters around the NCC particles.

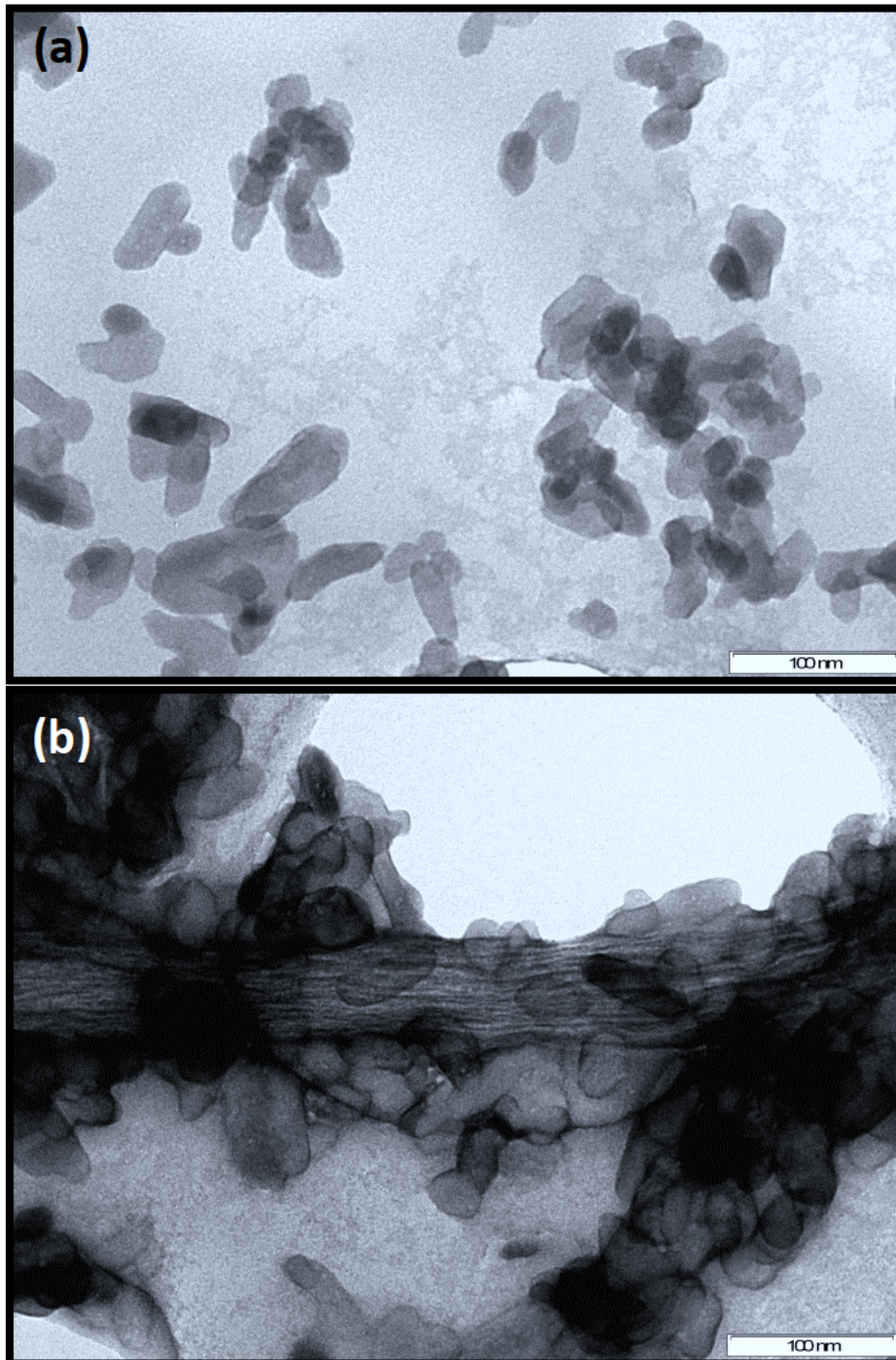


Figure 4.2. TEM micrograph of 40% NCC/HAp catalyst, (a) unstained and (b) stained

Figure 4.3a shows an SEM micrograph of the NCC/HAp composite which illustrates the catalyst surface morphology. The particles are large with elliptical irregular shapes. This micrograph shows that the HAp particles are aggregated and assembled on the NCC rods. A homogeneous distribution of calcium and phosphorous on the surface of the catalyst was quantified by EDS analysis (Figure 4.3b), with small but notable amounts of surface

enrichment of calcium. The morphology of the catalyst observed on the SEM micrographs points to a crystalline and homogenous sample.

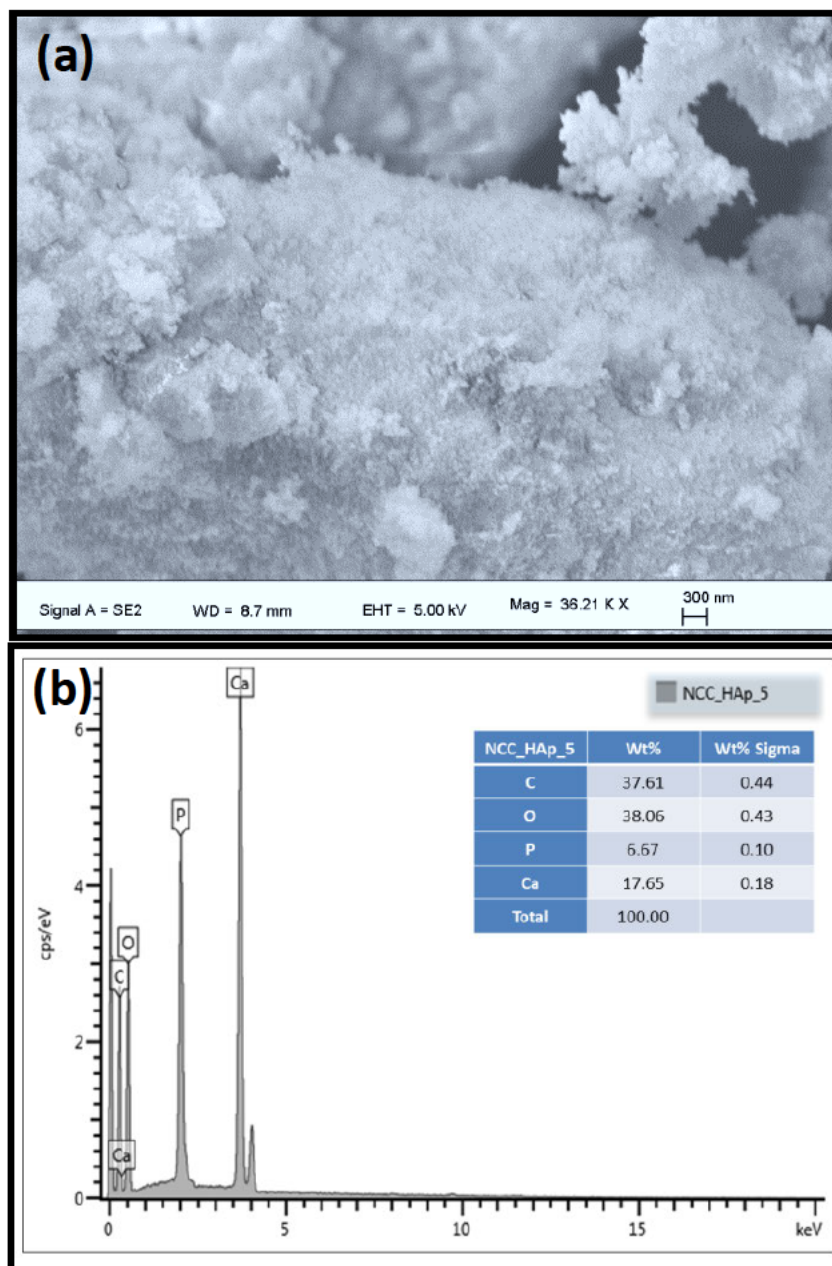


Figure 4.3. (a) SEM micrograph and (b) EDS spectra of 40% NCC/HAp catalyst.

BET surface area analysis

An N_2 adsorption/desorption study was carried out on the NCC/HAp catalyst (Figure 4.4). N_2 sorption resulted in a Type IV isotherm, with a narrow hysteresis loop within the P/P_0 range of 0.62-0.96, which is typical for mesoporous materials. The BET surface area of 40%, NCC/HAp catalyst was found to be $36.2 \text{ m}^2 \text{ g}^{-1}$ and pore volume $0.069 \text{ cm}^3/\text{g}$. Pore size distribution (Figure 4.4 inset) shows two local maxima with diameters of 167 and 248 nm.

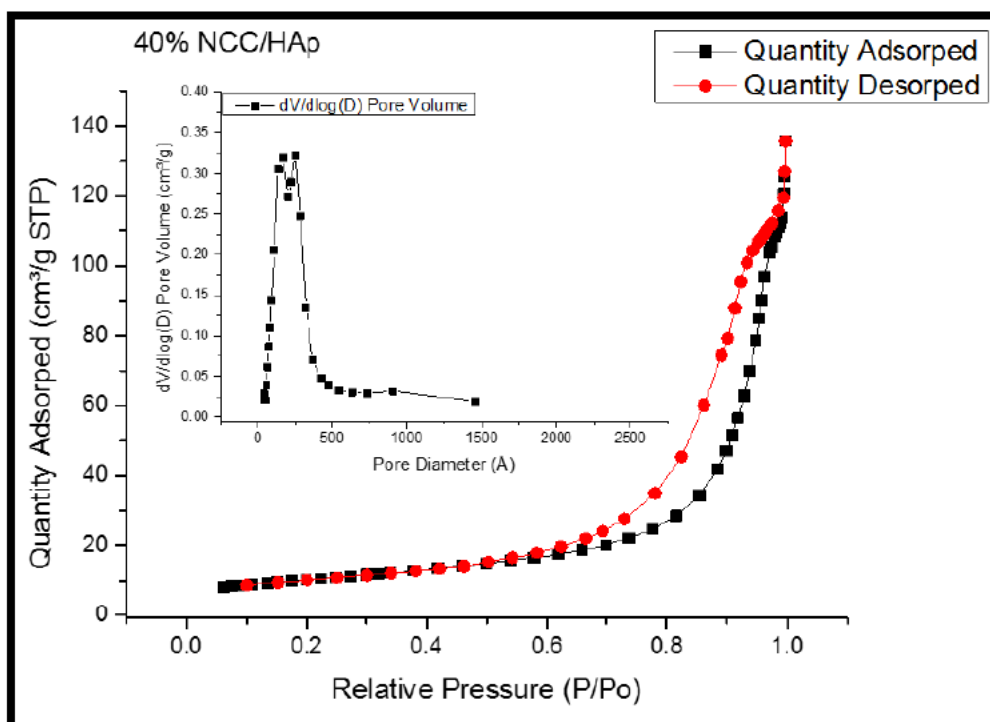


Figure 4.4. N₂ adsorption-desorption isotherms and (inset) pore size distribution of 40% NCC/HAp catalyst

Reusability of catalyst

The recyclability of a heterogeneous catalyst is an important requirement. Heterogeneous catalytic poisoning and leaching of metal during reactions are core limitations, which impacts on catalyst activity for further use. To determine catalyst stability, recyclability experiments were performed. After each run, the catalyst was separated by filtration and was subjected to washing with excess ethanol, for up to six cycles (Figure 4.5). No considerable catalyst degradation was perceived which was confirmed by ICP-OES, XRD (Figure 4.1) and N₂ isotherms (Figure 4.6). The catalytic activity of the NCC on HAp decreased when the recovered catalytic system was reused in the 6th run.

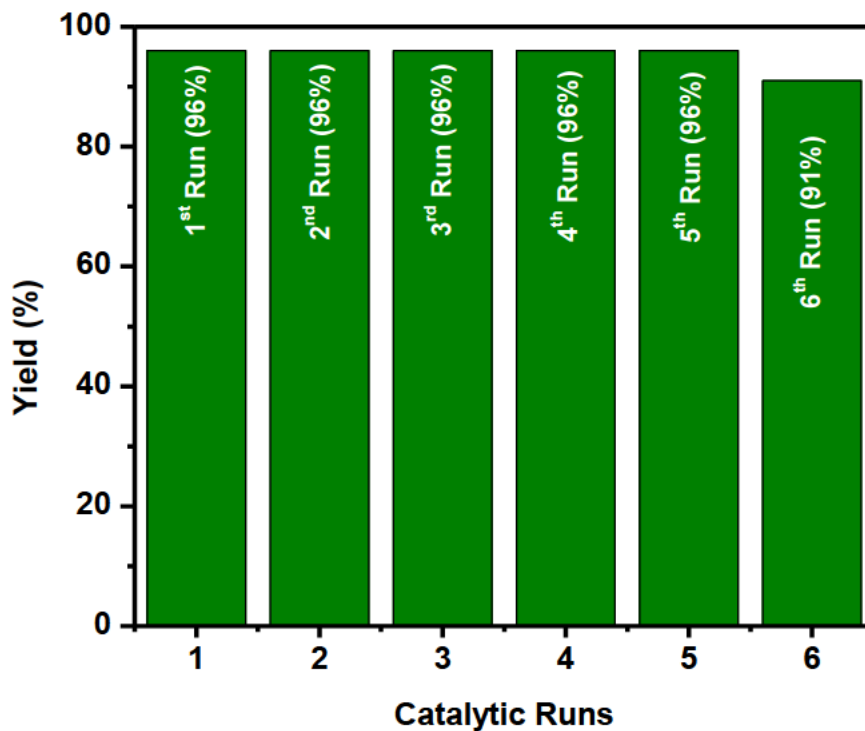


Figure 4.5. Recyclability of NCC/HAp catalyst.

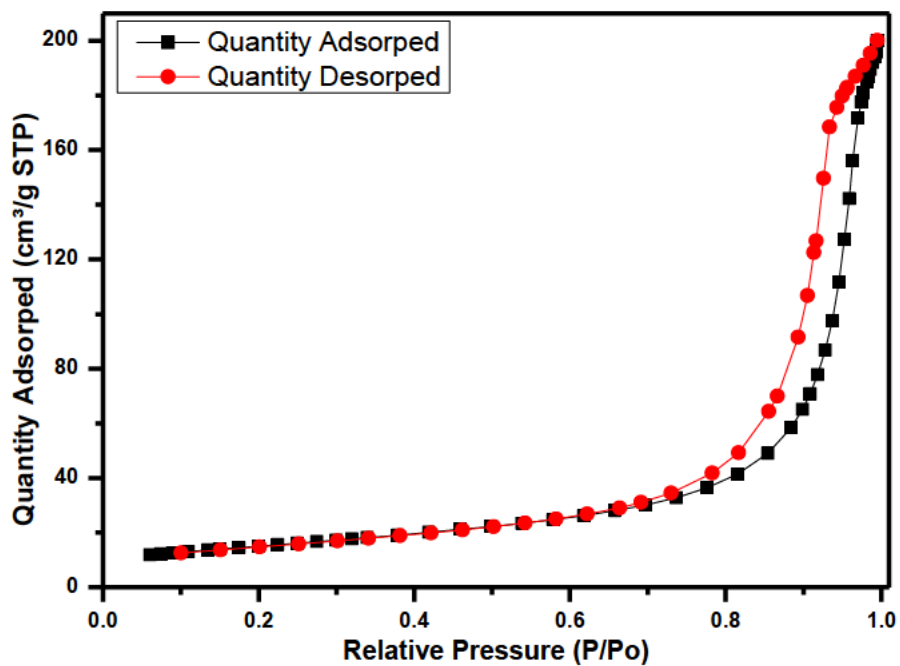


Figure 4.6 N₂ sorption of 40% NCC/HAp spent catalyst

4.4 Conclusion

The two-component one-pot synthesis of triazolidine-3-one derivatives was achieved in a simple, robust and green manner. The new derivatives were obtained in excellent yields using an NCC/HAp composite catalyst at RT. The catalyst proved effective for this MCR protocol with the added advantage of being recyclable. This favourable approach proves to be cost-effective, allows for an easy work up, and uses environment-friendly reaction conditions. The added advantages are shorter reaction times, green solvent, high yields and a reusable catalyst. This synthetic procedure is promising for a range of potentially bioactive heterocycles.

4.5 References

1. Fechete, I.; Wang, Y.; Védrine, J. C., The past, present and future of heterogeneous catalysis. *Catalysis Today* **2012**, *189* (1), 2-27.
2. Maddila, S.; Gangu, K. K.; Maddila, S. N.; Jonnalagadda, S. B., A facile, efficient, and sustainable chitosan/CaHAp catalyst and one-pot synthesis of novel 2,6-diaminopyran-3,5-dicarbonitriles. *Molecular Diversity* **2017**, *21* (1), 247-255.
3. Wan, J.-P.; Gan, S.-F.; Sun, G.-L.; Pan, Y.-J., Novel Regioselectivity: three-component cascade synthesis of unsymmetrical 1,4- and 1,2-dihydropyridines. *The Journal of Organic Chemistry* **2009**, *74* (7), 2862-2865.
4. Marcaccini, S.; Torroba, T., Multicomponent reactions, ed. J. Zhu and H. Bienaymé. Wiley-VCH: **2005**.
5. Weber, L., The application of multi-component reactions in drug discovery. *Current Medicinal Chemistry* **2002**, *9* (23), 2085-2093.
6. (a) Alfonsi, K.; Colberg, J.; Dunn, P. J.; Fevig, T.; Jennings, S.; Johnson, T. A.; Kleine, H. P.; Knight, C.; Nagy, M. A.; Perry, D. A.; Stefaniak, M., Green chemistry tools to influence a medicinal chemistry and research chemistry based organisation. *Green Chemistry* **2008**, *10* (1), 31-36; (b) Gu, Y., Multicomponent reactions in unconventional solvents: state of the art. *Green Chemistry* **2012**, *14* (8), 2091-2128.
7. Prakasam, M.; Locs, J.; Salma-Ancane, K.; Loca, D.; Largeteau, A.; Berzina-Cimdina, L., Fabrication, properties and applications of dense hydroxyapatite: a review. *Journal of Functional Biomaterials* **2015**, *6* (4), 1099.
8. Zahouily, M.; Abrouki, Y.; Bahlaouan, B.; Rayadh, A.; Sebti, S., Hydroxyapatite: new efficient catalyst for the Michael addition. *Catalysis Communications* **2003**, *4* (10), 521-524.
9. Tsuchida, T.; Kubo, J.; Yoshioka, T.; Sakuma, S.; Takeguchi, T.; Ueda, W., Reaction of ethanol over hydroxyapatite affected by Ca/P ratio of catalyst. *Journal of Catalysis* **2008**, *259* (2), 183-189.
10. Liptáková, B.; Hronec, M.; Cvengrošová, Z., Direct synthesis of phenol from benzene over hydroxyapatite catalysts. *Catalysis Today* **2000**, *61* (1-4), 143-148.
11. (a) Ishikawa, M.; Oaki, Y.; Tanaka, Y.; Kakisawa, H.; Salazar-Alvarez, G.; Imai, H., Fabrication of nanocellulose-hydroxyapatite composites and their application as water-resistant transparent coatings. *Journal of Materials Chemistry B* **2015**, *3* (28), 5858-5863; (b) Kaneda, K.; Mizugaki, T., Design of high-performance heterogeneous

- catalysts using apatite compounds for liquid-phase organic syntheses. *ACS Catalysis* **2017**, *7* (2), 920-935.
12. Maddila, S.; Pagadala, R.; B. Jonnalagadda, S., 1,2,4-Triazoles: A Review of Synthetic Approaches and the Biological Activity. *Letters in Organic Chemistry* **2013**, *10* (10), 693-714.
 13. Dömling, A.; Wang, W.; Wang, K., Chemistry and Biology Of Multicomponent Reactions. *Chemical Reviews* **2012**, *112* (6), 3083-3135.
 14. Ruddaraju, R. R.; Murugulla, A. C.; Kotla, R.; Chandra Babu Tirumalasetty, M.; Wudayagiri, R.; Donthabakthuni, S.; Maraju, R.; Baburao, K.; Parasa, L. S., Design, synthesis, anticancer, antimicrobial activities and molecular docking studies of theophylline containing acetylenes and theophylline containing 1,2,3-triazoles with variant nucleoside derivatives. *European Journal of Medicinal Chemistry* **2016**, *123*, 379-396.
 15. Kant, R.; Kumar, D.; Agarwal, D.; Gupta, R. D.; Tilak, R.; Awasthi, S. K.; Agarwal, A., Synthesis of newer 1,2,3-triazole linked chalcone and flavone hybrid compounds and evaluation of their antimicrobial and cytotoxic activities. *European Journal of Medicinal Chemistry* **2016**, *113*, 34-49.
 16. Liu, J.; Liu, Q.; Yang, X.; Xu, S.; Zhang, H.; Bai, R.; Yao, H.; Jiang, J.; Shen, M.; Wu, X.; Xu, J., Design, synthesis, and biological evaluation of 1,2,4-triazole bearing 5-substituted biphenyl-2-sulfonamide derivatives as potential antihypertensive candidates. *Bioorganic and Medicinal Chemistry* **2013**, *21* (24), 7742-7751.
 17. Chouaïb, K.; Delemasure, S.; Dutartre, P.; Jannet, H. B., Microwave-assisted synthesis, anti-inflammatory and anti-proliferative activities of new maslinic acid derivatives bearing 1,5- and 1,4-disubstituted triazoles. *Journal of Enzyme Inhibition and Medicinal Chemistry* **2016**, *31* (2), 130-147.
 18. Youssif, B. G.; Mohamed, Y. A.; Salim, M. T.; Inagaki, F.; Mukai, C.; Abdu-Allah, H. H., Synthesis of some benzimidazole derivatives endowed with 1, 2, 3-triazole as potential inhibitors of hepatitis C virus. *Acta pharmaceutica* **2016**, *66* (2), 219-231.
 19. Kharb, R.; Sharma, P. C.; Yar, M. S., Pharmacological significance of triazole scaffold. *Journal of Enzyme Inhibition and Medicinal Chemistry* **2011**, *26* (1), 1-21.
 20. (a) Liu, X.-H.; Xu, X.-Y.; Tan, C.-X.; Weng, J.-Q.; Xin, J.-H.; Chen, J., Synthesis, crystal structure, herbicidal activities and 3D-QSAR study of some novel 1,2,4-triazolo[4,3-a]pyridine derivatives. *Pest Management Science* **2015**, *71* (2), 292-301;

- (b) Chai, B.; Qian, X.; Cao, S.; Liu, H.; Song, G., Synthesis and insecticidal activity of 1, 2, 4-triazole derivatives. *Arkivoc* **2003**, 2, 141-145.
21. Ramesh, R.; Lalitha, A., PEG-assisted two-component approach for the facile synthesis of 5-aryl-1,2,4-triazolidine-3-thiones under catalyst-free conditions. *RSC Advances* **2015**, 5 (63), 51188-51192.
22. Patil, J. D.; Pore, D. M., [C16MPy]AlCl₃Br: an efficient novel ionic liquid for synthesis of novel 1,2,4-triazolidine-3-thiones in water. *RSC Advances* **2014**, 4 (28), 14314-14319.
23. Mane, M. M.; Pore, D. M., A novel one pot multi-component strategy for facile synthesis of 5-aryl-[1,2,4]triazolidine-3-thiones. *Tetrahedron Letters* **2014**, 55 (48), 6601-6604.
24. Mukherjee, N.; Ahammed, S.; Bhadra, S.; Ranu, B. C., Solvent-free one-pot synthesis of 1,2,3-triazole derivatives by the 'Click' reaction of alkyl halides or aryl boronic acids, sodium azide and terminal alkynes over a Cu/Al₂O₃ surface under ball-milling. *Green Chemistry* **2013**, 15 (2), 389-397.
25. Al-Zaydi, K. M., A simplified green chemistry approaches to synthesis of 2-substituted 1,2,3-triazoles and 4-amino-5-cyanopyrazole derivatives conventional heating versus microwave and ultrasound as ecofriendly energy sources. *Ultrasonics Sonochemistry* **2009**, 16 (6), 805-809.
26. (a) Pagadala, R.; Maddila, S.; Moodley, V.; van Zyl, W. E.; Jonnalagadda, S. B., An efficient method for the multicomponent synthesis of multisubstituted pyridines, a rapid procedure using Au/MgO as the catalyst. *Tetrahedron Letters* **2014**, 55 (29), 4006-4010; (b) Narayana Maddila, S.; Maddila, S.; E. van Zyl, W.; B. Jonnalagadda, S., Ru-hydroxyapatite: an efficient and reusable catalyst for the multicomponent synthesis of pyranopyrazoles under facile green conditions. *Current Organic Synthesis* **2016**, 13 (6), 893-900; (c) Maddila, S. N.; Maddila, S.; van Zyl, W. E.; Jonnalagadda, S. B., Ceria-vanadia/silica-catalyzed cascade for C-C and C-O bond activation: green one-pot synthesis of 2-amino-3-cyano-4H-pyrans. *ChemistryOpen* **2016**, 5 (1), 38-42; (d) Shabalala, S.; Maddila, S.; van Zyl, W. E.; Jonnalagadda, S. B., A facile, efficacious and reusable Sm₂O₃/ZrO₂ catalyst for the novel synthesis of functionalized 1,4-dihydropyridine derivatives. *Catalysis Communications* **2016**, 79, 21-25; (e) N. Maddila, S.; Maddila, S.; E. van Zyl, W.; B. Jonnalagadda, S., Swift and Green Protocol for One-pot Synthesis of Pyrano[2,3- c]pyrazole-3-carboxylates With RuCaHAp as Catalyst. *Current Organic Chemistry* **2016**, 20 (20), 2125-2133; (f) Maddila, S. N.;

- Maddila, S.; Gangu, K. K.; van Zyl, W. E.; Jonnalagadda, S. B., Sm₂O₃/Fluoroapatite as a reusable catalyst for the facile, green, one-pot synthesis of triazolidine-3-thione derivatives under aqueous conditions. *Journal of Fluorine Chemistry* **2017**, *195*, 79-84;
- (g) Maddila, S. N.; Maddila, S.; van Zyl, W. E.; Jonnalagadda, S. B., Mn doped ZrO₂ as a green, efficient and reusable heterogeneous catalyst for the multicomponent synthesis of pyrano[2,3-d]-pyrimidine derivatives. *RSC Advances* **2015**, *5* (47), 37360-37366.
27. (a) Maddila, S.; Gorle, S.; Seshadri, N.; Lavanya, P.; Jonnalagadda, S. B., Synthesis, antibacterial and antifungal activity of novel benzothiazole pyrimidine derivatives. *Arabian Journal of Chemistry* **2016**, *9* (5), 681-687; (b) Maddila, S.; Naicker, K.; Momin, M. I. K.; Rana, S.; Gorle, S.; Maddila, S.; Yalagala, K.; Singh, M.; Koorbanally, N. A.; Jonnalagadda, S. B., Novel 2-(1-(substitutedbenzyl)-1H-tetrazol-5-yl)-3-phenylacrylonitrile derivatives: synthesis, in vitro antitumor activity and computational studies. *Medicinal Chemistry Research* **2016**, *25* (2), 283-291; (c) Maddila, S.; Naicker, K.; Gorle, S.; Rana, S.; Yalagala, K.; N. Maddila, S.; Singh, M.; Singh, P.; B. Jonnalagadda, S., New Pyrano[2,3-d:6,5-d']dipyrimidine Derivatives-Synthesis, in vitro Cytotoxicity and Computational Studies. *Anti-Cancer Agents in Medicinal Chemistry- Anti-Cancer Agents* **2016**, *16* (8), 1031-1037.
28. Razavi, N.; Akhlaghinia, B., Hydroxyapatite nanoparticles (HAp NPs): a green and efficient heterogeneous catalyst for three-component one-pot synthesis of 2,3-dihydroquinazolin-4(1H)-one derivatives in aqueous media. *New Journal of Chemistry* **2016**, *40* (1), 447-457.

Chapter 5: Solar Photocatalytic Degradation of *o*-Chloranil on Nanocrystalline Cellulose Doped Titania

5.1. Introduction

Environmental pollution is one of the major and uncontrolled hazards of the modern world.¹ Progress in agricultural, medicinal, and alternative energy fields are necessary in order to keep up with the needs and demands of an ever-growing anthropological population.² Greener processes are required for the creation of environmentally friendly products. However, at present, the focus of research should be shifted to the eradication and reduction of existing environmental pollutants and move toward a sustainable society where green chemistry processes and environmental remediation are necessary.³

There has been a remarkable increase in awareness of the toxic and carcinogenic effects of many polluting chemicals that were not considered hazardous only two decades ago.⁴ One such pollutant has been identified as *o*-chloranil (2,3,5,6-tetrachloro-2,5-cyclohexadiene-1,4-dione), which was observed as an oxidation by-product of pentachlorophenol (PCP).⁵ In the past, *o*-chloranil was used as a fungicide and algicide under the trade name Spergon.⁶ Control of organic pollutants in water sources is an important measure in environmental protection. Biodegradation pathways have garnered great attention amongst the proposed and developed processes for the elimination of organic contaminants.⁴

5.1.1. Photo-catalysis process

Photocatalysis, in general, represents the catalysis of a photochemical reaction at a solid surface interface, usually a semiconductor.⁷ This simplified definition, while correct and useful, conceals the fact that there must be at least two reactions occurring concurrently. The first involves oxidation from photogenerated holes, while the second involves reduction from photo-generated electrons. During both processes, there must be an equivalent balance in a precise order for the preservation of the photocatalyst (which is one of the basic requirements for a heterogeneous catalyst).^{7h,7j,8}

Heterogeneous photocatalysis has proved to be of existential interest as an efficient tool for degrading both aquatic and atmospheric organic contaminants. One of the major applications of heterogeneous catalysis is photocatalytic oxidation to effect partial or total mineralization of contaminants to benign substances.⁹ Photocatalytic degradation encompasses the use of certain

semiconductors as catalysts for the production of highly reactive radicals under light/solar irradiation.^{7f, 10}

5.1.2. Titania (TiO₂) as a photocatalyst

TiO₂, as a semiconductor is known to have a large band gap, high surface area and offers excellent stability. It can be regarded as non-toxic and has a highly porous (pores ranging from 2–50 nm in diameter (mesoporous)) framework.¹¹ This collection of characteristics makes it a suitable material for photocatalysis.^{11b} The structure of TiO₂ has distinctive physical–chemical implications, which allows for the transfer of electrons within the material, and enables the simple recovery of the catalyst.¹² TiO₂ possess a wide band gap energy (3.2 eV) and requires electromagnetic radiation with equal or higher photon energy to excite electrons within the valence band (VB) to the conduction band (CB). This photon induced excitation leaves behind holes within the VB. The recombination of electrons (e⁻) and holes (h⁺) initiates redox reactions which allows a molecular species to be absorbed on to the surface of the catalyst (TiO₂).¹³ Due to the wide band gap energy and high electron-hole recombination rate, only ultraviolet irradiation ($\lambda < 387$ nm) possesses enough energy to overcome these shortcomings. This limits the application of TiO₂ under visible light conditions. TiO₂ is typically doped with a support, which enhances the separation of electron-hole pairs and in turn reduces electron-hole recombination rates thereby increasing the photocatalytic efficiency of TiO₂ as a photocatalyst.¹⁴ The ideal support leads to a composite material which can act as a trap-site for the photo-generated electrons, which can prevent electron-hole recombination, and thereby improve photocatalytic activity.^{8b}

Photocatalysed oxidative mineralization is promising chemical process that leads to the degradation of organic pollutants.¹⁵ The photocatalytic oxidation based systems have been developed in order to take advantage of the method of hydroxyl radical (\cdot OH) production.¹⁶ Since TiO₂ is surrounded by adsorbed water in the air or if it is used in aqueous suspension, water molecules are likely oxidized first to \cdot OH by photogenerated positive holes and then they react with organic compounds to form oxidized species and/or decomposed products.¹⁷ During this process, carbonyl compounds and carboxylic acids are formed *via* the degradation step. In addition, the oxidative reaction alone is not rapid, thus the radical formation step is executed. The reaction of the \cdot OH with pollutants is a quick process, therefore, reaction conditions need

to be considered. The catalyst surface basicity and acidity plays an important role in the process (point of zero charge (PZC)).¹⁸

Due to its potential photonic use as a chiral nematic material, which leads to iridescent coloured films, NCC was chosen as a second phase in the nanocomposite.¹⁹ Chiral nematic NCC could alter the electron double layer, and in turn, increase the efficiency of TiO₂ as a photocatalyst by lowering the rate of electron recombination. Thus a nanocomposite NCC/TiO₂ could be used for photocatalytic decomposition of organic pollutants. This thesis demonstrates the facile fabrication of an NCC/TiO₂ nanocomposite hybrid by the adsorption of TiO₂ (anatase) nanoparticles on wood-derived nanocrystalline cellulose as well as the use of this hybrid in the photocatalytic degradation of *o*-chloranil.

5.2. Materials and Methods

5.2.1. Materials

Bleached pulp was provided by the CSIR, Durban, South Africa. Ethanol, sodium hydroxide pellets, sulfuric acid, and titanium(IV) oxide (anatase) were purchased from Sigma-Aldrich. *o*-Chloranil was purchased from BDH Chemicals (Merck). All chemicals were used as received. Double distilled water was used for all reactions and dialysis.

5.2.2. Photocatalytic study

The photodegradation of *o*-chloranil with a fixed absorbance of 0.3281 (a.u.) at a λ_{\max} of 298 nm was undertaken. The light source used was sunlight, to mimic real-world conditions (26 °C and clear day). A 2L, 10 ppm solution of *o*-chloranil was prepared and further sonicated for 10 mins to allow total dissolution of *o*-chloranil. Afterwards, 250 mL of the *o*-chloranil solution was added to an 800 mL beaker containing 100 mg of catalyst (Control, bare TiO₂, NCC/TiO₂ (10%, 20%, 40% and 80% w/w%) and pure NCC). Initial absorbance measurements were taken 60 min prior to investigation in a darkroom with set-up moved to the reaction site under lightless conditions. The reaction was stirred for 120 min with absorbance measurements taken every 20 mins.

5.2.3. Catalyst preparation

After blending cellulose obtained from BP with a domestic blender, NCCs were isolated using 20 mL/g 64 wt% sulfuric acid at 45 °C in an oil bath for 45 minutes to remove the amorphous regions. After the completion of the hydrolysis, the suspensions were repeatedly diluted and centrifuged at 6000 rpm for 10 min to reduce the sulfuric acid concentration. The suspensions were later sonicated using a UP400S Ultrasonic processor, Hielscher, Germany at 50% amplitude and 0.5 cycles for 15 minutes to ensure complete dispersion of NCCs before dialysis to near neutral pH. The obtained NCCs were denoted as NCC-BP.

The photocatalysts were prepared by the wet impregnation method by impregnating TiO₂ on NCC. TiO₂ (0.9, 0.8, 0.6 and 0.2 g) was suspended in 50 mL of deionized water with vigorous stirring for 30 min. Then, NCC (prepared, 0.1, 0.2, 0.4 and 0.8 g) was added with additional stirring for 1.0 h. Thereafter, the pH was adjusted to 8.5 using 0.1 M NaOH solution. The suspension was vigorously stirred for a further 2 h. The suspensions were heated at 60-70 °C for 2 h in solution. The samples were then sonicated, filtered and washed with deionized water. The suspensions were then dried at 90-100 °C overnight to obtain the 10%, 20%, 40, and 80% w/w% of NCC/TiO₂ catalysts.

5.2.4. Characterization Techniques

Mass Spectral Analysis

The GC-MS analysis was done in EI mode using a Perkin Elmer Clarus 400 Gas Chromatograph equipped with an EI mode mass spectra photometer and the spectra were recorded in the interval 35–500 amu. Specification of the column used was as follows: J & W DB5MS, 30m length, 250 µm diameter and 0.25 µm film thickness. Helium was used as carrier gas, and the temperature ramp program used during GC analysis was as follows: 50 °C (2min), 20 °Cmin⁻¹ to 300 °C (10 min).

The mass spectra were recorded on an Agilent 1100 LC/MSD instrument, with method API-ES, at 70 eV.

Optical Spectroscopic Analysis

The study of the materials was performed using a Perkin Elmer LS 55 fluorescence spectrophotometer, for which the samples were excited with a high photon energy at 310 nm. UV-visible diffuse reflectance spectra were recorded with an Ocean Optics high-resolution spectrometer (HR2000+) equipped with an integrating sphere accessory, using BaSO₄ as the reference material.

Fourier transform infrared spectroscopy

The identification of the NCC/TiO₂ catalysts were analysed by FTIR study in the range 380-4000 cm⁻¹ at a resolution of 4 cm⁻¹ using a Spectrum 100 infrared spectrometer equipped with universal attenuated total reflection (UATR) accessory Perkin Elmer, USA.

Morphological structure analysis

The morphological characterisation, dimensions and elemental composition of the NCC/TiO₂ catalyst were established with the aid of electron microscopic study using; JEOL 1010 transmission electron microscope (TEM), Japan and ZEISS Ultra Plus field emission gun scanning electron microscope (FEGSEM) equipped with energy dispersive x-ray (EDX) detector, Germany. The emission current using a tungsten (W) filament was 100 μA and the accelerator voltage was 12 kV. TEM images of all samples were acquired using the NCC/TiO₂ catalysts, which was deposited on the TEM-grid. The TEM-grids were also negatively stained with uranyl acetate to aid visualization of NCC with the NCC/TiO₂ catalysts matrix. Similarly, samples for SEM images were coated with gold with the aid of sputter coater to minimize charging.

X-ray diffraction analysis

Powder X-ray diffraction (XRD) analysis of the NCC/TiO₂ catalyst was conducted using an X-ray diffractometer (Bruker AXS D8 Advance, Germany), equipped with Cu-Kα radiation source (wavelength = 0.154 nm) operating at 40 kV and 40 mA. The XRD pattern of the catalyst was recorded over the angular range $2\theta = 10 - 90^\circ$ at room temperature.

Crystallite size (D_{hkl}) of the isolated NCC/TiO₂ were calculated using Scherrer's formula as shown in Equation 5.1 where λ is the X-ray wavelength (0.154 nm), β is the angular width at half maximum intensity determined with the aid of Gaussian fit of the peaks on the

diffractograms of the isolated NCC and θ is the Bragg angle. The crystallographic plane adopted for the estimation was 101.

$$D_{hkl} \text{ (nm)} = 0.94\lambda/\beta \cos \theta \quad (5.1)$$

Specific surface area and porosity measurements

The nitrogen adsorption-desorption isotherms of the degassed samples (at 100 °C under vacuum for 24 h using Micromeritics VacPrep 061 sample degas system, USA) were measured at a bath temperature of -195.8 °C (77.2 K) using a surface area and porosity analyzer, Micromeritics Tristar II 3020 2.00, USA. Specific surface areas were calculated from the linear region of the isotherms using the Brunauer–Emmett–Teller (BET) equation in a relative P/P_o pressure range of 0.058 - 0.8. Pore size distributions were derived from the adsorption branch of the isotherms by Barrett–Joyner–Halenda (*BJH*) method. The total pore volumes were estimated from the amount adsorbed at a relative pressure of $P/P_o = 0.996$.

5.3. Results and Discussion

FT-IR analysis

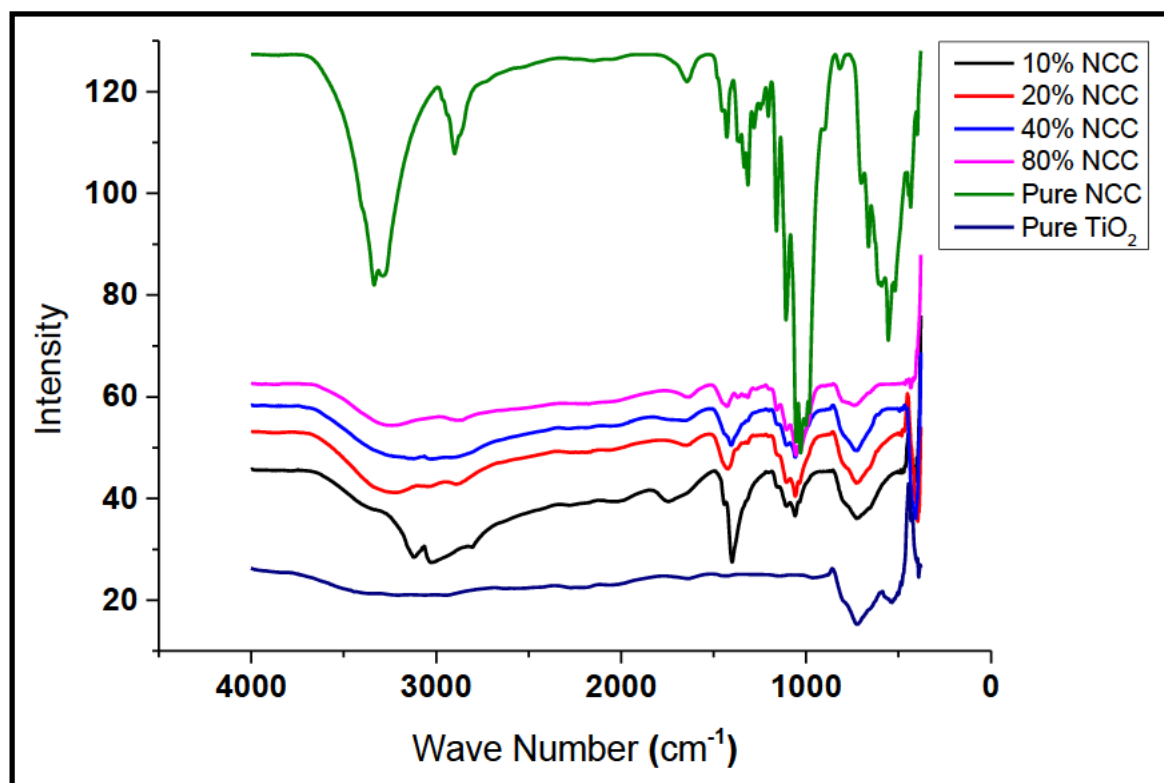


Figure 5.1. ATR-FTIR spectra of prepared NCC/TiO₂ photo-catalysts

The FT-IR spectra of the prepared NCC/TiO₂ photo-catalysts and pure NCC and pure TiO₂ are shown in Figure 5.1. The sequences of bands seen in these spectra correspond to the various lattice vibrational modes of NCC and TiO₂. The peaks at 1030 and 1415 cm⁻¹ display C-H₃ and O-H vibrational stretching modes which were attributed to the presence of NCC.²⁰ The two bands at 599 cm⁻¹ and 776 cm⁻¹ correspond to the presence of TiO₂.²¹ The broad absorption bands in the range of 3000–3441 cm⁻¹ are attributed to surface hydroxyl group peaks. The sharp peaks at 1628 cm⁻¹ can be attributed to absorbed water.²²

BET surface and elemental analysis

The N₂ sorption study was carried out over bare TiO₂ and NCC doped TiO₂ catalysts (Figure 5.2). N₂ sorption resulted in typical type IV isotherm, with a narrow H₂ hysteresis loop (IUPAC) lying in the P/P_0 range of 0.85–0.95, demonstrating mesoporous character.²³

Table 5.1. Surface area and pore volumes of synthesized catalysts.

Catalyst	Surface area m²/g	Pore Volume cm³/g
Pure Titania	8.6	0.104178
10% NCC/Titania	10.6	0.04967
20% NCC/Titania	10.1	0.059678
40% NCC/Titania	10.6	0.069155
80% NCC/Titania	2.0	0.029933

The BET surface areas of bare TiO₂, 10%, 20 %, 40 %, and 80% NCC/TiO₂ catalysts were found to be 8.6, 10.6, 10.1, 10.6, 2.0 m².g⁻¹, respectively. This may be attributed to the macropores caused by particle-particle porosity (inter-particle porosity). The catalysts also exhibit a step increase at this relative pressure range due to the filling of interparticle macropores of the catalyst with the nitrogen.²⁴ The isotherms and pore size distributions remained essentially the same over the range of NCC concentration which means that the NCC-containing species did not drastically disturb the pore structure of TiO₂.²⁵ It is evident from these results that there was a moderate change in the surface area from the TiO₂ to NCC doped TiO₂ catalyst. A drastic decrease in surface area and pore volume is observed as the NCC dopant becomes the major component (Table 5.1), which is attributed to the near non-porous NCC.

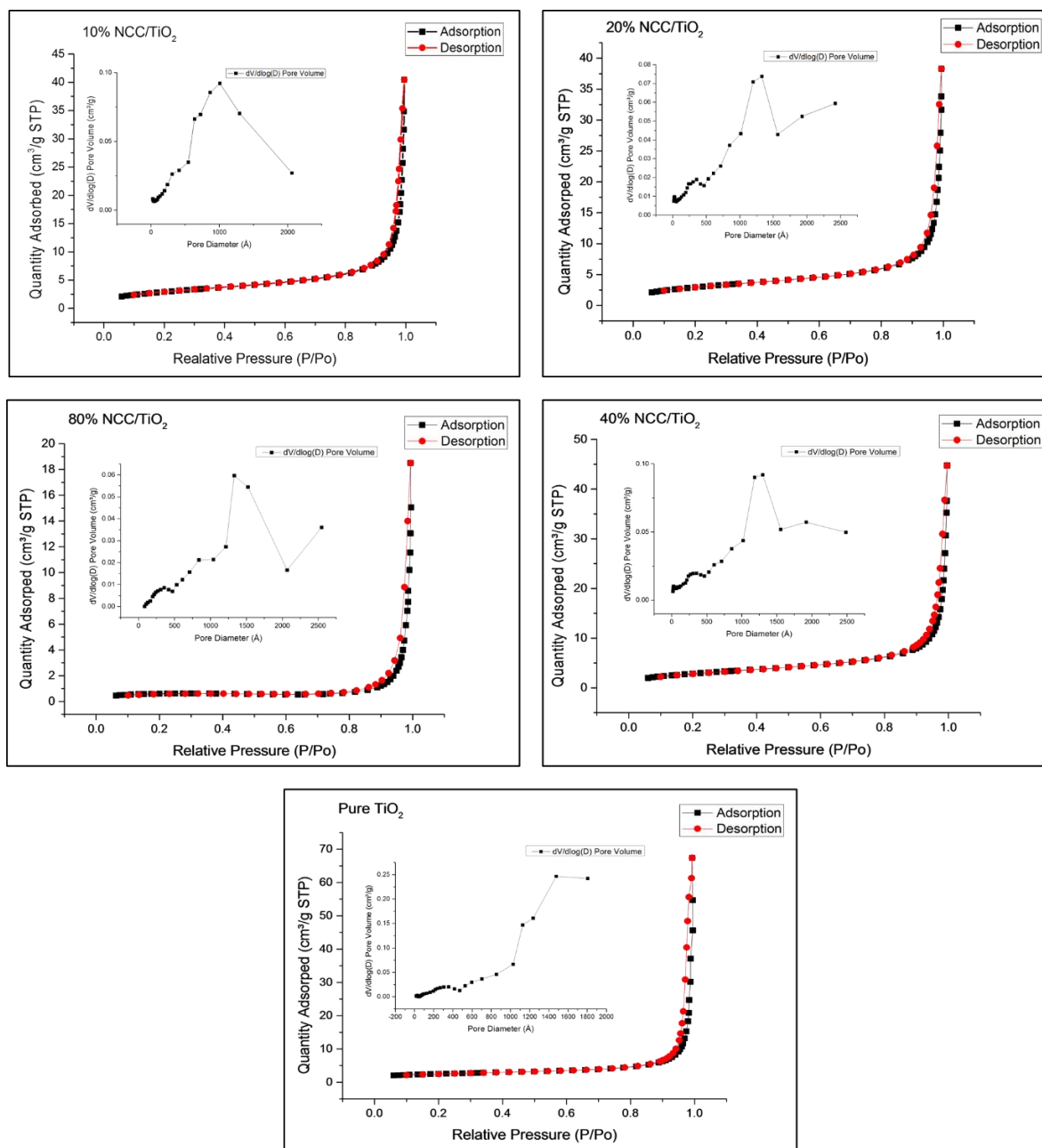


Figure 5.2. N₂ adsorption-desorption isotherm plots of synthesized catalysts with pore volume density (insets)

SEM and TEM analysis

The transition electron microscopy (TEM) micrographs of bare TiO₂, 10%, 20%, 40%, and 80% NCC/TiO₂ catalysts (Figure 5.3) showed disc-shaped particles with sizes ranging between 100 – 130 nm in length (Figure 5.4). The size of TiO₂ particles deposited on the NCC catalysts showed no significant changes when compared to the neat TiO₂ particles, however, strand/bone like NCC particles are evident upon staining of samples (Figure 5.3b, 5.3d, 5.3f and 5.3h). Sizes of NCC rods ranged between 100 – 250 nm in length which coincides with NCC

parameters (Chapter 3, Table 3.2). With the introduction of NCC into the TiO_2 matrix, the spherical particles appeared to have aggregated, forming clusters and colonizing the NCC particles. This aggregation is attributed to the interactions of NCC/ TiO_2 and NCC/NCC during the drying of the catalyst.²⁶

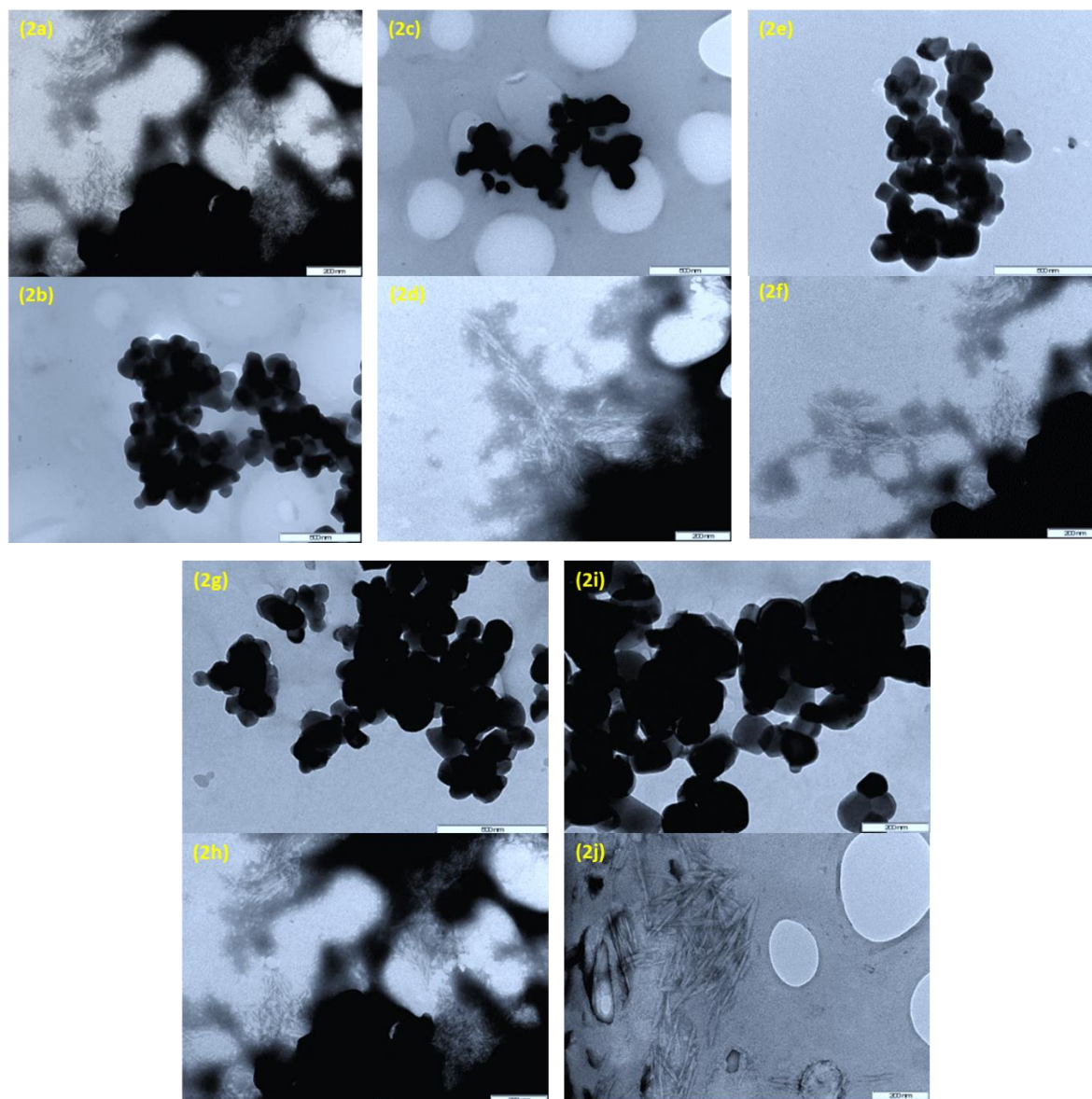


Figure 5.3. TEM micrographs of unstained and stained 10% (2a-2b), 20% (2c-2d), 40% (2e-2f) and 80% (2g-2h) NCC/ TiO_2 catalysts. Bare TiO_2 (2i) and NCC (2j) are shown.

The particles are large with an elliptical irregular shape which is perceived from the high magnification of SEM micrograph (Figure 5.5). The micrographs show that the TiO_2 particles are in an aggregative state and adhere to NCC rods. A homogeneous distribution of smaller TiO_2 particles is seen on the surface of larger TiO_2 particles (Figure 5.5g-h). This is quantified

by the EDS mapping (Figure 5.6). Furthermore, the morphology of the catalyst points to a semi-crystalline and homogenous sample.

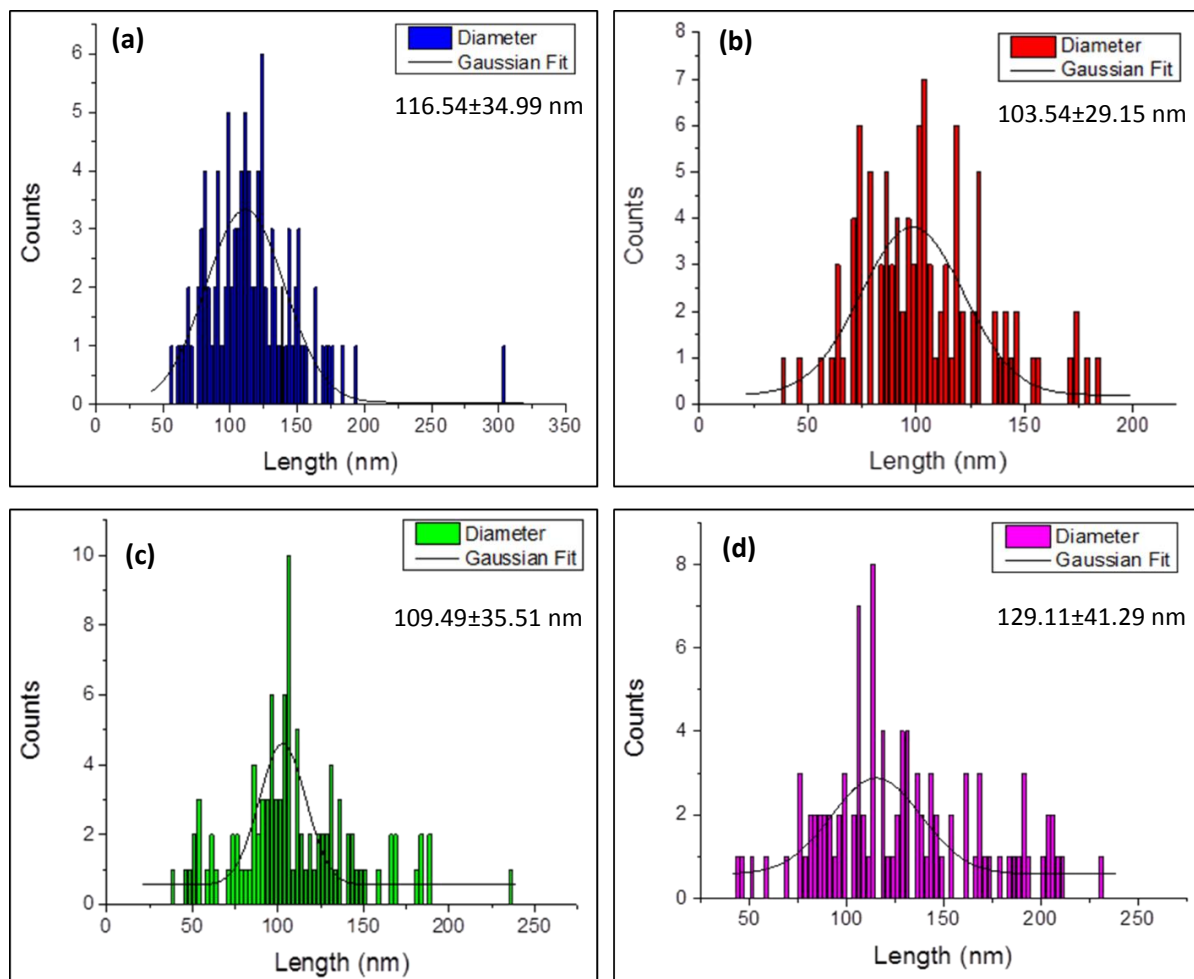


Figure 5.4. Particle size distribution graphs of 10% (a), 20% (b), 40% (c) and 80% (d) NCC/TiO₂ catalysts.

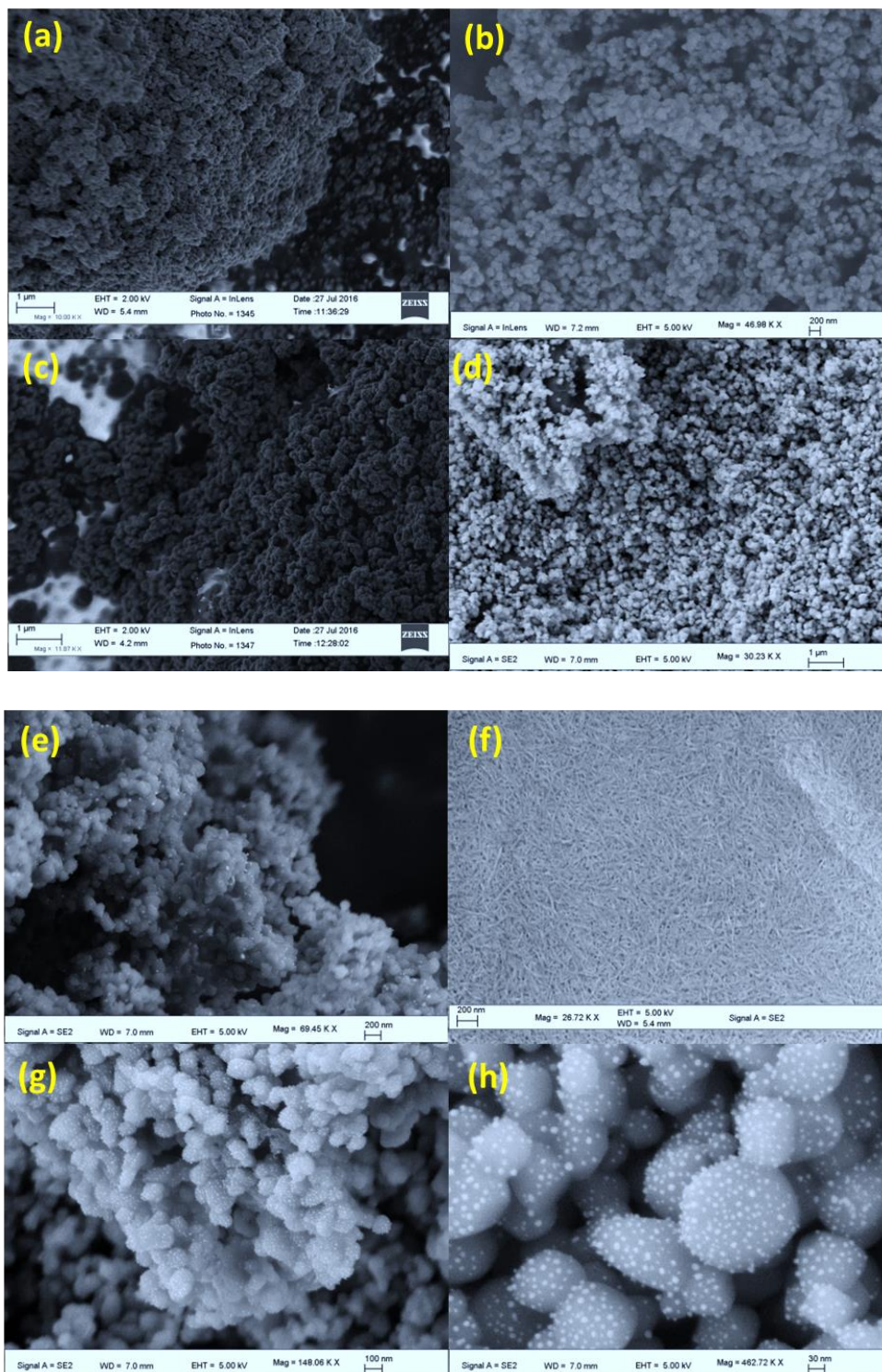


Figure 5.5. SEM micrographs of 10%, 20%, 40% and 80% (a-d) NCC/TiO₂ catalysts. Bare TiO₂ (e) and NCC (f). Magnification of 20% catalyst (g-h)

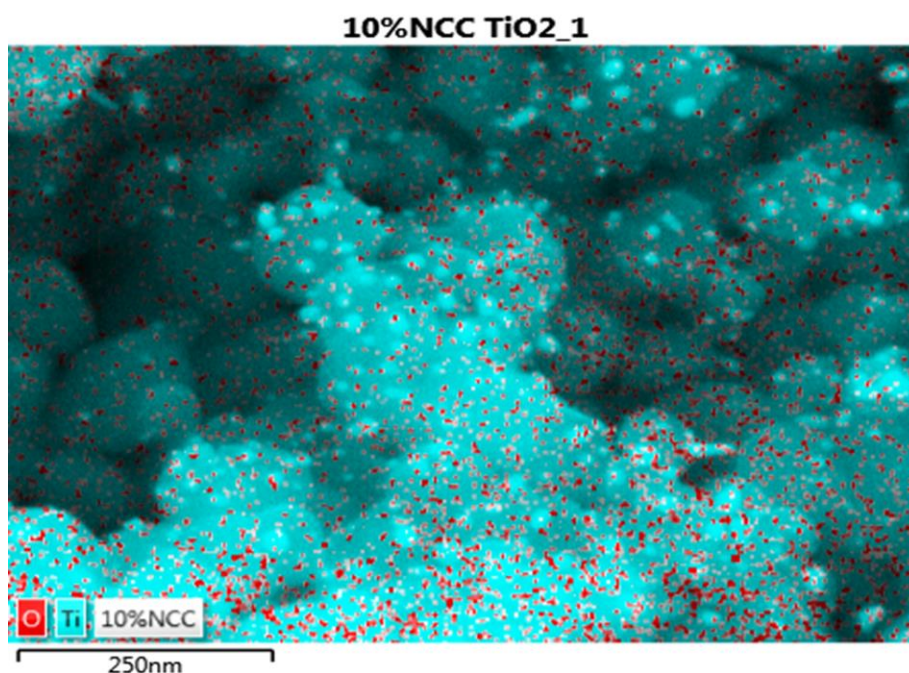


Figure 5.6. SEM-EDX mapping of 10% NCC/TiO₂.

XRD analysis

The prepared catalysts show the presence of the TiO₂ anatase phases. The diffraction peaks located at $2\theta = 25.2^\circ$, 37.9° , 48.0° and 62.0° are indexed to (101), (004), (200) and (204) planes of anatase phase TiO₂.²⁷ The anatase phase of TiO₂ correlates with those of literature.⁹ The increase in NCC loading was observed by slight peak shift in the XRD diffractogram at $2\theta = 16^\circ$ and 22° . By increasing in NCC loading, there is no evidence of an increase in the NCC peaks. This is largely attributed to the high crystallinity of TiO₂, which mask the NCC peaks. The average crystallite size of the catalysts was determined according to the Scherrer equation (Equation 5.1) using the full-width at half-maximum (FWHM) of the peak corresponding to the 101 reflection and taking into account the instrument broadening. It was found that the sizes for the 10%, 20%, 40% and 80% loadings were *ca.* 44.4, 44.0, 27.6 and 16.6 nm respectively. The decrease in crystallite size is attributed to the ultra-sonication of catalysts prior to the drying step, which may cause the fracture to crystallites. This estimation shows that with an increase in NCC loading, a corresponding decrease in crystallite size is observed. The increase in NCC loading leads to an increase in the dispersion of the TiO₂. This increase in dispersion allows for a greater fracture in the catalyst.²⁸

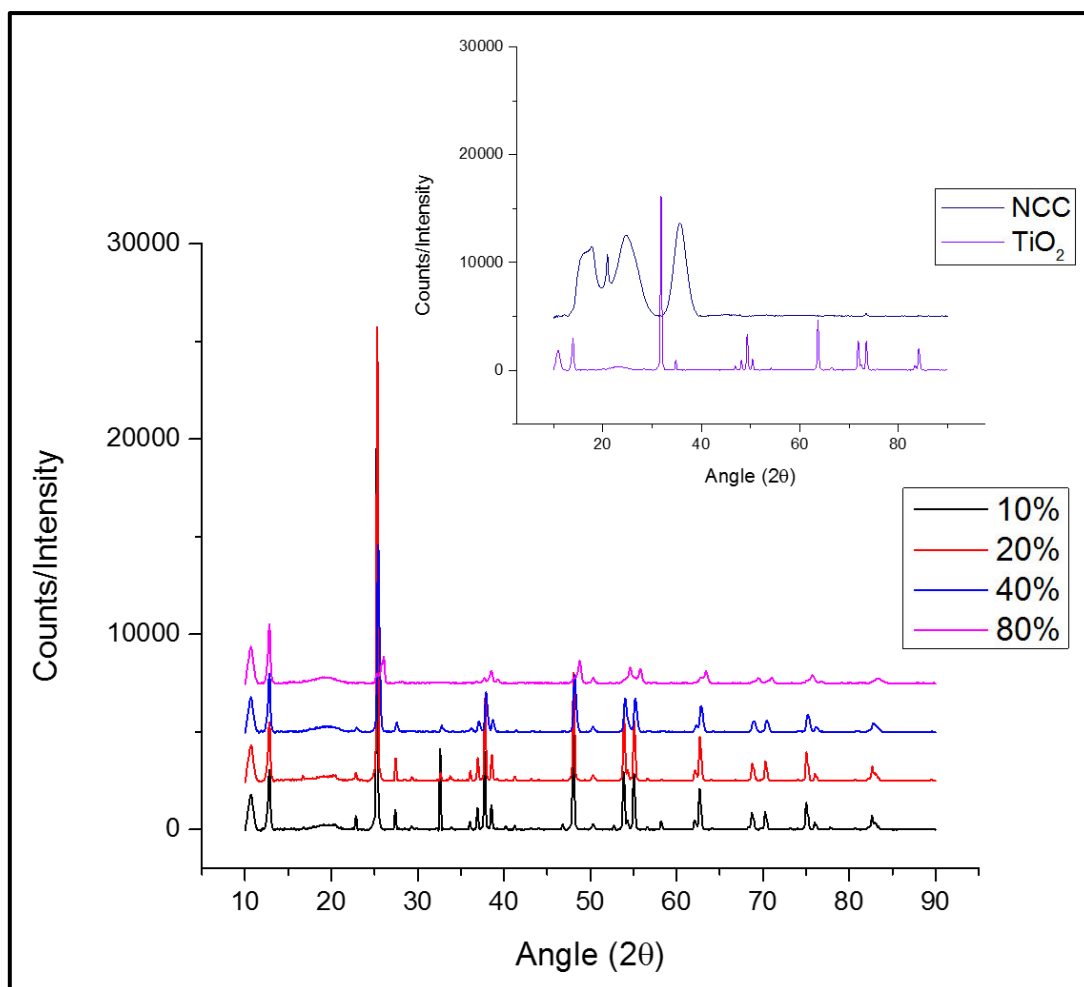


Figure 5.7. The PXRD pattern of (inset) pure NCC Bare TiO₂ (anatase), 10%, 20%, 40% and 80% NCC–TiO₂.

UV-diffuse reflectance spectra

The dense absorption band at nearly 372 nm (Figure 5.8) conforms to a band-gap energy of 3.21 eV calculated from the formula $E_g = 1239.8/\lambda$.^{7h, 29} Upon doping with NCC, a red-shift was detected which could foster the photocatalytic activities of the catalyst under visible light.

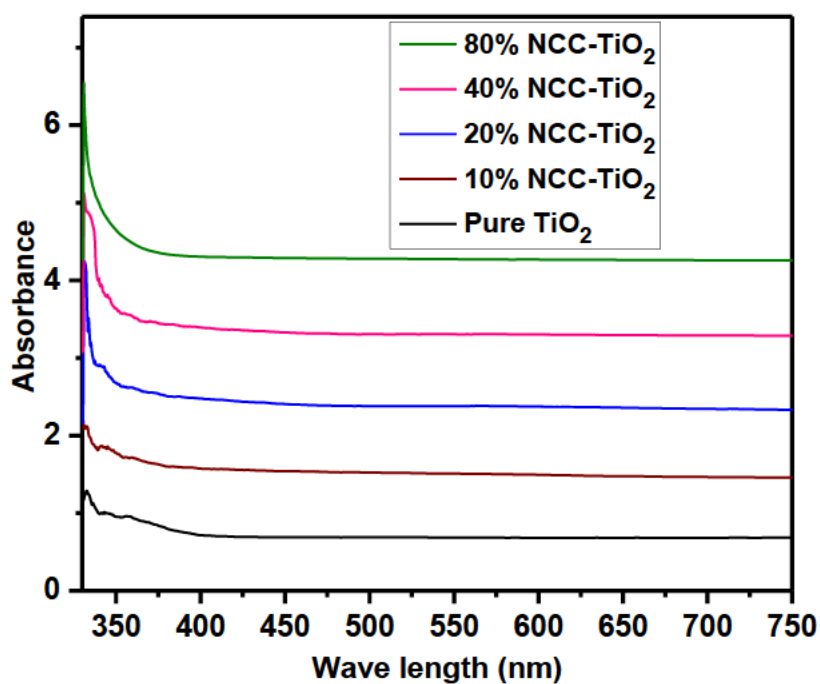


Figure 5.8. UV-DRS of bare TiO₂ and synthesized (% w/w) NCC doped TiO₂ catalysts

Photoluminescence spectra

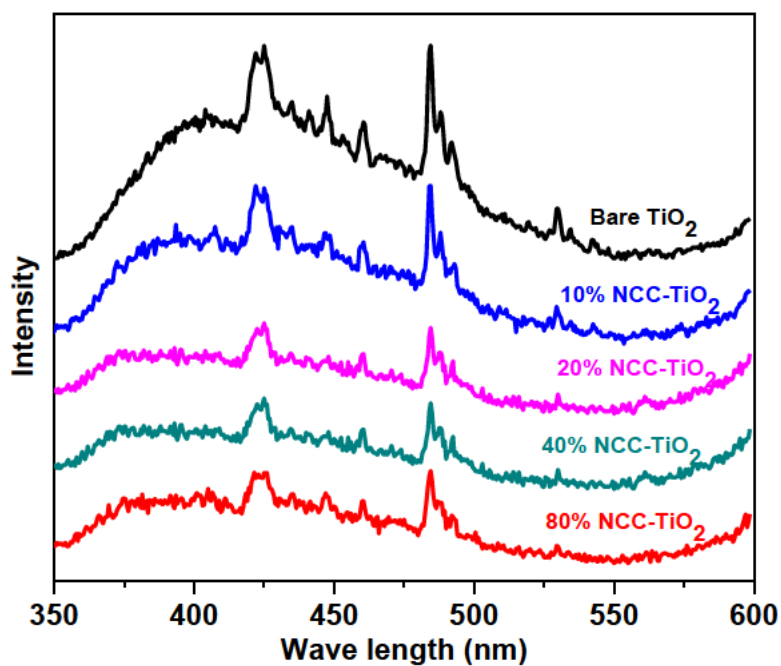


Figure 5.9. Photoluminescence spectra of bare TiO₂ and synthesized (% w/w) NCC doped TiO₂ catalysts

The PL spectra (Figure 5.9) of NCC/TiO₂ samples range between 350–500 nm with an excitation wavelength of 360 nm. The PL spectra might be closely related to the recombination of photoinduced electrons and holes, and free and self-trapped excitons, which possibly generate from surface defects in the TiO₂ crystals, such as lattice distortions and surface oxygen deficiencies.¹⁷ The spectra illustrate that with the increase of NCC loading, a decrease in intensity is seen. This indicates the reduction of the recombination centres for the electrons and holes in the samples. This suggests that the NCC/TiO₂ catalysts lead to low rates of electron-holes recombination under light irradiation and may show better photocatalytic activity than bare TiO₂.^{17d}

Catalyst loading concentration

The 20% NCC-TiO₂ photocatalyst loading was increased from 50 mg/L to 200 mg/L (Figure 5.10). The 100 mg/L catalyst load was the most efficient for *o*-chloranil photo-degradation. When the catalyst concentration increases, the reaction rate decreases. This may be due to the lack of accessibility of sufficient catalytic active sites on the catalyst material surface and also the penetration of light into the suspension.

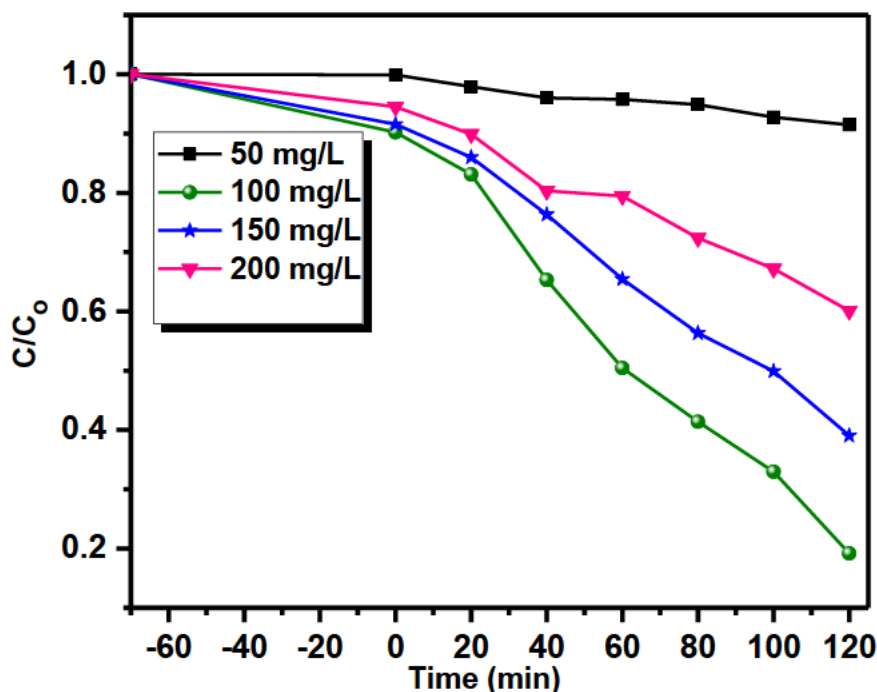


Figure 5.10. Influence of the amount of catalyst loading on the *o*-chloranil photo-degradation.

Degradation of *o*-chloranil

Figure 5.11 shows degradation of *o*-chloranil as a function of time using the synthesized catalysts, bare NCC and pure TiO₂ under visible light, after equilibrating in dark conditions for 60 min. The catalyst of NCC/TiO₂ with 20% NCC doping displays the highest photocatalytic activity due to the ability of nanocellulose assisting in the seizure of electrons to achieve a higher photocatalytic activity with a suitable doping concentration.^{7h, 7j}

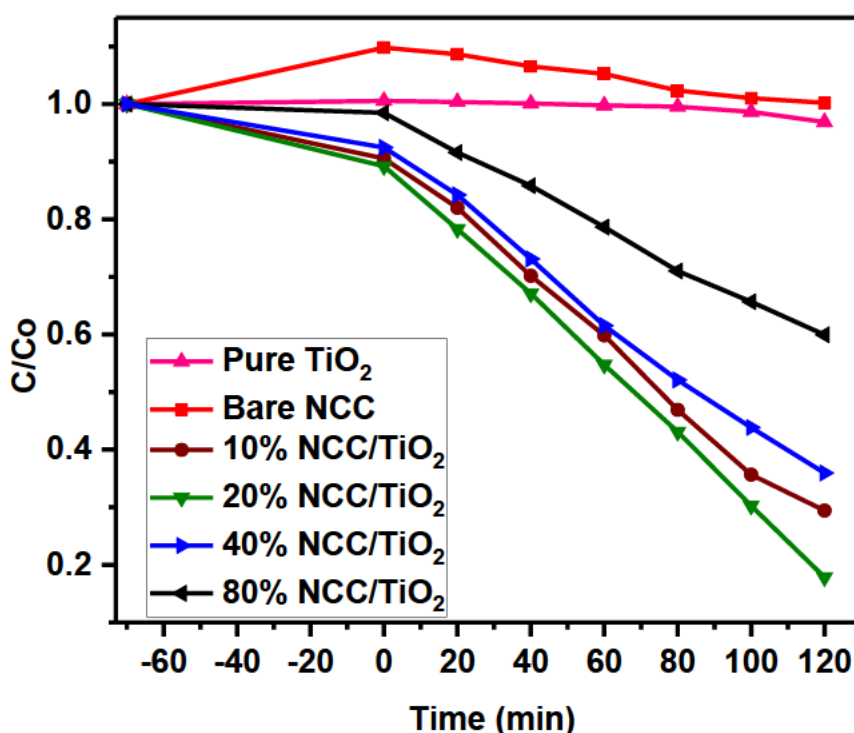


Figure 5.11. The photo-degradation *o*-chloranil as a function of time

With an increase in the concentration of cellulose dopant, the recombination of photogenerated electron-hole pairs may result, leading to a decrease in the photocatalytic activity. Therefore, a higher loading of NCC > 20 wt% was not required.

Identification of products

All the photo-catalyzed investigations were accompanied by exposing the reaction mixture to visible light. The organic portion of the reaction mixture was extracted and analyzed after every reaction with 20 min intervals. Three products were identified by gas chromatography (GC) after 120 min (Figure. 5.12a).

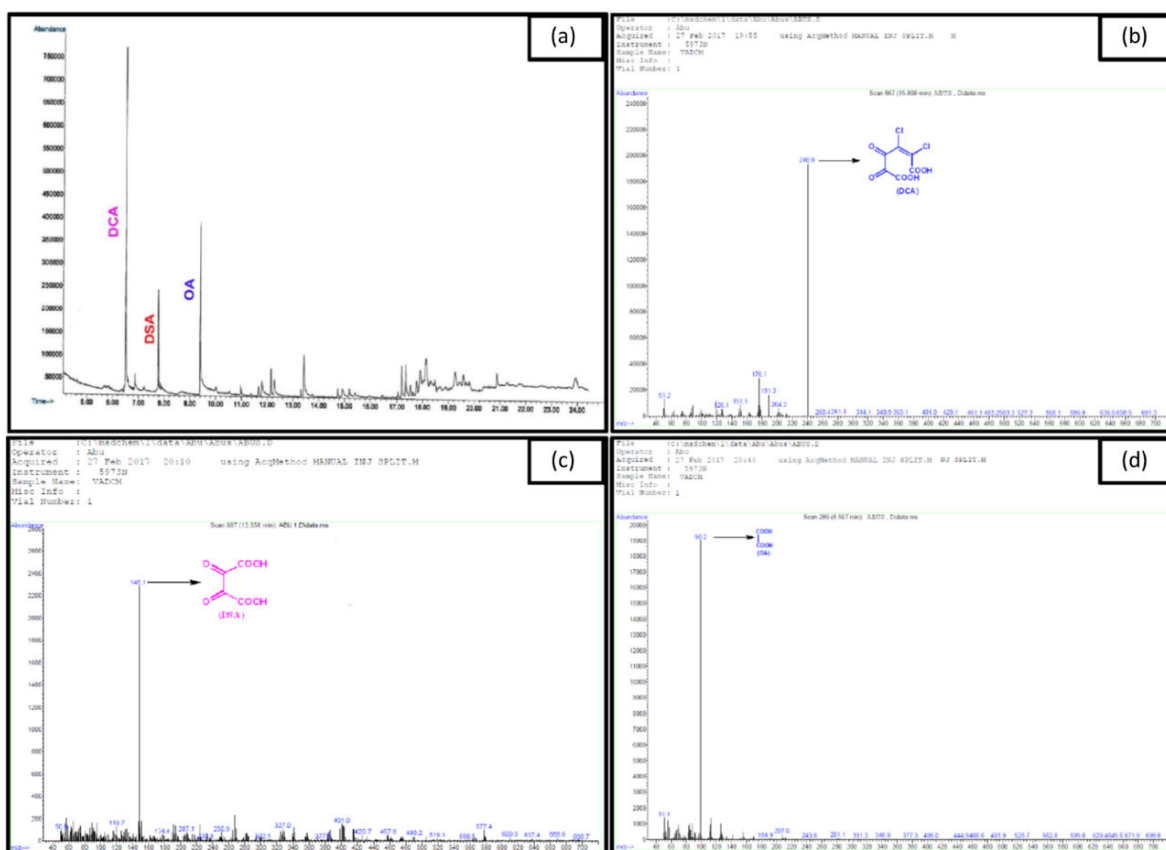
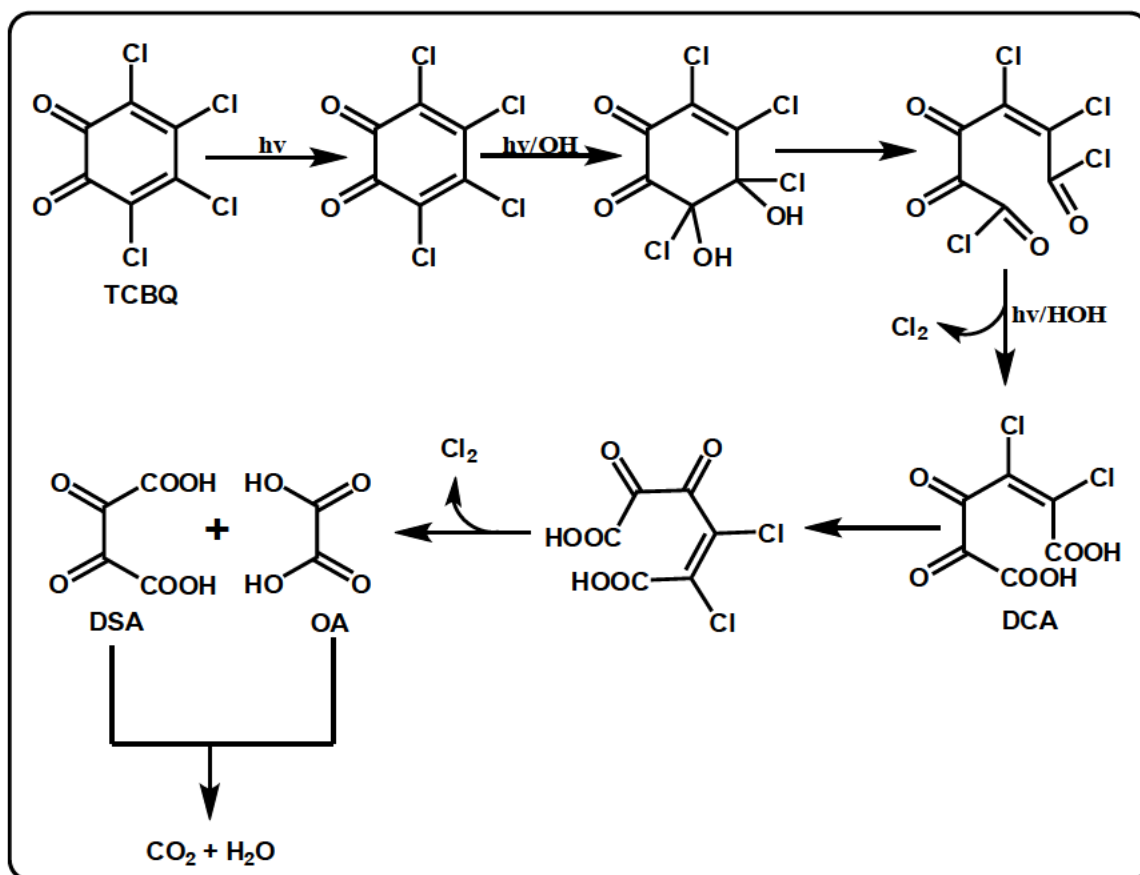


Figure 5.12. Degradation products confirmed by Gas Chromatography (5.12a) and LC mass spectra of degradation products (5.12b, 5.12c and 5.12d)

After GC-MS injection peaks were observed with retention times at 15.807, 13.558 and 8.507 minutes were confirmed and refer to the compounds of 2,3-dichloro-4,5-dioxohex-2-enedioic acid (DCA), 2,3-dioxosuccinic acid (DSA) and oxalic acid (OA), respectively. Furthermore, the formation of these products was confirmed by LC-MS with their respective (M^+) m/z values (Figure 5.12b, 5.12c and 5.12d).

Reaction mechanism

Based on the aforementioned results, a possible reaction mechanism (Scheme 5.1) for the photocatalytic degradation of *o*-chloranil is proposed.



Scheme 5.1. The proposed mechanism for the photo-degradation *o*-chloranil.

In an aromatic substituted compound, chloro functional groups are electron withdrawing groups,³⁰ this reduction in electron density on the carbon makes it susceptible to attack by the hydroxyl radical. The attack by the hydroxyl radical leads to the elimination of chlorides and a subsequent ring opening. A further attack by the $\cdot\text{OH}$ causes the formation of an aliphatic acid. The short-lived intermediate, DCA, favours the electrophilic substitution of $\cdot\text{OH}$ at the supplementary chloro position and forms a dechlorinated species through photo-oxidation. The further oxidation of the intermediate by $\cdot\text{OH}$ leads to oxygenated aliphatic compounds and formation of degraded aliphatic carboxylic acids. Two aliphatic acids (DSA and OA) were identified in this study. Further oxidation of these acid products leads to complete mineralization, to the final products of CO_2 and H_2O .

5.4. Conclusion

It was shown that NCC doped TiO₂ could efficiently catalyze the solar photodegradation and mineralization of the pollutant of *o*-chloranil in the presence of light. Using a wet-impregnation method, materials with different loadings of NCC on TiO₂ catalysts were prepared successfully and fully characterized. NCC doping on TiO₂ potentially captured the photo-holes, retarding the recombination of photogenerated electron-hole pairs relative to pure TiO₂. Overall 20 w/w% NCC/TiO₂ proved to be an ideal catalyst for solar photocatalysed degradation of *o*-chloranil. These outcomes show that the rate of degradation can be influenced by the various parameters such as substrate concentration and photocatalyst loading. The intermediate product (DCA) formed during the process could be responsible for the slow mineralization of the model pollutant and is also a useful source of information for the degradation pathway. The investigations suggest that DCA, DSA and OA are the main intermediates formed during the photodegradation of the model contaminant. Thus NCC/TiO₂ could be employed as a photocatalyst in the degradation of harmful contaminants.

5.5. References

1. Suk, W. A.; Murray, K.; Avakian, M. D., Environmental hazards to children's health in the modern world. *Mutation Research/Reviews in Mutation Research* **2003**, *544* (2), 235-242.
2. Colby, M. E., Environmental management in development: the evolution of paradigms. *Ecological Economics* **1991**, *3* (3), 193-213.
3. Fiksel, J., Designing resilient, sustainable systems. *Environmental Science & Technology* **2003**, *37* (23), 5330-5339.
4. Dincer, I., Energy and environmental impacts: present and future perspectives. *Energy Sources* **1998**, *20* (4-5), 427-453.
5. Ricotta, A.; Unz, R. F.; Bollag, J.-M., Role of a Laccase in the Degradation of Pentachlorophenol. *Bulletin of Environmental Contamination and Toxicology* **1996**, *57* (4), 560-567.
6. Basler, A., Dioxins and related compounds. *Environmental Science and Pollution Research* **1995**, *2* (2), 117-121.
7. (a) Pelizzetti, E.; Serpone, N., *Homogeneous and heterogeneous photocatalysis*. Springer Science & Business Media: **2012**; Vol. 174; (b) Serpone, N.; Pelizzetti, E., *Photocatalysis: fundamentals and applications*. Wiley-Interscience: **1989**; (c) Kamat, P. V., Photochemistry on nonreactive and reactive (semiconductor) surfaces. *Chemical Reviews* **1993**, *93* (1), 267-300; (d) Ollis, D. F.; Al-Ekabi, H., Photocatalytic purification and treatment of water and air. *Proceedings of the 1st International Conference on TiO₂ Photocatalytic Purification and Treatment of Water and Air*, London, Ontario, Canada, 8-13 November, 1992. Elsevier Science Ltd: **1993**; (e) Heller, A., Chemistry and Applications of Photocatalytic Oxidation of Thin Organic Films. *Accounts of Chemical Research* **1995**, *28* (12), 503-508; (f) Hoffmann, M. R.; Martin, S. T.; Choi, W.; Bahnemann, D. W., Environmental Applications of Semiconductor Photocatalysis. *Chemical Reviews* **1995**, *95* (1), 69-96; (g) Mills, A.; Le Hunte, S., An overview of semiconductor photocatalysis. *Journal of Photochemistry and Photobiology A: Chemistry* **1997**, *108* (1), 1-35; (h) Fujishima, A.; Hashimoto, K.; Watanabe, T., *TiO₂ photocatalysis: fundamentals and applications*. BKC Incorporated: **1999**; (i) Tryk, D. A.; Fujishima, A.; Honda, K., Recent topics in photoelectrochemistry: achievements and future prospects. *Electrochimica Acta* **2000**, *45* (15), 2363-2376; (j) Fujishima, A.; Zhang, X., Titanium dioxide photocatalysis:

- present situation and future approaches. *Comptes Rendus Chimie* **2006**, *9* (5–6), 750-760; (k) Fujishima, A.; Zhang, X.; Tryk, D. A., Heterogeneous photocatalysis: From water photolysis to applications in environmental cleanup. *International Journal of Hydrogen Energy* **2007**, *32* (14), 2664-2672.
8. (a) Fujishima, A.; Rao, T. N.; Tryk, D. A., Titanium dioxide photocatalysis. *Journal of Photochemistry and Photobiology C: Photochemistry Reviews* **2000**, *1* (1), 1-21; (b) Fujishima, A.; Zhang, X.; Tryk, D. A., TiO₂ photocatalysis and related surface phenomena. *Surface Science Reports* **2008**, *63* (12), 515-582.
 9. Chetty, E. C.; Dasireddy, V. B.; Maddila, S.; Jonnalagadda, S. B., Efficient conversion of 1,2-dichlorobenzene to mucochloric acid with ozonation catalyzed by V₂O₅ loaded metal oxides. *Applied Catalysis B: Environmental* **2012**, *117–118*, 18-28.
 10. Zhang, Y.-G.; Ma, L.-L.; Li, J.-L.; Yu, Y., In Situ Fenton Reagent Generated from TiO₂/Cu₂O Composite Film: a New Way to Utilize TiO₂ under Visible Light Irradiation. *Environmental Science & Technology* **2007**, *41* (17), 6264-6269.
 11. (a) Lorret, O.; Francová, D.; Waldner, G.; Stelzer, N., W-doped titania nanoparticles for UV and visible-light photocatalytic reactions. *Applied Catalysis B: Environmental* **2009**, *91* (1), 39-46; (b) Pekakis, P. A.; Xekoukoulotakis, N. P.; Mantzavinos, D., Treatment of textile dyehouse wastewater by TiO₂ photocatalysis. *Water Research* **2006**, *40* (6), 1276-1286.
 12. Ibhaddon, A.; Fitzpatrick, P., Heterogeneous Photocatalysis: Recent Advances and Applications. *Catalysts* **2013**, *3* (1), 189.
 13. (a) Fox, M. A.; Dulay, M. T., Heterogeneous photocatalysis. *Chemical Reviews* **1993**, *93* (1), 341-357; (b) Tamaki, Y.; Furube, A.; Murai, M.; Hara, K.; Katoh, R.; Tachiya, M., Direct Observation of Reactive Trapped Holes in TiO₂ Undergoing Photocatalytic Oxidation of Adsorbed Alcohols: Evaluation of the Reaction Rates and Yields. *Journal of the American Chemical Society* **2006**, *128* (2), 416-417.
 14. Venkatachalam, N.; Palanichamy, M.; Murugesan, V., Sol-gel preparation and characterization of alkaline earth metal doped nano TiO₂: Efficient photocatalytic degradation of 4-chlorophenol. *Journal of Molecular Catalysis A: Chemical* **2007**, *273* (1), 177-185.
 15. Javier Benitez, F.; Acero, J. L.; Real, F. J., Degradation of carbofuran by using ozone, UV radiation and advanced oxidation processes. *Journal of Hazardous Materials* **2002**, *89* (1), 51-65.

16. Farré, M. J.; Franch, M. I.; Malato, S.; Ayllón, J. A.; Peral, J.; Doménech, X., Degradation of some biorecalcitrant pesticides by homogeneous and heterogeneous photocatalytic ozonation. *Chemosphere* **2005**, *58* (8), 1127-1133.
17. (a) Jaeger, C. D.; Bard, A. J., Spin trapping and electron spin resonance detection of radical intermediates in the photodecomposition of water at titanium dioxide particulate systems. *The Journal of Physical Chemistry* **1979**, *83* (24), 3146-3152; (b) Hiroyuki, N.; Kazuo, O.; Hiroaki, O.-N.; Hitoshi, K., Efficient Hydroxyl Radical Production and Their Reactivity with Ethanol in the Presence of Photoexcited Semiconductors. *Bulletin of the Chemical Society of Japan* **1994**, *67* (8), 2031-2037; (c) Riegel, G.; Bolton, J. R., Photocatalytic Efficiency Variability in TiO₂ Particles. *The Journal of Physical Chemistry* **1995**, *99* (12), 4215-4224; (d) Nosaka, Y.; Komori, S.; Yawata, K.; Hirakawa, T.; Nosaka, A. Y., Photocatalytic ·OH radical formation in TiO₂ aqueous suspension studied by several detection methods. *Physical Chemistry Chemical Physics* **2003**, *5* (20), 4731-4735.
18. (a) Hu, J. Y.; Wang, Z. S.; Ng, W. J.; Ong, S. L., The effect of water treatment processes on the biological stability of potable water. *Water Research*. **1999**, *33* (11), 2587-2592; (b) Chetty, E. C.; Maddila, S.; Southway, C.; Jonnalagadda, S. B., Ozone Initiated Ni/Metal Oxide Catalyzed Conversion of 1,2-Dichlorobenzene to Mucochloric Acid in Aqueous Solutions. *Industrial & Engineering Chemistry Research* **2012**, *51* (7), 2864-2873.
19. (a) Kelly, J. A.; Giese, M.; Shopsowitz, K. E.; Hamad, W. Y.; MacLachlan, M. J., The development of chiral nematic mesoporous materials. *Accounts of Chemical Research* **2014**, *47* (4), 1088-1096; (b) Zhou, Y.; Fuentes-Hernandez, C.; Khan, T. M.; Liu, J.-C.; Hsu, J.; Shim, J. W.; Dindar, A.; Youngblood, J. P.; Moon, R. J.; Kippelen, B., Recyclable organic solar cells on cellulose nanocrystal substrates. *Scientific Reports* **2013**, *3*, 1536.
20. Kumar, A.; Negi, Y. S.; Choudhary, V.; Bhardwaj, N. K., Characterization of cellulose nanocrystals produced by acid-hydrolysis from sugarcane bagasse as agro-waste. *Journal of Materials Physics and Chemistry* **2014**, *2* (1), 1-8.
21. (a) Nakamoto, K., Infrared and Raman spectra of inorganic and coordination compounds. In *Handbook of Vibrational Spectroscopy*, John Wiley & Sons, Ltd: **2006**; (b) Nyquist, R. A.; Kagel, R. O., *Handbook of infrared and raman spectra of inorganic compounds and organic salts: infrared spectra of inorganic compounds*. Academic press: **2012**; Vol. 4.

22. Tang, Y.; Yang, S.; Zhang, N.; Zhang, J., Preparation and characterization of nanocrystalline cellulose *via* low-intensity ultrasonic-assisted sulfuric acid hydrolysis. *Cellulose* **2014**, *21* (1), 335-346.
23. Kamiya, Y.; Nishikawa, E.; Satsuma, A.; Yoshimune, M.; Okuhara, T., Highly porous vanadium phosphorus oxides derived from vanadyl n-butylphosphate. *Microporous Mesoporous Mater.* **2002**, *54* (3), 277-283.
24. Bhattacharyya, K.; Varma, S.; Tripathi, A. K.; Bharadwaj, S. R.; Tyagi, A. K., Effect of vanadia doping and its oxidation state on the photocatalytic activity of TiO₂ for gas-phase oxidation of ethene. *The Journal of Physical Chemistry C* **2008**, *112* (48), 19102-19112.
25. Yang, Y.; Lim, S.; Wang, C.; Harding, D.; Haller, G., Multivariate correlation and prediction of the synthesis of vanadium substituted mesoporous molecular sieves. *Microporous Mesoporous Materials* **2004**, *67* (2), 245-257.
26. (a) Mohamed, M. A.; Salleh, W. N. W.; Jaafar, J.; Asri, S. E. A. M.; Ismail, A. F., Physicochemical properties of "green" nanocrystalline cellulose isolated from recycled newspaper. *RSC Advances* **2015**, *5* (38), 29842-29849; (b) Silvério, H. A.; Flauzino Neto, W. P.; Dantas, N. O.; Pasquini, D., Extraction and characterization of cellulose nanocrystals from corncob for application as reinforcing agent in nanocomposites. *Industrial Crops and Products* **2013**, *44*, 427-436; (c) Kampeerappun, P., Extraction and characterization of cellulose nanocrystals produced by acid hydrolysis from corn husk. *Journal of Metals, Materials and Minerals* **2015**, *25* (1).
27. Luo, Y.; Liu, X.; Huang, J., Heterogeneous nanotubular anatase/rutile titania composite derived from natural cellulose substance and its photocatalytic property. *CrystEngComm* **2013**, *15* (28), 5586-5590.
28. Colmenares, J. C.; Aramendía, M. A.; Marinas, A.; Marinas, J. M.; Urbano, F. J., Synthesis, characterization and photocatalytic activity of different metal-doped titania systems. *Applied Catalysis A: General* **2006**, *306*, 120-127.
29. Lhomme, L.; Brosillon, S.; Wolbert, D., Photocatalytic degradation of a triazole pesticide, cyproconazole, in water. *Journal of Photochemistry and Photobiology A: Chemistry* **2007**, *188* (1), 34-42.
30. (a) Zhou, Y.; Chen, W.; Wang, D., Mononuclear, dinuclear, hexanuclear, and one-dimensional polymeric silver complexes having ligand-supported and unsupported argentophilic interactions stabilized by pincer-like 2,6-bis(5-pyrazolyl)pyridine ligands. *Dalton Transactions* **2008**, (11), 1444-1453; (b) Fukui, M.; Kouda, H.;

Tanaka, A.; Hashimoto, K.; Kominami, H., Heterogeneous Meerwein-Ponndorf-Verley-type Reduction of Aromatic Aldehydes Having Other Reducible Functional Groups over a TiO₂ Photocatalyst. *ChemistrySelect* **2017**, 2 (7), 2293-2299.

Chapter 6: Bioactivity and catalyzed synthesis of biscoumarin derivatives using biologically synthesized silver nanoparticles supported by nanocrystalline cellulose

6.1. Introduction

The increased demand for noble metal nanoparticles in the global market has seen a growth in the relative applicable fields of study (catalysis, optics, medicinal etc.). These noble metal nanoparticles are manufactured in various forms such as nanopowders, colloids, emulsions etc. and are tailored to the desired applications.¹ The two classical approaches of the ‘top-down’ and ‘bottom-up’ have been used accordingly, to the necessitate the production of metal nanoparticles. However, these methods usually encompass harsh conditions, expensive chemicals and in general lacks a green protocol. This broadens the scope to improve the synthetic procedure of these metal nanoparticles.²

Among the various synthesis procedures, the wet chemical synthesis is thought to be the simplest route. Desired morphologies and the nature of nanoparticles can be ascertained by tuning different parameters of the procedure. In general, this method involves the reduction of metal ions to metal nanoparticles using a suitable reducing and stabilizing agent in a solution phase. A paradigm shift toward an environmentally friendly and cost-effective procedure has focused research on the use of a reducing agent and stabilizer from biological sources while maintaining an aqueous solution phase as the reaction medium. Microorganisms and plant extracts (using different extraction techniques and from different sections of plants including roots, leaves, seeds, fruit, etc.) are extensively used for this purpose.³ Several studies have shown that the obtained plant extracts predominantly contain phenolic compounds, flavonoids, terpenoids, polysaccharides, enzymes and other proteins, etc., which are responsible for reduction of metal ions and stabilization of nanoparticles.⁴ In South Africa, plant species that are rich with such active ingredients have been traditionally used as medicines, cosmetics, and food.⁵ However, the search for an ideal plant species with potential reducing and stabilizing abilities leads to an extensive study of the preparation of nanomaterials using the plant, is needed.

6.1.1. Silver nanoparticles

Silver is a noble transition metal belonging to the group 11 elements. It is soft, white and lustrous in nature and possesses high electrical and thermal conductivity. It forms part of the coinage metals and was widely used as cutlery during the Victorian era.⁶ Apart from the utilitarian applications silver has also been employed as medicinal and therapeutic agents with a research-driven realization (during the 20th century) that it can be used in low concentrations against microbes that cause infections.⁷ These applications see silver used in many forms such as coins, vessels, solutions, foils, sutures and colloids (usually as a lotion or ointment). It is the foremost used therapeutic agent in medicine for infectious diseases and surgical infections, with the benefits outweighing the risk.^{7b} Nanoscience is an interdisciplinary subject that hinges on the fundamental properties of nanosized objects and allows for the manipulation of these properties which may not be understood in bulk materials.⁸ Nanoparticles possess extraordinary optical, electronic, magnetic and catalytic properties in comparison to the relative bulk material, which is owed to the high surface area to volume ratio seen in most nanosized materials.⁹ The Surface Plasmon Resonance (SPR) phenomenon differentiates group 11 metal nanoparticles from others by a visual colour difference.¹⁰ It is a collective oscillation of free electrons of the metal nanoparticles in resonance with the frequency of the light wave interactions which causes the SPR band to appear in the visible and infrared region.¹¹ Silver nanoparticles (AgNP) research has escalated owing to the properties it possesses as bulk silver and in nanoform. These include the growing use as a catalyst and bactericidal agent in nanobiotechnological research.¹²

6.1.2. Plant-mediated synthesis of silver nanoparticles.

The literature on the prescribed topic is vast. Here the thesis simply aims to introduce the concept of phytomediated synthesis of silver nanoparticles and its related applications. The use of plant extracts as reducing and stabilizing agents to obtain silver nanoparticles with varying size and morphology are shown in Table 5.1. Silver nanoparticles synthesized using the antioxidant constituents from blackberry, blueberry, pomegranate, and turmeric extracts displayed particle sizes between 20 and 500 nm. This was dependent on the nature of extracts and preparation methods.¹³ Shinde *et al.* demonstrated that AgNP thin films of the large area were obtained using guava leaves extract through the successive Ionic Layer Adsorption and Reaction (SILAR) method.¹⁴ Das and Velusamy revealed AgNPs of various shapes like truncated octahedron, rhombic-dodecahedron, cubic, octahedron, and octagon assemblies

using banana stem extract. These particles were found with sizes ranging from 75 nm to 1220 nm.¹⁵ Abdelhamid *et al.* synthesized nanotriangles and hexagon shaped AgNPs using *Potamogeton pectinatus L.* extract and established that continuous growth was evident as the concentration of silver nitrate was increased, which finally resulted in polydisperse nanoparticles.¹⁶

Table 6.1. List of plant species used in the biosynthesis of AgNPs with corresponding sizes.

Plant Species	Size (nm)	Reference
<i>Myrmecodia pendans</i>	10 – 20	17
<i>Tectona grandis</i>	30 – 40	18
<i>Syzygium cumini</i>	10 – 15	19
<i>Rhynchosyris ellipticum</i>	51 – 73	20
<i>Alternaria alternata</i>	27 – 79	21
<i>Citrus maxima</i>	2.5 – 5.7	22
<i>Desmodium gangeticum</i>	18 – 39	23
Latex of <i>Thevetia peruviana</i>	10 – 30	24
<i>Lycopersicon esculentum</i> Mill	30 – 40	25
<i>Piper pedicellatum</i>	2 – 3	26
<i>Centella asiatica L.</i>	30 – 50	27
Neem leaves	43	28
<i>Triphala</i>	59	28
Pomegranate seed	30	29
<i>Mentha piperita</i>	90	30
<i>Murraya koenigii</i>	10 – 25	31

Veeranna *et al.* used water-soluble organics present in the aqueous extracts of the plant materials. It was proven that these compounds were mainly responsible for the reduction of silver(I) to AgNPs.³² Water soluble compounds such as saponins present in the leaf extract of *Memecylon edule* were reported by Elavazhagan and Arunachalam. This was responsible for the reduction of silver ions (which was incubated under dark conditions at 150 rpm in a shaker) to majority square shaped AgNPs. These particles ranged in size from 50 to 90 nm.³³ Zargar *et al.* prepared spherical shaped AgNPs (with an average size of 18.2 ± 8.9 nm) using the leaf

methanolic extract of *Vitex negundo*. These AgNPs exhibited antibacterial activity against both Gram positive and Gram negative bacteria.³³

Synthesis of metallic nanoparticles using plant extracts is inexpensive, easily scaled-up, and environmentally benign. Different characterization techniques are used in evaluating its potential applications.^{4b}

6.1.3. The plant species *Lippia javanica* (Burm.f.) Spreng.

Lippia javanica (Burm.f.) Spreng. (Verbenaceae) (Figure 6.1a) belongs to the Verbenaceae family (Verbenaceae) comprising of 32 genera and 840 species.³⁴



Figure 6.1. (a) Flowers and leaves of *Lippia javanica* (Burm.f.) Spreng. (photographer: BT Wursten)³⁵ and (b) *L. javanica* herbal tea known as Zumbani.³⁶

L. javanica is an upright woody perennial herb or shrub, reaching lengths of up to 4.5m. It comprises of strong aromatic leaves which exudes a ‘lemon-like’ scent when crushed.³⁷ *L. javanica* occurs naturally in central, eastern, and southern Africa and has also been recorded in the tropical Indian subcontinent.³⁸ It has a long history of traditional use in tropical Africa as an indigenous herbal tea (Figure 6.1b), a beverage, or a food additive based on the perceived health and medicinal properties it possesses.³⁶ Multiple classes of phytochemicals including volatile and nonvolatile secondary metabolites, such as alkaloids, amino acids, flavonoids, iridoids, and triterpenes as well as several minerals, have been identified from *L. javanica*.^{5a, 38b,39} Phenolic compounds found in plants are known to play an important role as antioxidants in exhibiting the medicinal properties such as antibiotic, anti-inflammatory, anticancer, and anti-allergic properties.^{5d,40} Simple phenolic compounds and caffeic acid and its derivatives are some of the compounds that have been identified in *L. javanica*, with a few examples seen in Table 6.2.

Table 6.2. Selected Phenolic compounds isolated from the plant species *L. javanica*.

Phenolic compounds	Reference
<i>Coumarin</i>	39d
<i>Verbascoside</i>	39i
<i>Isoverbascoside</i>	39i
<i>Theveside-Na</i>	41
<i>Theveridoside</i>	41
<i>4-ethylnonacosane</i>	39j
<i>Apigenin</i>	39j, 42
<i>Cirsimaritin</i>	39j, 42
<i>6-Methoxy luteolin 4'-methyl ether</i>	39j
<i>6-Methoxy luteolin 3',4',7-trimethyl ether</i>	39j
<i>Crassifolioside</i>	42
<i>Luteolin</i>	42
<i>Diosmetin</i>	42
<i>Chrysoeriol</i>	43
<i>Tricin</i>	43
<i>Isothymusin</i>	43
<i>Eupatorin</i>	43
<i>5-Dimethyl noboletin</i>	43
<i>Genkwanin</i>	43
<i>Salvigenin</i>	43
<i>Lippialactone</i>	44

6.1.4. NCC supported Silver Nanoparticles

Applications of nanocelluloses as a metal NP support has attracted a lot of attention in the past decade. Metal NPs possess properties which are unique and distinct from those of their bulk or molecular counterparts.⁴⁵ Metal NPs are thermodynamically unstable and tend to aggregate to form bulk metal particles without the use of capping agents, ligands or supports in their synthesis. Because of their high surface area, reductive surface functional groups and water suspendability, nanocellulose are attractive supports for metal NPs.⁴⁶

6.1.5. Background to biological activity

Microorganisms are the earliest known life forms that have existed on the earth and exhibit the greatest genetic and metabolic diversity.⁴⁷ These microbes have led to a number of infectious diseases which has necessitated the need for antimicrobial chemotherapy. However, with recent studies, resistance to antimicrobial agents from bacteria, parasites, viruses and other disease-causing organisms has led to a worldwide public health pandemic.⁴⁸ The hindrance in the development of antibiotics and their application to clinical medicine has seen the enhancement of bacterial resistance towards antibacterial drugs. This is, in part, due to constant use of antibiotics which in turn increases the drug-resistant bacterial population. This allows for the survival and growth of resistant strains and eradicates susceptible microbes.⁴⁹ With this antimicrobial resistance fast becoming a global concern and a rapid increase in emerging multidrug-resistant bacteria,⁵⁰ research is driven toward a search for new antimicrobial materials. This includes metal nanoparticles of biologically important materials⁵¹ which sees the use of silver and in turn AgNPs as antimicrobial agents.^{7a}

In this study focus was directed to the antibacterial activities of the biologically synthesized AgNPs (NCC supported and unsupported) on the following bacteria: *Staphylococcus aureus* (ATCC 29263) which is a Gram-positive aerobic organism.⁵² Methicillin-Resistant *Staphylococcus aureus* (ATCC BAA-1683), a Gram-positive bacterium that is genetically different from other strains of *Staphylococcus aureus*.⁵³ *Escherichia coli* (ATCC 25922), a Gram-negative, rod-shaped bacterium.⁵² *Klebsiella pneumoniae* (ATCC 31488), a Gram-negative, encapsulated, non-motile bacterium.⁵⁴ *Salmonella Typhimurium* (ATCC 14028), a Gram-negative, flagellated, facultative anaerobic and primary enteric pathogen infecting both humans and animals.⁵⁵

6.1.6. Biscoumarin and its derivatives

Research pertaining to natural and synthetic coumarins (2*H*-1-benzopyran-2-ones) and their derivatives reveals the excellent chemical reactivity and different bioactivity that these compounds possess.

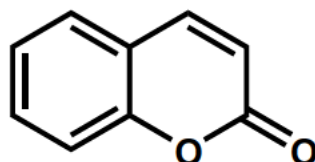


Figure 6.2. Coumarin (2*H*-1-benzopyran-2-ones) moiety

Natural coumarins, in particular, play a vital role in plant biochemistry and physiology.⁵⁶ The majority of the known natural coumarins have been isolated from natural products.⁵⁷ The synthetic coumarin counterparts have been obtained *via* retrosynthesis to the coumarin ring. Ideally, a substitution can occur at any of the six available sites of the basic molecule. In addition, these compounds are widely variable in structure and activity.⁵⁸ The bioactivity of coumarin derivatives, with regard to their therapeutic application as an anticoagulant and antibacterial agents,⁵⁹ has stimulated interest in this class of compounds.

With peaked interest in this moiety, research has burgeoned in the analysis of biscoumarins (benzylidene-bis-(4-hydroxycoumarin)).⁵⁸ Preparation of biscoumarins involve an energy intensive protocol, long reaction times and harsh reaction conditions. A need to overcome these shortcomings has seen the incorporation of a catalyst in the overall preparation. Among the various catalysts used for the synthesis of biscoumarins, including sulfuric acid, phosphorus pentoxide, aluminumchloride, iodine, and trifluoroacetic acid.⁶⁰ These catalysts are usually non-recoverable and necessitates the need for inert environments.⁶¹

In this present study, the synthesis of silver colloids in an aqueous medium using an aqueous extract of *L. javanica* as a reducing as well as a stabilizing agent was investigated. In addition, an attempt to utilize the synthesized AgNPs as a tool to combat ‘multidrug resistant’ microorganisms, a study of the antibacterial activity was undertaken against several bacterial strains. A further application investigating the catalytic activity of the NCC supported AgNPs in the synthesis of benzylidene-bis-(4-hydroxycoumarin) derivatives was examined.

6.2. Materials and Methods

6.2.1. Materials

The following chemicals and consumables were purchased from the Sigma-Aldrich Chemical Co.: Whatman® no. 1 filter paper and sulfuric acid; 2-methoxybenzaldehyde (96%); 4-methoxybenzaldehyde (99%); 2-fluorobenzaldehyde (97%); 2-Chlorobenzaldehyde (99%); 4-bromobenzaldehyde (99%); 4-ethylbenzaldehyde ($\geq 97\%$); 2,3-dimethoxybenzaldehyde (98%); 3,4-dimethoxybenzaldehyde (99%); 2,5-dimethoxybenzaldehyde (99%); silver nitrate (99%) was obtained from Merck. *Lippia javanica* plant material was obtained from the Warwick market, Durban, South Africa.

6.2.2. Preparation of aqueous extract of *Lippia javanica*

Preparation of the aqueous extract of *Lippia javanica* obtained from a local market, commenced with the separation of the plant material from the large stems of the plant. The separated samples were then washed with deionized water to remove any fine particulate. The remaining plant matter was then dried in an oven at 60 °C for 24 hours. The dried plant material was then crushed to a powder using a mortar and pestle to ensure extraction. 5 g of plant material was added to a 250 mL beaker containing 100 mL of double-distilled water and allowed to stir for 30 minutes. The mixture was then further stirred at 80 °C for 2 hours, followed by cooling. This dark solution was then filtered to remove the remaining insoluble mass, using Whatman no. 1 filter paper. The brownish filtrate was added to 100 mL volumetric and stored at 5 °C and used for the synthesis of silver nanoparticles.

6.2.3. Synthesis of silver colloids using *Lippia javanica* plant extract (LPE)

The silver colloids were prepared using 3 different concentrations (1, 5 and 10 mM) of AgNO₃. Initial preparation involved the addition of 100, 200 and 400 µL of LPE to 1 mL of the various concentrations of AgNO₃. All samples were then made up to 5 mL and sonicated for 10 minutes using UP400S Ultrasonic processor, Hielscher, Germany at 40% amplitude and 0.75 cycle. Samples were stored in Teflon tube under dark conditions at an ambient temperature of 25 °C.

6.2.4. Preparation of NCC

After blending cellulose (obtained from filter paper) with a domestic blender, NCCs were isolated using 20 mL/g 64 wt% sulfuric acid at 45 °C in an oil bath for 45 minutes to remove the amorphous regions. After the completion of the hydrolysis, the suspensions were repeatedly diluted and centrifuged at 6000 rpm for 10 min to reduce the sulfuric acid concentration. The suspensions were later sonicated using UP400S Ultrasonic processor, Hielscher, Germany at 50% amplitude and 0.5 cycle for 15 minutes to ensure complete dispersion of NCCs before dialysis to near neutral pH.

6.2.5. Preparation of NCC supported AgNPs

NCC supported AgNPs were prepared *via* a colloidal synthesis pseudo wet impregnation technique. NCC (2.5, 5, 10, 20 and 100 mg) was added to the colloidal solution of 400 µL of plant extract (LPE) in 1 mL of 10 mM AgNO₃ (C9) and was made up to 5 mL. The mixture was stirred for 1 h using a magnetic stirrer at RT. Thereafter, samples were sonicated for 10 minutes using UP400S Ultrasonic processor, Hielscher, Germany at 40% amplitude and 0.75 cycle. Samples were stored in Teflon tube under dark conditions at an ambient temperature of 25 °C. Sample **C9e** was chosen as the ideal catalyst and was scaled up (10 times (1000 mg NCC, 4 mL of LPE in 10 mL of 10 mM AgNO₃ and made up to 50 mL)). After sonication the sample was placed in a petri dish and dried at 75 °C in an oven. After drying the resultant film was ground and filtered through a 300 µm mesh size. The sieved product was further used to catalyse the biscoumarin reaction.

6.2.6. General procedure for the synthesis of benzylidene-bis-(4-hydroxycoumarin) derivatives (6a-i)

In a 50 mL round bottom flask at 50 °C, aromatic aldehyde (1.0 mmol), 4-hydroxycoumarin (2.0 mmol) and AgNP/NCC (bulk C9e, 50 mg) were added while stirring using ethanol (5 mL) as solvent. The progress of reaction was monitored by TLC. After completion of the reaction, sufficient ethanol was added to dissolve the organic compound formed and the solid catalyst was recovered by filtration.⁵⁸ The final product was recovered after recrystallization in ethanol and recovery under vacuum filtration. The products were characterized and validated by

various techniques (^1H NMR, ^{13}C NMR and HR-MS). All the spectral instrumentation details are reported below.

3,3'-(2-Methoxybenzylidene)-bis-(4-hydroxy-2H-chromen-2-one) (6a): White solid; mp 241 – 243 °C; FT-IR (selected values) $\nu_{\text{max}}/\text{cm}^{-1}$: 3072 (OH), 1601 (CO); ^1H NMR (400 MHz, DMSO- d_6) δ = 3.56 (s, 3H, OCH₃), 6.07 (s, 1H, CH), 6.84 (d, J = 8.04 Hz, 1H, ArH), 6.93 (t, J = 7.80 Hz, 1H, ArH), 7.26 (m, 2H, ArH), 7.36 (m, 4H, ArH), 7.58 (t, J = 7.08 Hz, 2H, ArH), 8.00 (d, J = 7.00 Hz, 2H, ArH), 11.21 (s, 2H, OH); ^{13}C NMR (100 MHz, DMSO- d_6): δ = 33.40, 55.55, 110.99, 116.75, 120.47, 123.58, 124.49, 128.38, 132.43, 152.17, 157.81, 163.78; HRMS of [$\text{C}_{26}\text{H}_{17}\text{O}_7$ - H] (m/z): 441.0972; Calcd.: 441.0974.

3,3'-(4-Methoxybenzylidene)-bis-(4-hydroxy-2H-chromen-2-one) (6b): White solid; mp 251 – 254 °C; FT-IR (selected values) $\nu_{\text{max}}/\text{cm}^{-1}$: 3031 (OH), 1603 (CO); ^1H NMR (400 MHz, DMSO- d_6) δ = 3.78 (s, 3H, OCH₃), 6.03 (s, 1H, CH), 6.84 (d, J = 6.88 Hz, 2H, ArH), 7.11 (d, J = 8.04 Hz, 2H, ArH), 7.39 (d, J = 8.29 Hz, 4H, ArH), 7.61 (m, 2H, ArH), 8.02 (d, J = 16.57 Hz, 2H, ArH), 11.49 (s, 2H, OH); ^{13}C NMR (100 MHz, DMSO- d_6): δ = 35.52, 55.28, 114.03, 116.62, 124.38, 124.86, 126.94, 127.62, 132.81, 158.43; HRMS of [$\text{C}_{26}\text{H}_{17}\text{O}_7$ - H] (m/z): 441.0960; Calcd.: 441.0974.

3,3'-(2,3-Dimethoxybenzylidene)-bis-(4-hydroxy-2H-chromen-2-one) (6c): White solid; mp 182 – 184 °C; FT-IR (selected values) $\nu_{\text{max}}/\text{cm}^{-1}$: 3072 (OH), 1601 (CO); ^1H NMR (400 MHz, DMSO- d_6) δ = 3.52 (s, 3H, OCH₃), 3.82 (s, 3H, OCH₃), 6.15 (s, 1H, CH), 6.89 (m, 2H, ArH), 7.01 (t, J = 8.08 Hz, 1H, ArH), 7.35 (m, 4H, ArH), 7.57 (m, 2H, ArH), 8.01 (d, J = 7.80 Hz, 2H, ArH), 11.62 (s, 2H, OH); ^{13}C NMR (100 MHz, DMSO- d_6): δ = 33.47, 55.74, 111.73, 116.54, 120.18, 123.60, 124.31, 124.74, 129.30, 132.50, 147.28, 152.16, 152.94; HRMS of [$\text{C}_{27}\text{H}_{19}\text{O}_8$ - H] (m/z): 471.1086; Calcd.: 471.1080.

3,3'-(2,5-Dimethoxybenzylidene)-bis-(4-hydroxy-2H-chromen-2-one) (6d): White solid; mp 213 – 214 °C; FT-IR (selected values) $\nu_{\text{max}}/\text{cm}^{-1}$: 3061 (OH), 1600 (CO); ^1H NMR (400 MHz, DMSO- d_6) δ = 3.50 (s, 3H, OCH₃), 3.71 (s, 3H, OCH₃), 6.05 (s, 1H, CH), 6.76 (s, 2H, ArH), 6.87 (s, 1H, ArH), 7.36 (m, 4H, ArH), 7.58 (m, 2H, ArH), 8.00 (d, J = 7.84 Hz, 2H, ArH), 11.20 (s, 2H, OH); ^{13}C NMR (100 MHz, DMSO- d_6): δ = 33.50, 55.72, 56.12, 111.58, 111.84, 115.94, 116.49, 116.78, 124.31, 124.72, 125.04, 132.46, 151.87, 152.15, 153.45, 163.82; HRMS of [$\text{C}_{27}\text{H}_{19}\text{O}_8$ - H] (m/z): 471.1083; Calcd.: 471.1080.

3,3'-(2-Chlorobenzylidene)-bis-(4-hydroxy-2H-chromen-2-one) (6e): White solid; mp 198 – 200 °C; FT-IR (selected values) $\nu_{\text{max}}/\text{cm}^{-1}$: 3350 (OH), 1601 (CO); ^1H NMR (400 MHz, DMSO- d_6) δ = 6.14 (s, 1H, CH), 7.23 (m, 1H, ArH), 7.26 (m, 1H, ArH), 7.36 (m, 5H, ArH),

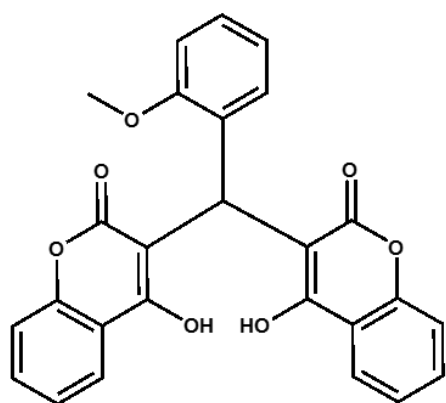
7.45 (d, $J = 8.33$ Hz, 2H, ArH), 7.60 (m, 2H, ArH), 8.02 (s, 2H, OH); ^{13}C NMR (100 MHz, DMSO- d_6): $\delta = 35.72, 116.51, 124.43, 124.90, 126.78, 128.61, 129.25, 130.85, 132.87, 133.55$; HRMS of $[\text{C}_{25}\text{H}_{14}\text{ClO}_6 - \text{H}]$ (m/z): 445.0474; Calcd.: 445.0479.

3,3'-(3,4-Dimethoxybenzylidene)-bis-(4-hydroxy-2H-chromen-2-one) (6f): White solid; mp 273 – 275 °C; FT-IR (selected values) $\nu_{\text{max}}/\text{cm}^{-1}$: 3363 (OH), 1601 (CO); ^1H NMR (400 MHz, DMSO- d_6) $\delta = 3.71$ (s, 3H, OCH₃), 3.85 (s, 3H, OCH₃), 6.06 (s, 1H, CH), 6.69 (s, 1H, ArH), 6.75 (m, 1H, ArH), 6.80 (d, $J = 8.49$, 1H, ArH), 7.40 (d, $J = 8.33$, 4H, ArH), 7.64 (m, 2H, ArH), 8.02 (m, 2H, ArH), 11.27 (s, 1H, OH), 11.50 (s, 1H, OH); ^{13}C NMR (100 MHz, DMSO- d_6): $\delta = 35.76, 55.89, 56.10, 110.35, 111.23, 116.65, 118.92, 124.37, 124.91, 127.53, 132.86, 148.04, 149.11$; HRMS of $[\text{C}_{27}\text{H}_{19}\text{O}_8 - \text{H}]$ (m/z): 471.1083; Calcd.: 471.1080.

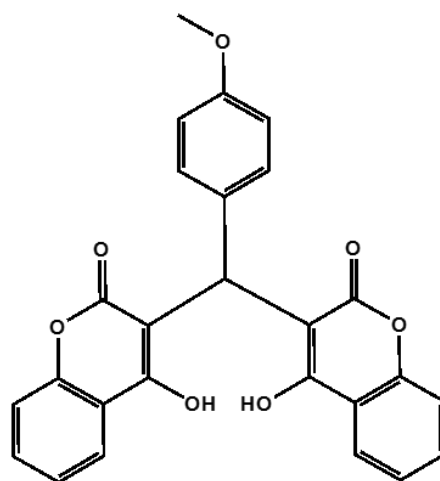
3,3'-(4-Bromobenzylidene)-bis-(4-hydroxy-2H-chromen-2-one) (6g): White solid; mp 271 – 272 °C; FT-IR (selected values) $\nu_{\text{max}}/\text{cm}^{-1}$: 3048 (NH), 1602 (CO); ^1H NMR (400 MHz, DMSO- d_6) $\delta = 6.00$ (s, 1H, CH), 7.09 (d, $J = 7.64$ 2H, ArH), 7.42 (m, 6H, ArH), 7.62 (m, 2H, ArH), 8.02 (dd, $J = 8.01, 30.38$ Hz, 2H, ArH), 11.29 (s, 1H, OH), 11.52 (s, 1H, OH); ^{13}C NMR (100 MHz, DMSO- d_6): $\delta = 35.89, 116.70, 120.81, 124.43, 125.00, 128.35, 131.72, 133.05, 134.44$; HRMS of $[\text{C}_{25}\text{H}_{14}\text{BrO}_6 - \text{H}]$ (m/z): 488.9967/490.9948; Calcd.: 488.9974/490.9953.

3,3'-(4-Fluorobenzylidene)-bis-(4-hydroxy-2H-chromen-2-one) (6h): White solid; mp 215 – 217 °C; FT-IR (selected values) $\nu_{\text{max}}/\text{cm}^{-1}$: 3040 (OH), 1604 (CO); ^1H NMR (400 MHz, DMSO- d_6) $\delta = 6.04$ (s, 1H, CH), 7.00 (t, $J = 8.61$, 2H, ArH), 7.17 (m, 2H, ArH), 7.40 (m, 4H, ArH), 7.63 (m, 2H, ArH), 8.03 (m, 2H, ArH), 11.39 (s, 2H, OH); ^{13}C NMR (100 MHz, DMSO- d_6): $\delta = 35.68, 115.41, 115.63, 116.66, 124.41, 124.97, 128.12, 128.20, 132.98$; HRMS of $[\text{C}_{25}\text{H}_{14}\text{FO}_6 - \text{H}]$ (m/z): 429.0772; Calcd.: 429.00774.

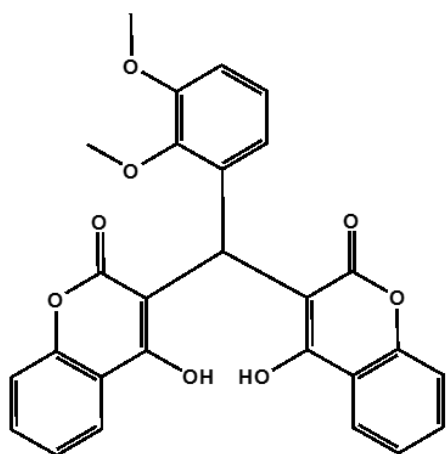
3,3'-(4-Ethylbenzylidene)-bis-(4-hydroxy-2H-chromen-2-one) (6i): White solid; mp 259 – 260 °C; FT-IR (selected values) $\nu_{\text{max}}/\text{cm}^{-1}$: 3022 (OH), 1603 (CO); ^1H NMR (400 MHz, DMSO- d_6) $\delta = 1.22$ (t, $J = 7.67$ Hz, 3H, CH₃), 2.63 (q, $J = 7.60, 15.17$ Hz, 2H, CH₂), 6.05 (s, 1H, CH), 7.12 (m, 4H, ArH), 7.39 (m, 4H, ArH), 7.61 (m, 2H, ArH), 8.03 (m, 2H, ArH), 11.49 (s, 2H, OH); ^{13}C NMR (100 MHz, DMSO- d_6): $\delta = 15.42, 28.34, 35.90, 116.63, 124.39, 124.85, 126.42, 128.13, 132.27, 132.79, 142.82$; HRMS of $[\text{C}_{27}\text{H}_{19}\text{O}_6 - \text{H}]$ (m/z): 439.1173; Calcd.: 439.1182.



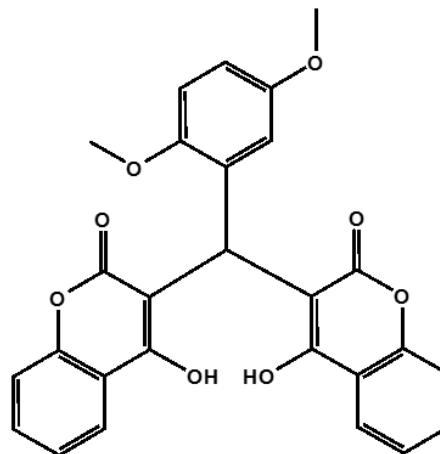
6a



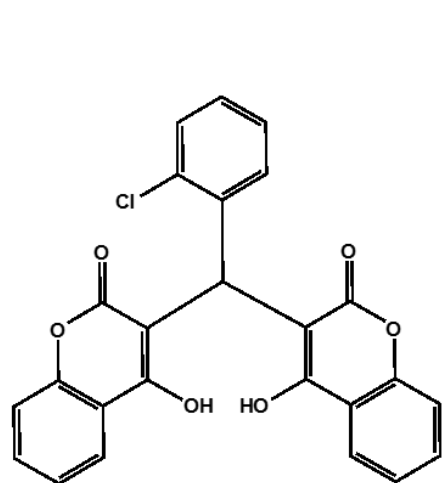
6b



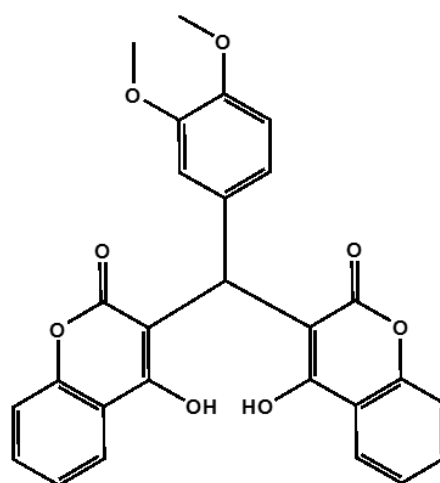
6c



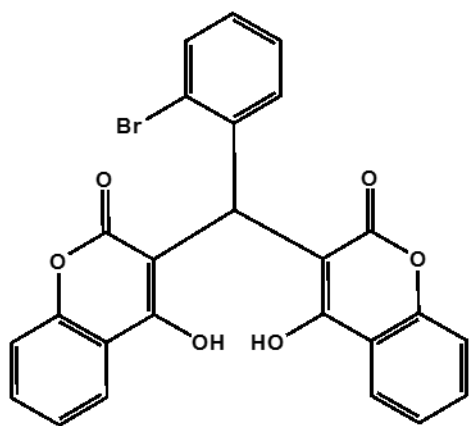
6d



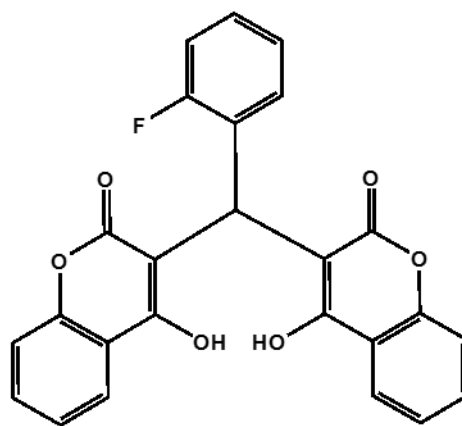
6e



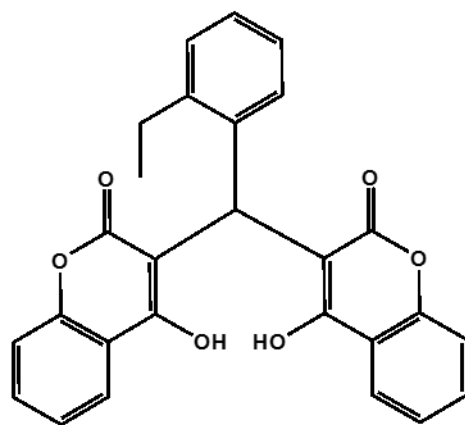
6f



6g



6h



6i

6.2.7. Antibacterial Assay

6.2.7.1. Microbial Strains

The antimicrobial activity of the synthesized colloids C1 – C9 as well as the NCC supported colloids C9a – C9e were tested against two Gram-positive bacteria, *Staphylococcus aureus* ATCC 29263 and *S. aureus Rosenbach* ATCC BAA-1683 (methicillin resistant *S. aureus* (MRSA)) and three Gram-negative bacteria, *Klebsiella pneumonia* ATCC 31488, *Escherichia coli* ATCC 25922 and *Salmonella Typhimurium* ATCC 14028 according to the disc diffusion method.

6.2.7.2. Disc diffusion method

The standard antibiotics ciprofloxacin and ampicillin were used as controls for comparison. Mueller Hilton agar was prepared (38 g in 1 L of water), poured into sterile pre-labelled Petri dishes and allowed to set and dry at room temperature. Bacterial organisms were standardized using a 0.5 McFarland standard turbidity and then swabbed onto agar plates. Antibiotic assay discs (6 mm; Whatman®, UK) were then placed on the swabbed surfaces in marked areas. The colloidal samples were prepared 7 days in advance. 10 µL of each aqueous colloidal sample as well as pure plant extract, three concentrations of AgNO₃ and NCC were pipetted onto the discs. The agar plates were then inverted and incubated at 35-37 °C for 24 hours. The diameter of the zone of inhibition was measured in mm. All samples that demonstrated inhibition zones of > 8 mm were considered active and further evaluated for the determination of minimum bactericidal concentration (MBC). MBC values were obtained using a microdilution assay with ampicillin and ciprofloxacin as the control and following the method by Andrews.⁶²

6.2.7.3. Determination of minimum bactericidal concentration (MBC)

The MBC values were determined against all microbial strains using broth dilution method.⁶³ The bacterial cultures were grown in Nutrient Broth for 24 h at 37 °C in a shaking incubator (100 rpm) and diluted to 1.5×10^8 CFU/mL (0.5 McFarland) with Mueller Hilton Broth. Serial dilutions (ten) of colloids were prepared in double distilled water and incubated with bacterial cultures at 37 °C in a shaking incubator at 100 rpm. After incubation for 18 h, the dilutions were spotted (10 µl) on MHA plates and incubated for a further 24 h. The minimum concentration at which no bacterial growth was observed was considered as the MBC. Ampicillin and ciprofloxacin were used as the control. All experiments were performed in triplicate.

6.2.8. Characterization Techniques

¹H, ¹³C and ¹⁵N NMR spectroscopy

¹H and ¹³C NMR spectra of isolated biscoumarin moieties were recorded in solution NMR experiments, on a Bruker Avance 400 MHz spectrometer in deuterated dimethyl sulfoxide solvent.

Mass Spectral Analysis

Mass spectral analyses were performed on a Waters API Quattro Micro spectrometer. 500 ppm solutions of each sample were made up in dimethyl sulfoxide solvent. This followed with a direct injection into the instrument.

Optical Spectroscopic Analysis

The absorption spectra of various synthesized AgNPs samples were obtained in the wavelength range 300-900 nm using UV-3600 Plus UV-VIS-NIR Spectrophotometer, Shimadzu, Japan. All samples were blanked with double distilled water and the corresponding volume of plant extract (LPE).

Fourier transform infrared spectroscopy

The identification of the plant extract, pure AgNPs, NCC/AgNPs catalyst and resultant biscoumarin compounds were confirmed by FTIR study in the range 380-4000 cm⁻¹ at a resolution of 4 cm⁻¹ using Spectrum 100 infrared spectrometer equipped with universal attenuated total reflection (UATR) accessory Perkin Elmer, USA.

Morphological structure analysis

The morphological characterisation, dimensions and elemental composition of the silver colloids (C1 – C9) and NCC supported AgNP (C9a – C9e) were established with the aid of electron microscopic study using; JEOL 1010 transmission electron microscope (TEM), Japan and ZEISS Ultra Plus field emission gun scanning electron microscope (FEGSEM) equipped with energy dispersive x-ray (EDX) detector, Germany. TEM images of all samples were acquired using the synthesized materials, which were deposited on the TEM-grid. The TEM-grids were also negatively stained with 2 w/v% uranyl acetate to aid visualization of NCC within the NCC-AgNP matrix. Similarly, samples for SEM images were coated with gold with the aid of sputter coater to minimize charging.

X-ray diffraction analysis

Powder X-ray diffraction (XRD) analysis of the dried silver colloid (C9 made in bulk (40 mL of PE in 100 mL of 10 mM AgNO₃ and made up to 500 mL) using a low background (silicon-carbide holder) and NCC supported AgNP catalyst (C9e) was conducted using an X-ray diffractometer (Bruker AXS D8 Advance, Germany). The instrument was equipped with Cu K α radiation source (wavelength = 0.154 nm) operating at 40 kV and 40 mA. The XRD pattern of the catalyst was recorded over the angular range $2\theta = 5\text{--}90^\circ$ at room temperature.

Crystallite size (D_{hkl}) of the isolated dried AgNPs (C9) catalyst was calculated using Scherrer's formula as shown in Equation 6.1 where λ is the X-ray wavelength (0.154 nm), β is the angular width at half maximum intensity determined with the aid of Gaussian fit of the peaks on the diffractograms of the isolated NCC and θ is the Bragg angle. The crystallographic plane adopted for the estimation was 111.

$$D_{hkl} \text{ (nm)} = 0.94\lambda/\beta \cos \theta \quad (6.1)$$

6.3. Results and Discussion

FT-IR analysis of dried samples

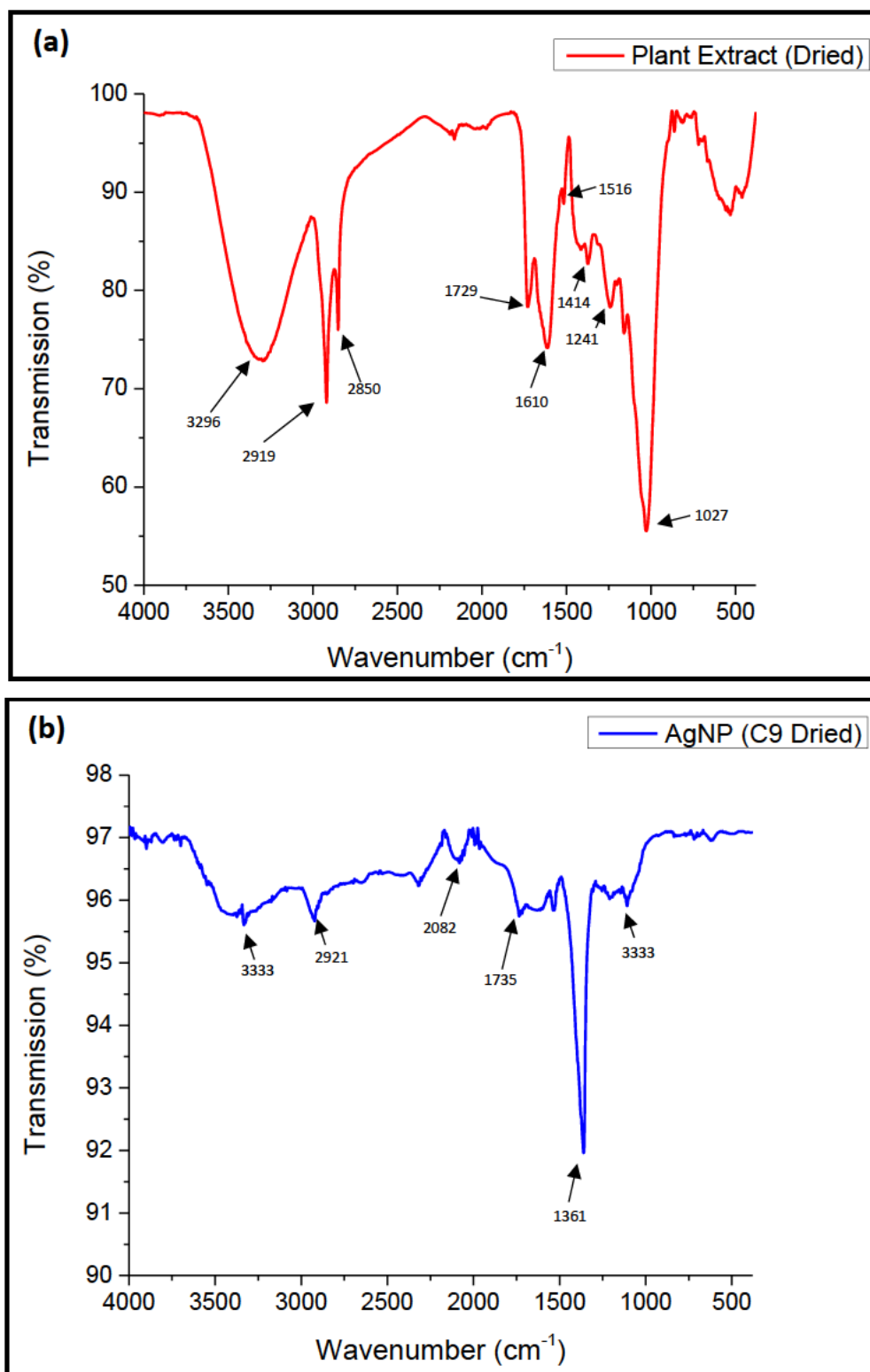


Figure 6.3. ATR-FTIR spectra of (a) *L. javanica* Plant Extract (LPE), (b) AgNP synthesized from plant extract (C9)

The FTIR spectrum of the pristine *L. javanica* aqueous-extract (LPE) (Fig. 6.3a) shows a very broad peak centred at 3296 cm^{-1} . The first peak can be assigned to O–H stretching of an alcoholic group. This broad peak, as well as the sharp peak at 2919 cm^{-1} , is the simultaneous contribution of unsaturation ($=\text{C–H}$), O–H stretching of carboxylic acids, and N–H stretching of amides. Further peaks can be assigned to C–H stretching (2850 cm^{-1}), C=O of aldehydes, esters or carboxylic acids (1729 and 1610 cm^{-1}), C=O of amides (1516 cm^{-1}), methyl groups (1414 cm^{-1}), primary alcoholic groups attached to cyclohexane (1241 cm^{-1}), and ether linkages (1027 cm^{-1}). All of these functional groups are related to alkaloids, amino acids, flavonoids, iridoids, triterpenes and various oligosaccharides present in the LPE.^{36,38a} FTIR of the AgNP-SE sample (Fig. 6.3b) shows peaks at 3333 , 2921 , 2082 , 1735 , 1361 and 1108 cm^{-1} . The shift of the broad peak centred at 3296 cm^{-1} along with the peaks at 1241 cm^{-1} and 1610 cm^{-1} suggests the involvement of alcoholic OH and C=O, respectively, in the reduction process. The reappearance and shifting of the other peaks related to unsaturation ($=\text{C–H}$), O–H stretching of carboxylic acids, N–H stretching of amides, C–H stretching and ether (C–O–C) linkages indicate the significant role of these functional groups in stabilizing the AgNPs.

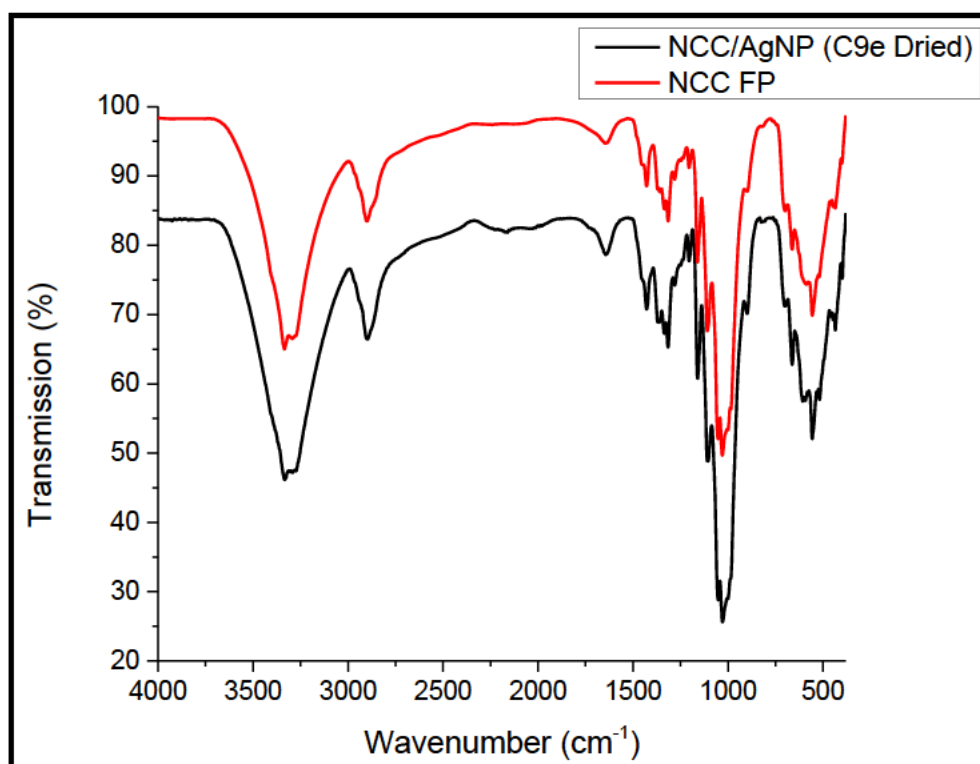


Figure 6.4. ATR-FTIR spectra of prepared NCC supported AgNP (C9e) and bare NCC prepared from filter paper

The FTIR spectrum of the NCC supported AgNPs synthesized from LPE (Figure 6.4) is similar to that of the NCC synthesized from filter paper as discussed in Chapter 3 (Section 3.3). There

are no visible peaks correlating to AgNP, however, this is masked by the intense peaks as of the NCC-FP.

TEM and UV-Vis analysis

The transmission electron microscopy (TEM) micrographs of the 3 concentrations of silver, as well as the 3 supplementary volumes *L. javanica* aqueous-extract (LPE) (C1 – C9, Table 6.3), were captured and analysed. All samples displayed elliptical shaped AgNPs with the occurrence of triangles, hexagons and squares at certain concentrations (Figure 1.2, Chapter 1).

Table 6.3. Sample codes denoting each colloidal solution

Volume/Concentration	1 mM (1 mL)	5 mM (1 mL)	10 mM (1 mL)
100 μL	C1	C4	C7
200 μL	C2	C5	C8
400 μL	C3	C6	C9

Colloids C1 – C3 (Figure 6.5) represents the 1 mM AgNO₃ concentration with a variation of the volume of LPE. Sample C1 (100 μ L LPE, 1 mM AgNO₃) showed a low concentration of particles with the average particle size of *ca.* 32.951 \pm 12.656 nm (Figure 6.5a and 6.5b). With an increase in the volume of LPE (C2 (200 μ L LPE, 1 mM AgNO₃)), there is an increase in the concentration of particles, however, the average particle size is equivalent at *ca.* 32.545 \pm 12.447 nm (Figure 6.5c and 6.5d). This indicates that an increase in the volume of LPE leads to an increased number of particles. When the volume of LPE is doubled as with colloid C3 (400 μ L LPE, 1 mM AgNO₃), a drastic increase in the number of particles is observed with a sharp decrease (*ca.* 18.206 \pm 11.367 nm) in average particle size (Figure 6.5e and 6.5f).

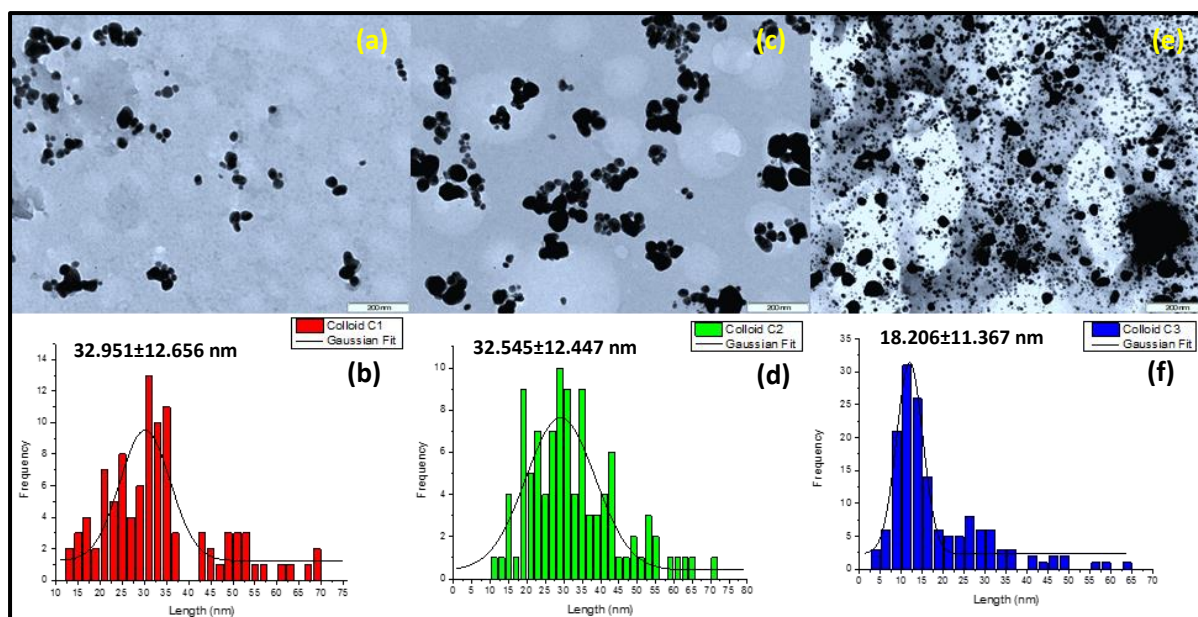


Figure 6.5. TEM micrographs and corresponding particle size distribution of colloids C1 (a-b), C2 (c-d), and C3 (e-f).

On examination of the UV-VIS spectra for colloids C1 – C3 (Figure 6.6), it is seen that the correlation drawn with respect to the relative average particle size present in the TEM micrographs (Figure 6.5), holds true. UV-VIS samples run after 24 hours (Figure 6.6a) shows that colloid C1 has maximum at 474 nm and colloid C2 has a maximum at 476 nm. This corresponds to the two colloidal solutions sharing similar average particle sizes. The intensity of the peak for C2 is greater than that of C1 which reiterates the fact that there is a greater number of particles in C2 than C1. The slightly blue shifted peak (448 nm) for colloid C3 illustrates the smaller average particle size and higher intensity demonstrates the presence of a larger number of particles in C3 than in C2 and C1. The UV-VIS spectra for colloids C1, C2 and C3 were done after 7 days (Figure 6.6b). Similar trends are seen with the exception of a higher intensity for all samples. This suggests that a greater number of particles formed after 7 days. The three peaks are blue shifted with respect to samples run after 24 hours indicating that a greater number of smaller particles are formed and the average size remains the same with little or no aggregation.

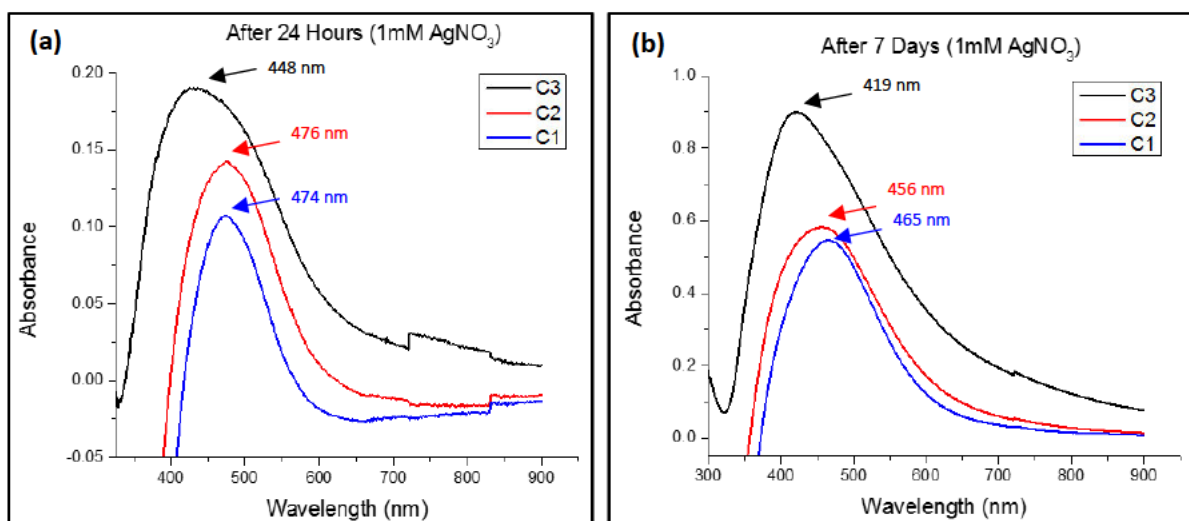


Figure 6.6. UV-VIS spectra of colloids C1 – C3, after (a) 24 Hours and (b) 7 days.

Colloids C4 – C6 (Figure 6.7) represents the 5mM AgNO₃ concentration with a variation of the volume of LPE. These samples follow a similar trend to that of C1 – C3. Sample C4 (100 μ L LPE, 5 mM AgNO₃) showed a relatively low concentration of particles with the average particle size of *ca.* 33.119 \pm 11.978 nm (Figure 6.7a and 6.7b). A decrease in average particle size (*ca.* 27.834 \pm 9.739 nm) was observed for colloid C5 (200 μ L LPE, 5 mM AgNO₃) (Figure 6.7c and 6.7d). As the volume of LPE increased, as is the case with colloid C6 (400 μ L LPE, 5 mM AgNO₃), a further decrease in average particle size (Figure 6.7e and 6.7f) to *ca.* 16.363 \pm 5.629 nm is seen. The UV-VIS spectra were run for the colloid samples C4 – C6 at the same time intervals of 24 hours (Figure 6.8a) and 7 days (Figure 6.8b) were also examined. After 24 hours the samples followed the same trend as colloids C1 – C3, with the maximum peak intensity of 448 nm (C4), 438 nm (C5) and 436 nm (C6) observed. However, the peaks are more intense after 24 hours at an AgNO₃ concentration of 5 mM than those at 1 mM. This indicates that as the concentration of AgNO₃ increases the rate at which AgNPs form increases.

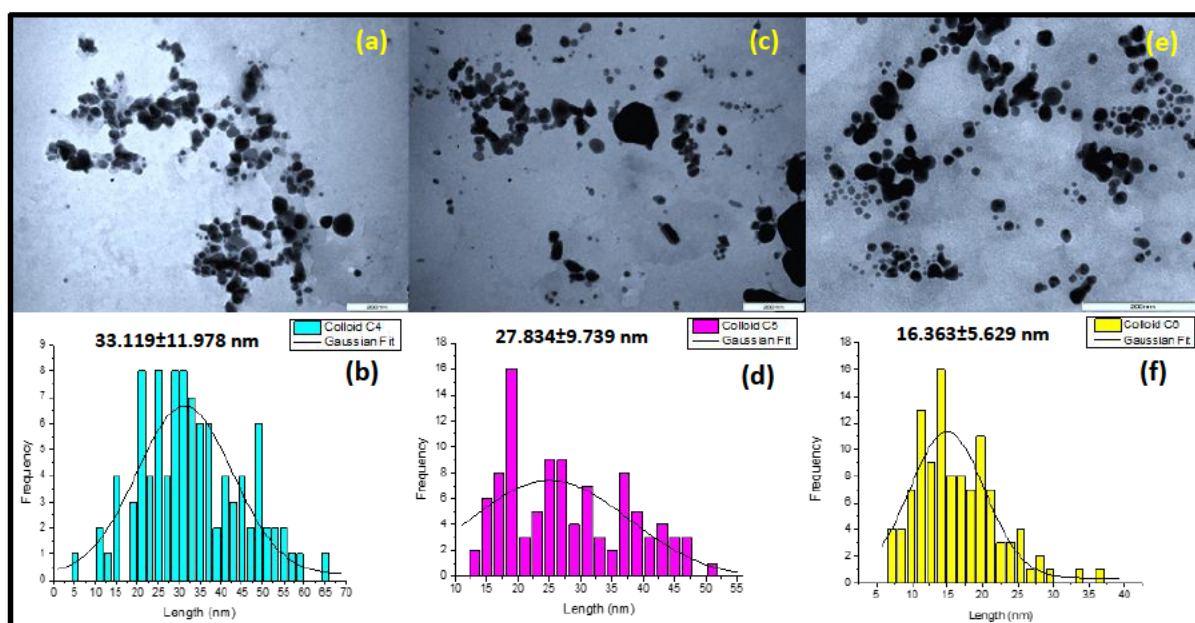


Figure 6.7. TEM micrographs and corresponding particle size distribution of colloids C4 (a-b), C5 (c-d), and C6 (e-f).

After 7 days it was observed that larger number of nanoparticles had formed due to the intense peaks. Sample C6 was diluted (3x dilution) in order to obtain a coherent depiction. The colloidal sample C6 sees a red shift after 7 days compared to that run after 24 hours from 436 nm to 439 nm indicating a slight increase in the average particles size.

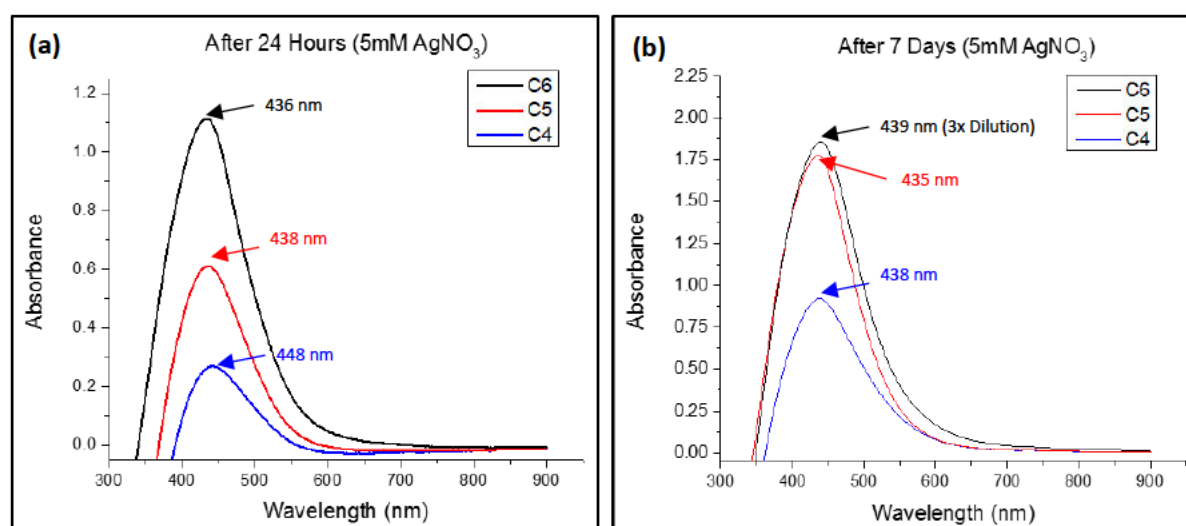


Figure 6.8. UV-VIS spectra of colloids C4 – C6, after (a) 24 Hours and (b) 7 days.

Samples C5 and C4 showed a blue shift with the indication of a smaller average particle size. This rational points to slight aggregation in C6 while colloids C4 and C5 are stabilized by the LPE.

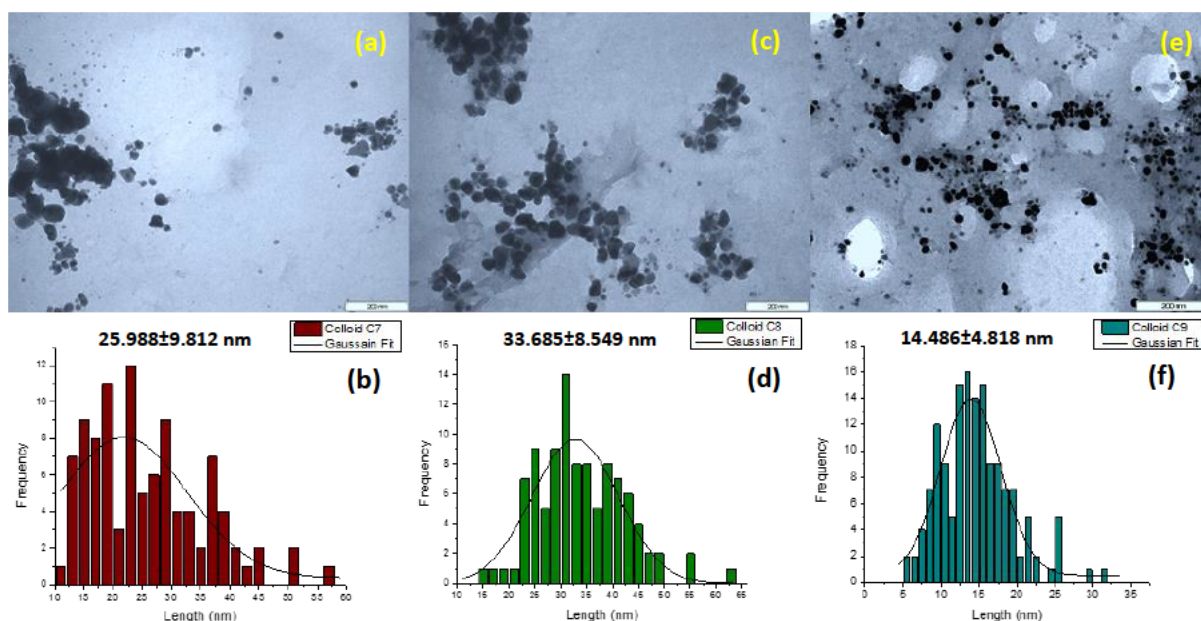


Figure 6.9. TEM micrographs and corresponding particle size distribution of colloids C7 (a-b), C8 (c-d), and C9 (e-f).

The final concentration of AgNO_3 used was 10mM. The TEM micrographs (Figure 6.9) depicts a similar trend as seen in Figure 6.5 (colloids C1 – C3) and Figure 6.7 (colloids C4 – C6) i.e. as the volume of LPE extract increases, the number of AgNPs observed increases.

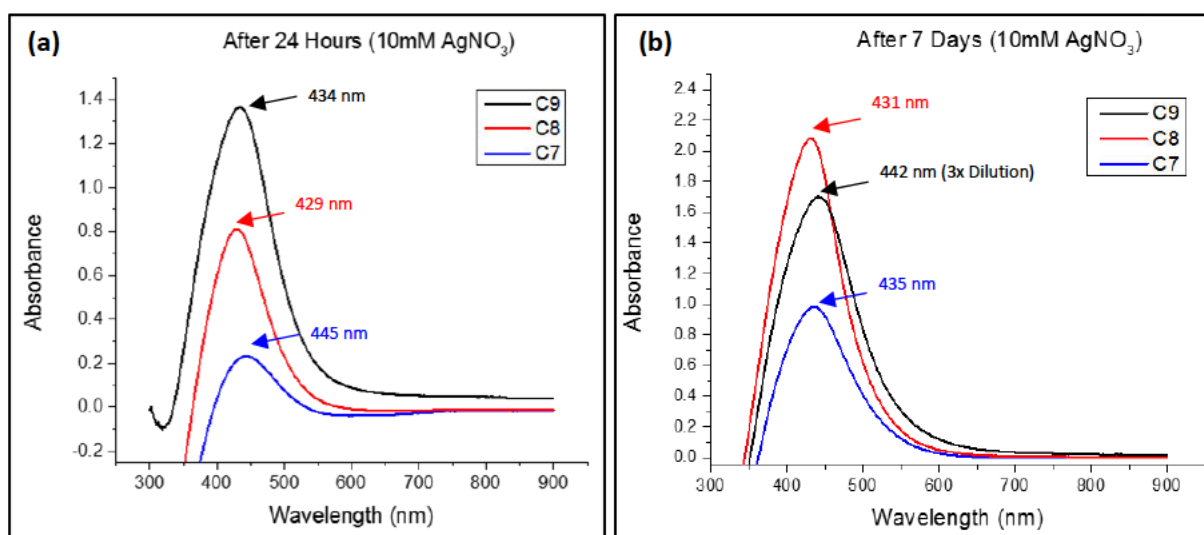


Figure 6.10. UV-VIS spectra of colloids C7 – C9, after (a) 24 Hours and (b) 7 days.

Colloid C7 (100 μL LPE, 10 mM AgNO_3), C8 (200 μL LPE, 10 mM AgNO_3) and C9 (400 μL LPE, 10 mM AgNO_3) showed an average particle size of 25.988 ± 9.812 , 33.685 ± 8.549 and 14.486 ± 4.818 nm respectively. On inspection of the increase in AgNO_3 concentration for colloids C3, C6 and C9 (Figure 6.5e and 6.5f, 6.7e and 6.5f and 6.9e and 6.5f), it is noted that as the concentration increases, the average particle size decreases. The UV-VIS spectra of

colloids C7 – C9 are seen in Figure 6.10. Samples C7 – C9 followed a similar trend as that of previous samples after 24 hours (Figure 6.10a) with maxima of 445 nm (C7), 429 nm (C8) and 434 nm (C9). After 7 days (Figure 6.10b) colloid C9 was diluted to ascertain a concise pattern. Colloids C8 and C9 show red shifted maxima's of 431 and 442 nm, respectively. This indicates moderate aggregation with an increase in average particle size.

These results lead to a general trend that as AgNO_3 concentration increases, the number of particles increases and the average size of particles decreases (stabilization by LPE). The larger the volume of plant extract dispensed into the silver solutions, the greater the number of particles formed. Particles are generally stable with little or no aggregation, hence the *L. javanica* aqueous-extract contains the necessary compounds (functional groups) to firstly reduce the Ag^+ ions to AgNPs and finally stabilize these nanoparticles, preventing aggregation. Thus further experiments pertaining to this study uses colloid C9 (400 μL LPE, 10 mM AgNO_3) as the base sample. The next study involved the addition of NCC to the colloidal sample, investigating the morphology and stability of the samples. The colloidal samples C9a (2.5 mg NCC), C9b (5 mg NCC), C9c (10 mg NCC), C9d (20 mg NCC) and C9e (100 mg NCC) were doped with respective amounts of NCC (Table 6.4).

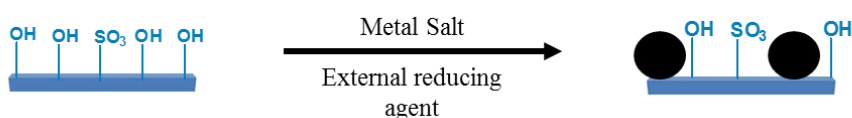
Table 6.4. Sample codes denoting each NCC supported colloidal solution

Mass (mg)	400 μL in 1 mL of 10 mM (C9)
2.5	C9a
5	C9b
10	C9c
20	C9d
100	C9e

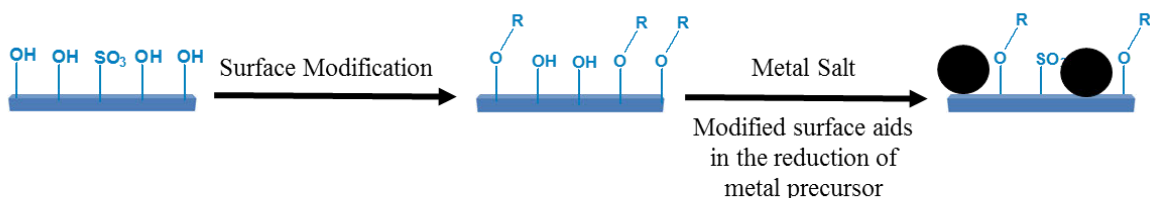
All samples showed the formation of AgNPs with the presence of NCC. AgNPs are quasi-spherical shaped in nature lying on an island of NCC rods (Figure 6.12). NCC in low weight % tend to aid in the reduction of Ag^+ ion.⁶⁴ As the weight % increases a decrease in the reduction of AgNPs is observed.⁶⁴ This is due to the alignment of NCC rods in solution. As the NCC rods align, the Van der Waals interactions form dative bonds with the Ag^+ ions in

solution and create a cage effect which slows down the rate of AgNP formation.^{46i,65} With the use of an external stimulus (LPE in the current study) acting as the reducing agent, it becomes difficult for Ag⁺ ions to interact with the reducing agent during entrapment, thus a delay in reduction of the Ag⁺ ion is observed. Upon agitation of the solution, it is observed that the reducing agent interacts with the Ag⁺ ions that are entrapped by the NCC and AgNP formation is observed. Scheme 6.1 illustrates the formation of AgNPs *via* three synthetic routes with the incorporation of NCC into the matrix.

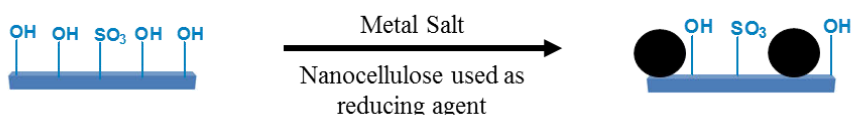
(a) Silver reduction using an external reducing agent



(b) Silver reduction using a modified nanocellulose surface



(c) Silver reduction using an external reducing agent



Scheme 6.1. Formation of AgNP with the introduction of NCC into samples with (a) an external reduction source, (b) a modified nanocellulose surface as the reducing agent and (c) unaltered nanocellulose as the reducing agent

The TEM micrographs (Figure 6.11) show the formation of AgNPs of different sizes with the introduction of NCC to colloidal sample C9 (400 μ L LPE, 10 mM AgNO₃). The average particle size of bare C9 was 14.486 \pm 4.818 nm. With the introduction of 2.5 mg NCC (colloid C9a), it is observed that the average particle size increases to 21.993 \pm 10.071 nm (Figure 6.12a and 6.12b, Figure 6.13 a) from that of colloid C9. This reiterates the fact that NCC (in low concentration) aids the LPE in the reduction of Ag⁺ ions, leading to aggregation of AgNP. Subsequently, when NCC loading is doubled to 5 mg NCC (colloid C9b), a decrease in average particle size to 10.061 \pm 5.675 nm was observed (Figure 6.11c and 6.11d, Figure 6.12b). This showed that the Ag⁺ ions were first entrapped followed by the slow reduction to AgNPs,

leading to a smaller average particle size. This was also observed for colloid C9c (10 mg NCC) with an average particle size of 10.547 ± 4.576 nm (Figure 6.11e and 6.11f, Figure 6.12c).

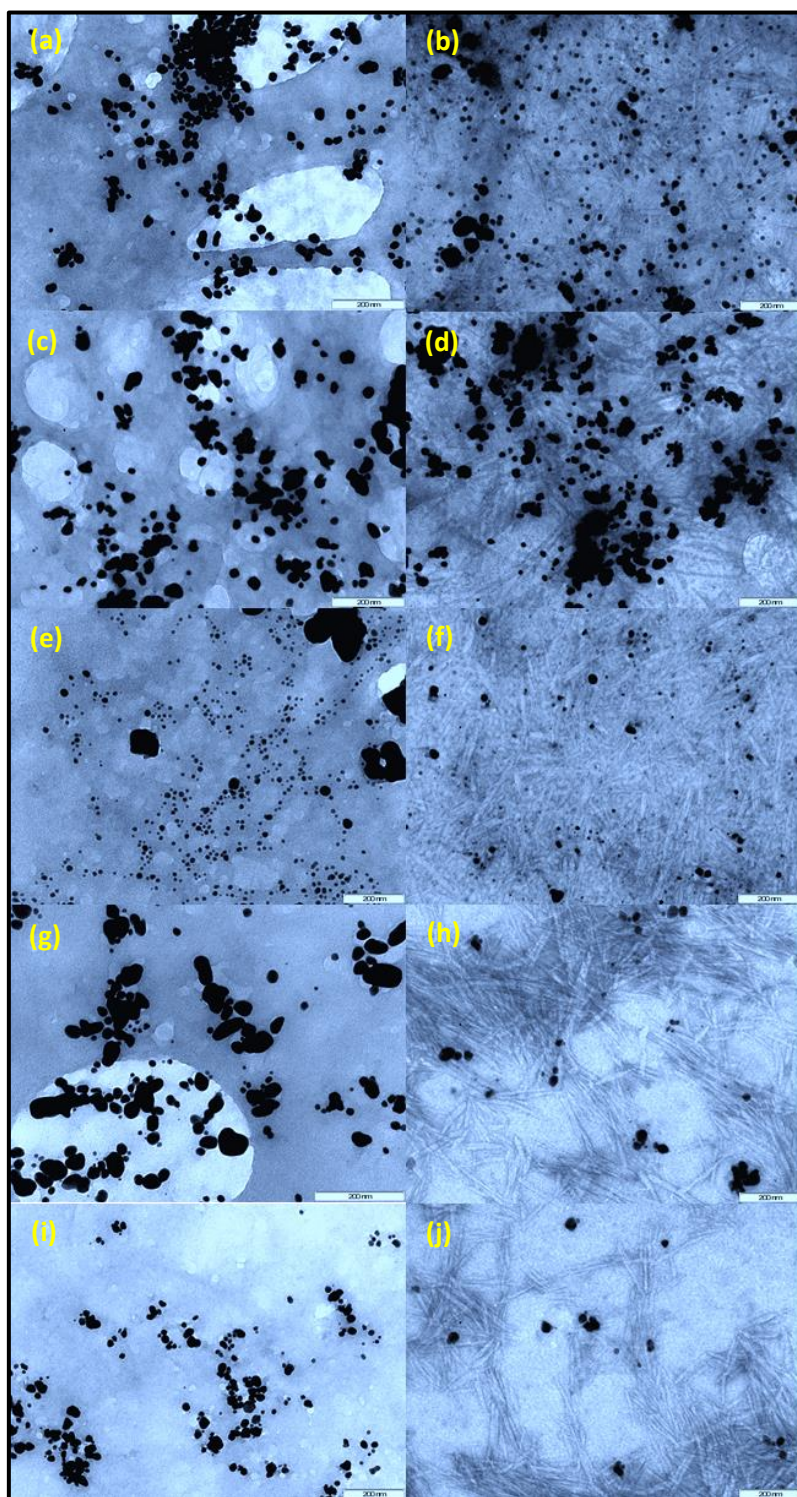


Figure 6.11. TEM micrographs of stained and unstained colloids C9a (a-b), C9b (c-d), C9c (e-f), C9d (g-h), and C9e (i-j).

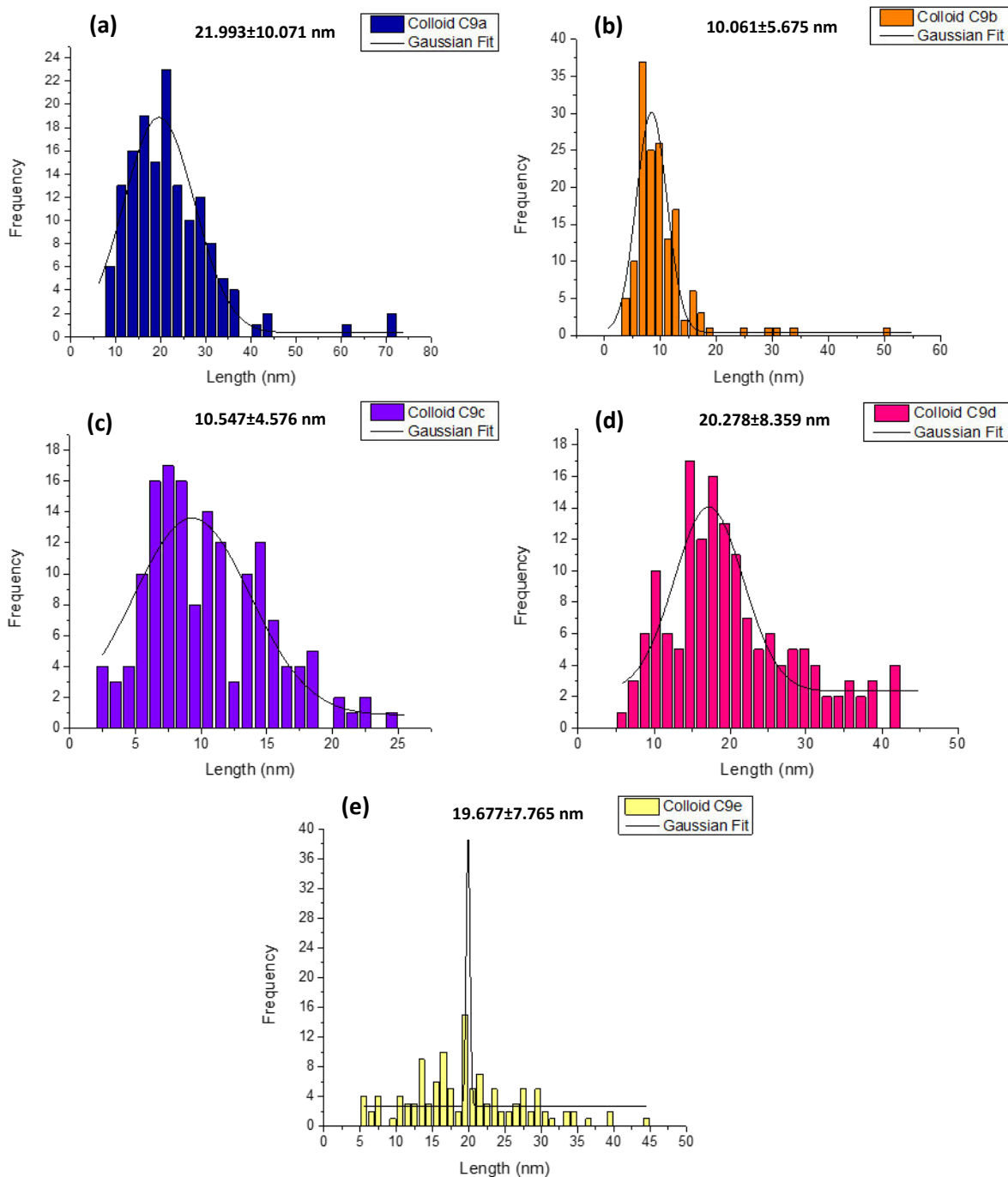


Figure 6.12. Particle size distribution of colloids C9a (a), C9b (b), C9c (c), C9d (d), and C9e (e).

Colloid C9d (20mg NCC) marked the turning point with an average particle size of 20.278 ± 8.359 nm (Figure 6.11g and 6.11h, Figure 6.12e). This result indicated that both NCC and LPE acted as reducing agents generating slightly larger AgNPs. Samples were then stabilized by the LPE and further by NCC. On addition of 100 mg (colloid C9e), similar results were observed to that of colloid C9d with an average particles size of 19.677 ± 7.765 nm (Figure 6.11i and 6.11j, Figure 6.12f). The UV-VIS spectra of all NCC containing colloids are

shown in Figure 6.13. Initial analysis shows that no formation of AgNPs were visible after 24 hours (Figure 6.13a) for colloids C9d (20 mg NCC) and C9e (100 mg NCC), which leads to the fact that the greater the concentration of NCC, the slower the reduction of Ag^+ ions to AgNPs. The formation of AgNPs was evident after 24 hours for colloid C9a (2.5 mg NCC), C9b (5 mg NCC) and C9c (10mg NCC) with peak maxima's at 433, 432 and 433 nm, respectively. The intensity of C9a was greater than that of the other peaks ($\text{C9a} < \text{C9b} < \text{C9c}$), proving the introduction of NCC in low concentrations, increased the rate of formation of AgNPs. However, with the increase in the concentration of NCC, the rate of formation of AgNPs decreased which was demonstrated by the lower intensities of C9b and subsequently C9c. The UV-VIS spectra after 7 days (Figure 6.13b) points to the fact that reduction of Ag^+ ions occurred for all samples. All samples were diluted by appropriate dilution factors to show a generalized pattern. All samples fall within a local maxima range of 418 – 423 nm, which points to a relatively coherent average particle size in bulk solution. However, in accordance with the dilution factor for each sample, it was apparent that the number of particles formed was greater for samples C9d and C9e. All samples were blue shifted in comparison to the NCC bare colloidal sample C9 (434 nm).

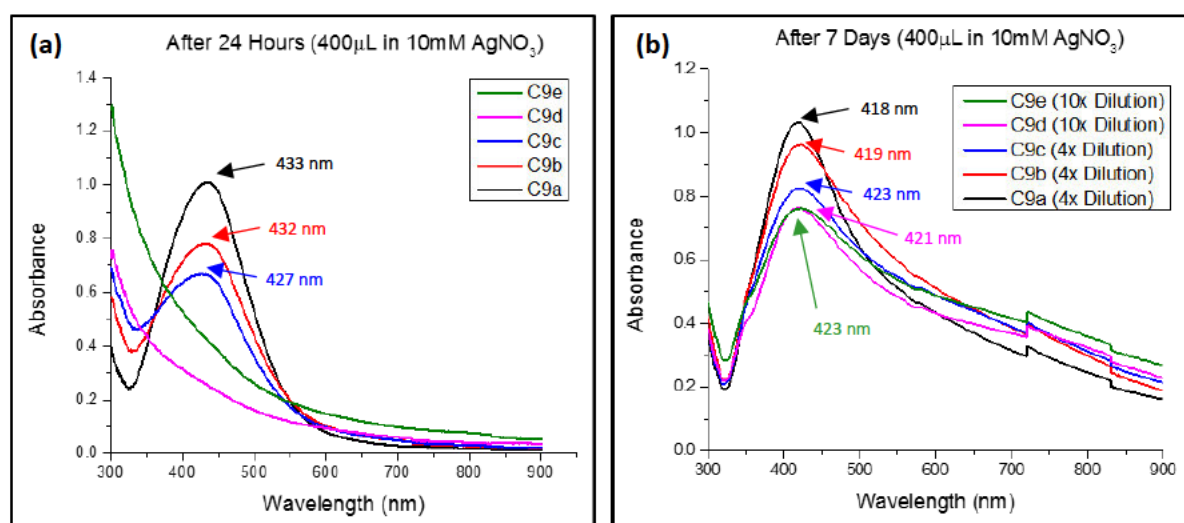


Figure 6.13. UV-VIS spectra of colloids C9a – C9e, after (a) 24 Hours and (b) 7 days.

This study led to the use of all samples in biological testing and colloidal sample C9e as a suitable catalyst for the formation of biscoumarins.

SEM analysis

SEM analysis showed the presence of NCC and AgNPs in the samples. The aggregation of NCC is a common effect which illustrates van der Waals interactions occurring between each

rod.⁶⁶ The surface morphology may indicate AgNPs on the surface as well as lying in-between a layer of NCC. The electron beam tends to be destructive toward the sample. The chosen C9e sample was then made up in bulk (1000 mg NCC, 4 mL of LPE in 10 mL of 10 mM AgNO₃ and made up to 50 mL) to be used further. This sample was then dried and successively crushed aiding its further application.

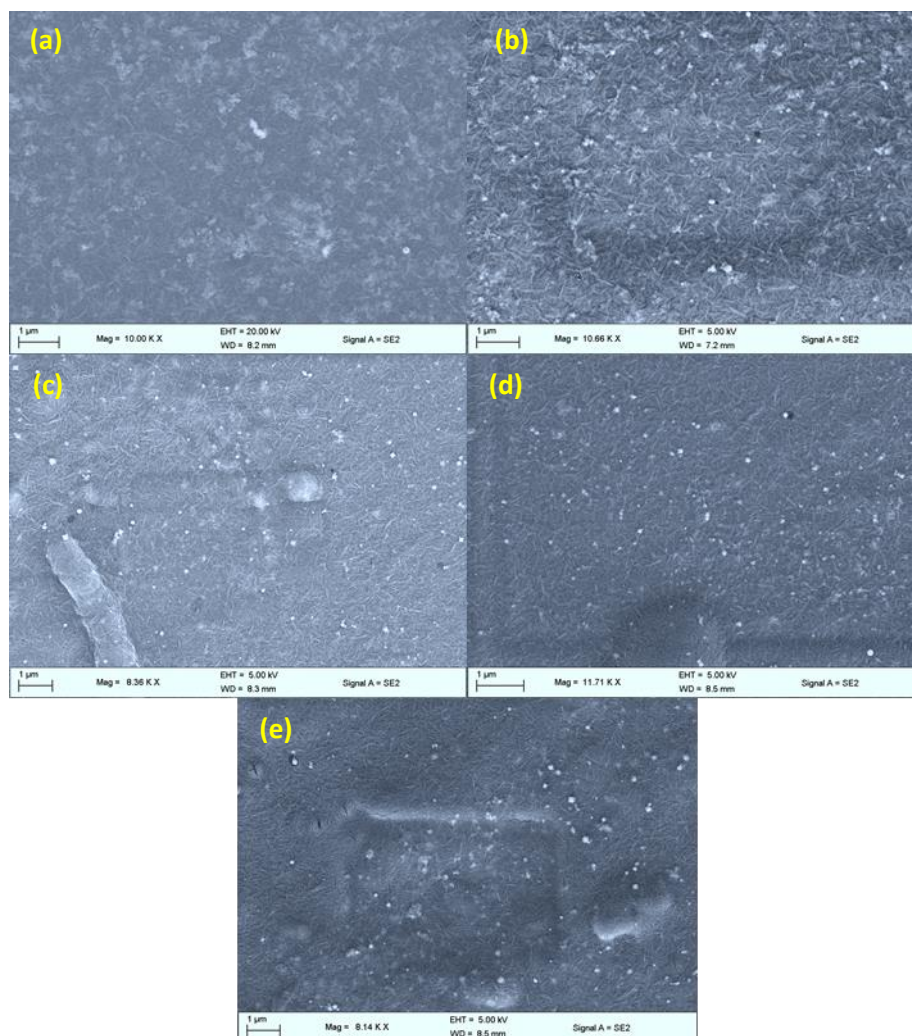


Figure 6.14. SEM micrographs of colloids C9a (a), C9b (b), C9c (c), C9d (d) and C9e (e)

The surface morphology of the crushed bulk sample (Figure 6.15a) was analysed illustrating an anisotropic layer by layer formation of NCC with the presence of AgNP in each layer.

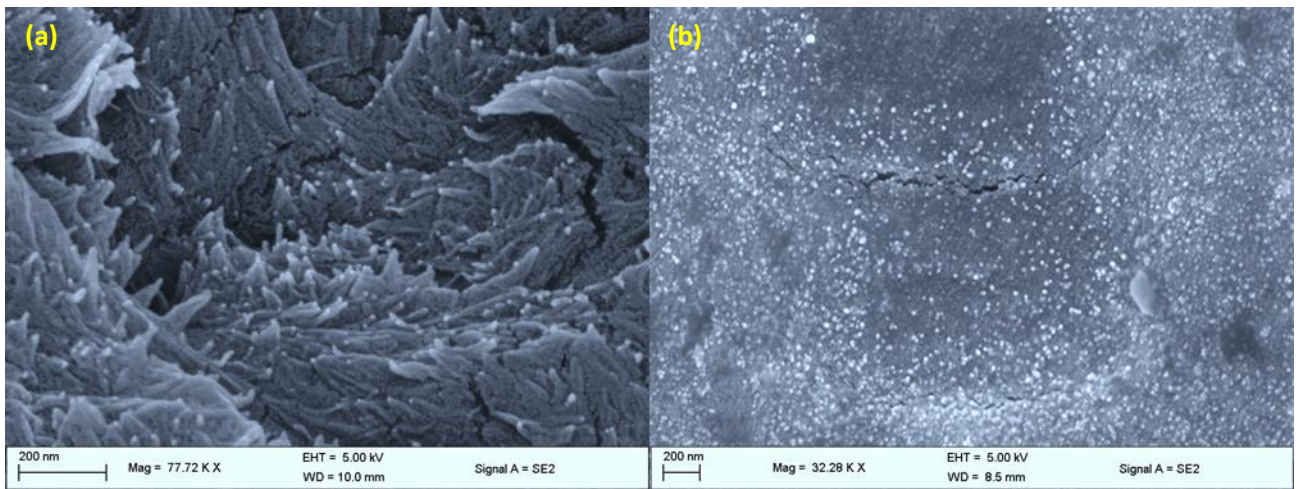


Figure 6.15. SEM micrographs of (a) colloid C9e (crushed and sieved) and (b) C9e (film)

The SEM micrograph (Figure 6.15b) of the sheet formed (prior to crushing and sieving) showed a concise layer of NCC with AgNPs above. The presence of AgNPs within each layer of NCC was further verified by EDX mapping of a cross section of the dried C9e sample (Figure 6.16). The elemental analysis showed the presence of $1.81 \pm 0.08\%$ of silver within the prescribed area (Figure 6.16b).

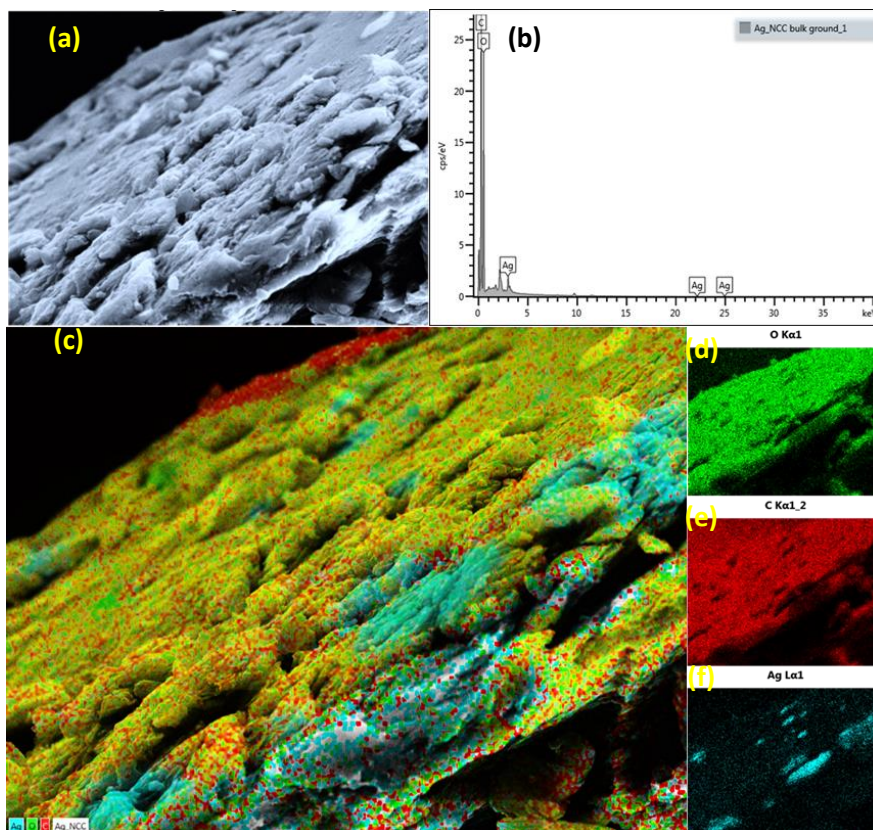


Figure 6.16. (a) SEM micrograph of cross-section of C9e sample, (b) SEM-EDX elemental analysis of cross-section of C9e sample and (c) SEM-EDX mapping of cross-section of C9e sample with each present mapped element (d) Oxygen, (e) Carbon and (f) Silver.

XRD analysis

The prepared colloidal AgNPs (C9) showed the presence of the silver phase (Figure 6.19). The diffraction peaks located at $2\theta = 38.7^\circ$, 44.8° , 64.9° and 74.9° are indexed to (111), (200), (220) and (311) planes of silver [JCPDS File no. 04-0783] which correlate with literature.⁶⁷ The inclusion of NCC (dried sample of C9e) showed a diffraction pattern identical to that of NCC-FP (Chapter 3, Figure 3.6) with peak shifts in the XRD diffractogram at $2\theta = 16^\circ$, 22° and 34° . This is attributed to the large weight % of NCC in comparison to silver content.

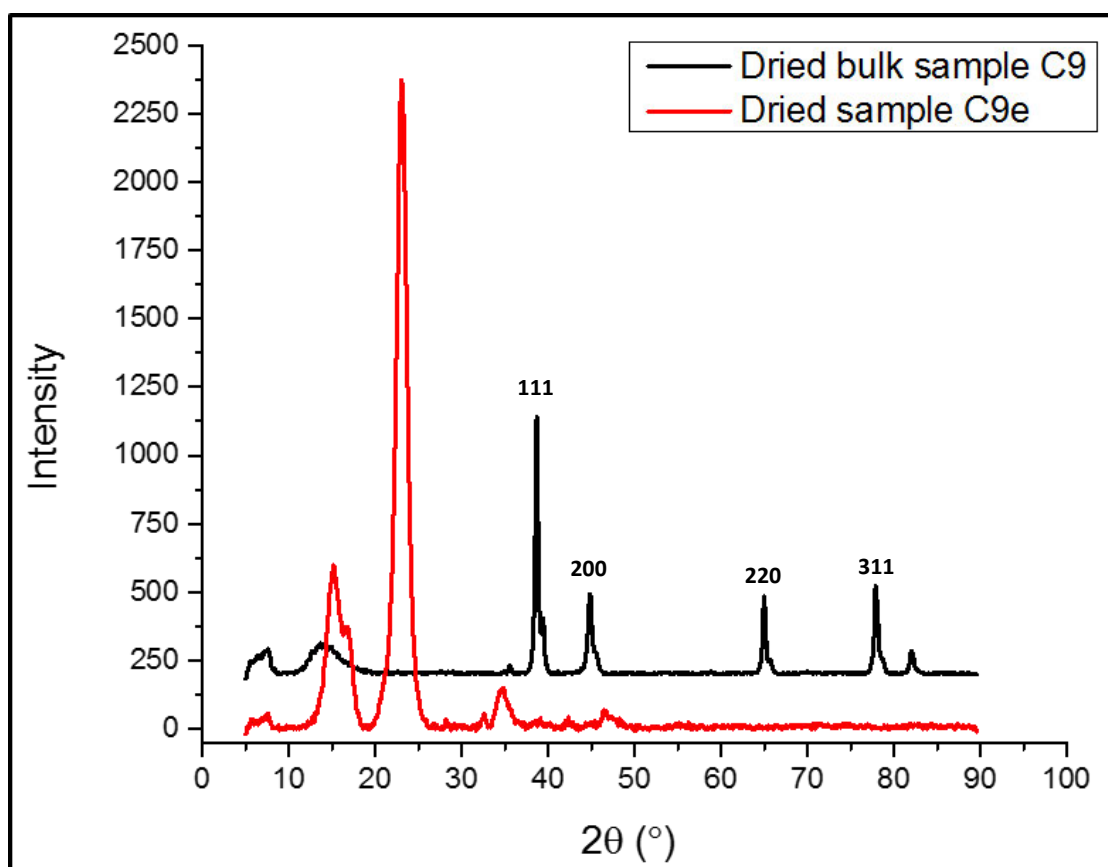


Figure 6.17. The PXRD pattern of bulk sample C9e and dried colloidal sample C9 (in bulk)

To investigate the presence of AgNPs in the dried bulk sample, TEM analysis was performed (Figure 6.19a). The presence of quasi-spherical particles indicates that AgNPs were stable upon drying of the sample. The average particle size of 14.858 ± 6.298 nm was correlated with colloidal sample C9 (Figure 6.10f). Dried bulk sample C9e was further used as the catalyst in the formation of biscoumarins.

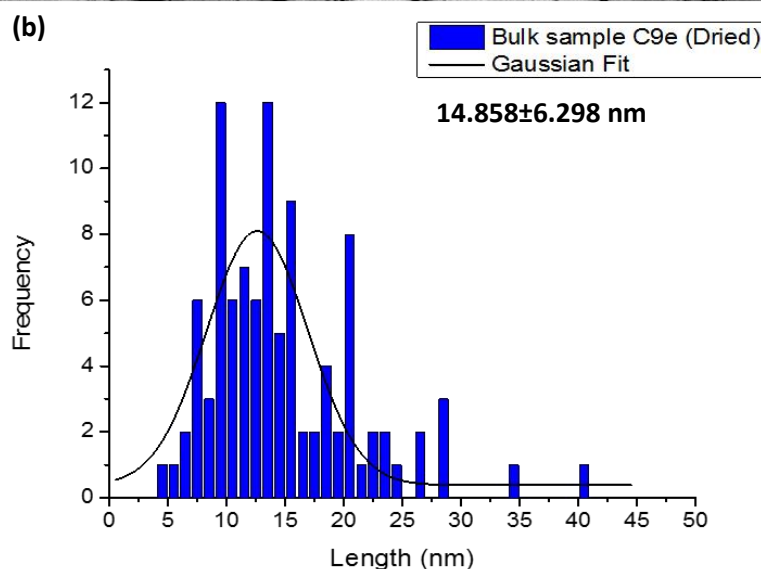
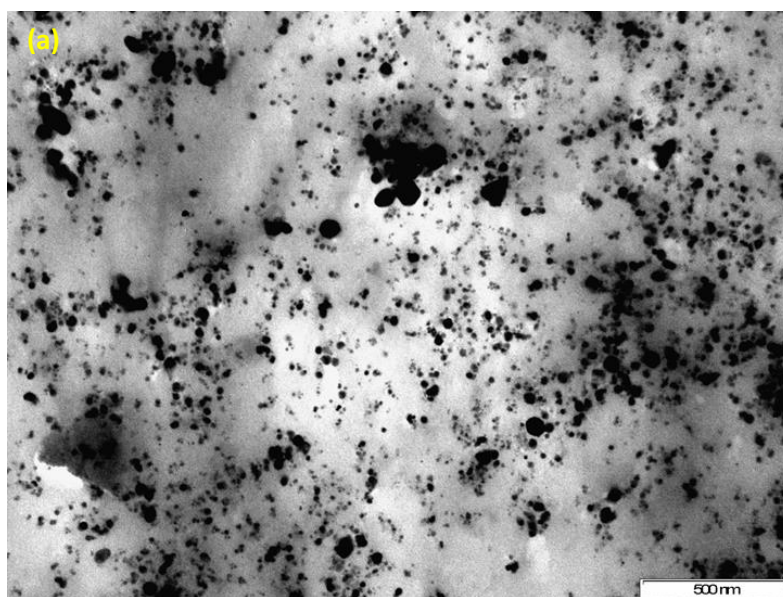
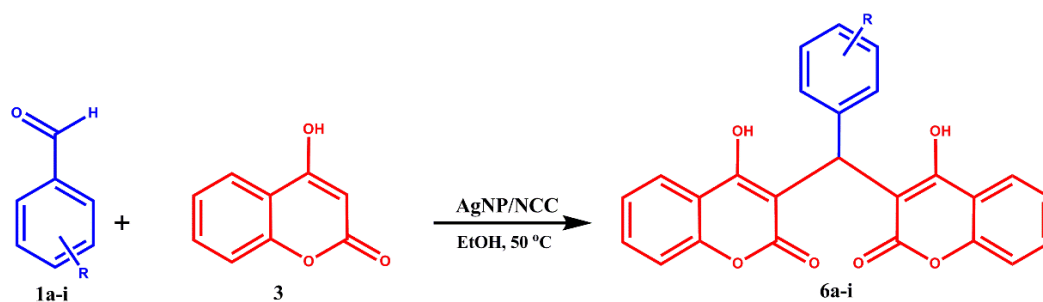


Figure 6.18. TEM micrograph of dried sample colloids C9e (a) and corresponding particle size distribution (b)

Preparation and reaction optimization of benzylidene-bis-(4-hydroxycoumarin) derivatives.

The fully optimized (model conditions) three-component reaction of substituted aldehydes and 4-hydroxycoumarin using an NCC supported AgNP catalyst (C9e) is shown in Scheme 6.1. The model reaction of 2-methoxybenzaldehyde and 4-hydroxycoumarin (molar ratio 1:2) was performed. Optimization of the reaction started with varying the solvent used.



Scheme 6.2. Synthesis of benzylidene-bis-(4-hydroxycoumarin) derivatives

The effects of solvent used were assessed, as polar solvents are generally favoured in multicomponent reactions as described in Chapter 4. The reaction (Scheme 6.2) was carried out using various polar and non-polar solvents such as MeOH, EtOH, *n*-hexane, toluene and isopropyl-alcohol, as well as solvent-free conditions (Table 6.5).

Table 6.5. Optimization of various solvent conditions for C9e catalyst^a

Entry	Solvent	Time (minutes)	Yield* (%)
1	No solvent	120	NR
2	<i>n</i> -hexane	120	NR
3	toluene	120	NR
4	MeOH	60	90
5	EtOH	30	94
6	isopropanol	90	60

^aReaction conditions: 2-methoxybenzaldehyde (1 mmol) and 4-Hydroxycoumarin (2 mmol), catalyst (50 mg (0.4 wt% Ag)) and solvent (5 mL) were stirred at 50 °C. * = Isolated yields. NR = No Reaction observed.

No reaction occurred under solvent-free conditions (Table 6.5, entry 1). The model reaction was carried out in the presence of non-polar solvents, i.e. *n*-hexane and toluene, with no reaction observed (Table 6.5, entries 2 & 3). As determined in chapter 4, polar protic solvents tend to favour multicomponent reactions, MeOH, EtOH and isopropyl-alcohol all gave good to moderate reactivity (Table 6.5, entries 4-6). Based on the calculated yields, EtOH was chosen as the ideal solvent for the present reaction system and was used for all further reactions of benzylidene-bis-(4-hydroxycoumarin) derivatives.

The NCC supported AgNP catalyst proved to be an adaptable catalyst for this system. The catalyst loading with respect to the model substrate (2-methoxybenzaldehyde) was analysed.

The results indicated that an increase in mass of catalyst from 20 mg to 40 mg, resulted in an increase in yield from 76% to 92% (Table 6.6, entries 1-3) and decrease in reaction time. When using 50 mg of catalyst, the yield increased from 92% to 96% with two fold decrease in reaction time. A further increase in wt% of catalyst to 60 mg had no further positive effect on product yield and reaction time (Table 6.6, entries 4-5). Hence 50 mg of catalyst was used for the additional reactions.

Table 6.6. Optimization of various weight % for C9e (0.4 wt% Ag) catalyst^a

Entry	Catalyst (mg)	Time (min)	Yield* (%)
1	20	120	72
2	30	60	80
3	40	60	92
4	50	30	94
5	60	30	94

^aReaction conditions: 2-methoxybenzaldehyde (1 mmol) and 4-Hydroxycoumarin (2 mmol), catalyst and solvent (5 mL) were stirred at room temperature. * = Isolated yields

Utilizing the optimised reaction conditions, the procedure was applied toward the synthesis of benzylidene-bis-(4-hydroxycoumarin) derivatives from various substituted aromatic aldehydes. The C9e heterogeneous catalyst proved to catalyse the simplistic one-pot synthesis of benzylidene-bis-(4-hydroxycoumarin) derivatives with exceptional yields. All the benzylidene-bis-(4-hydroxycoumarin) derivatives with supplementary details are shown in Table 6.7. Notably, the aldehydes with both electron-donating and electron-withdrawing (*ortho*, *meta* and *para*) substituents performed well under the reaction conditions in forming the corresponding target products (**6a-i**).

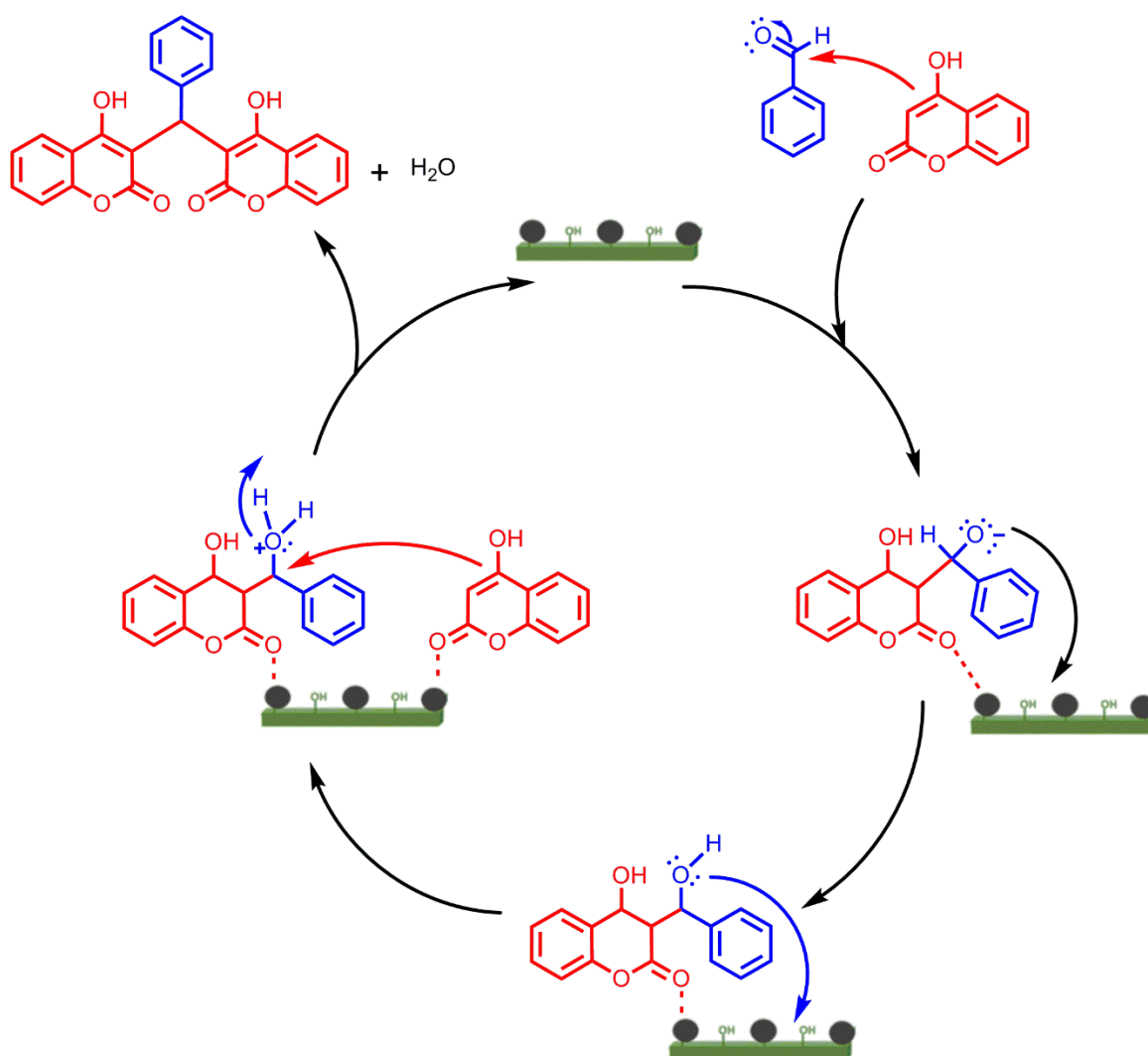
Table 6.7. Synthesis of benzylidene-bis-(4-hydroxycoumarin) derivatives with C9e catalyst^a

Entry	R	Product	Yield* (%)	Mp °C
1	2-OMe	6a	94	252-255
2	4-OMe	6b	94	205-206
3	2,3-(OMe) ₂	6c	92	229-231
4	2,5-(OMe) ₂	6d	94	218-221
5	2-Cl	6e	91	240-242
6	3,4-(OMe) ₂	6f	90	197-198
7	4-Br	6g	92	239-241
8	4-F	6h	91	221–223
9	4-Et	6i	90	246–248

^aReaction conditions: 4-Hydroxycoumarin (2mmol), substituted benzaldehyde (1 mmol), catalyst (50 mg) and ethanol solvent (5 mL) were stirred at room temperature. R = substituted benzaldehydes. * = Isolated yields

Based on the aforementioned results, a reaction mechanism (Scheme 6.2) for the synthesis benzylidene-bis-(4-hydroxycoumarin) is proposed.

In the first step, the reactive double bond of the 4-hydroxycoumarin provided nucleophilic attack on the aldehyde carbonyl group. This may cause a weak interaction with the AgNPs. Presumably, after the attack, a short-lived zwitterionic intermediate that becomes protonated by the moderately acidic NCC supported AgNP catalyst/protic solvent combination, was formed. Due to the high concentration of 4-hydroxycoumarin in solution, the further attack was propagated (by 4-hydroxycoumarin) at the same position. This resulted in the formation of a second zwitterionic intermediate which was protonated by a combination of moderately acidic NCC supported AgNP catalyst/protic solvent. The cyclization was complete upon elimination of water, presumably aided by the basic sites found on the NCC supported AgNP catalyst. The catalyst was released back into the catalytic cycle after production of a benzylidene-bis-(4-hydroxycoumarin) derivative.



Scheme 6.3. The proposed mechanism for the formation of benzylidene-bis-(4-hydroxycoumarin derivatives).

Reusability of catalyst

The recyclability of a heterogeneous catalyst is a significant requisite. Heterogeneous catalytic poisoning and leaching of metal during reactions are core limitations, which impacts on catalyst activity for further use.⁶⁸ To determine catalyst stability, recyclability experiments were performed. After each run, the catalyst was separated by filtration and was subjected to washing with excess ethanol, for up to five cycles (Figure 6.20). No considerable catalyst degradation was perceived. The catalytic activity of the NCC supported AgNP catalyst decreased when the recovered catalytic system was reused in the 5th run.

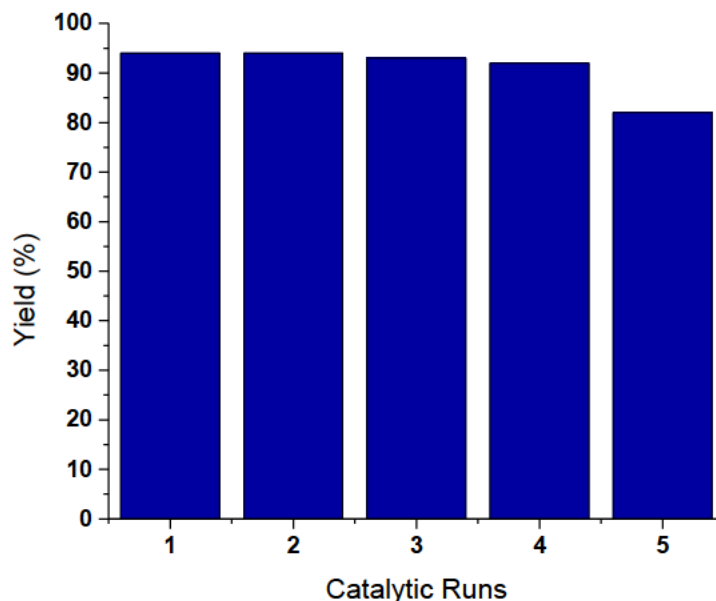


Figure 6.19. Recyclability of NCC supported AgNP catalyst.

In comparison to normal conditions using a catalyst free setup,⁵⁸ the catalytic formation of benzylidene-bis-(4-hydroxycoumarin) derivatives used milder reaction conditions and shorter reaction times. This protocol thus provides an efficient and rapid production of benzylidene-bis-(4-hydroxycoumarin) derivatives.

Anti-bacterial Activity of synthesized colloids

The biosynthesized silver colloids (C1 – C9), NCC supported AgNP colloids (C9a – C9e), pure 10 mM AgNO₃, and pure aqueous *L. javanica* plant extract (LPE) were analysed against two Gram positive bacteria, *Staphylococcus aureus* ATCC 29263 (SA) and *S. aureus* Rosenbach ATCC BAA-1683 (methicillin resistant *S. aureus* (MRSA)) and three Gram negative bacteria, *Klebsiella pneumonia* ATCC 31488 (KP), *Escherichia coli* ATCC 25922 (EC) and *Salmonella Typhimurium* ATCC 14028 (ST), by the disk diffusion method. The samples with the respective growth inhibition zones are reported in Table 6.8. Samples that showed growth inhibition zones greater than 11 mm in diameter were considered for minimum bactericidal concentration (MBC). All samples were pipetted at an initial *ca.* silver concentration of 215 µg.mL⁻¹.

Table 6.8. Diameter of Zones of Inhibition (mm) of the samples against the bacterial strains.

Sample	Zone of Inhibition (mm)				
	Gram -ve Bacteria			Gram +ve Bacteria	
	KP	ST	EC	SA	MRSA
C1	-	-	-	6	6
C2	-	6	5	8	5
C3	-	7	6	7	5
C4	10	10	8	9	10
C5	8	9	10	8	8
C6	8	10	9	8	10
C7	10	12	12	11	10
C8	10	12	14	12	11
C9	11	13	14	21	15
C9a	11	12	12	15	15
C9b	14	11	12	15	11
C9c	10	12	11	12	14
C9d	10	11	12	13	12
C9e	12	12	11	12	13
Bulk C9e	15	14	12	14	12
10 mM AgNO₃	6	7	5	6	5
Pure LPE	-	-	-	-	-

The zones of inhibitions of all active colloids and pure AgNO₃ ranged from 5 to 21 mm and exhibited greater activity against Gram-positive than Gram-negative organisms from initial screening results. It was notable that the activity of pure AgNO₃ was not as remarkable when compared to colloidal solutions and the pure LPE showed no activity against the bacterial strains. This consideration was understandable since AgNPs are considered a reservoir to introduce Ag⁺ ions upon exposure to the biological system.^{7a} Silver interacts with the thiol and amino groups of the cell wall and in doing so distract the biological processes. This allows for the uptake of silver (ions and small nanoparticles) within the cell of the organism.⁶⁹ During this process AgNPs that are in direct contact with the bacteria and tend to cause a bactericidal effect by penetrating the cell wall and releasing silver ions. In general, cells readily take up nanoparticles.⁷⁰ Eucaryotic, non-phagocytising cells take up silver nanoparticles by endocytosis and macropinocytosis.⁷¹ Thus AgNPs allow for a greater uptake of silver ions than pure silver ions in solution (AgNPs act as a carrier).^{1c, 72}

The samples C9, C9a – C9e and bulk C9e were analysed further for minimum bactericidal concentration (MBC) determination due to the largest possible concentration of AgNPs. All samples were analysed in comparison to controls (Ampicillin and Ciprofloxacin).

Table 6.9. Diameter of Inhibition (mm) of the Colloids against the bacterial strains. Lowest MBC values are indicated in blue.

Sample	Minimum Bactericidal Concentration ($\mu\text{g.mL}^{-1}$)				
	Gram -ve Bacteria			Gram +ve Bacteria	
	KP	ST	EC	SA	MRSA
C9	27	27	27	0.84	54
C9a	6.75	1.7	6.75	0.84	54
C9b	27	3.4	6.75	0.21	27
C9c	6.75	13.5	3.4	0.84	6.75
C9d	13.5	6.75	6.75	0.11	13.5
C9e	6.75	1.7	3.4	0.84	27
Bulk C9e	6.75	27	3.4	0.42	54
Ampicillin	310.98	7.55	310.98	19.57	310.98
Ciproflaxcin	12.26	0.97	0.57	0.57	0.57

In general the colloidal samples were active in very low concentration in comparison to the standards (ampicillin and ciproflaxacin). However, the deliberation of the toxic dosage levels of silver needs to be considered. The tolerated oral dosages of silver nanoparticles range from 250 to 800 mg/kg/day for small mammals,⁷³ which is much smaller when compared to the 2000 mg/kg/day for ciproflaxacin⁷⁴ and ampicillin.⁷⁵ Taking this into account, analysis of the results for the minimum bactericidal concentration (MBC) for bacterial strain KP showed a range from 6.75 – 27 $\mu\text{g.mL}^{-1}$ for colloidal samples C9 – bulk C9e. The results illustrated that the silver colloids were more active than the standards at low concentrations. In particular, C9a, C9c, C9e and bulk C9e showed the best results with a MBC of 6.75 $\mu\text{g.mL}^{-1}$. The bacterial strain ST demonstrated MBC's of 1.7 – 27 $\mu\text{g.mL}^{-1}$, which was similar to the MBC's of the standards (7.55 $\mu\text{g.mL}^{-1}$ for ampicillin and 0.97 $\mu\text{g.mL}^{-1}$ for ciproflaxacin). Samples C9a and C9e both showed a MBC of 1.7 $\mu\text{g.mL}^{-1}$. The last of the Gram-negative bacterial strains EC, illustrated

MBC's of $3.4 - 27 \mu\text{g.mL}^{-1}$ for colloids C9a – bulk C9e against the bacterial strain. The colloids all demonstrated better MBC's compared to ampicillin ($310.98 \mu\text{g.mL}^{-1}$), but were not as active as ciproflaxacin ($0.57 \mu\text{g.mL}^{-1}$). Samples C9c, C9e and bulk C9e showed the best MBC's ($3.4 \mu\text{g.mL}^{-1}$) from the colloidal samples. Comparing the gram +ve bacterial strains which belong to the same genus, it was seen that the colloidal MBC's were higher for MRSA than SA. The same trend was seen for the ampicillin standard but differs in ciproflaxacin with similar MBC's seen for both. The MBC's for SA ranged from $0.11 - 0.84 \mu\text{g.mL}^{-1}$, with colloid C9d showing the best result compared to the ampicillin ($19.57 \mu\text{g.mL}^{-1}$) and ciproflaxacin ($0.57 \mu\text{g.mL}^{-1}$). Analyses of all results showed that MBC's for MRSA was higher than all of the other strains. The MBC's of the colloidal samples ranged from $6.75 - 54 \mu\text{g.mL}^{-1}$ which is superior to ampicillin ($310.98 \mu\text{g.mL}^{-1}$) but mediocre in comparison to ciproflaxacin ($0.57 \mu\text{g.mL}^{-1}$). The lowest MBC of $6.75 \mu\text{g.mL}^{-1}$ was seen in colloid C9c. The average particle size of all samples were also considered with respect to the MBC's for the bacterial strain ST and SA. It was seen that particles with an average particle size greater than 20 nm leads to a greater bactericidal effect in both the SA and ST bacterial strain. The MRSA bacterial strain showed a greater bactericidal effect with colloidal solutions with smaller average particle size of 10 nm. The increase in NCC weight % demonstrated better MBC's for the Gram -ve bacterial strains, which may be due to increased order of AgNPs in colloidal solution i.e. additional smaller AgNPs are present in pipetted solution due to the Van der Waals interactions present between AgNPs and NCC, which allows for AgNPs to be in closer proximity with little aggregation (NCC aids in stabilization of AgNPs). The gram +ve bacterial strains showed lower MBC's with the addition of NCC as demonstrated by colloids C9d (20 mg NCC, MBC: $0.11 \mu\text{g.mL}^{-1}$) for SA and C9c (10 mg NCC, MBC: $6.75 \mu\text{g.mL}^{-1}$) for MRSA in comparison to the colloid C9 which contains no NCC (8 fold lower than NCC containing counterparts). In general, colloidal silver samples shows better MBC values and in lower dosages it can substitute known drugs in the prevention and cure of bacterial infections as well as combating drug-resistant strains.

6.4. Conclusion

Silver nanoparticles (AgNPs) were synthesized from an aqueous extract of the plant species *Lippia javanica*. The synthesized AgNPs (with varied LPE and AgNO_3 concentration) were well characterized by ATR-FTIR, XRD, TEM, FEGSEM equipped with EDX detector and

UV-VIS analysis. Nanocrystalline cellulose (from a filter paper source) was then incorporated into the quasi-spherical shaped nanoparticle matrix. This caused a significant delay in the formation of AgNPs after 24 hours which aided in the formation of smaller nanoparticles. All samples were then biologically tested against 5 bacterial strains to determine the biological effect as a bacteriacidal agent. All samples showed good activity, however, samples with the highest concentration of AgNPs were chosen for further MBC testing. The results demonstrated that all samples were relatively superior compared to the anti-biotic standards. Further use of colloidal sample C9e (once dried), proved to be successful as a catalyst for a three component reaction in the formation benzylidene-bis-(4-hydroxycoumarin) derivatives. The advantages of using a catalyst in the preparation of benzylidene-bis-(4-hydroxycoumarin) derivatives sees a greener, more efficient and faster protocol with the added advantage of being recyclable. Finally, a biosynthetic approach in the formation of AgNPs in colloidal form is possible with great advantages over co-chemical formation. These AgNPs can be used in a multitude of applications as demonstrated.

6.5. References

1. (a) Pradeep, T.; Anshup, Noble metal nanoparticles for water purification: A critical review. *Thin Solid Films* **2009**, *517* (24), 6441-6478; (b) Narayanan, R., Nanoparticles of Different Shapes for Biosensor Applications. In *Functional Nanoparticles for Bioanalysis, Nanomedicine, and Bioelectronic Devices Volume 1*, American Chemical Society: 2012; Vol. 1112, pp 281-292; (c) Jain, P. K.; Huang, X.; El-Sayed, I. H.; El-Sayed, M. A., Noble Metals on the Nanoscale: Optical and Photothermal Properties and Some Applications in Imaging, Sensing, Biology, and Medicine. *Accounts of Chemical Research* **2008**, *41* (12), 1578-1586; (d) Dreaden, E. C.; El-Sayed, M. A., Detecting and Destroying Cancer Cells in More than One Way with Noble Metals and Different Confinement Properties on the Nanoscale. *Accounts of Chemical Research* **2012**, *45* (11), 1854-1865; (e) Bansal, A.; Zhang, Y., Photocontrolled Nanoparticle Delivery Systems for Biomedical Applications. *Accounts of Chemical Research* **2014**, *47* (10), 3052-3060; (f) Qu, X.; Brame, J.; Li, Q.; Alvarez, P. J. J., Nanotechnology for a Safe and Sustainable Water Supply: Enabling Integrated Water Treatment and Reuse. *Accounts of Chemical Research* **2013**, *46* (3), 834-843.
2. (a) Kumar, A.; Vemula, P. K.; Ajayan, P. M.; John, G., Silver-nanoparticle-embedded antimicrobial paints based on vegetable oil. *Nature Materials* **2008**, *7*, 236; (b) Sintubin, L.; Verstraete, W.; Boon, N., Biologically produced nanosilver: Current state and future perspectives. *Biotechnology and Bioengineering* **2012**, *109* (10), 2422-2436.
3. (a) Korbekandi, H.; Iravani, S.; Abbasi, S., Optimization of biological synthesis of silver nanoparticles using *Lactobacillus casei* subsp. *casei*. *Journal of Chemical Technology & Biotechnology* **2012**, *87* (7), 932-937; (b) Lee, H.-J.; Song, J. Y.; Kim, B. S., Biological synthesis of copper nanoparticles using *Magnolia kobus* leaf extract and their antibacterial activity. *Journal of Chemical Technology & Biotechnology* **2013**, *88* (11), 1971-1977.
4. (a) Yang, N.; Wei, X.-F.; Li, W.-H., Sunlight irradiation induced green synthesis of silver nanoparticles using peach gum polysaccharide and colorimetric sensing of H₂O₂. *Mater. Lett.* **2015**, *154*, 21-24; (b) Mittal, A. K.; Chisti, Y.; Banerjee, U. C., Synthesis of metallic nanoparticles using plant extracts. *Biotechnology Advances* **2013**, *31* (2), 346-356.
5. (a) Shikanga, E. A.; Combrinck, S.; Regnier, T., South African Lippia herbal infusions: Total phenolic content, antioxidant and antibacterial activities. *South African Journal*

- of Botany* **2010**, 76 (3), 567-571; (b) Parratt, N. T., The Potential of Non-Timber Forest Products of Botswana. *Botswana Notes and Records* **1996**, 28, 203-218; (c) Motlhanka, D. M.; Makhabu, S. W., Medicinal and edible wild fruit plants of Botswana as emerging new crop opportunities. *Journal of Medicinal Plants Research* **2011**, 5 (10), 1836-1842; (d) Bhebhe, M.; Füller, T. N.; Chipurura, B.; Muchuweti, M., Effect of Solvent Type on Total Phenolic Content and Free Radical Scavenging Activity of Black Tea and Herbal Infusions. *Food Analytical Methods* **2016**, 9 (4), 1060-1067; (e) Maroyi, A.; Mosina, G. K., Medicinal plants and traditional practices in peri-urban domestic gardens of the Limpopo province, South Africa. **2014**.
6. Cotton, A. F.; Wilkinson, G.; Bochmann, M.; Murillo, C. A., *Advanced inorganic chemistry*. Wiley: 1999.
 7. (a) Chernousova, S.; Epple, M., Silver as Antibacterial Agent: Ion, Nanoparticle, and Metal. *Angewandte Chemie International Edition* **2013**, 52 (6), 1636-1653; (b) Alexander, J. W., History of the medical use of silver. *Surgical infections* **2009**, 10 (3), 289-292.
 8. (a) Abou El-Nour, K. M. M.; Eftaiha, A. a.; Al-Warthan, A.; Ammar, R. A. A., Synthesis and applications of silver nanoparticles. *Arabian Journal of Chemistry* **2010**, 3 (3), 135-140; (b) Mohanpuria, P.; Rana, N. K.; Yadav, S. K., Biosynthesis of nanoparticles: technological concepts and future applications. *Journal of Nanoparticle Research* **2008**, 10 (3), 507-517.
 9. (a) Poulouse, S.; Panda, T.; Nair, P. P.; Theodore, T., Biosynthesis of Silver Nanoparticles. *Journal of Nanoscience and Nanotechnology* **2014**, 14 (2), 2038-2049; (b) Vijayakumar, M.; Priya, K.; Nancy, F. T.; Noorlidah, A.; Ahmed, A. B. A., Biosynthesis, characterisation and anti-bacterial effect of plant-mediated silver nanoparticles using *Artemisia nilagirica*. *Industrial Crops and Products* **2013**, 41, 235-240.
 10. He, L.; Musick, M. D.; Nicewarner, S. R.; Salinas, F. G.; Benkovic, S. J.; Natan, M. J.; Keating, C. D., Colloidal Au-Enhanced Surface Plasmon Resonance for Ultrasensitive Detection of DNA Hybridization. *Journal of the American Chemical Society* **2000**, 122 (38), 9071-9077.
 11. Parsons, J. G.; Peralta-Videa, J. R.; Gardea-Torresdey, J. L., Chapter 21 Use of plants in biotechnology: Synthesis of metal nanoparticles by inactivated plant tissues, plant extracts, and living plants. In *Developments in Environmental Science*, Sarkar, D.; Datta, R.; Hannigan, R., Eds. Elsevier: **2007**; Vol. 5, pp 463-485.

12. (a) Sharma, V. K.; Yngard, R. A.; Lin, Y., Silver nanoparticles: Green synthesis and their antimicrobial activities. *Advances in Colloid and Interface Science* **2009**, *145* (1), 83-96; (b) Fayaz, A. M.; Balaji, K.; Girilal, M.; Yadav, R.; Kalaichelvan, P. T.; Venketesan, R., Biogenic synthesis of silver nanoparticles and their synergistic effect with antibiotics: a study against gram-positive and gram-negative bacteria. *Nanomedicine: Nanotechnology, Biology and Medicine* **2010**, *6* (1), 103-109.
13. Nadagouda, M. N.; Iyanna, N.; Lalley, J.; Han, C.; Dionysiou, D. D.; Varma, R. S., Synthesis of Silver and Gold Nanoparticles Using Antioxidants from Blackberry, Blueberry, Pomegranate, and Turmeric Extracts. *ACS Sustainable Chemistry & Engineering* **2014**, *2* (7), 1717-1723.
14. Shinde, N. M.; Lokhande, A. C.; Bagi, J. S.; Lokhande, C. D., Biosynthesis of large area (30×30cm²) silver thin films. *Materials Science in Semiconductor Processing* **2014**, *22*, 28-36.
15. Das, J.; Velusamy, P., Biogenic synthesis of antifungal silver nanoparticles using aqueous stem extract of banana. *Nano Biomedicine and Engineering* **2013**, *5* (1), 34-38.
16. AbdelHamid, A. A.; Al-Ghobashy, M. A.; Fawzy, M.; Mohamed, M. B.; Abdel-Mottaleb, M. M. S. A., Phytosynthesis of Au, Ag, and Au–Ag Bimetallic Nanoparticles Using Aqueous Extract of Sago Pondweed (*Potamogeton pectinatus* L.). *ACS Sustainable Chemistry & Engineering* **2013**, *1* (12), 1520-1529.
17. Zuas, O.; Hamim, N.; Sampora, Y., Bio-synthesis of silver nanoparticles using water extract of *Myrmecodia pendan* (Sarang Semut plant). *Materials Letters* **2014**, *123*, 156-159.
18. Nalvothula, R.; Nagati, V. B.; Koyyati, R.; Merugu, R.; Padigya, P. R. M., Biogenic synthesis of silver nanoparticles using *tectona grandis* leaf extract and evaluation of their antibacterial potential. *International Journal of ChemTech Research* **2014**, *6*(1), 293-298.
19. Mittal, A. K.; Bhaumik, J.; Kumar, S.; Banerjee, U. C., Biosynthesis of silver nanoparticles: Elucidation of prospective mechanism and therapeutic potential. *Journal of Colloid and Interface Science* **2014**, *415*, 39-47.
20. Hazarika, D.; Phukan, A.; Saikia, E.; Chetia, B., Phytochemical screening and synthesis of silver nanoparticles using leaf extract of *Rhynchoetechum ellipticum*. *International Journal of Pharmacy and Pharmaceutical Sciences* **2014**, *6* (1), 672-674.

21. Baharvandi, A.; Soleimani, M. J.; Zamani, P., Mycosynthesis of nanosilver particles using extract of *Alternaria alternata*. *Archives of Phytopathology and Plant Protection* **2015**, *48* (4), 313-318.
22. Sarvamangala, D.; Kondala, K.; Murthy, U.; Rao, B. N.; Sharma, G.; Satyanarayana, R., Biogenic synthesis of AGNP's using Pomelo fruit—characterization and antimicrobial activity against Gram+ Ve and Gram– Ve bacteria. *International Journal of Pharmaceutical Sciences Review and Research* **2013**, *19* (2), 30-35.
23. Thirunavoukkarasu, M.; Balaji, U.; Behera, S.; Panda, P. K.; Mishra, B. K., Biosynthesis of silver nanoparticle from leaf extract of *Desmodium gangeticum* (L.) DC. and its biomedical potential. *Spectrochimica Acta Part A: Molecular and Biomolecular Spectroscopy* **2013**, *116*, 424-427.
24. Rupiasih, N. N.; Aher, A.; Gosavi, S.; Vidyasagar, P. B., Green Synthesis of Silver Nanoparticles Using Latex Extract of *Thevetia Peruviana*: A Novel Approach Towards Poisonous Plant Utilization. In *Recent Trends in Physics of Material Science and Technology*, Gaol, F. L.; Shrivastava, K.; Akhtar, J., Eds. Springer Singapore: Singapore, **2015**; 1-10.
25. Asmathunisha, N.; Kandasamy, K., Rapid biosynthesis of antimicrobial silver and gold nanoparticles by in vitro callus and leaf extracts from *Lycopersicon esculentum* Mill. **2013**; *4*, 334-344.
26. Tamuly, C.; Hazarika, M.; Borah, S. C.; Das, M. R.; Boruah, M. P., In situ biosynthesis of Ag, Au and bimetallic nanoparticles using *Piper pedicellatum* C.DC: Green chemistry approach. *Colloids and Surfaces B: Biointerfaces* **2013**, *102*, 627-634.
27. Rout, A.; Jena, P. K.; Parida, U. K.; Bindhani, B. K., Green synthesis of silver nanoparticles using leaves extract of *Centella asiatica* L. For studies against human pathogens. *International Journal of Pharma and Bio Sciences* **2013**, *4* (4), 661-74.
28. Gavhane, A. J.; Padmanabhan, P.; Kamble, S. P.; Jangle, S. N., Synthesis of silver nanoparticles using extract of neem leaf and triphala and evaluation of their antimicrobial activities. *International Journal of Pharma and Bio Sciences* **2012**, *3* (3), 88-100.
29. Chauhan, S.; Upadhyay, M. K.; Rishi, N.; Rishi, S., Phytofabrication of silver nanoparticles using pomegranate fruit seeds. *International journal of Nanomaterials and Biostructures* **2011**, *1* (2), 17-21.
30. MubarakAli, D.; Thajuddin, N.; Jeganathan, K.; Gunasekaran, M., Plant extract mediated synthesis of silver and gold nanoparticles and its antibacterial activity against

- clinically isolated pathogens. *Colloids and Surfaces B: Biointerfaces* **2011**, 85 (2), 360-365.
31. Christensen, L.; Vivekanandhan, S.; Misra, M.; Mohanty, A. K., Biosynthesis of silver nanoparticles using *murraya koenigii* (curry leaf): an investigation on the effect of broth concentration in reduction mechanism and particle size. *Advanced Materials Letters* **2011**, 2(6), 429-434.
 32. Veeranna, S.; Burhanuddin, A.; Khanum, S.; Narayan, S. L.; Pratima, K., Biosynthesis and antibacterial activity of silver nanoparticles. *Research Journal of Biotechnology* **2013**, 8 (1), 11-17.
 33. Elavazhagan, T.; Arunachalam, K. D., Memecylon edule leaf extract mediated green synthesis of silver and gold nanoparticles. *International Journal of Nanomedicine* **2011**, 6, 1265-1278.
 34. Marx, H. E.; O'Leary, N.; Yuan, Y.-W.; Lu-Irving, P.; Tank, D. C.; Múlgura, M. E.; Olmstead, R. G., A molecular phylogeny and classification of Verbenaceae. *American Journal of Botany* **2010**, 97 (10), 1647-1663.
 35. Wursten, B. T. *Lippia javanica* (Burm.f.) Spreng. http://www.zimbabweflora.co.zw/speciesdata/imagedisplay.php?species_id=148720&image_id=1 (accessed 03/09/2017).
 36. Maroyi, A., *Lippia javanica* (Burm. f.) Spreng.: Traditional and Commercial Uses and Phytochemical and Pharmacological Significance in the African and Indian Subcontinent. *Evidence-Based Complementary and Alternative Medicine* **2017**, 2017.
 37. Van Wyk, B.-E.; Gericke, N., *People's plants: A guide to useful plants of Southern Africa*. Briza Publications: **2000**.
 38. (a) Kumar, S.; Singh, M.; Halder, D.; Mitra, A., *Lippia javanica*: a cheap natural source for the synthesis of antibacterial silver nanocolloid. *Applied Nanoscience* **2016**, 6 (7), 1001-1007; (b) Patiri, B.; Borah, A., *Wild edible plants of Assam*. Geetakhi Printers and Publishers, Guwahati **2007**.
 39. (a) Mwangi, J. W.; Addae-Mensah, I.; Munavu, R. M.; Lwande, W., Essential oils of Kenyan *Lippia* species. Part III. *Flavour and Fragrance Journal* **1991**, 6 (3), 221-224; (b) Manenzhe, N. J.; Potgieter, N.; van Ree, T., Composition and antimicrobial activities of volatile components of *Lippia javanica*. *Phytochemistry* **2004**, 65 (16), 2333-2336; (c) Viljoen, A. M.; Subramoney, S.; Vuuren, S. F. v.; Başer, K. H. C.; Demirci, B., The composition, geographical variation and antimicrobial activity of *Lippia javanica* (Verbenaceae) leaf essential oils. *J. Ethnopharmacol.* **2005**, 96 (1),

271-277; (d) Lukwa, N.; Molgaard, P.; Furu, P.; Bogh, C., *Lippia javanica* (Burm F) Spreng: its general constituents and bioactivity on mosquitoes. *Tropical biomedicine* **2009**, *26* (1), 85-91; (e) Chagonda, L. S.; Chalchat, J.-C., Essential oil Composition of *Lippia javanica* (Burm.f.) Spreng chemotype from Western Zimbabwe. *Journal of Essential Oil Bearing Plants* **2015**, *18* (2), 482-485; (f) Mahlangeni, N. T.; Moodley, R.; Jonnalagadda, S. B., Elemental composition of *Cyrtanthus obliquus* and *Lippia javanica* used in South African herbal tonic, Imbiza. *Arabian Journal of Chemistry* **2014**; (g) Samie, A.; Housein, A.; Lall, N.; Meyer, J. J. M., Crude extracts of, and purified compounds from, *Pterocarpus angolensis*, and the essential oil of *Lippia javanica*: their in-vitro cytotoxicities and activities against selected bacteria and *Entamoeba histolytica*. *Annals of Tropical Medicine & Parasitology* **2009**, *103* (5), 427-439; (h) Katerere, D. R.; Graziani, G.; Thembo, K. M.; Nyazema, N. Z.; Ritieni, A., Antioxidant activity of some African medicinal and dietary leafy African vegetables. *African Journal of Biotechnology* **2012**, *11* (17), 4103-4108; (i) Olivier, D. K.; Shikanga, E. A.; Combrinck, S.; Krause, R. W. M.; Regnier, T.; Dlamini, T. P., Phenylethanoid glycosides from *Lippia javanica*. *South African Journal of Botany* **2010**, *76* (1), 58-63; (j) Mujovo, S. F.; Hussein, A. A.; Meyer, J. J. M.; Fourie, B.; Muthivhi, T.; Lall, N., Bioactive compounds from *Lippia javanica* and *Hoslundia opposita*. *Natural Product Research* **2008**, *22* (12), 1047-1054; (k) Ludere, M. T.; van Ree, T.; Vlegaar, R., Isolation and relative stereochemistry of lippialactone, a new antimalarial compound from *Lippia javanica*. *Fitoterapia* **2013**, *86*, 188-192; (l) Neidlein, R.; Staehle, R., Constituents of *Lippia javanica*. III. *Deutsche Apotheker Zeitung* **1974**, *40*, 1588-1592; (m) Frum, Y.; Viljoen, A., In vitro 5-lipoxygenase and anti-oxidant activities of South African medicinal plants commonly used topically for skin diseases. *Skin Pharmacology and Physiology* **2006**, *19* (6), 329-335; (n) Chagonda, L. S.; Makanda, C. D.; Chalchat, J.-C., Essential Oils of Wild and Cultivated *Lippia javanica* (Spreng) and *L. oatesii* (Rolfe) from Zimbabwe. *Journal of Essential Oil Research* **2000**, *12* (1), 1-6; (o) Muchuweti, M.; Nyamukonda, L.; Chagonda, L. S.; Ndhkala, A. R.; Mupure, C.; Benhura, M., Total phenolic content and antioxidant activity in selected medicinal plants of Zimbabwe. *International Journal of Food Science & Technology* **2006**, *41*, 33-38; (p) Shikanga, E.; Regnier, T.; Combrinck, S.; Botha, B., Polar *Lippia* extracts as alternatives for the postharvest control of Guazatine®-resistant strains of *Penicillium digitatum* in citrus. *Fruits* **2009**, *64* (2), 75-82; (q) Sandasi, M.; Kamatou, G. P. P.; Combrinck, S.; Viljoen, A. M., A

- chemotaxonomic assessment of four indigenous South African Lippia species using GC–MS and vibrational spectroscopy of the essential oils. *Biochemical Systematics and Ecology* **2013**, *51*, 142-152.
40. (a) Borneo, R.; León, A. E.; Aguirre, A.; Ribotta, P.; Cantero, J. J., Antioxidant capacity of medicinal plants from the Province of Córdoba (Argentina) and their in vitro testing in a model food system. *Food Chemistry* **2009**, *112* (3), 664-670; (b) Huang, W.-Y.; Cai, Y.-Z.; Zhang, Y., Natural Phenolic Compounds From Medicinal Herbs and Dietary Plants: Potential Use for Cancer Prevention. *Nutrition and Cancer* **2009**, *62* (1), 1-20.
 41. Rimpler, H.; Sauerbier, H., Iridoid glucosides as taxonomic markers in the genera Lantana, Lippia, Aloysia and Phyla. *Biochemical Systematics and Ecology* **1986**, *14* (3), 307-310.
 42. Lukwa, N., Do traditional mosquito repellent plants work as mosquito larvicides? *The Central African Journal of Medicine* **1994**, *40* (11), 306-309.
 43. Bruschi, P.; Morganti, M.; Mancini, M.; Signorini, M. A., Traditional healers and laypeople: A qualitative and quantitative approach to local knowledge on medicinal plants in Muda (Mozambique). *Journal of Ethnopharmacology* **2011**, *138* (2), 543-563.
 44. Cooposamy, R.; Naidoo, K., An ethnobotanical study of medicinal plants used by traditional healers in Durban, South Africa. *African Journal of Pharmacy and Pharmacology* **2012**, *6* (11), 818-823.
 45. Ornelas, C.; Ruiz, J.; Salmon, L.; Astruc, D., Sulphonated “Click” Dendrimer-Stabilized Palladium Nanoparticles as Highly Efficient Catalysts for Olefin Hydrogenation and Suzuki Coupling Reactions Under Ambient Conditions in Aqueous Media. *Advanced Synthesis & Catalysis* **2008**, *350* (6), 837-845.
 46. (a) Cirtiu, C. M.; Dunlop-Briere, A. F.; Moores, A., Cellulose nanocrystallites as an efficient support for nanoparticles of palladium: application for catalytic hydrogenation and Heck coupling under mild conditions. *Green Chemistry* **2011**, *13* (2), 288-291; (b) Xiong, R.; Lu, C.; Zhang, W.; Zhou, Z.; Zhang, X., Facile synthesis of tunable silver nanostructures for antibacterial application using cellulose nanocrystals. *Carbohydrate Polymers* **2013**, *95* (1), 214-219; (c) Azizi, S.; Ahmad, M.; Hussein, M.; Ibrahim, N., Synthesis, Antibacterial and Thermal Studies of Cellulose Nanocrystal Stabilized ZnO-Ag Heterostructure Nanoparticles. *Molecules* **2013**, *18* (6), 6269; (d) Tian, C.; Fu, S.; Lucia, L. A., Magnetic Cu_{0.5}Co_{0.5}Fe₂O₄ ferrite nanoparticles immobilized in situ on the surfaces of cellulose nanocrystals. *Cellulose* **2015**, *22* (4), 2571-2587; (e) Shin, Y.; Bae, I.-T.; Arey, B. W.; Exarhos, G. J., Simple preparation and stabilization of nickel

- nanocrystals on cellulose nanocrystal. *Materials Letters* **2007**, *61* (14), 3215-3217; (f) Shin, Y.; Blackwood, J. M.; Bae, I.-T.; Arey, B. W.; Exarhos, G. J., Synthesis and stabilization of selenium nanoparticles on cellulose nanocrystal. *Materials Letters* **2007**, *61* (21), 4297-4300; (g) Kaushik, M.; Li, A. Y.; Hudson, R.; Masnadi, M.; Li, C.-J.; Moores, A., Reversing aggregation: direct synthesis of nanocatalysts from bulk metal. Cellulose nanocrystals as active support to access efficient hydrogenation silver nanocatalysts. *Green Chemistry* **2016**, *18* (1), 129-133; (h) Johnson, L.; Thielemans, W.; Walsh, D. A., Nanocomposite oxygen reduction electrocatalysts formed using bioderived reducing agents. *Journal of Materials Chemistry* **2010**, *20* (9), 1737-1743; (i) Wu, X.; Lu, C.; Zhou, Z.; Yuan, G.; Xiong, R.; Zhang, X., Green synthesis and formation mechanism of cellulose nanocrystal-supported gold nanoparticles with enhanced catalytic performance. *Environmental Science: Nano* **2014**, *1* (1), 71-79; (j) Wu, X.; Lu, C.; Zhang, W.; Yuan, G.; Xiong, R.; Zhang, X., A novel reagentless approach for synthesizing cellulose nanocrystal-supported palladium nanoparticles with enhanced catalytic performance. *Journal of Materials Chemistry A* **2013**, *1* (30), 8645-8652.
47. Boyd, R. N., Introduction. In *Stardust, Supernovae and the Molecules of Life: Might We All Be Aliens?*, Springer New York: New York, NY, **2012**; 1-19.
 48. Saga, T.; Yamaguchi, K., History of antimicrobial agents and resistant bacteria. *JMAJ*: **2009**; Vol. 52, 103-108.
 49. Yanling, J.; Xin, L.; Zhiyuan, L., The Antibacterial Drug Discovery. In *Drug Discovery*, El-Shemy, H. A., Ed. InTech: Rijeka, **2013**; Chapter 10.
 50. Saha, S.; Dhanasekaran, D.; Chandraleka, S.; Thajuddin, N.; Panneerselvam, A., Synthesis, characterization and antimicrobial activity of cobalt metal complex against drug resistant bacterial and fungal pathogens. *Advances in Biological Research* **2010**, *4* (4), 224-229.
 51. Hajipour, M. J.; Fromm, K. M.; Akbar Ashkarran, A.; Jimenez de Aberasturi, D.; Larramendi, I. R. d.; Rojo, T.; Serpooshan, V.; Parak, W. J.; Mahmoudi, M., Antibacterial properties of nanoparticles. *Trends in Biotechnology* **2012**, *30* (10), 499-511.
 52. Feng, Q.; Wu, J.; Chen, G.; Cui, F.; Kim, T.; Kim, J., A mechanistic study of the antibacterial effect of silver ions on *Escherichia coli* and *Staphylococcus aureus*. *Journal of biomedical materials research* **2000**, *52* (4), 662-668.

53. Lowy, F. D., Staphylococcus aureus Infections. *New England Journal of Medicine* **1998**, 339 (8), 520-532.
54. Knothe, H.; Shah, P.; Krcmery, V.; Antal, M.; Mitsuhashi, S., Transferable resistance to cefotaxime, cefoxitin, cefamandole and cefuroxime in clinical isolates of *Klebsiella pneumoniae* and *Serratia marcescens*. *Infection* **1983**, 11 (6), 315-317.
55. Kubori, T.; Matsushima, Y.; Nakamura, D.; Uralil, J.; Lara-Tejero, M.; Sukhan, A.; Galán, J. E.; Aizawa, S.-I., Supramolecular Structure of the *Salmonella typhimurium* Type III Protein Secretion System. *Science* **1998**, 280 (5363), 602-605.
56. Weinmann, I., History of the development and applications of coumarin and coumarin-related compounds. *Coumarins: biology, applications and mode of action*. John Wiley & Sons, Inc., New York, NY **1997**.
57. Marcu, M. G.; Schulte, T. W.; Neckers, L., Novobiocin and Related Coumarins and Depletion of Heat Shock Protein 90-Dependent Signaling Proteins. *JNCI: Journal of the National Cancer Institute* **2000**, 92 (3), 242-248.
58. Završnik, D.; Muratović, S.; Makuc, D.; Plavec, J.; Cetina, M.; Nagl, A.; Clercq, E. D.; Balzarini, J.; Mintas, M., Benzylidene-bis-(4-Hydroxycoumarin) and Benzopyrano-Coumarin Derivatives: Synthesis, ¹H/¹³C-NMR Conformational and X-ray Crystal Structure Studies and In Vitro Antiviral Activity Evaluations. *Molecules* **2011**, 16 (7), 6023.
59. Borges, F.; Roleira, F.; Milhazes, N.; Santana, L.; Uriarte, E., Simple Coumarins and Analogues in Medicinal Chemistry: Occurrence, Synthesis and Biological Activity. *Current Medicinal Chemistry* **2005**, 12 (8), 887-916.
60. (a) Yadav, Jhillu S.; Reddy, Basi V. S.; Basak, Ashok K.; Visali, B.; Narsaiah, Akkiralu V.; Nagaiah, K., Phosphane-Catalyzed Knoevenagel Condensation: A Facile Synthesis of α -Cyanoacrylates and α -Cyanoacrylonitriles. *European Journal of Organic Chemistry* **2004**, 2004 (3), 546-551; (b) Narsaiah, A. V.; Nagaiah, K., An Efficient Knoevenagel Condensation Catalyzed by LaCl₃·7H₂O in Heterogeneous Medium[#]. *Synthetic Communications* **2003**, 33 (21), 3825-3832.
61. Vahabi, V.; Hatamjafari, F., A Novel Synthesis of Biscoumarin Derivatives Catalyzed by ZnCl₂ Under Solvent-Free Conditions. *Oriental Journal of Chemistry* **2014**, 30 (2), 853-855.
62. Andrews, J. M., Determination of minimum inhibitory concentrations. *Journal of Antimicrobial Chemotherapy* **2001**, 48 (suppl 1), 5-16.

63. Pino-Ramos, V. H.; Ramos-Ballesteros, A.; López-Saucedo, F.; López-Barriguete, J. E.; Varca, G. H. C.; Bucio, E., Radiation Grafting for the Functionalization and Development of Smart Polymeric Materials. *Topics in Current Chemistry* **2016**, *374* (5), 63.
64. Lokanathan, A. R.; Uddin, K. M. A.; Rojas, O. J.; Laine, J., Cellulose Nanocrystal-Mediated Synthesis of Silver Nanoparticles: Role of Sulfate Groups in Nucleation Phenomena. *Biomacromolecules* **2014**, *15* (1), 373-379.
65. (a) Kaushik, M.; Friedman, H. M.; Bateman, M.; Moores, A., Cellulose nanocrystals as non-innocent supports for the synthesis of ruthenium nanoparticles and their application to arene hydrogenation. *RSC Advances* **2015**, *5* (66), 53207-53210; (b) Zhou, Z.; Lu, C.; Wu, X.; Zhang, X., Cellulose nanocrystals as a novel support for CuO nanoparticles catalysts: facile synthesis and their application to 4-nitrophenol reduction. *RSC Advances* **2013**, *3* (48), 26066-26073.
66. Elazzouzi-Hafraoui, S.; Nishiyama, Y.; Putaux, J.-L.; Heux, L.; Dubreuil, F.; Rochas, C., The Shape and Size Distribution of Crystalline Nanoparticles Prepared by Acid Hydrolysis of Native Cellulose. *Biomacromolecules* **2008**, *9* (1), 57-65.
67. Govarthanan, M.; Selvankumar, T.; Manoharan, K.; Rathika, R.; Shanthi, K.; Lee, K.-J.; Cho, M.; Kamala-Kannan, S.; Oh, B.-T., Biosynthesis and characterization of silver nanoparticles using panchakavya, an Indian traditional farming formulating agent. *International Journal of Nanomedicine* **2014**, *9*, 1593-1599.
68. Astruc, D.; Lu, F.; Aranzaes, J. R., Nanoparticles as Recyclable Catalysts: The Frontier between Homogeneous and Heterogeneous Catalysis. *Angewandte Chemie International Edition* **2005**, *44* (48), 7852-7872.
69. (a) Sotiriou, G. A.; Pratsinis, S. E., Engineering nanosilver as an antibacterial, biosensor and bioimaging material. *Current Opinion in Chemical Engineering* **2011**, *1* (1), 3-10; (b) Sotiriou, G. A.; Pratsinis, S. E., Antibacterial Activity of Nanosilver Ions and Particles. *Environmental Science & Technology* **2010**, *44* (14), 5649-5654.
70. (a) Stark, W. J., Nanoparticles in Biological Systems. *Angewandte Chemie International Edition* **2011**, *50* (6), 1242-1258; (b) Limbach, L. K.; Li, Y.; Grass, R. N.; Brunner, T. J.; Hintermann, M. A.; Muller, M.; Gunther, D.; Stark, W. J., Oxide Nanoparticle Uptake in Human Lung Fibroblasts: Effects of Particle Size, Agglomeration, and Diffusion at Low Concentrations. *Environmental Science & Technology* **2005**, *39* (23), 9370-9376; (c) Teeguarden, J. G.; Hinderliter, P. M.; Orr, G.; Thrall, B. D.; Pounds, J. G., Particokinetics In Vitro: Dosimetry Considerations for

- In Vitro Nanoparticle Toxicology Assessments. *Toxicological Sciences* **2007**, *97* (2), 614-614; (d) Brandenberger, C.; Mühlfeld, C.; Ali, Z.; Lenz, A.-G.; Schmid, O.; Parak, W. J.; Gehr, P.; Rothen-Rutishauser, B., Quantitative Evaluation of Cellular Uptake and Trafficking of Plain and Polyethylene Glycol-Coated Gold Nanoparticles. *Small* **2010**, *6* (15), 1669-1678; (e) Sokolova, V.; Epple, M., Inorganic Nanoparticles as Carriers of Nucleic Acids into Cells. *Angewandte Chemie International Edition* **2008**, *47* (8), 1382-1395; (f) Kim, J. A.; Åberg, C.; Salvati, A.; Dawson, K. A., Role of cell cycle on the cellular uptake and dilution of nanoparticles in a cell population. *Nature Nanotechnology* **2011**, *7*, 62; (g) Sahay, G.; Alakhova, D. Y.; Kabanov, A. V., Endocytosis of nanomedicines. *Journal of Controlled Release* **2010**, *145* (3), 182-195; (h) Sokolova, V.; Rotan, O.; Klesing, J.; Nalbant, P.; Buer, J.; Knuschke, T.; Westendorf, A. M.; Epple, M., Calcium phosphate nanoparticles as versatile carrier for small and large molecules across cell membranes. *Journal of Nanoparticle Research* **2012**, *14* (6), 910.
71. (a) Luther, E. M.; Koehler, Y.; Diendorf, J.; Epple, M.; Dringen, R., Accumulation of silver nanoparticles by cultured primary brain astrocytes. *Nanotechnology* **2011**, *22* (37), 375101; (b) Greulich, C.; Diendorf, J.; Simon, T.; Eggeler, G.; Epple, M.; Köller, M., Uptake and intracellular distribution of silver nanoparticles in human mesenchymal stem cells. *Acta Biomaterialia* **2011**, *7* (1), 347-354.
72. Naja, G.; Bouvrette, P.; Hrapovic, S.; Luong, J. H. T., Raman-based detection of bacteria using silver nanoparticles conjugated with antibodies. *Analyst* **2007**, *132* (7), 679-686.
73. Hadrup, N.; Lam, H. R., Oral toxicity of silver ions, silver nanoparticles and colloidal silver – A review. *Regulatory Toxicology and Pharmacology* **2014**, *68* (1), 1-7.
74. Kletter, Y.; Riklis, I.; Shalit, I.; Fabian, I., Enhanced repopulation of murine hematopoietic organs in sublethally irradiated mice after treatment with ciprofloxacin. *Blood* **1991**, *78* (7), 1685-1691.
75. Stewart, G., Toxicity of the Penicillins. *Postgraduate medical journal* **1964**, *40* (Suppl), 160.

Chapter 7: Conclusions and Future Work

7.1. Conclusion

This study pertained to the synthesis and characterization of nanocrystalline cellulose (NCC) from two sources (filter paper and bleached pulp) and the application of the nanomaterial. This was done *via* an acid-hydrolysis (chemical digestion of the majority of the amorphous region within the cellulose structure) route, using sulfuric acid as the preferred digestive medium. The isolated NCCs were obtained in reasonable yields and through the use of various characterization techniques, the confirmation of NCC formation was established. The rod-shaped particles revealed a high crystallinity, small crystallite sizes and good thermal stabilities. These results enabled the use the prepared NCC's as a composite material in the pursuit to prepare a new class of materials in an array of applications.

The initial composite preparation involved the synthesis of an NCC/hydroxyapatite (HAp) combination. This material was well characterized and proved to be a versatile catalyst in the preparation of the two-component one-pot synthesis of triazolidine-3-one derivatives. Through reaction optimization, it was established that the 40 w/w% NCC/HAp composite catalyst yielded the best results. The new triazolidine-3-one derivatives (**4a** - **4k**) were synthesized in good yield and maintained great atom economy. The catalyst proved effective for this protocol with the added advantage of being recyclable. This approach to organic multicomponent reactions (MCRs) proves to be a cost-effective strategy and allows for an easy work up with environment-friendly reaction conditions. Compared to non-catalytic protocols this approach commands shorter reaction times. Thus this new composite material allows for the synthesis of a promising range of potentially bioactive heterocycles.

Building on this, TiO₂ was then considered for its potential use as a photocatalyst. The creation of an NCC doped on to TiO₂ composite allowed for the use of NCC to successfully overcome the shortcomings associated with TiO₂. The NCC/TiO₂ material was characterized *via* a multitude of techniques to establish if it possessed potential to be used as a photocatalyst. Proceeding this the NCC/TiO₂ material was used in the solar-driven photodegradation mineralization of *o*-chloranil (2,3,5,6-tetrachloro-2,5-cyclohexadiene-1,4-dione), a commonly used pesticide. This endeavour proved successful with the mineralization of *o*-chloranil to 2,3-dichloro-4,5-dioxohex-2-enedoic acid (DCA), 2,3-dioxosuccinic acid (DSA) and oxalic acid (OA), respectively. The 20 w/w% NCC/TiO₂ exhibited the best results and thus established

that NCC could be used as a successful composite material with TiO₂. These outcomes show that the rate of degradation can be influenced by the various parameters such as substrate concentration and photocatalyst loading. The intermediate product (DCA) formed during the mineralization process could possibly slow down the progression of the reaction and provided useful insight into the degradation pathway. Thus it was determined that the NCC/TiO₂ material could be employed as a successful photocatalyst.

The final study involved the synthesis of silver nanoparticles (AgNPs) *via* biological route using a plant extract (*Lippia javanica*, LPE). The preparation of the colloidal AgNPs involved a variation in the LPE and AgNO₃ concentration to determine the ideal morphology of AgNPs formed. Samples were characterized *via* a number of spectroscopic and microscopic analyses and the ideal colloidal solution C9 (400 μL LPE, 10 mM AgNO₃) was chosen for the further incorporation of NCC. NCC (from a filter paper source) was then incorporated into the quasi-spherical shaped nanoparticle matrix and further characterized, analysed and applied as a catalyst to the synthesis of benzylidene-bis-(4-hydroxycoumarin) derivatives and as a potential bactericidal agent. All samples were biologically tested against 5 bacterial strains and demonstrated good activity, however, samples with the highest concentration of AgNPs were chosen for further MBC testing. The results established that all samples were relatively superior compared to the anti-biotics used as standards. Further use of the bulk synthesis of colloidal sample C9e (1000 mg NCC, 4 mL of LPE in 10 mL of 10 mM AgNO₃ and made up to 50 mL), once dried, proved to be successful as a catalyst for a three-component reaction in the formation benzylidene-bis-(4-hydroxycoumarin) derivatives. The advantages of using a catalyst in the preparation of benzylidene-bis-(4-hydroxycoumarin) derivatives sees a greener, more efficient and faster protocol with the added benefit of being recyclable. Thus a biosynthetic approach in the formation of AgNPs in colloidal form is possible with superior advantages over the co-chemical formation. These AgNPs can be used in a multitude of applications as demonstrated with the inclusion of NCC as a support.

In summary, nanocrystalline cellulose was successfully synthesized from two sources (filter paper and bleached pulp). These cellulosic derivatives were then successfully incorporated into the three composite materials synthesized. This allowed for the potential use of these composites as a heterogeneous catalyst in organic reactions, a heterogeneous photocatalyst in the photo-driven degradation of organic pollutants as well as an anti-bacterial agent of 'drug resistant' bacterial strains.

7.2 Future work

With the use of cellulose and in conjunction nanocellulose growing annually this biocompatible material has massive potential in a variety of fields. Possible ways to further enhance this would be to generate this desirable material from a number of greener pathways. This includes the isolation of nanocelluloses from waste materials in the industry. Thereafter the incorporation of these cellulosic materials in other matrices will allow for more robust products.

A promising field in the isolation of fuel stockpiles (additives and fuel sources) from this burgeoning material is another approach to be considered. This will allow the conversion of cellulosic materials to the platform molecule of levulinic acid and further to gamma-valerolactone (GVL).

Another field of exploration is the use of NCC derived materials as carbon based electrodes for the capacitive deionisation of brackish water. This should entail the carbonization of the NCC for its potential use.

Nano crystalline cellulose is “cheap” and “cheerful” material, with great abundance. The eventual aim would be for the commercialisation of any discoveries made to benefit all that are involved.